



UNIVERSITY OF
LIVERPOOL

Organic Nanoparticles for Photocatalytic Hydrogen Evolution

Haofan Yang

August 2021

Supervisor: Prof. Andrew I. Cooper

Thesis submitted in accordance with the requirements of the
University of Liverpool for the degree of Doctor of Philosophy

Abstract

Organic Nanoparticles for Photocatalytic Hydrogen Evolution

Haofan Yang

Solar energy is one of the most promising renewable energies. Photocatalytic solar hydrogen production provides a technologically simple and green way for hydrogen production, which is considered as the energy of the future. To be scalable, however, this approach requires more efficient photocatalysts. Photocatalysts at the nanoscale have extraordinary properties, resulting in orders of magnitude greater catalytic activities compared to bulk materials. The formation of heterojunction has also been demonstrated to be an effective strategy to enhance photocatalytic activities. This thesis will focus on the design and synthesis of efficient nano-photocatalysts for hydrogen production.

A mini-emulsion evaporation induced self-assembly method was used to incorporate titanium dioxide dots into the polymer matrix to form heterojunction nanoparticles with high morphology purity. High-resolution electron microscopy was employed to image the internal structure of the resulting nanoparticles. We then tested photocatalytic performance and found that heterojunction nanoparticles outperformed nanoparticles of the individual components and physical mixtures thereof. The most active one had a hydrogen production rate that was 4.25 times higher than pure polymer nanoparticles prepared under the same condition. We ascribe this to energy transfer between the titanium dioxide dots and polymer, where direct phase contact is essential.

The power conversion efficiency has been significantly improved by introducing donor-acceptor bulk heterojunctions in the field of organic photovoltaics (OPV). We transferred this strategy to photocatalysis by making donor-acceptor nanocomposites (DANCs) via a nanoprecipitation method. A library of 237 organic binary/ternary nanocomposites consisting of conjugated polymers donors and either fullerene or non-fullerene molecular acceptors was prepared and screened for sacrificial photocatalytic hydrogen evolution. The best one showed a high hydrogen evolution rate (HER) of $105.2 \text{ mmol g}^{-1} \text{ h}^{-1}$ under visible light ($\lambda > 420 \text{ nm}$). A machine learning method was applied to further accelerate material discovery. About 100 ternary nanocomposites were initially tested and the results were used to train the machine learning model. This model was subsequently used for the prediction of high-performance nanocomposites.

We also synthesised a new small organic molecule, 2,6-bis(4-cyanophenyl)-4-(9-phenyl-9*H*-carbazol-3-yl)pyridine-3,5-dicarbonitrile (CN90). This molecule can be processed into amorphous nanospheres and crystalline nanofibres by the nanoprecipitation method. The transformation from nanospheres to nanofibres can be achieved under certain conditions. This transformation process was studied by a series of in-situ spectroscopic characterisations. Nanofibres showed much higher photocatalytic H₂ production performance than nanospheres, whereas nanospheres achieved significantly higher photocatalytic H₂O₂ production performance. The different aggregate states result in their photophysical properties, such as energy band levels and light absorption, being different, which triggers the photocatalytic direction switching between photocatalytic H₂ evolution and H₂O₂ production.

Acknowledgements

First, I would like to thank Professor Andy Cooper for giving me the opportunity to work on this project and valuable supervision to finish this project. Thanks also to Dr Xiaobo Li for your guidance, support, and supervision throughout this work and completion of this thesis. Thanks also to Dr Reiner Sebastian Sprick and Dr Marc Little for your valuable supervision and guidance. Thank you for all your supervision and it guides me a lot for my future.

I would also like to thank all those I have collaborated with on this work, especially Chao Li and Prof. Alex Cowan at the Stephenson Institute for Renewable Energy, and Dr Mounib Bahri, Dr Houari Amari, and Prof. Nigel Browning at the Albert Crewe Centre for Electron Microscopy. This work would not have been possible without your help and guidance. Thanks also to the Leverhulme Research Centre for Functional Materials Design for providing funding for my research and living costs.

Thanks to Bonnie, Rob, Marc, Xiaofeng, Linjiang, Ming, Yongjie, various Wei (Kewei, Weiwei, Wei Zhao), Yang, Xiaoyan, Lunjie, Zhongfu, Zhiwei, Peng, Christian, Ben Alston and Burger, Sam, Qiang, Xue, Yu and Chengxi for giving a lot of help and discussion on research. Thanks must also go to Ammar, Duncan, and Cath for valuable advice on my work and enjoy the great football time together. Thanks to all AIC group members past and present for sharing the wonderful lab time. Also, thanks to Rob Clowes for fixing all the instruments and Kewei and Yongjie for teaching and helping with organic synthesis.

Special thanks to Craig for reminding me not to cause trouble all the time in the lab and very valuable and meaningful AJ talk every Friday as well as help on making corrections on the thesis. Special thanks also go to Ai, Hui, and Hongmei for simple drinking and eating friendship.

Thanks also to many nice places in UK like lake district, peak district, Mr Chilli, and FSK (free style kitchen) for hosting many memorable Cooper group socializing events. I enjoy having a couple of drinks in the pub, the best Fish and Chips in West Kirby, going hiking, climbing the mountain, and even sleeping on a ferry.

Finally, I must thank my friends and family for everything they've done for me during the last four years. In particular, thanks to my parents and my girlfriend Ni for your continuous love, encouragement, and support. I couldn't have done this without you.

List of Publications

“Nano-assemblies of a soluble conjugated organic polymer and an inorganic semiconductor for sacrificial photocatalytic hydrogen production from water”

Haofan Yang, Houari Amari, Lunjie Liu, Chengxi Zhao, Hui Gao, Ai He, Nigel D. Browning, Marc A. Little, Reiner Sebastian Sprick, and Andrew I. Cooper, *Nanoscale*, 2020, 12, 24488-24494.

“Conjugated polymer donor–molecular acceptor nanohybrids for photocatalytic hydrogen evolution”

Haofan Yang, Xiaobo Li, Reiner Sebastian Sprick, and Andrew I. Cooper, *Chem. Commun.*, 2020, 56, 6790-6793.

“Crosslinked Polyimide and Reduced Graphene Oxide Composites as Long Cycle Life Positive Electrode for Lithium-Ion Cells”

Hui Gao, Bingbing Tian, Haofan Yang, Alex R. Neale, Marc A. Little, Reiner Sebastian Sprick, Laurence J. Hardwick, and Andrew I. Cooper, *ChemSusChem*, 2020, 13, 5571.

“Synthesis of Stable Thiazole-Linked Covalent Organic Frameworks via a Multicomponent Reaction”

Kewei Wang, Zhifang Jia, Yang Bai, Xue Wang, Sophie E. Hodgkiss, Linjiang Chen, Samantha Y. Chong, Xiaoyan Wang, Haofan Yang, Yongjie Xu, Feng Feng, John W. Ward, and Andrew I. Cooper, *J. Am. Chem. Soc.*, 2020, 142, 11131-11138.

“Photocatalytic Polymers of Intrinsic Microporosity for Hydrogen Production from Water”

Yang Bai, Liam Wilbraham, Hui Gao, Rob Clowes, Haofan Yang, Martijn Zwijnenburg, Andrew Cooper, and Reiner Sebastian Sprick, *J. Mater. Chem. A*, 2021.

Table of Content

Abstract.....	I
Acknowledgements	III
List of Publications	IV
Table of Content.....	V
List of Abbreviations	IX
Chapter 1 Introduction.....	1
1.1. Clean Energy Production in a Sustainable Manner.....	2
1.1.1. Current Energy Production	2
1.1.2. Renewable Energies	2
1.1.3. Solar-to-chemical Energy Conversion.....	4
1.2. Photocatalytic Water Splitting	5
1.2.1. Hydrogen Applications and Production	5
1.2.2. Processes in Photocatalytic Water Splitting	6
1.2.3. Sacrificial Water Splitting	7
1.2.4. Overall Water Splitting.....	8
1.2.5. Approaches to Boost Photocatalytic Activity.....	9
1.3. Bulk Materials for Photocatalytic Water Splitting.....	10
1.3.1. Inorganic Materials.....	10
1.3.2. Organic Materials	13
1.3.2.1. Organic Photocatalysts.....	13
1.3.2.2. Design Rules	16
1.3.3. Heterojunction Materials	17
1.3.3.1. Inorganic/inorganic Heterojunctions	19
1.3.3.2. Inorganic/organic Heterojunctions.....	19
1.3.3.3. Organic/organic Heterojunctions	20
1.4. Nanomaterials for Photocatalytic Water Splitting	21
1.4.1. Inorganic Nanomaterials.....	21
1.4.2. Organic Nanomaterials	22
1.4.2.1. Nanoprecipitation Mechanism	22
1.4.2.2. Conjugated Polymer Nanoparticles	22
1.4.3. Heterojunction Nanomaterials	25
1.5. Experimental Techniques.....	27

1.5.1. High Throughput Methodology	28
1.6. Project Aims	28
1.7. Reference.....	31
Chapter 2 Organic Polymer-Inorganic Dots Nanocomposites	39
2.1. Contributions to this Chapter	40
2.2. Background	40
2.3. Preparation of Nano-assemblies.....	41
2.3.1. Preparation and Characterisation of Titanium Dioxide Dots	41
2.3.2. Preparation and Characterisation of Soluble Polymer.....	42
2.3.3. Formation of Nanoassemblies	44
2.4. Morphology and Optical Properties	47
2.4.1. Morphology and Internal Structure	47
2.4.2. Absorption and Emission Properties	51
2.5. Photocatalytic Hydrogen Production from Water	58
2.5.1. Nanoparticles and Nanocomposites.....	58
2.5.1.1. Photocatalytic Test on Solar Simulator.....	58
2.5.1.2. Photocatalytic Test on Xe Lamp.....	59
2.5.2. Physical Mixtures and Other Control Experiment	62
2.6. Conclusions	66
2.7. Experimental	67
2.7.1. Preparation Methods.....	67
2.7.2. Characterisation Methods	69
2.7.3. Measurement Methods	70
2.8. References	73
Chapter 3 Donor-acceptor Nanocomposites.....	76
3.1. Contributions to this Chapter	77
3.2. Background	77
3.3. High Throughput Photocatalytic Performance.....	77
3.3.1. Conjugated Polymer Donors/fullerene acceptors	79
3.3.2. Conjugated Polymer Donors/non-fullerene acceptors.....	85
3.4. Characterisations	86
3.4.1. Morphology and Absorption Properties	86
3.4.2. Emission Properties	88

3.5. Kinetic Photocatalytic Performance	91
3.5.1. Photocatalytic Performance	91
3.5.2. Characterisations after Photocatalysis	95
3.6. Ternary System	97
3.6.1. Random Screen on Ternary System	97
3.6.2. Machine Learning Assisted Ternary System.....	100
3.6.2.1. Background.....	100
3.6.2.2. Dataset.....	102
3.6.2.3. Descriptor Engineering	102
3.6.2.4. Model Selection and Machine Learning	103
3.6.2.5. Machine Learning Guided Search Outcome.....	105
3.7. Conclusions	107
3.8. Experimental	108
3.8.1. Preparation Methods.....	108
3.8.2. Characterisation Methods	111
3.8.3. Measurement Methods	111
3.9. References	113
Chapter 4 Organic Molecular Nanoparticles	115
4.1. Contributions to this Chapter	116
4.2. Background	116
4.3. Molecular Structure and Solution-state Properties	117
4.4. Nanoparticles.....	121
4.4.1. Morphology	121
4.4.2. Structure.....	122
4.4.3. Absorption and Emission.....	127
4.4.4. Morphology Transformation	129
4.5. Photocatalysis Measurement.....	133
4.5.1. Photocatalytic Hydrogen Evolution.....	134
4.5.2. Photocatalytic Hydrogen Peroxide Evolution	135
4.6. Conclusions	144
4.7. Experimental	145
4.7.1. Preparation Methods.....	145
4.7.2. Characterisation Methods	147

4.7.3. Measurement Methods	148
4.7.3.1. Photocatalysis Measurements	148
4.7.3.2. Apparent Quantum Yield Measurements.....	149
4.7.3.3. Density Functional Theory Calculations	150
4.7.3.4. Photoelectrochemical Measurements.....	150
4.8. References	151
Chapter 5 Summary & outlook	154

List of Abbreviations

λ_{exc}	Excitation wavelength
λ_{em}	Emission maxima wavelength
AM1.5G	Air mass 1.5 global filter
CPN	Conjugated polymer nanoparticles
EQE	External quantum efficiency
C ₃ N ₄	Carbon nitride
P3HT	Poly(3-hexylthiophene)
D-A	Donor-acceptor
IRF	Instrument response
EDX	Energy-dispersive X-ray spectroscopy
TDs	Titanium dioxide dots
CSCP	Cyano-benzene-co-fluorene polymer
HER	Hydrogen evolution rate
g-C ₃ N ₄	Graphitic carbon nitride
CMPs	Conjugated microporous polymers
COF	Covalent organic framework
FS-COF	Fused sulfone-containing COF
CTF	Covalent triazine-based framework
EISA	Evaporation induced self-assembly
e^-	Electron
AA	Ascorbic acid
AQY	Apparent quantum yield
FS	Fluorene-dibenzo[<i>b,d</i>]thiophene sulfone copolymer
SA-TCPP	Self-assembled tetra(4-carboxylphenyl)porphyrin
FT-IR	Fourier transform infrared
FTO	Fluorine-doped tin oxide
GC	Gas chromatography
DANCs	Donor-acceptor nanocomposites
QDs	Quantum dots

FFT	Fast Fourier transform pattern
h^+	Hole
HOMO	Highest occupied molecular orbital
HT	High throughput
GPC	Gel permeation chromatography
ICP-OES	Inductively coupled plasma-optical emission spectrometry
PLGA	Poly(lactic-co-glycolic acid)
LUMO	Lowest unoccupied molecular orbital
CPNs	Conjugated polymer nanoparticles
PCE	Power conversion efficiency
PTB7-Th	Poly([2,6'-4,8-di(5-ethylhexylthienyl) benzo[1,2-b;3,3-b]dithiophene]{3-fluoro-2[(2-ethylhexyl)carbonyl]thieno[3,4-b]thiophenediyil})
HRTEM	High-resolution transmission electron microscopy
BF-STEM	Bright-field transmission electron microscopy
M_n	Number-average molecular weight
M_w	Weight-average molecular weight
NMR	Nuclear magnetic resonance
SDS	Sodium <i>n</i> -dodecyl sulfate
OWS	Overall water splitting
O.D.	Optical density
CN90	2,6-Bis(4-cyanophenyl)-4-(9-phenyl-9 <i>H</i> -carbazol-3-yl)pyridine-3,5-dicarbonitrile
CN90-s	CN90 nanosphere
HONTO	Highest occupied natural transition orbitals
LUNTO	lowest unoccupied natural transition orbitals
CN90-f	CN90 nanofibre
OSC	Organic solar cells
TSC	Ternary solar cells
DDA	Donor-donor-acceptor

DAA	Donor-acceptor-acceptor
PFBT	Poly[(9,9'-dioctylfluorenyl-2,7-diyl)-co-(1,4-benzo-{2,1',3}thiadiazole)]
PS-PEG-COOH	Carboxyl-group-functionalized ethylene oxide
OPV	Organic photovoltaic
PCN	Polymeric carbon nitride
PDI	Perylene tetracarboxylic diimide
PFO	Poly(9,9-di- <i>n</i> -octylfluorenyl-2,7-diyl)
PCzF	Poly(<i>N</i> -decanyl-2,7-carbazole- <i>alt</i> -9,9-dioctylfluorene)
STEM	Scanning transmission electron microscopy
HAADF-STEM	High-angle annular dark-field STEM
STEM-EELS	Scanning transmission electron microscopy-electron energy loss spectroscopy
PXRD	Powder X-ray diffraction
THF	Tetrahydrofuran
OLM	Oleylamine
OA	Oleic acid
PS	Polystyrene
TBT	Titanium (IV) n-butoxide
PV	Photovoltaic
XANES	X-ray absorption near-edge structure
EH-IDTBR	5,5'-[[4,4,9,9-Tetrakis(2-ethylhexyl)-4,9-dihydro-s-indaceno[1,2-b:5,6-b']dithiophene-2,7-diyl]bis(2,1,3-benzothiadiazole-7,4-diylmethylidyne)]bis[3-ethyl-2-thioxo-4-thiazolidinone]
RGO	Reduced graphene oxide
TEM	Transmission electron microscopes
SHE	Standard hydrogen electrode
NHE	Normal hydrogen electrode
RHE	Reversible Hydrogen Electrode

STH	Solar-to-hydrogen
FE-SEM	Field emission scanning electron microscope
Pdots	Polymer dots
TCSPC	Time-correlated single photon counting
DLS	Dynamic light scattering
OA	Oleic acid
(TD)-DFT	Time-dependent density functional theory
TEA	Triethylamine
2CZPN	4,5-Di(carbazol-9-yl)phthalonitrile
THPP	5,10,15,20-Tetrakis(4-(hydroxyl)phenyl)porphyrin
PTT	Photothermal therapy
TEOA	Triethanolamine
PANI	Polyaniline
TGA	Thermogravimetric analysis
TD-DFT	Time-dependent DFT
UV	Ultraviolet
SEM	Scanning electron microscope
UV-vis	Ultraviolet-visible
CB	Conduction band
VB	Valence band
NPs	Nanoparticles
NCs	Nanocomposites
CV	Cyclic voltammetr
BE	Polybenzothiadiazole

Chapter 1

Introduction

1.1. Clean Energy Production in a Sustainable Manner

1.1.1. Current Energy Production

Energy generation has been dominated by using fossil fuels, such as petroleum and other liquids, coal, and natural gas, for the last hundred years. Around 80% of energy consumption is provided by fossil fuels in 2020.¹ Fossil fuel burning is essential for our daily energy consumption, but this also brings economic and environmental issues. The prices of fossil fuels are expected to increase because fossil fuels are limited in nature. Another issue is emissions of greenhouse gases, such as carbon dioxide, which are responsible for global warming and detrimental to human health.

1.1.2. Renewable Energies

Reducing the use of fossil fuels is important for environmental protection. However, energy demands are increasing due to the rising population. The only way to reduce the use of fossil fuels and meet the growing energy demands is to search for replacement renewable energies, which can produce energy in an environmentally benign and sustainable manner. The benefits of doing this are global.

Renewable energies are energy sources that are derived directly from the Sun (such as thermal, photochemical, and photo-electric), indirectly from the Sun (such as wind, hydropower, and photosynthetic energy stored in biomass), or from other natural movements and mechanisms of the environment (such as geothermal and tidal energy).² Before 2017, more than half of the electricity generation by renewable energies came from hydropower (**Figure 1.1**).³ The use of non-hydro renewable energies shows a gradual increase from 2010 to 2025 and is expected to surpass the use of hydropower in 2024 (**Figure 1.1**).³ One of the unique features of renewable energies is that they can be continually replenished by nature, which makes them different from limited resources like fossil fuels. Therefore, renewable energies are promising candidates to replace fossil fuels because of their ability to produce clean energy sustainably.

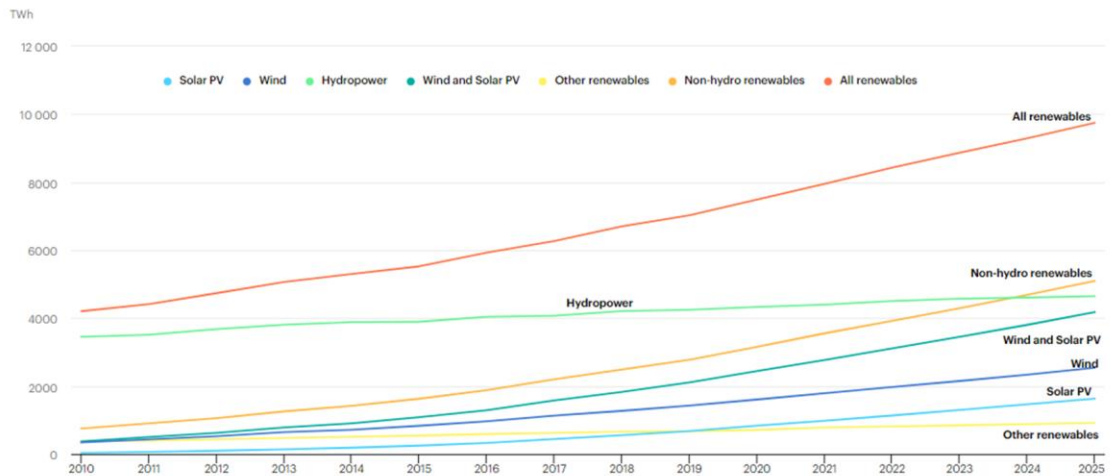


Figure 1.1. Renewable electricity generation by technology, 2010-2025.³

Figure 1.2 shows the prediction of future energy consumption. Petroleum and other liquids fuels will still be the primary energy consumption in the next three decades. However, the energy consumption by renewables will experience a significant increase, and for the first time become the most used energy source by 2050. The consumption by renewables for power generation shows a similar pattern (**Figure 1.3**).

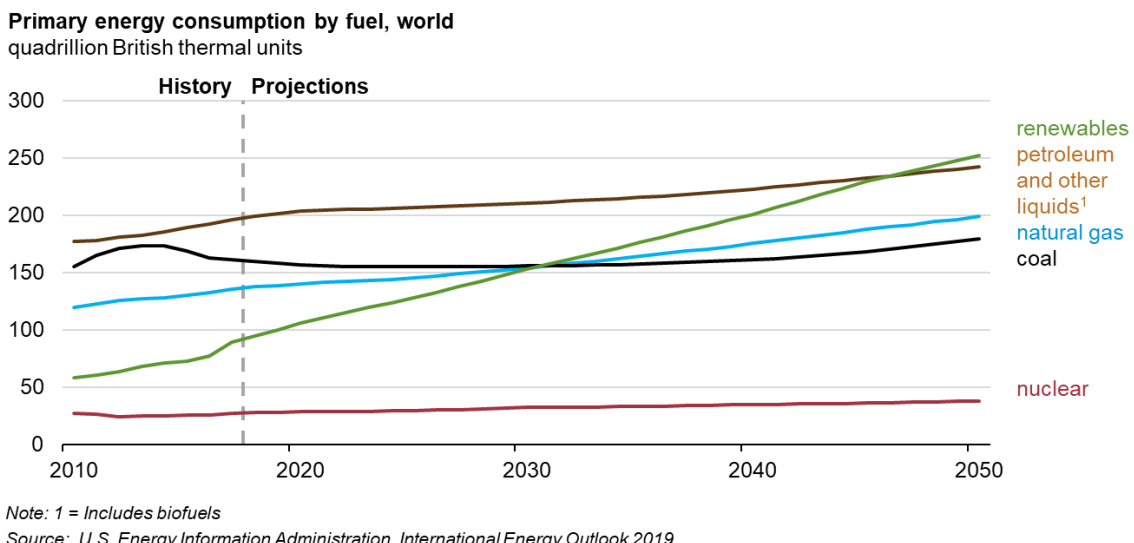


Figure 1.2. Global energy consumption and future demand prediction by U.S. Energy Information Administration.¹

It is also expected that renewables play a more important role in power generation (**Figure 1.3**). Renewables will become the primary energy source for power generation in the next few years, and their consumption is expected to grow more than four times between 2010 and 2050.

Moreover, consumption by renewables for power generation will be more than two times higher than the second-highest energy consumption (coal) by 2050.

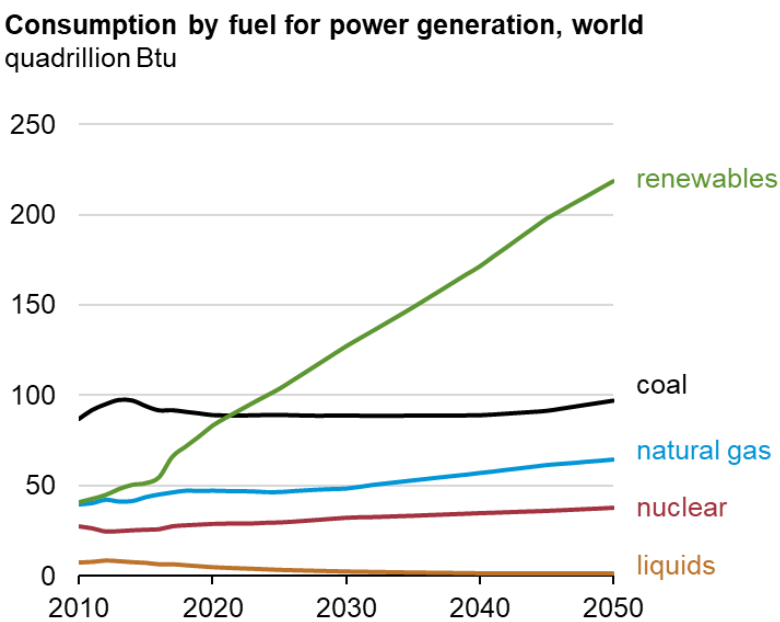


Figure 1.3. Prediction of consumption by fuel for power generation by U.S. Energy Information Administration.¹

For both solar and wind systems, the fuel cost is not only constant, but it is also zero, for the life of the system.⁴ The Sun offers a huge amount of energy to Earth every second. Approximately 10^{17} joules of energy released by the San Francisco earthquake in 1906 is roughly equal to the amount of energy the Sun offers to the Earth in one second.⁵ The Sun delivers huge power to Earth, roughly 1.2×10^5 terawatts.⁵ The amount of energy delivered to earth from every other energy source is not comparable to this number. Moreover, thanks to technological advancements, the price of harnessing solar power is dropping each year. Solar energy is not only an abundant and widespread source of energy but also holds great potential to generate other energies like fuels and power in an environmentally friendly and sustainable manner. Therefore, switching to using solar energy would be one of the most promising ways to address the global energy and climate problems.

1.1.3. Solar-to-chemical Energy Conversion

Solar energy can be converted to heat or electricity via solar photothermal or photovoltaic (PV).⁶ Over the last few years, dramatic improvements have been achieved in developing high-performance photovoltaic devices with long-term stability. One well-known example is inorganic/organic hybrid perovskite.⁷ Photothermal therapy (PTT) has shown great potential

for cancer therapy through converting photon energy to thermal energy.⁸ Solar heating is also achieved by using the thermal energy of the Sun to produce hot water for individual and industry applications.⁴ Compared to photovoltaic, photocatalysis has been considered to be cheaper due to its technological simplicity.⁹

The past century has witnessed the great development of photocatalysis, which can directly convert and store solar energy into chemical energy. Many novel semiconductor-based photocatalysts have been synthesised and utilised in the fields of hydrogen (H_2) production,^{10–14} oxygen (O_2) evolution,¹⁵ hydrogen peroxide (H_2O_2) generation,^{16,17} overall water splitting (OWS),^{18–22} nitrogen (N_2) fixing,²³ carbon dioxide (CO_2) reduction,^{12,22,24,25} organic pollutant decomposition,^{26–29} organic synthesis,^{30,31} biomass reforming,^{32,33} and bacterial disinfection.^{34,35} Solar-to-chemical energy conversion through photocatalysis offers a solution to harness solar energy and minimize environmental impact.

1.2. Photocatalytic Water Splitting

1.2.1. Hydrogen Applications and Production

Hydrogen is a very important molecule with an enormous breadth and extent of application and use.³⁶ Hydrogen is an important reactant for production of ammonia through the Haber-Bosch process and high-value and low-molecular weight products, for example, petrol, via hydrocracking in petroleum processing.³⁶ Besides the significant role of raw materials for industrial production, hydrogen is known as a future fuel owing to its high energetic yield (122 kJ/g); this value is 2.75 times higher than hydrocarbon fuels.³⁷ This makes hydrogen one of the most efficient fuels in energy conversion for the transportation sector. Additionally, hydrogen can be burned with oxygen in fuel cells to generate electricity without any emission but with the production of water as a by-product.

Hydrogen demands are growing year by year.³⁷ As shown in **Figure 1.4**, around 96% of hydrogen is generated from natural gas, oil, and coal.³⁸ This does not match the future goal of a low-carbon society and reducing the use of fossil fuels. Switching to clean and renewable energy is an evidently important strategy to meet the future hydrogen demand. Solar energy is a good choice because solar energy is abundant, zero-cost, and zero-emission. Therefore, using sunlight as the only energy input to split H_2O into H_2 and O_2 represents a promising strategy to produce hydrogen.¹⁹

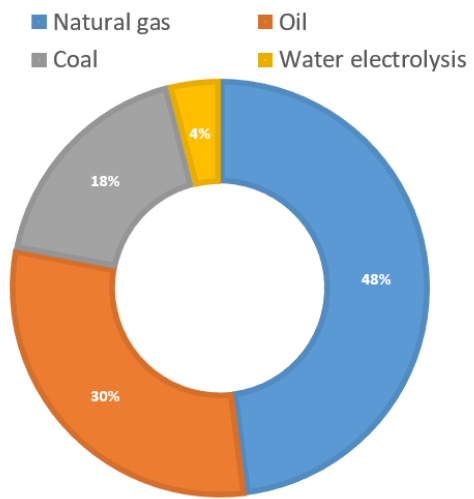


Figure 1.4. Hydrogen production from different sources in 2005.³⁸

1.2.2. Processes in Photocatalytic Water Splitting

Numerous researchers have studied water splitting by using either semiconductor-based photoelectrodes or particulate photocatalysts, since photoelectrochemical water splitting was realized by using titanium dioxide (TiO_2) to produce H_2 in 1972.³⁹ The powdered photocatalyst system is simple and easy to operate, and therefore this system has great potential to make solar water splitting scalable (**Figure 1.5**).¹⁸

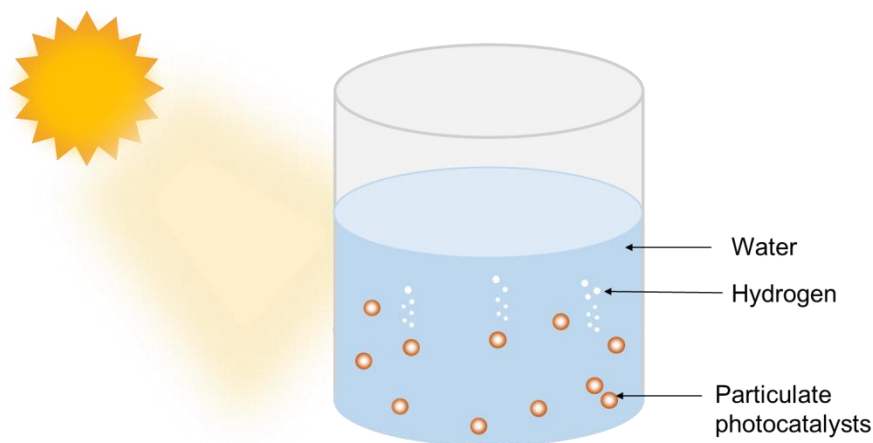


Figure 1.5. Diagram of particulate catalysts for photocatalytic hydrogen production from water.

Particulate catalyst-based photocatalysis can be described in three steps; photon absorption, charge separation, and surface reaction.¹⁸ Electron-hole pairs (excitons) will be formed after

absorbing photons by semiconductors. The bandgap of semiconductors should be smaller than the energy of the incident photon. The next step is the separation and migration of electron-hole pairs. Finally, redox reactions occur on the surface of semiconductors. **Figure 1.6a** depicts the general process of a photocatalytic reaction.

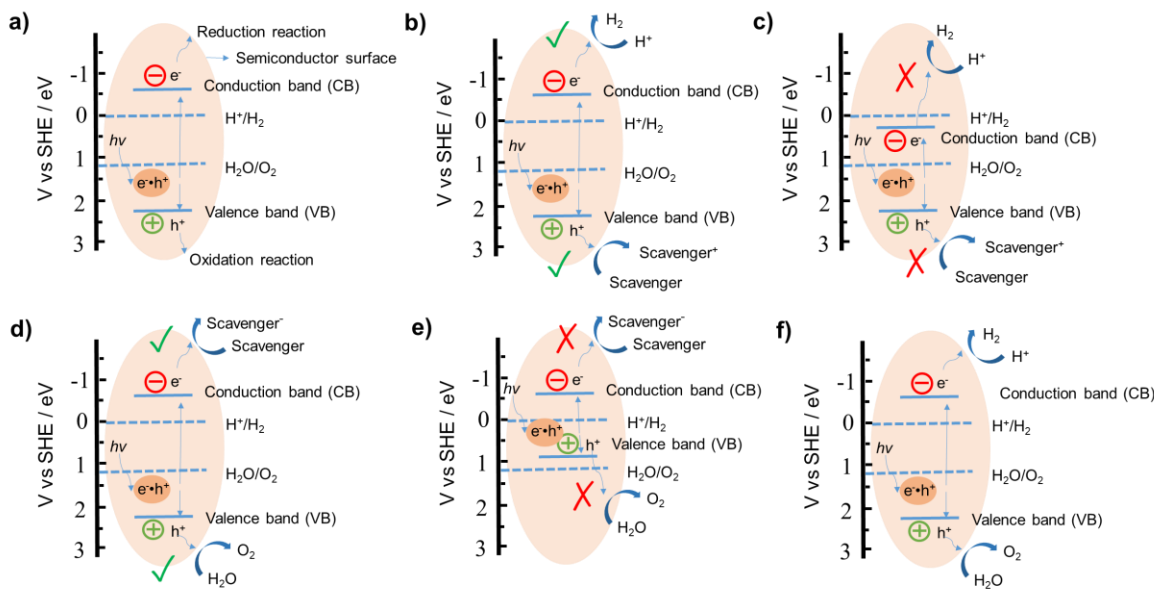
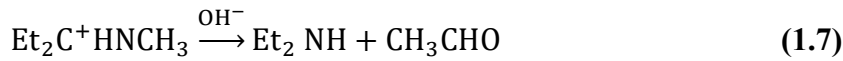
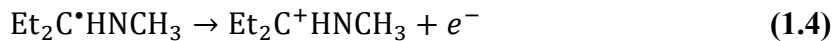


Figure 1.6. **a)** Main process for photocatalysis reaction on the semiconductor surface. **b)** Photocatalytic hydrogen production from water in the presence of sacrificial reagents when energy level is suitable. **c)** Energy level is not suitable for photocatalytic hydrogen production from water in the presence of sacrificial reagents. **d)** Photocatalytic oxygen production from water in the presence of sacrificial reagents when energy level is suitable. **e)** Energy level is not suitable for photocatalytic oxygen production from water in the presence of sacrificial reagents. **f)** Photocatalytic water splitting into hydrogen and oxygen without sacrificial reagents.

1.2.3. Sacrificial Water Splitting

Two-electron photocatalytic hydrogen production can be achieved through half-reaction of water splitting in the presence of a sacrificial reagent. As shown in **Figure 1.6b and 1.6c**, the conduction band bottom level of semiconductor photocatalysts should be more negative than the redox potential of H^+/H_2 . The photogenerated holes irreversibly oxidize the sacrificial reagent instead of water, which enables photogenerated electrons to persist and participate in the proton reduction to produce hydrogen from water. The hydrogen production performance is strongly dependent on the choice of sacrificial reagents. The commonly used sacrificial reagents are triethylamine (TEA), triethanolamine (TEOA), and ascorbic acid. Yanagida

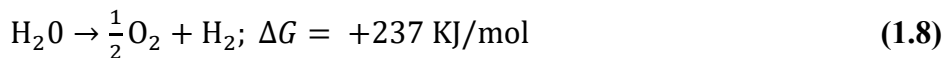
hypothesized that TEA converts to diethylamine and acetaldehyde in sacrificial hydrogen production (**Reactions 1.1-1.7**).⁴⁰



The water oxidation half-reaction involves a four-electron transfer process, and the overpotential is usually very large (>700 mV), with sluggish O-H bond breaking and O-O molecular bond formation kinetics.^{41,42} To achieve sacrificial oxygen evolution, the valence band top level of semiconductor photocatalysts should be in theory more positive than the redox potential of O₂/H₂O. The photogenerated electrons react with electron scavengers, such as silver nitrate and sodium iodate, thus enabling holes to persist and take part in the water oxidation reaction (**Figure 1.6d and 1.6e**). The large energy consumption in the water oxidation reaction may induce oxidative corrosion of the photocatalysts.¹¹ However, water oxidation half-reaction still needs to be addressed to achieve the goal of sustainable hydrogen production from overall water splitting without using any sacrificial reagent.⁴³

1.2.4. Overall Water Splitting

The ideal goal is to achieve photocatalytic overall water splitting that produces stoichiometric amounts of H₂ and O₂ without using any sacrificial reagent. From the thermodynamic point of view, the bottom level of the conduction band for semiconductors has to be located more negative than the H⁺/H₂ energy level (0 V vs NHE, PH = 0) to reduce protons into H₂ (**Figure 1.6f**). Meanwhile, to oxidize water into O₂, the top level of the valence band for semiconductors must be more positive than the O₂/H₂O energy level (1.23 V vs NHE, PH = 0).¹⁸ Therefore, the overall water splitting process (**Reaction 1.8**) is a thermodynamically uphill reaction with a minimum energy barrier of 1.23 eV or 237 kJ mol⁻¹.⁴⁴



“Bandgap” is known to be the energy difference between the conduction band and valence band. It is worth noting that if a photocatalyst can achieve both sacrificial water reduction and oxidation reaction, it does not guarantee this photocatalyst will be capable of splitting water into H₂ and O₂ without using sacrificial reagents.¹⁸

1.2.5. Approaches to Boost Photocatalytic Activity

Many factors can affect photocatalytic performances. If we take a look at each step in the photocatalytic water splitting process (**Figure 1.6a**), any process that benefits these three steps should be considered. Therefore, photocatalysts should have the following properties: the ability to generate sufficient charge carriers upon irradiation, efficient charge carriers separation and migration, and large surface area with more active reaction sites.

Firstly, the small bandgap is preferred to absorb more photons to generate sufficient charge carriers. Under irradiation, semiconductors can also generate heat and phonons, which should be minimized.¹⁰

Secondly, the photogenerated charge carriers can recombine at the bulk or surface, reducing the number of free charge carriers available for redox reactions. All materials have defects, and most defects induce localized energetic states (electronic traps) within the bandgap. The electronic traps often directly limit photocatalytic performances because these electronic traps act as capture sites for recombination of charge carriers through a non-radiative way. Charge carriers can also recombine in the absence of defects through a radiative way.⁴⁵ Also, electron-hole pairs with the high binding energy are likely to relax in a radiative way because the high binding energy causes difficulty in electron-hole dissociation. Both radiative and non-radiative recombinations are undesirable for photocatalysis. To avoid recombination of charge carriers, any approach beneficial to the charge separation and transport should be considered, such as designing photocatalysts with low exciton binding energy and fabrication of heterojunctions. Semiconductors with high crystallinity can induce a strong built-in electric field, which also facilitates charge carriers’ separation and transportation.⁴⁶

Thirdly, searching for materials with a large surface area is in principle beneficial to maximize the interface between the photocatalysts and water.⁴⁷ It is also important to create sufficient photo-active sites on the surface by approaches like co-catalyst loading and element doping.^{48,49} Co-catalyst loading can provide trapping sites for separation of charge carriers, improve the

photostability, and lower the reaction activation energy.⁴⁸ Some co-catalysts like Rh can promote the reaction of H₂ and O₂ back into the water, but this can be addressed by forming a core-shell structure, in which the co-catalyst is covered by a shell to prevent permeation of O₂ to the co-catalyst surface.⁵⁰

Additional properties, such as particle size, also dramatically affect photocatalytic activities. The small particle size shortens the distance for photogenerated electrons and holes to migrate to the photocatalysts' surface, thus decreasing the recombination possibility.¹⁸ Wettability of photocatalysts is essential for photocatalytic water splitting activity.^{51–53} Materials with some functional groups, such as sulfone and cyano, are considered to have adequate hydrophilicity, which can be correlated with the high photocatalytic H₂ production performance.^{54,55} Some other factors such as temperature, pH, and choice of sacrificial reagents, are also crucial.^{56,57} In addition, the photocatalytic activities can be improved by strategies including bandgap engineering,⁵⁸ dye sensitisation,⁵⁹ and heterostructure formation.^{60–62} Formation of heterostructures to boost photocatalytic activities has been intensively studied (See section 1.3.3).^{60–62}

There are still some obstacles that must be overcome to achieve photocatalytic water splitting. It is difficult to determine the photocatalytic performance from a single property as changing one property often causes changes on the others. This brings difficulty in designing a general way to improve performance. Also, materials with excellent long-term stability against photocorrosion should be developed for real applications. Moreover, the photocatalytic overall water splitting would be economically viable for hydrogen production when the solar-to-hydrogen (STH) energy conversion efficiency reaches 5–10%.⁶³ However, particulate photocatalysts only achieved approximately 1%.⁶⁴ Despite these obstacles, significant progress has been made for photocatalytic water splitting over the last few decades.

1.3. Bulk Materials for Photocatalytic Water Splitting

1.3.1. Inorganic Materials

After the pioneering work on photoelectrochemical water splitting by Fujishima and Honda,⁶⁵ the particulate photocatalyst was first used for water splitting in 1977.⁶⁶ Since then, numerous inorganic materials have been investigated as promising photocatalysts for sacrificial and overall water splitting reactions.^{10,67–69} Chalcogenides and metal oxides are commonly used as photocatalysts for sacrificial water splitting. Titanium dioxide (TiO₂), strontium titanate

(SrTiO₃), and cadmium sulfide (CdS) are often used for sacrificial hydrogen production, while tungsten trioxide (WO₃), bismuth vanadate (BiVO₄), and cerium oxide (CeO₂) are examples used for sacrificial oxygen production.

The influence of metal co-catalysts and reaction media on photocatalytic H₂ production using TiO₂-based photocatalysts has been studied in detail.⁷⁰ Three types of metal precursors were used to prepare M/TiO₂ (M = Pd, Pt, Au) photocatalysts. The results showed improved H₂ production performance for all co-catalysts as a result of the retarded recombination of electron-hole pairs revealed by photoluminescence data. TiO₂ loading with Pd produced the highest amount of H₂ compared to other co-catalysts under UV irradiation. The best sacrificial reagent was determined to be glycerol among a series of alcohols. Another example, Nb₂O₅, can efficiently produce H₂ from a methanol-water mixture by using Pt as co-catalyst under UV irradiation.⁷¹ Moreover, Arakawa and co-workers reported that CeO₂ was active for photocatalytic oxidation of water to O₂ in an aqueous solution using Fe³⁺ and Ce⁴⁺ as the scavengers.⁷² Most of these unmodified inorganic materials have large bandgaps, which can only absorb UV light, resulting in poor solar light utilisation. Some prophase studies were carried out to make visible-active photocatalysts like CdS⁷³ and WO₃.⁷⁴ However, instability is a drawback of CdS because of serious photocorrosion.⁷⁵ WO₃ was found to have a relatively positive conduction band, leading to low proton reduction ability, which is not suited for photocatalytic H₂ production.⁷⁶

Visible-active inorganic photocatalysts can be made by several common approaches (only two are listed here): (1) ions doping; (2) surface sensitisation.¹⁰ Taking TiO₂ as an example, many studies demonstrated that both cations and anions can extend light absorption of TiO₂ into the visible region.⁶² In some cases, codoping with two cations exhibits better stability⁷⁷ and higher activity⁷⁸ than single cation doping for sacrificial H₂ production. Another common strategy for TiO₂-based photocatalysts to harvest visible light is surface sensitisations, including transition-metal complexes sensitisation (for instance, ruthenium)^{79,80} and organic dyes sensitisation (for instance, perylene).⁸¹ Besides the extension of light absorption, fabrication of heterojunctions (**Section 1.3.3**) and co-catalysts loading have been widely applied to boost photocatalytic H₂ production rate.

On the other hand, some inorganic materials can split H₂O into H₂ and O₂ without sacrificial reagents under UV light owing to the wide bandgap. There are too many examples to list but transition metal cations with d⁰ (such as Zr⁴⁺, Ti⁴⁺, Nb⁵⁺, W⁶⁺, and Ta⁵⁺) and main group metal

cations with d^{10} electronic configurations (such as In^{3+} , Ga^{3+} , Ge^{4+} , Sn^{4+} , and Sb^{5+}) are generally used.^{18,69} The photocatalytic overall water splitting can be classified into a one-step excitation reaction (above mentioned) and two-step excitation reaction (Z-scheme by using I^-/IO_3^- as redox shuttle) as shown in **Figure 1.7** (The Z-scheme¹⁸ is composed of an H_2 -evolution photocatalyst, an O_2 -evolution photocatalyst, and an electron mediator). Pt-TiO_2 is active for sacrificial hydrogen production from water using iodide (I^-) as an electron donor, whereas TiO_2 can oxidize water to oxygen using iodate (IO_3^-) as the sacrificial electron acceptor. Combining these two reactions into one catalytic system was found to produce stoichiometric amounts of H_2 and O_2 . Thereafter, a similar system was built by combining Pt-TiO_2 and Pt-WO_3 photocatalysts for overall water splitting.⁸² The highest STH efficiency (around 1%) reported so far for photocatalytic overall water splitting was also achieved by using the Z-scheme system (**Figure 1.8**).⁶⁴ Nonetheless, it is still far behind the commercially viable value (5%).⁸³

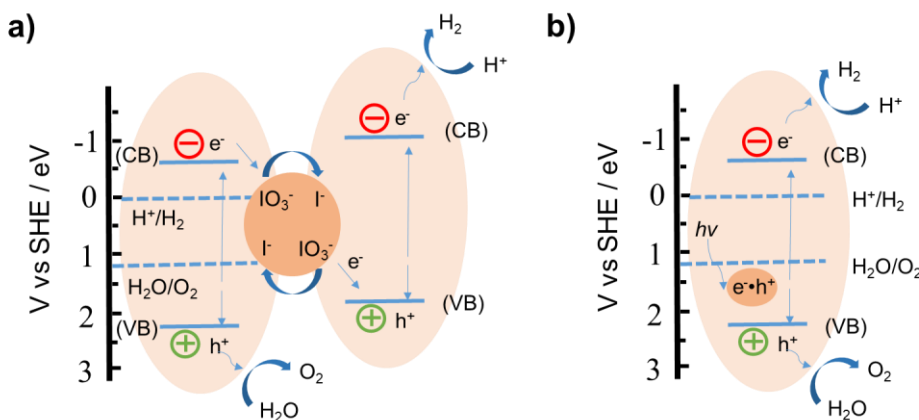


Figure 1.7. Photocatalytic overall water splitting by **a)** one-step and **b)** two-step reaction.

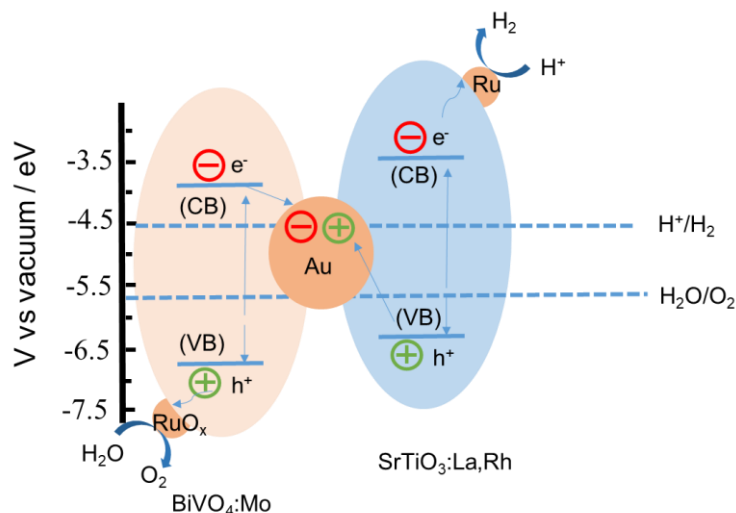


Figure 1.8. Photocatalytic overall water splitting by Ru modified $\text{SrTiO}_3:\text{La,Rh}/\text{Au}/\text{BiVO}_4:\text{Mo}$

sheet.⁶⁴

Over the years, significant progress has been achieved in photocatalytic water splitting by using inorganic materials. However, the limited tunability of these materials is an inevitable drawback. Moreover, in most cases, toxic and precious metal co-catalysts are required to obtain satisfactory performance. Organic photocatalysts have a series of complementary advantages and, therefore attract increasing attention in recent years.

1.3.2. Organic Materials

1.3.2.1. Organic Photocatalysts

Compared with inorganic materials, the conjugated polymer materials have two main advantages; improved visible light absorption owing to their delocalized π -system and great structural tunability due to the large scope of monomer building blocks.⁸⁴ Similar to the excitation process in inorganic materials, electrons in organic materials can be excited from the highest occupied molecular orbital (HOMO, top of the valence band in a periodic crystal perspective) to the lowest unoccupied molecular orbital (LUMO, bottom of the conduction band), leading to the formation of excited electron-hole pairs.⁸⁵ After excitation, excited electron-hole pairs can be separated, and then migrate to the material's surface to induce the redox reactions.

Poly(*p*-phenylene)s was reported as the first conjugated polymer photocatalyst for H₂ evolution in 1985 by Yanagida and coworkers.⁸⁶ In 2009, a report on photocatalytic water splitting by using metal-free graphitic carbon nitride (g-C₃N₄) polymer represented a milestone in the area of water splitting by organic photocatalysts.⁸⁷ This work paves the way for subsequent research on photocatalytic H₂ evolution by using conjugated polymers, including carbon nitrides (C₃N₄), linear polymers, conjugated microporous polymers (CMP), covalent triazine-based frameworks (CTF), and covalent Organic Frameworks (COF).

Carbon nitrides are synthesized by condensation of nitrogen-rich monomers at high temperatures. The exact structures of C₃N₄ are often unknown, but it is commonly believed that *s*-triazine and tri-*s*-triazine (heptazine) coexisted as two building units to form the ideal polymeric carbon nitride units.⁸⁸ g-C₃N₄ related photocatalysts have been intensively studied owing to their great properties, such as high stability and desired bandgap.^{89,90} Photocatalytic H₂ production activities have been drastically improved for g-C₃N₄ by loading co-catalysts⁹¹ and improving crystallinity.⁹² Moreover, the formation of heterostructures with other

semiconductors has proved to be an efficient strategy to enhance photocatalytic performance, which will be detailed in **Section 1.3.3**. However, low processability, unclear composition, and high-temperature synthesis are disadvantages of C_3N_4 materials.

Linear polymers have also attracted lots of attention probably because the first report of an organic photocatalyst for H_2 evolution was a linear polymer.⁸⁶ Compared with C_3N_4 , linear polymers are generally synthesized at low temperatures. Our group has reported a series of conjugated linear polymers for efficient H_2 evolution in a mixture solution (Methanol, TEA, and water), in particular P7 and P10, showing a hydrogen evolution rate (HER) of 1.49 mmol $\text{g}^{-1} \text{ h}^{-1}$ with an external quantum efficiency (EQE) of 7.2% at 420 nm for P7 and HER of 3.26 mmol $\text{h}^{-1} \text{ g}^{-1}$ with an EQE of 11.6% at 420 nm for P10, respectively (**Figure 1.9**).^{53,93} Chen and colleagues also reported a highly active conjugated linear polymer photocatalyst (B-BT-1,4-E) for sacrificial H_2 evolution, achieving a high HER of 0.355 mmol $\text{h}^{-1} \text{ g}^{-1}$ with an EQE of 3.7% at 420 nm (**Figure 1.9**).⁹⁴ Forming heterostructures with other semiconductors has been studied as an efficient strategy to further boost photocatalytic performance (**Section 1.3.3**). Moreover, by incorporation of solubilizing side-chains, a soluble linear polymer was made in our group (**Figure 1.9**).⁵¹ This polymer is soluble in some common organic solvents, therefore making it processable.

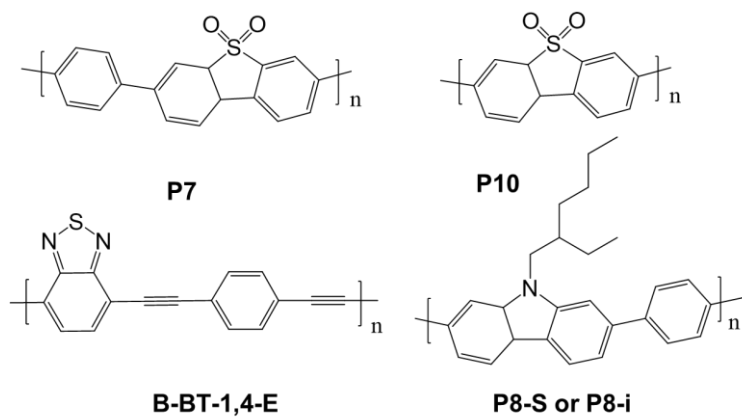


Figure 1.9. Chemical structures of linear polymers.

The surface area is generally considered to play a key role in determining photocatalytic activities. However, these linear polymers have low surface areas. In 2007, our group reported the first explicit example of a conjugated polymer with permanent porosity (conjugated microporous polymer),⁹⁵ and, subsequently, in 2015, the conjugated microporous polymer was first applied for photocatalytic H_2 evolution.⁹⁶ In 2019, porous dibenzo[*b,d*]thiophene sulfone-containing polymer with an apparent quantum yield (AQY) of 13.2% at 420 nm outperformed

its linear structural analogue ($3.11 \text{ mmol h}^{-1} \text{ g}^{-1}$ for porous polymer *versus* $0.83 \text{ mmol h}^{-1} \text{ g}^{-1}$ for linear structural analogue), suggesting that microporosity may be beneficial to photocatalytic performance (**Figure 1.10**).⁵²

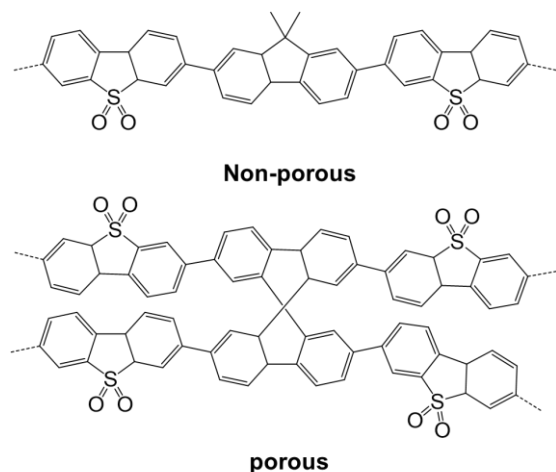


Figure 1.10. Chemical structures of a conjugated microporous polymer and its non-porous structural analogue.

A potential drawback of conjugated microporous polymers (CMPs) is that they are amorphous. Crystalline materials are generally believed to have high charge carrier mobilities and, consequently, may be beneficial to photocatalytic activities.^{97,98} Therefore, covalent organic frameworks (COFs) and covalent triazine-based frameworks (CTFs) have been frequently used for photocatalytic H₂ production in recent years. Most of the reported CTFs are synthesized under highly dynamic condensation reactions, leading to the formation of amorphous or semicrystalline materials.⁹⁹ New strategies have been developed recently to produce highly crystalline CTFs. CTF-HUST-C1 with high crystallinity showed much improved photocatalytic H₂ evolution activity than CTF-HUST-1 with low crystallinity or amorphous counterpart under the same conditions (**Figure 1.11**). Higher photocurrent and lower electrochemical impedance of CTF-HUST-C1 are believed to be beneficial for charge transport, which is suggested to be the reason for the higher photocatalytic performance of CTF-HUST-C1.¹⁰⁰

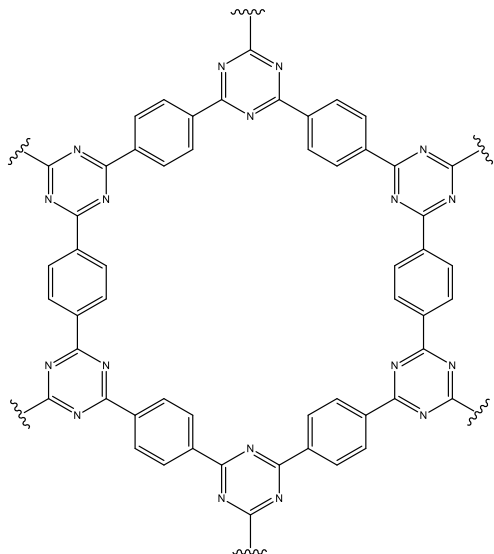


Figure 1.11. Chemical structures of CTF-HUST-C1 and CTF-HUST-1.

COFs are crystalline porous materials synthesized under highly reversible reactions like Schiff base reaction, allowing self-correction to form thermodynamically stable crystalline architectures.^{101,102} Some COFs were reported to show photocatalytic H₂ production activities.^{103–105} Crystalline sulfone-containing COF (FS-COF) showed around nine times higher photocatalytic activity than its amorphous counterpart, again demonstrating the importance of crystallinity in photocatalytic activity.¹⁰⁴ Photocatalytic H₂ production activities of CMP, CTF, and COF can also be improved by forming heterostructures.^{106–108}

1.3.2.2. Design Rules

In organic materials, free electrons can reduce protons to H₂ when electron affinity (EA, often approximated in the literature by the energy of the LUMO) of the material is more negative than the energy level of the proton reduction half-reaction.¹⁴ On the other hand, free holes can drive water oxidation if polymer has a more positive ionisation potential (IP) than the energy level of water oxidation.¹⁴ To achieve efficient hydrogen production activity from water, the design of polymers with suitable electron affinity and ionisation potential should be considered. The numerous polymer photocatalysts have been screened in our group and, the EA levels of these polymers were predicted.¹⁰⁹ The results showed a strong dependence of photocatalytic hydrogen production activities to EA and IP levels of photocatalysts.

The polymers with predicted EA values more positive than -1.5 V showed low hydrogen production rates.¹⁰⁹ The experimental hydrogen production rates rise with increasing EA to a peak at around -2 eV before decreasing again for more positive EA values. The predicted IP

values have a similar trend with the peak at around 1.2 eV for high hydrogen production rates.¹⁰⁹

Introducing active groups into the conjugated skeletons of polymers can improve intrinsic photocatalytic activity of the existing photocatalysts through bandgap and energy level engineering.¹¹ For instance, the incorporation of strong electron-withdrawing groups, such as cyano groups,¹¹⁰ diimide groups,¹¹¹ thiadiazole groups,¹¹² lowers the LUMO energy levels of polymers because of the loss of electrons in π -backbone of conjugated polymers.¹¹

1.3.3. Heterojunction Materials

As mentioned above for both inorganic and organic materials, a general strategy to improve photocatalytic performance seems to be the formation of heterojunctions. Wang and co-workers summarized that photocatalytic efficiencies can be enhanced by a variety of strategies and, forming heterojunctions has been widely studied because of its perfect effectiveness in improving photocatalytic performance.⁶¹ Heterostructure photocatalysts not only possess excellent properties from those of single components but also bring new features that are different from those of single components.⁸⁴

There are three types of band alignments (type-I, type-II, and type-III) for conventional semiconductor heterojunctions as shown in **Figure 1.12(a-c)**.⁶⁰ In type-I heterojunction, CB of semiconductor 2 is more negative than that of semiconductor 1, whereas semiconductor 2 has a more positive VB than semiconductor 1. This band alignment forces the photogenerated electrons and holes to accumulate on semiconductor 1, leading to poor separation efficiency of charge carriers. As semiconductor 1 has lower redox potential, the redox ability of photocatalyst with type-I heterojunction is reduced. In type-II heterojunction, semiconductor 2 has higher CB and VB levels compared to semiconductor 1. After excitation, photogenerated electrons and holes move in opposite directions, resulting in spatial separated electrons and holes. Therefore, the formation of type-II heterojunction can ideally separate photogenerated electrons and holes, leading to improved photocatalytic performance. But, type-II heterojunction photocatalysts have reduced redox ability. In type-III heterojunction, photogenerated electrons and holes cannot move between the two semiconductors because the bandgap of semiconductor 1 does not overlap with semiconductor 2. Consequently, type-III heterojunction does not show any positive effect on the separation of charge carriers.

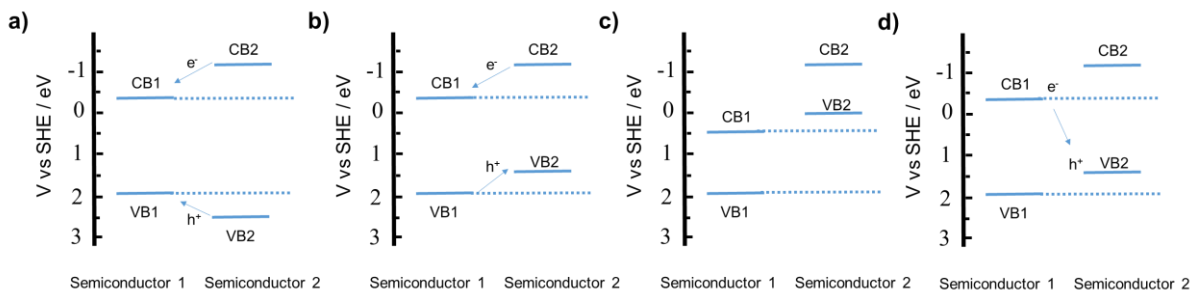


Figure 1.12. Schematic energy band diagrams of **a)** type-I, **b)** type-II, **c)** type-III heterojunction and **d)** direct Z-scheme heterojunction.^{60,113}

Different from conventional heterojunctions, p–n heterojunction is formed when combining a p-type semiconductor and an n-type semiconductor (**Figure 1.13**). The CB of n-type semiconductors and VB of p-type semiconductors are near their Fermi energy level. After contact, the electrons in n-type semiconductors near the contact surface tend to diffuse into p-type semiconductors, whereas the holes in the p-type semiconductors tend to move to the n-type semiconductors, leading to the formation of a built-in electric field.^{114,115} The diffusion of electrons and holes will continue until the Fermi level equilibrium is achieved. This built-in electric field forces photogenerated electrons migrating to n-type semiconductors and holes migrating to the p-type semiconductor rapidly. Therefore, the formation of p–n heterojunction can efficiently reduce the recombination of photogenerated charge carriers. However, p–n heterojunction photocatalysts also have reduced redox ability.

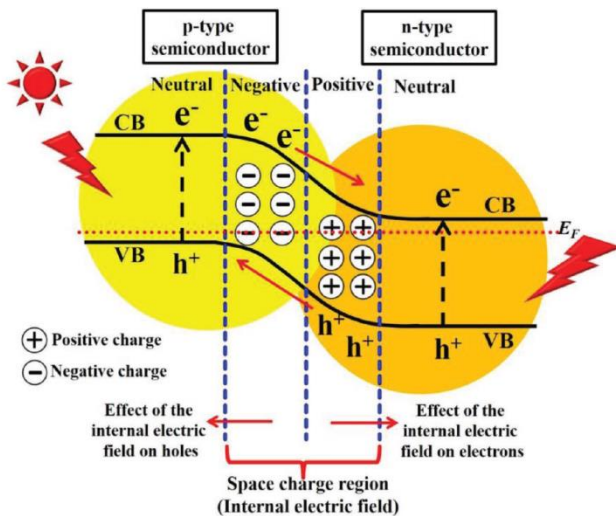


Figure 1.13. Schematic energy band diagram of p–n heterojunction.¹¹³

As shown in **Figure 1.12d**, electrons and holes can be spatially separated in a direct Z-scheme heterojunction system. Electrons in CB of semiconductor 1 recombine with holes in VB of

semiconductor 2, resulting in spatially separated holes and electrons in semiconductor 1 and semiconductor 2, respectively. This recombination process is favorable due to electrostatic attraction between electrons and holes. Recombination of electrons and holes with low redox potential allows the reservation of spatially separated electrons and holes with high reduction and oxidation potential.^{116,117} Moreover, electrostatic attraction facilitates the recombination of electrons and holes with low redox potential.¹¹³ Therefore, the direct Z-scheme heterojunction system overcomes the drawback existing in the traditional type I, type II, and p-n heterojunctions. The formation of direct Z-scheme heterojunction is believed to be an efficient strategy to boost photocatalytic performance. Apart from direct Z-scheme heterojunction, all-solid-state and acceptor-donor mediated Z-scheme heterojunctions have also attracted a lot of attention.¹¹³

1.3.3.1. Inorganic/inorganic Heterojunctions

Inorganic semiconductors can form heterojunctions with either inorganic semiconductors or organic semiconductors. ZnO/CdS photocatalyst was fabricated for sacrificial H₂ generation from water by deposition of CdS nanoparticles on ZnO surface through a chemical bath deposition method.¹¹⁸ The pristine ZnO sample had barely any photocatalytic performance but photocatalytic performance increased sharply by the introduction of CdS. When the mass ratio of CdS was 30.9%, ZnO/CdS had the highest photocatalytic hydrogen generation performance (4.13 mmol h⁻¹ g⁻¹). The formation of ZnO/CdS heterojunction greatly improved the separation efficiency of photogenerated charge carriers through a direct Z-scheme charge transfer mechanism.

1.3.3.2. Inorganic/organic Heterojunctions

Inorganic/organic heterojunction photocatalysts combine the excellent electronic properties of inorganic materials as well as the high tunability of organic materials and, therefore have been intensively studied. There are numerous examples of inorganic/C₃N₄ heterojunction photocatalysts. Zou and co-workers synthesized a novel ZnS/g-C₃N₄ photocatalyst by depositing ZnS on the surface of g-C₃N₄ via a hydrothermal method.¹¹⁹ ZnS/g-C₃N₄ heterostructure with optimal composition displayed around 30 and 7.6 times higher HER (713.68 μmol h⁻¹ g⁻¹) than the parent g-C₃N₄ (24.09 μmol h⁻¹ g⁻¹) and ZnS (93.81 μmol h⁻¹ g⁻¹), respectively. The significantly enhanced performance can be mainly attributed to improved charge carriers transfer and separation of type-II ZnS/g-C₃N₄ heterojunction. ZnS/g-C₃N₄ heterostructure also produced more H₂ compared to the physical mixtures of ZnS and g-C₃N₄,

suggesting heterojunction played a key role. Apart from C₃N₄, the linear polymers can also form heterojunctions with inorganic semiconductors to enhance photocatalytic H₂ production activity. BE/CdS was fabricated by in-situ polycondensation of polybenzothiadiazole (B-BT-1,4-E, noted as BE) in the presence of CdS nanorods.¹²⁰ BE/CdS-10.0 (10% of BE and 90% of CdS) hybrid achieved remarkable HER of 41.0 mmol h⁻¹ g⁻¹, which is 8.3 and 23.3 times higher than CdS and BE, respectively, with a high AQY of 7.5% at 420 nm. Z-scheme charge transfer was proposed to be the reason for improved photocatalytic performance.

1.3.3.3. Organic/organic Heterojunctions

Conjugated polymers can form heterojunctions with conjugated polymers to effectively separate photogenerated electrons and holes. Some of these organic/organic heterojunctions photocatalysts exhibit remarkable photocatalytic performance. A series of polyfluorene polymers/g-C₃N₄ type-II heterojunctions were fabricated by simple evaporation of chloroform solutions containing polyfluorene polymer and g-C₃N₄.¹²¹ PCzF (poly(*N*-decanyl-2,7-carbazole-alt-9,9-dioctylfluorene)) was synthesized by introducing the electron-donating carbazole unit into the PFO (9,9-dioctylfluorene) backbone. Electron transfer from polyfluorene polymers to g-C₃N₄ was clearly demonstrated by X-ray absorption near-edge structure (XANES) spectra. This charge carrier transfer process was more favorable in PCzF/g-C₃N₄ compared to PFO/g-C₃N₄, resulting in improved photocatalytic H₂ production performance for PCzF/g-C₃N₄ with an excellent AQY of 27% at 440 nm.

A robust poly(3-hexylthiophene) P3HT/g-C₃N₄ heterojunction photocatalyst was made by rotary evaporation of P3HT chloroform solution containing g-C₃N₄.¹²² This heterojunction photocatalyst containing 3% of P3HT achieved an AQY of 77.4% at 420 nm. 3% P3HT/g-C₃N₄ exhibited HER of 83.8 mmol h⁻¹ g⁻¹ under $\lambda \geq 500$ nm irradiation, which significantly outperformed Pt/g-C₃N₄ (1.2 mmol h⁻¹ g⁻¹) and Pt/P3HT (around 0.15 mmol h⁻¹ g⁻¹) under the same conditions. The synergistic effect of extended visible light absorption and efficient charge transfer at the interface of P3HT and g-C₃N₄ was suggested to be the reason for the extremely high H₂ production performance. The efficient electron transfer from P3HT to g-C₃N₄ was investigated by photoluminescence and time-resolved photoluminescence spectra. It is worth noting that small organic molecules can also form heterojunctions with conjugated polymer or inorganic materials.^{84,123}

1.4. Nanomaterials for Photocatalytic Water Splitting

Nanostructure materials have been intensively studied in recent years due to their improved mechanical and physical properties in comparison with conventional grain materials.¹²⁴ Nanotechnology offers great potential to boost photocatalytic activities.¹²⁵

1.4.1. Inorganic Nanomaterials

Inorganic nanoparticles have received a lot of attention because they are easy and cheap to synthesize in a large amount. There is a wide variety of techniques for synthesizing inorganic nanoparticles. Domen and co-workers prepared tantalum (V) nitride (Ta_3N_5) nanoparticles by using carbon nitride as the template.¹²⁶ The small Ta_3N_5 particles (around 7 nm) showed one magnitude higher activity than the large Ta_3N_5 particles (a few hundreds of nanometers) for photocatalytic H_2 evolution under visible light irradiation. The high surface area and low density of defects are likely to be the reason for the high photocatalytic performance of small particles. A similar template-assisted strategy was employed to synthesize CdS nanoparticles.¹²⁷ These nanoparticles also produced more hydrogen than the bulk samples under the same photocatalysis conditions.

It should be noted that charge recombination becomes dominant when particle size is too small.^{128,129} Sphere-like nanoparticles, smaller than a certain dimension (about 10 nm), might show lower photocatalytic performance.¹²⁸ Apart from spherical nanoparticles, morphology engineering strategies were applied to synthesize rod-shaped nanoparticles.¹³⁰ The high surface-to-volume ratio of nanorods offers a large number of active sites and a high charge transfer rate. It is also believed that increased delocalisation of charge carriers in nanorods leads to reduced overlap of the electron and hole wave functions and hence reduced recombination of charge carriers.¹³¹ CdS nanorods were prepared by a facile one-pot solvothermal method, followed by modification with Pt co-catalyst.¹³² CdS nanorods with only 0.06% Pt loading achieved a remarkable HER of $10.29 \text{ mmol h}^{-1} \text{ g}^{-1}$, which was attributed to the unique 1D nanorod structure and promotion effect of Pt.

The dramatic quantisation effects can occur when the length scale of nanocrystal diameter is less than about 25 to 10 nm. When the charge carriers are confined by potential barriers in three spatial dimensions, this regime is termed a quantum dot (QD).¹³³ Quantum dots (QDs) have tunable absorption profiles and large extinction coefficients that are beneficial for photocatalysis.¹³⁴ Another advantage of QDs is their high processability. Moreover, their

solubility can be modified by changing surface stabilizers or capping agents.¹³⁵ Oleic acid (OA) capped CdSe QDs were prepared and then dispersed in water by replacing oleic acid with a hydrophilic ligand (3-mercaptopropionic acid). After loading with Pt co-catalyst, CdSe QDs showed an unprecedented HER of around $250 \mu\text{mol mg}^{-1}$ in the first 2 hours using 450 nm LED irradiation.¹³⁶

1.4.2. Organic Nanomaterials

1.4.2.1. Nanoprecipitation Mechanism

The nanoprecipitation mechanism is based on the reduction of the solvent quality, which can be achieved by adding salt, changing the pH, adding a non-solvent phase, and so on.¹³⁷ There are four steps in a typical non-solvent-based precipitation method; that is the formation of supersaturation, nucleation, growth, and coagulation.¹³⁸ The supersaturation state forms after the addition of non-solvent that reduce solvent potency to dissolve the solute. To gain thermodynamic stability, the nucleation step occurs. The association of solute molecules results in the growth of nuclei until the solute concentration is reduced below the critical supersaturation and nuclei size is stable against dissolution. If the nuclei have stronger attractive interactions than the repulsive interactions, coagulation (aggregation) occurs.^{139,140} In principle, any factor that influence these four steps can be used to control nanoparticles size, including parameters used in the emulsification process, oil-to-polymer ratio, oil-to-water ratio, polymer concentration and so on.^{140,141}

1.4.2.2. Conjugated Polymer Nanoparticles

Polymer nanoparticles have many desired properties for photocatalysis, such as easy synthesis, tunable properties, and less toxicity.¹⁴² Organic solvents are generally required to increase the dispersibility of organic polymers in water, which plays an important role in determining photocatalytic performance.^{109,143} Despite the aforementioned two advantages (reduced recombination of charge carriers and high surface area) of nanoparticle photocatalysts, polymer nanoparticles have higher dispersibility compared to bulk polymers.

Conjugated polymer nanoparticles (CPNs) are prepared mainly by three methods; mini-emulsion evaporation, mini-emulsion polymerisation, and nanoprecipitation. In the mini-emulsion evaporation method as shown in **Figure 1.14a**, the polymer is first dissolved in a non-polar organic solvent and mixed with an aqueous solution containing surfactant.¹⁴⁴ Ultrasonication is then applied to form a stable mini-emulsion containing small droplets of the

polymer solution. After evaporation of the organic solvent, a stable dispersion of polymer nanoparticles in water is obtained. The size of the resulting nanoparticles can be varied by using different polymer concentrations, types of surfactants, and ratios of two immiscible solutions. Solubility in non-polar solvents like chloroform is required for the mini-emulsion evaporation method. Consequently, this is not a general way to produce CPNs. A direct mini-emulsion polymerisation method is then developed to prepare CPNs.^{145,146} This method can be extended to synthesize conjugated microporous polymer nanoparticles as displayed in **Figure 1.14b**.¹⁴⁷ Polymerisation occurs in small droplets of the monomer solution to produce stable nanoparticles.

Two miscible solutions are used in the nanoprecipitation method (**Figure 1.14c**). Polymer is dissolved in a good solvent (e.g., tetrahydrofuran (THF)). This solution is then quickly injected into a poor solvent (e.g., water), which is miscible with the good solvent. After sonication or vigorous stirring, the good solvent is removed to produce polymer nanoparticles in water. Nanoprecipitation is considered to be a facile method to prepare polymer nanoparticles without using any surfactant or additive. All three methods are transferrable to prepare supramolecular nano-assemblies by using small organic molecules.

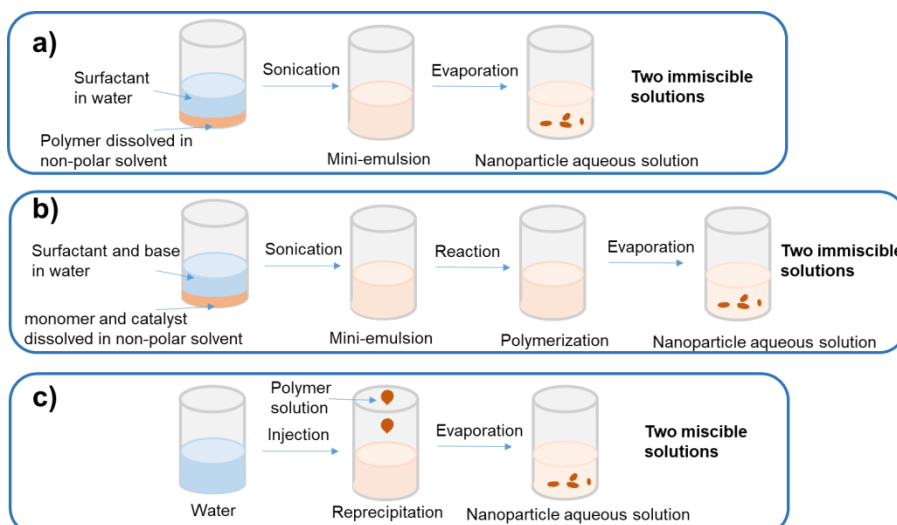


Figure 1.14. Schematic representation of three preparation methods for conjugated polymer nanoparticles. **a)** Mini-emulsion evaporation. **b)** Mini-emulsion polymerisation. **c)** Nanoprecipitation.

In 2016, organic polymer dots (Pdots) were first applied as photocatalysts for H₂ evolution from water.¹⁴⁸ Pdots containing poly[(9,9'-dioctylfluorenyl-2,7-diyl)-co-(1,4-benzo-{2,1',3} thiadiazole)] (PFBT) and polystyrene grafting with carboxyl-group-functionalized ethylene

oxide (PS-PEG-COOH) were prepared by a nanoprecipitation method. This polymer nano-photocatalyst showed an initial HER of $8.3 \text{ mmol h}^{-1} \text{ g}^{-1}$, which was 5 orders of magnitude higher than that of bulk PFBT polymer. Two years later, our group reported the preparation of a polymer nano-photocatalyst based on dibenzo[*b,d*]thiophene sulfone via a direct mini-emulsion polymerisation method.¹⁴⁹ An impressive HER of $60.6 \text{ mmol h}^{-1} \text{ g}^{-1}$ was achieved under visible light with AQY as high as 20.4% at 420 nm. This is the highest reported rate for an organic polymer and, between two and three times higher than the bulk polymer.

Supramolecular assemblies are crystalline organic materials that can be self-assembled by a discrete number of molecular structural units through noncovalent bonds (e.g., hydrogen bonds, Van der Waals forces, and electrostatic interactions).¹⁵⁰ Noncovalent π - π stacking in supramolecular assemblies narrows the bandgap and offers a channel for fast charge transfer via delocalized π -electrons, leading to better migration efficiency of photogenerated charge carriers.^{151–155} Moreover, structure flexibility and morphology tunability of supramolecular systems provide an opportunity to fine-tune the properties of a material.^{156–158}

With these advantages, supramolecular materials have been used as efficient photocatalysts for sacrificial H₂ evolution under visible light irradiation. A supramolecular photocatalyst 2CzPN (4,5-Di(carbazol-9-yl)phthalonitrile) based on cyanocarbazole was prepared.¹⁵⁰ This nano-photocatalyst showed a high HER of $4.6 \text{ mmol h}^{-1} \text{ g}^{-1}$ ($\lambda > 420 \text{ nm}$) with an AQY of 7.5% at 420 nm, which outperformed analogous polymer ($2.4 \text{ mmol h}^{-1} \text{ g}^{-1}$). Fan and co-workers prepared self-assembled porphyrin nanostructure using 5,10,15,20-tetrakis(4-(hydroxyl)phenyl)porphyrin (THPP) as the building block.¹⁵⁹ This supramolecular photocatalyst achieved a remarkable HER of $19.5 \text{ mmol h}^{-1} \text{ g}^{-1}$, which was 20 times higher than the bulk THPP. They proposed that enhanced absorption and efficient energy transfer lead to high photocatalytic performance.

Some supramolecular photocatalysts have also been applied for sacrificial oxygen evolution from water. Supramolecular photocatalysts derived from perylene tetracarboxylic diimide (PDI) were shown to be active for water oxidation.^{160,161} A few years later, Zhu and co-workers prepared a self-assembled tetra(4-carboxylphenyl)porphyrin (SA-TCPP) supramolecular photocatalyst. This material was active for both hydrogen ($40.8 \mu\text{mol g}^{-1} \text{ h}^{-1}$) and oxygen evolution ($36.1 \mu\text{mol g}^{-1} \text{ h}^{-1}$) in the presence of sacrificial reagents without any co-catalyst.¹⁶² Although the photocatalytic activities are low, this work highlights a potential avenue to achieve overall water splitting by using supramolecular photocatalysts.

1.4.3. Heterojunction Nanomaterials

Inorganic materials generally have good crystallinity and control over morphology. Therefore, inorganic heterojunction nanomaterials can be synthesized through many approaches, including direct synthesis, seed-mediated growth, step-by-step deposition, sol-gel, mechanic mixing, co-precipitation, self-assembly, and so on.¹⁶³ The morphology of inorganic heterojunction nanomaterials can also be finely controlled by the process parameters. A core-shell heterojunction nanomaterial MoS₂/CdS was prepared by a two-step hydrothermal growth method.¹⁶⁴ Under visible light irradiation ($\lambda > 420$ nm), MoS₂/CdS achieved a remarkable HER rate of 775 $\mu\text{mol h}^{-1}$ by using only 20 mg of catalyst, which was much higher than pure CdS (12 $\mu\text{mol h}^{-1}$) and Pt-CdS (64 $\mu\text{mol h}^{-1}$) under the identical conditions. The authors stated that the formation of the heterojunction improved the charge carriers' mobility and retard the recombination of photogenerated electron-hole pairs.

Compared to inorganic nanomaterials, it is difficult to control the morphology of organic nanomaterials and obtain highly ordered organic nanomaterials, especially for conjugated polymers. As a result, only a few effective strategies have been applied to make organic/inorganic or organic heterostructure nanomaterials. An in-situ polymerisation technique was used to coat a thin layer of homogeneous polyaniline (PANI) on CdS to construct PANI@CdS core-shell nanospheres.¹⁶⁵ The H₂ production activity of PANI@CdS nanospheres was improved compared to CdS nanospheres, which was attributed to photogenerated holes migrating from the VB of CdS to the HOMO of PANI. However, adding inorganic components into the monomers before performing the polymerisation has severely introduced synthetic limitations and, more importantly, also reduced control over the physical incorporation of the inorganic components limiting tunability.

Recently, assembly of multiple building blocks into clusters using the mini-emulsion evaporation induced assembly method was reported.¹⁶⁶ This approach has been used for making heterostructure nanomaterials containing inorganic QDs and solution processable alkyl-polymers.^{160,166–169} Nano-sized hydrophobic droplets containing poly(lactic-co-glycolic acid) (PLGA) and black phosphorus quantum dots (BPQDs) were well-dispersed in water after sonication with the aid of a surfactant (polyvinyl alcohol).¹⁶⁹ BPQDs were incorporated into PLGA matrix to form PLGA/BPQDs heterostructure nanomaterials by desolvation of the hydrophobic droplets (**Figure 1.15**). However, none of these reported polymers showed extended conjugation. The use of conjugated polymers is likely to extend the potential of these

organic/inorganic heterostructure nanomaterials to many other applications including photocatalysis.

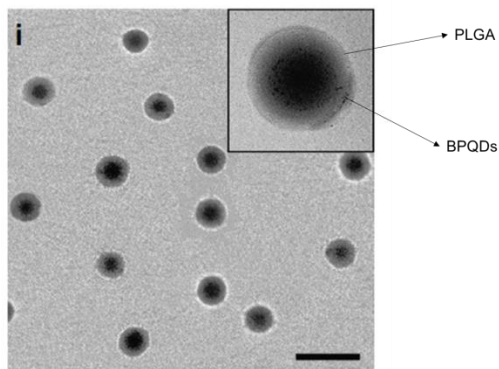


Figure 1.15. TEM image of the PLGA/BPQDs heterostructured nanospheres (scale bar, 200 nm) with the inset displaying the magnified TEM image of a PLGA/BPQDs.¹⁶⁹

The strategies to prepare organic nanoparticles can be transferred to construct organic heterostructure nanomaterials. A donor-acceptor (D-A) heterojunction nanomaterial was fabricated by the mini-emulsion evaporation method using sodium dodecyl sulfate (SDS) as surfactant, from a donor polymer poly([2,6'-4,8-di(5-ethylhexylthienyl) benzo[1,2-b;3,3-b]dithiophene]{3-fluoro-2[(2-ethylhexyl)carbonyl]thieno[3,4-b]thiophenediyil}) (PTB7-Th) and a non-fullerene acceptor 5,5'-[[4,4,9,9-tetrakis(2-ethylhexyl)-4,9-dihydro-s-indaceno[1,2-b:5,6-b']dithiophene-2,7-diyl]bis(2,1,3-benzothiadiazole-7,4-diylmethylidyne)]bis[3-ethyl-2-thioxo-4-thiazolidinone] (EH-IDTBR) (**Figure 1.16**).¹⁷⁰ The resulting photocatalyst showed remarkable HER of over 60 mmol h⁻¹ g⁻¹ under 350 to 800 nm illumination with AQY over 6% at 700 nm. The internal D-A semiconductor heterojunction with type-II energy offset greatly improved charge transfer (**Figure 1.16**), which was the reason for significantly enhanced photocatalytic activity compared to the parent nanoparticles formed from the single organic semiconductor.

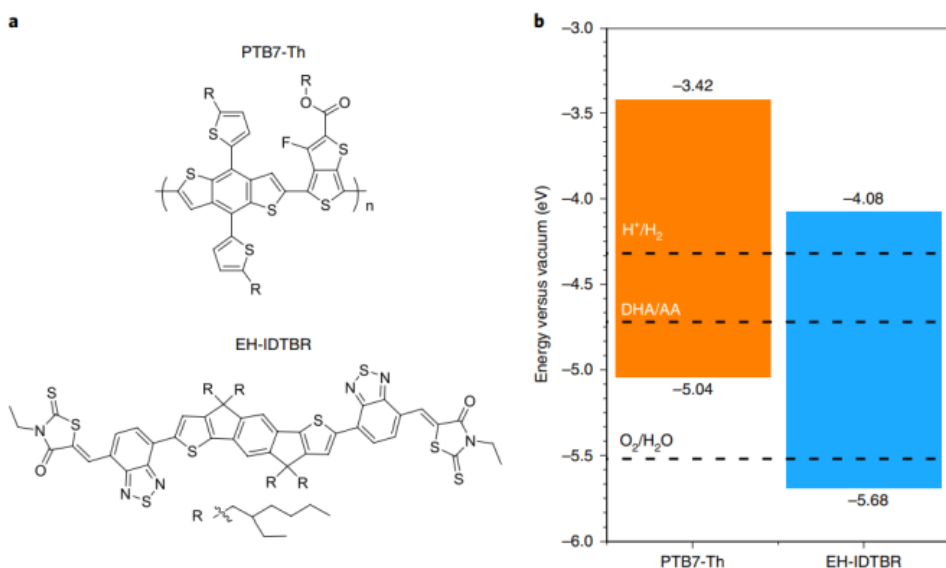


Figure 1.16. a) Chemical structures of polymer donor (PTB7-Th) and molecular acceptor (EH-IDTBR). **b)** Energy levels of PTB7-Th and EH-IDTBR.¹⁷⁰

Nano-particulate photocatalysts have two main advantages. Photogenerated electrons and holes have a considerably shorter distance to move from bulk material to surface reaction sites, leading to a reduced possibility of recombination.¹⁸ Moreover, reducing the particle size results in quadratic growth of the specific surface area, which provides more reactive sites for photocatalytic redox reactions. Many publications have exploited this and synthesised nanosized materials that are orders of magnitude more active than bulk photocatalysts.^{20,62,68,125,171,172} However, most of these works are based on inorganic materials. Over the last ten years, it has become clear that organic materials have great potential for photocatalytic H₂ evolution from water. This motivates further investigation into organic nanomaterials and organic/inorganic heterojunction nanomaterials for photocatalytic H₂ evolution.

1.5. Experimental Techniques

Materials in this thesis are characterized by some common techniques such as ultraviolet-visible (UV-vis) absorption spectroscopy, photoluminescence (PL) spectroscopy, Raman spectroscopy, gel permeation chromatography (GPC), powder X-ray diffraction (PXRD), thermogravimetric analysis (TGA), dynamic light scattering (DLS), Fourier-transform infrared spectroscopy (FT-IR), time-correlated single photon counting (TCSPC), inductively coupled plasma optical emission spectrometry (ICP-OES), field emission scanning electron microscope (FE-SEM), scanning transmission electron microscope (STEM), and high resolution

transmission electron microscope (HR-TEM). The photocatalytic hydrogen evolution performance is evaluated by a high throughput methodology, as introduced previously by our group.¹⁰⁹ The high throughput methodology is outlined in greater detail below.

1.5.1. High Throughput Methodology

Many measurement conditions have significant impacts on photocatalytic hydrogen production performance, including scavenger concentrations, types of scavengers, types of co-catalysts, amount of co-catalyst loading, the mass of catalysts, and so on. It is time-consuming to optimize the photocatalytic performance by the conventional method, in which the other factors are kept the same but changing one factor each time to obtain the optimal condition. Our group developed a high throughput methodology to screen and optimize photocatalytic hydrogen evolution performance, allowing 48 samples to be tested parallelly in one run (**Figure 1.17**).¹⁰⁹

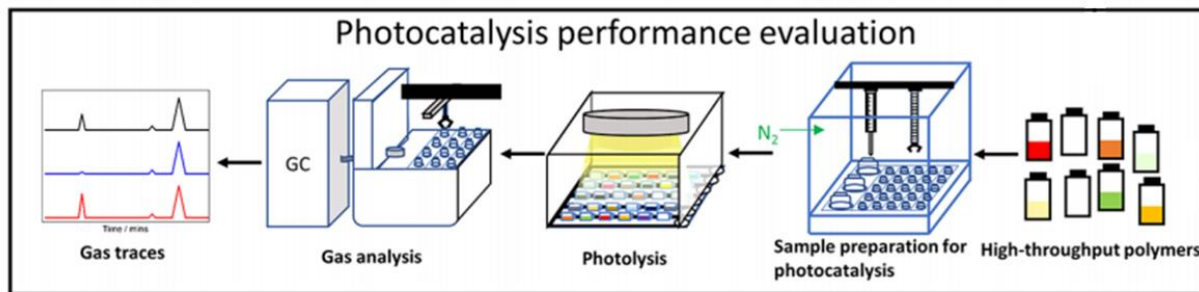


Figure 1.17. Workflow for high throughput measurement.¹⁰⁹

There are three main parts in the high throughput method; degassing, irradiation, and analysis. Photocatalysts were added into sample vials (volume = 12.5 mL) and purged with nitrogen in a Sweigher Chemspeed Technologies robot for at least 3 hours. Liquid solutions were then added into each vial through the liquid handling system under inert conditions. A capper tool was applied to cap vials with pierceable caps. Next, up to 48 vials were transferred to a solar simulator (A4.5G, Class AAA, IEC/JIS/ASTM, 1440 W xenon, 12 × 12 in., MODEL:94123A) and illuminated for a specific time. Samples were rotated and rocked to prevent sedimentation during irradiation. Finally, gaseous products were injected one by one automatically via a headspace injector and analyzed using a Shimadzu headspace gas chromatography.

1.6. Project Aims

This thesis aims to process organic materials into nanoparticles and heterostructure nanoparticles to achieve high performance for photocatalytic H₂ production from water in the

presence of sacrificial reagents. As discussed above, nano-particulate photocatalysts have some unique properties that are different from bulk photocatalysts but are beneficial for photocatalysis performance. The small size of photocatalyst provides a shorter distance for photogenerated electrons and holes to travel from bulk material to surface reaction sites.¹⁸ The photogenerated electrons and holes have a better chance to reach to catalyst surface and then induce redox reaction if photocatalyst has a smaller size. Also, photocatalyst with small size generally has a large surface area, which is often correlated with high photocatalytic activity. Nanosized photocatalysts have been demonstrated to be orders of magnitude more active than bulk photocatalysts.^{62,171,172} On the other hand, the formation of heterojunctions is beneficial for the separation of photogenerated electrons and holes. Design and synthesis of new nanomaterials and heterojunction nanomaterials by using emerging organic materials hold great promise to boost photocatalytic H₂ production performance.

Incorporation of polymer in inorganic nanoparticles offers a potential strategy to make organic/inorganic nanoparticles. However, conjugated polymers are generally synthesised at high temperatures with the use of organic solvent. These polymerisation reaction conditions are believed to induce aggregation of inorganic nanoparticles, and therefore it is difficult to form polymer/inorganic heterostructure nanoparticles by in-situ polymerisation in the presence of inorganic nanoparticles. To avoid polymerisation reactions, parent materials should be synthesized separately. Evaporation induced self-assembly method offer a chance to form organic/inorganic nanoparticles by simply evaporation of organic solvent droplet containing both as-synthesized parent materials. This method requires each parent material to be soluble in nonpolar or low polar solvents, such as chloroform and toluene. However, many photo-active conjugated polymers are insoluble in these organic solvents. Side-chain engineering offers a chance to make conjugated polymer soluble in organic solvents. We therefore want to prepare conjugated polymer/inorganic dots nano-heterojunctions (**Chapter 2**) to study the impact of introducing inorganic dots on optical properties and photocatalytic activities of conjugated polymers.

Organic photocatalysts also have some inherent limitations, such as strong exciton binding energies and low charge carrier mobilities, which restrict their photocatalytic activity due to recombination of charge carriers. In the field of organic photovoltaics (OPV), these issues have been addressed by introducing donor-acceptor bulk heterojunctions. We want to transfer this method to the photocatalysis area and see if the formation of donor-acceptor nanocomposites would reduce recombination of photogenerated charge carriers and boost photocatalytic

performance. The recombination of photogenerated charge carriers can be studied by emission spectroscopy. Moreover, structure diversity offers a large number of donors and acceptors. It could be time- and energy-consuming to screen these donor-acceptor combinations, especially for ternary system. The machine learning method can be used to predict performance of these nanocomposites based on a small amount of experimental data and therefore significantly accelerate discovery of high-performance materials (**Chapter 3**).

Crystallinity is also crucial for photocatalysis. Noncovalent π - π stacking in crystalline supramolecular assembly offers a channel for fast charge transfer, which is beneficial for the separation of photogenerated charge carriers. Moreover, structure flexibility and morphology tunability of supramolecular systems provide an opportunity to fine-tune the photochemical properties and, therefore establish structure- and morphology-activity relationships. A further aim of this research is to study the aggregation-state properties of small organic assembly and understand the key factors that determine photocatalytic activity of aggregation-state (**Chapter 4**). The influence of morphology and structure on optical and electronic properties, as well as the photocatalytic activities, will be investigated by a series of spectroscopy.

1.7. Reference

- 1 L. Capuano, International Energy Outlook 2020 (IEO2020). Website: <https://www.eia.gov/outlooks/ieo/pdf/ieo2020.pdf>, Date accessed: October 14th, 2020.
- 2 O. Ellabban, H. Abu-Rub and F. Blaabjerg, *Renew. Sustain. Energy Rev.*, 2014, **39**, 748–764.
- 3 IEA, Renewable electricity generation by technology, 2010-2025, IEA, Paris. Website: <https://www.iea.org/data-and-statistics/charts/renewable-electricity-generation-by-technology-2010-2025>, Date accessed: November 6th, 2020.
- 4 S. R. Bull, *Proc. IEEE*, 2001, **89**, 1216–1226.
- 5 G. W. C. and N. S. Lewis, *Phys. Today*, 2007, **60**, 37–42.
- 6 C. L. and M. R. W. J. Gong, *Chem. Soc. Rev.*, 2019, **48**, 1862–1864.
- 7 M. Jung, S. G. Ji, G. Kim and S. Il Seok, *Chem. Soc. Rev.*, 2019, **48**, 2011–2038.
- 8 Y. Liu, P. Bhattacharai, Z. Dai and X. Chen, *Chem. Soc. Rev.*, 2019, **48**, 2053–2108.
- 9 B. A. Pinaud, J. D. Benck, L. C. Seitz, A. J. Forman, Z. Chen, T. G. Deutsch, B. D. James, K. N. Baum, G. N. Baum, S. Ardo, H. Wang, E. Miller and T. F. Jaramillo, *Energy Environ. Sci.*, 2013, **6**, 1983–2002.
- 10 X. Chen, S. Shen, L. Guo and S. S. Mao, *Chem. Rev.*, 2010, **110**, 6503–6570.
- 11 C. Zhao, Z. Chen, R. Shi, X. Yang and T. Zhang, *Adv. Mater.*, 2020, **32**, 1–52.
- 12 T. Banerjee, F. Podjaski, J. Kröger, B. P. Biswal and B. V. Lotsch, *Nat. Rev. Mater.*, 2020, **6**, 168–190.
- 13 G. Zhang, Z. A. Lan and X. Wang, *Angew. Chemie - Int. Ed.*, 2016, **55**, 15712–15727.
- 14 Y. Wang, A. Vogel, M. Sachs, R. S. Sprick, L. Wilbraham, S. J. A. Moniz, R. Godin, M. A. Zwijnenburg, J. R. Durrant, A. I. Cooper and J. Tang, *Nat. Energy*, 2019, **4**, 746–760.
- 15 S. Lin, H. Huang, T. Ma and Y. Zhang, *Adv. Sci.*, 2021, **8**, 23–25.
- 16 Q. Wu, J. Cao, X. Wang, Y. Liu, Y. Zhao, H. Wang, Y. Liu, H. Huang, F. Liao, M. Shao and Z. Kang, *Nat. Commun.*, 2021, **12**, 1–10.
- 17 H. Hou, X. Zeng and X. Zhang, *Angew. Chemie - Int. Ed.*, 2020, **59**, 17356–17376.
- 18 A. Kudo and Y. Miseki, *Chem. Soc. Rev.*, 2009, **38**, 253–278.
- 19 J. Ran, J. Zhang, J. Yu, M. Jaroniec and S. Z. Qiao, *Chem. Soc. Rev.*, 2014, **43**, 7787–7812.
- 20 M. Ni, M. K. H. Leung, D. Y. C. Leung and K. Sumathy, *Renew. Sustain. Energy Rev.*, 2007, **11**, 401–425.
- 21 S. J. A. Moniz, S. A. Shevlin, D. J. Martin, Z. X. Guo and J. Tang, *Energy Environ. Sci.*, 2015, **8**, 731–759.
- 22 S. Ye, R. Wang, M. Z. Wu and Y. P. Yuan, *Appl. Surf. Sci.*, 2015, **358**, 15–27.

- 23 X. Chen, N. Li, Z. Kong, W. J. Ong and X. Zhao, *Mater. Horizons*, 2018, **5**, 9–27.
- 24 O. Ola and M. M. Maroto-Valer, *J. Photochem. Photobiol. C Photochem. Rev.*, 2015, **24**, 16–42.
- 25 J. Low, B. Cheng and J. Yu, *Appl. Surf. Sci.*, 2017, **392**, 658–686.
- 26 Z. Wu, X. Yuan, J. Zhang, H. Wang, L. Jiang and G. Zeng, *ChemCatChem*, 2017, **9**, 41–64.
- 27 R. Gusain, K. Gupta, P. Joshi and O. P. Khatri, *Adv. Colloid Interface Sci.*, 2019, **272**, 102009.
- 28 D. Ayodhya and G. Veerabhadram, *Mater. Today Energy*, 2018, **9**, 83–113.
- 29 N. R. Khalid, A. Majid, M. B. Tahir, N. A. Niaz and S. Khalid, *Ceram. Int.*, 2017, **43**, 14552–14571.
- 30 L. Marzo, S. K. Pagire, O. Reiser and B. König, *Angew. Chemie - Int. Ed.*, 2018, **57**, 10034–10072.
- 31 S. Subudhi, D. Rath and K. M. Parida, *Catal. Sci. Technol.*, 2018, **8**, 679–696.
- 32 L. I. Granone, F. Sieland, N. Zheng, R. Dillert and D. W. Bahnemann, *Green Chem.*, 2018, **20**, 1169–1192.
- 33 X. Liu, X. Duan, W. Wei, S. Wang and B. J. Ni, *Green Chem.*, 2019, **21**, 4266–4289.
- 34 W. Wang, G. Li, D. Xia, T. An, H. Zhao and P. K. Wong, *Environ. Sci. Nano*, 2017, **4**, 782–799.
- 35 P. V. Laxma Reddy, B. Kavitha, P. A. Kumar Reddy and K. H. Kim, *Environ. Res.*, 2017, **154**, 296–303.
- 36 R. Ramachandran and R. K. Menon, *Int. J. Hydrogen Energy*, 1998, **23**, 593–598.
- 37 I. K. Kapdan and F. Kargi, *Enzyme Microb. Technol.*, 2006, **38**, 569–582.
- 38 B. C. R. Ewan and R. W. K. Allen, *Int. J. Hydrogen Energy*, 2005, **30**, 809–819.
- 39 K. Fujishima, A., & Honda, *Nature*, 1972, **238**, 37–38.
- 40 S. Matsuoka, H. Fujii, T. Yamada, C. Pac, A. Ishida, S. Takamuku, M. Kusaba, N. Nakashima, S. Yanagida, K. Hashimoto and T. Sakata, *J. Phys. Chem.*, 1991, **95**, 5802–5808.
- 41 M. R. Gao, Y. F. Xu, J. Jiang, Y. R. Zheng and S. H. Yu, *J. Am. Chem. Soc.*, 2012, **134**, 2930–2933.
- 42 K. Maeda, A. Xiong, T. Yoshinaga, T. Ikeda, N. Sakamoto, T. Hisatomi, M. Takashima, D. Lu, M. Kanehara, T. Setoyama, T. Teranishi and K. Domen, *Angew. Chemie*, 2010, **122**, 4190–4193.
- 43 Z.-A. Lan, Y. Fang, Y. Zhang and X. Wang, *Angew. Chemie*, 2018, **130**, 479–483.
- 44 G. Zhang, Z. A. Lan and X. Wang, *Chem. Sci.*, 2017, **8**, 5261–5274.
- 45 O. Voznyy, B. R. Sutherland, A. H. Ip, D. Zhitomirsky and E. H. Sargent, *Nat. Rev. Mater.*, 2017, **2**, 1–10.

- 46 Z. Zhang, X. Chen, H. Zhang, W. Liu, W. Zhu and Y. Zhu, *Adv. Mater.*, 2020, **32**, 1–6.
- 47 A. G. Slater and A. I. Cooper, *Science (80-.).*, 2015, **348**, 8075.
- 48 J. Yang, D. Wang, H. Han and C. Li, *Acc. Chem. Res.*, 2013, **46**, 1900–1909.
- 49 L. Jiang, X. Yuan, Y. Pan, J. Liang, G. Zeng, Z. Wu and H. Wang, *Appl. Catal. B Environ.*, 2017, **217**, 388–406.
- 50 K. Maeda, K. Teramura, D. Lu, N. Saito, Y. Inoue and K. Domen, *Angew. Chemie*, 2006, **118**, 7970–7973.
- 51 D. J. Woods, R. S. Sprick, C. L. Smith, A. J. Cowan and A. I. Cooper, *Adv. Energy Mater.*, 2017, **7**, 1700479.
- 52 R. S. Sprick, Y. Bai, A. A. Y. Guilbert, M. Zbiri, C. M. Aitchison, L. Wilbraham, Y. Yan, D. J. Woods, M. A. Zwijnenburg and A. I. Cooper, *Chem. Mater.*, 2019, **31**, 305–313.
- 53 M. Sachs, R. S. Sprick, D. Pearce, S. A. J. Hillman, A. Monti, A. A. Y. Guilbert, N. J. Brownbill, S. Dimitrov, X. Shi, F. Blanc, M. A. Zwijnenburg, J. Nelson, J. R. Durrant and A. I. Cooper, *Nat. Commun.*, 2018, **9**, 1–11.
- 54 X. Wang, L. Chen, S. Y. Chong, M. A. Little, Y. Wu, W. H. Zhu, R. Clowes, Y. Yan, M. A. Zwijnenburg, R. S. Sprick and A. I. Cooper, *Nat. Chem.*, 2018, **10**, 1180–1189.
- 55 Y. Wu, X. Zhang, Y. Xing, Z. Hu, H. Tang, W. Luo, F. Huang and Y. Cao, *ACS Mater. Lett.*, 2019, **1**, 620–627.
- 56 A. Reynal, E. Pastor, M. A. Gross, S. Selim, E. Reisner and J. R. Durrant, *Chem. Sci.*, 2015, **6**, 4855–4859.
- 57 J. J. Velázquez, R. Fernández-González, L. Díaz, E. Pulido Melián, V. D. Rodríguez and P. Núñez, *J. Alloys Compd.*, 2017, **721**, 405–410.
- 58 Y. Yan, J. Chen, N. Li, J. Tian, K. Li, J. Jiang, J. Liu, Q. Tian and P. Chen, *ACS Nano*, 2018, **12**, 3523–3532.
- 59 X. Zhang, T. Peng and S. Song, *J. Mater. Chem. A*, 2016, **4**, 2365–2402.
- 60 Y. Wang, Q. Wang, X. Zhan, F. Wang, M. Safdar and J. He, *Nanoscale*, 2013, **5**, 8326–8339.
- 61 H. Wang, L. Zhang, Z. Chen, J. Hu, S. Li, Z. Wang, J. Liu and X. Wang, *Chem. Soc. Rev.*, 2014, **43**, 5234–5244.
- 62 Y. Ma, X. Wang, Y. Jia, X. Chen, H. Han and C. Li, *Chem. Rev.*, 2014, **114**, 9987–10043.
- 63 B. A. Pinaud, J. D. Benck, L. C. Seitz, A. J. Forman, Z. B. Chen, T. G. Deutsch, B. D. James, K. N. Baum, G. N. Baum, S. Ardo, H. L. Wang, E. Miller and T. F. Jaramillo, *Energy Environ. Sci.*, 2013, **6**, 1983–2002.
- 64 Q. Wang, T. Hisatomi, Q. Jia, H. Tokudome, M. Zhong, C. Wang, Z. Pan, T. Takata, M. Nakabayashi, N. Shibata, Y. Li, I. D. Sharp, A. Kudo, T. Yamada and K. Domen, *Nat. Mater.*, 2016, **15**, 611–615.
- 65 A. Fujishima and K. Honda, *Nature*, 1972, **238**, 37–38.

- 66 G. N. Schrauzer and T. D. Guth, *J. Am. Chem. Soc.*, 1977, **99**, 7189–7193.
- 67 J. Xing, W. Q. Fang, H. J. Zhao and H. G. Yang, *Chem. - An Asian J.*, 2012, **7**, 642–657.
- 68 F. E. Osterloh, *Chem. Soc. Rev.*, 2013, **42**, 2294–2320.
- 69 A. A. Ismail and D. W. Bahnemann, *Sol. Energy Mater. Sol. Cells*, 2014, **128**, 85–101.
- 70 Z. H. N. Al-Azri, W. T. Chen, A. Chan, V. Jovic, T. Ina, H. Idriss and G. I. N. Waterhouse, *J. Catal.*, 2015, **329**, 355–367.
- 71 X. Chen, T. Yu, X. Fan, H. Zhang, Z. Li, J. Ye and Z. Zou, *Appl. Surf. Sci.*, 2007, **253**, 8500–8506.
- 72 G. R. Bamwenda, T. Uesugi, Y. Abe, K. Sayama and H. Arakawa, *Appl. Catal. A Gen.*, 2001, **205**, 117–128.
- 73 M. Matsumura, Y. Saho and H. Tsubomura, *J. Phys. Chem.*, 1983, **87**, 3807–3808.
- 74 J. R. Darwent and A. Mills, *J. Chem. Soc. Faraday Trans. 2 Mol. Chem. Phys.*, 1982, **78**, 359–367.
- 75 D. Meissner, R. Memming and B. Kastening, *J. Phys. Chem.*, 1988, **92**, 3476–3483.
- 76 W. Erbs, J. Desilvestro, E. Borgarello and M. Grätzel, *J. Phys. Chem.*, 1984, **88**, 4001–4006.
- 77 R. Niishiro, H. Kato and A. Kudo, *Phys. Chem. Chem. Phys.*, 2005, **7**, 2241–2245.
- 78 T. Sun, J. Fan, E. Liu, L. Liu, Y. Wang, H. Dai, Y. Yang, W. Hou, X. Hu and Z. Jiang, *Powder Technol.*, 2012, **228**, 210–218.
- 79 F. Lakadamyali and E. Reisner, *Chem. Commun.*, 2011, **47**, 1695–1697.
- 80 E. Reisner, D. J. Powell, C. Cavazza, J. C. Fontecilla-Camps and F. A. Armstrong, *J. Am. Chem. Soc.*, 2009, **131**, 18457–18466.
- 81 S. Chen, Y. Li and C. Wang, *RSC Adv.*, 2015, **5**, 15880–15885.
- 82 R. Abe, K. Sayama and H. Sugihara, *J. Phys. Chem. B*, 2005, **109**, 16052–16061.
- 83 T. Takata and K. Domen, *ACS Energy Lett.*, 2019, **4**, 542–549.
- 84 T. Lv, Z. Jin, L. Zhang and Y.-J. Zeng, *Organic–Inorganic Semiconductor Heterojunction Photocatalysts*, 2020.
- 85 P. Guiglion, C. Butchosa and M. A. Zwijnenburg, *Macromol. Chem. Phys.*, 2016, **217**, 344–353.
- 86 S. Yanagida, A. Kabumoto, K. Mizumoto, C. Pac and K. Yoshino, *J. Chem. Soc. - Ser. Chem. Commun.*, 1985, 474–475.
- 87 X. Wang, K. Maeda, A. Thomas, K. Takanabe, G. Xin, J. M. Carlsson, K. Domen and M. Antonietti, *Nat. Mater.*, 2009, **8**, 76–80.
- 88 C. Butchosa, P. Guiglion and M. A. Zwijnenburg, *J. Phys. Chem. C*, 2014, **118**, 24833–24842.
- 89 W. J. Ong, L. L. Tan, Y. H. Ng, S. T. Yong and S. P. Chai, *Chem. Rev.*, 2016, **116**,

- 7159–7329.
- 90 S. Cao, J. Low, J. Yu and M. Jaroniec, *Adv. Mater.*, 2015, **27**, 2150–2176.
- 91 X. Han, D. Xu, L. An, C. Hou, Y. Li, Q. Zhang and H. Wang, *Appl. Catal. B Environ.*, 2019, **243**, 136–144.
- 92 L. Wang, Y. Hong, E. Liu, Z. Wang, J. Chen, S. Yang, J. Wang, X. Lin and J. Shi, *Int. J. Hydrogen Energy*, 2020, **45**, 6425–6436.
- 93 R. S. Sprick, B. Bonillo, R. Clowes, P. Guiglion, N. J. Brownbill, B. J. Slater, F. Blanc, M. A. Zwijnenburg, D. J. Adams and A. I. Cooper, *Angew. Chemie*, 2016, **128**, 1824–1828.
- 94 X. H. Zhang, X. P. Wang, J. Xiao, S. Y. Wang, D. K. Huang, X. Ding, Y. G. Xiang and H. Chen, *J. Catal.*, 2017, **350**, 64–71.
- 95 J. X. Jiang, F. Su, A. Trewin, C. D. Wood, N. L. Campbell, H. Niu, C. Dickinson, A. Y. Ganin, M. J. Rosseinsky, Y. Z. Khimyak and A. I. Cooper, *Angew. Chemie - Int. Ed.*, 2007, **46**, 8574–8578.
- 96 R. S. Sprick, J. X. Jiang, B. Bonillo, S. Ren, T. Ratvijitvech, P. Guiglion, M. A. Zwijnenburg, D. J. Adams and A. I. Cooper, *J. Am. Chem. Soc.*, 2015, **137**, 3265–3270.
- 97 J. Liu, W. Fu, Y. Liao, J. Fan and Q. Xiang, *J. Mater. Sci. Technol.*, 2021, **91**, 224–240.
- 98 S. Chen, T. Takata and K. Domen, *Nat. Rev. Mater.*, 2017, **2**, 1–17.
- 99 M. Liu, L. Guo, S. Jin and B. Tan, *J. Mater. Chem. A*, 2019, **7**, 5153–5172.
- 100 M. Liu, Q. Huang, S. Wang, Z. Li, B. Li, S. Jin and B. Tan, *Angew. Chemie - Int. Ed.*, 2018, **57**, 11968–11972.
- 101 X. Feng, X. Ding and D. Jiang, *Chem. Soc. Rev.*, 2012, **41**, 6010–6022.
- 102 J. L. Segura, S. Royuela and M. Mar Ramos, *Chem. Soc. Rev.*, 2019, **48**, 3903–3945.
- 103 V. S. Vyas, F. Haase, L. Stegbauer, G. Savasci, F. Podjaski, C. Ochsenfeld and B. V. Lotsch, *Nat. Commun.*, 2015, **6**, 1–9.
- 104 X. Wang, L. Chen, S. Y. Chong, M. A. Little, Y. Wu, W. H. Zhu, R. Clowes, Y. Yan, M. A. Zwijnenburg, R. S. Sprick and A. I. Cooper, *Nat. Chem.*, 2018, **10**, 1180–1189.
- 105 P. Pachfule, A. Acharjya, J. Roeser, T. Langenhahn, M. Schwarze, R. Schomäcker, A. Thomas and J. Schmidt, *J. Am. Chem. Soc.*, 2018, **140**, 1423–1427.
- 106 Y. Xiang, X. Wang, X. Zhang, H. Hou, K. Dai, Q. Huang and H. Chen, *J. Mater. Chem. A*, 2018, **6**, 153–159.
- 107 N. Xu, Y. Liu, W. Yang, J. Tang, B. Cai, Q. Li, J. Sun, K. Wang, B. Xu, Q. Zhang and Y. Fan, *ACS Appl. Energy Mater.*, 2020, **3**, 11939–11946.
- 108 J. Thote, H. B. Aiyappa, A. Deshpande, D. Díaz Díaz, S. Kurungot and R. Banerjee, *Chem. - A Eur. J.*, 2014, **20**, 15961–15965.
- 109 Y. Bai, L. Wilbraham, B. J. Slater, M. A. Zwijnenburg, R. S. Sprick and A. I. Cooper,

J. Am. Chem. Soc., 2019, **141**, 9063–9071.

- 110 J. H. Park, K. C. Ko, N. Park, H. W. Shin, E. Kim, N. Kang, J. Hong Ko, S. M. Lee, H. J. Kim, T. K. Ahn, J. Y. Lee and S. U. Son, *J. Mater. Chem. A*, 2014, **2**, 7656–7661.
- 111 S. Chu, C. Wang, J. Feng, Y. Wang and Z. Zou, *Int. J. Hydrogen Energy*, 2014, **39**, 13519–13526.
- 112 C. Yang, B. C. Ma, L. Zhang, S. Lin, S. Ghasimi, K. Landfester, K. A. I. Zhang and X. Wang, *Angew. Chemie*, 2016, **128**, 9348–9352.
- 113 J. Low, J. Yu, M. Jaroniec, S. Wageh and A. A. Al-Ghamdi, *Adv. Mater.*, 2017, **29**, 1601694.
- 114 J. Lin, J. Shen, R. Wang, J. Cui, W. Zhou, P. Hu, D. Liu, H. Liu, J. Wang, R. I. Boughton and Y. Yue, *J. Mater. Chem.*, 2011, **21**, 5106–5113.
- 115 J. Cao, X. Li, H. Lin, S. Chen and X. Fu, *J. Hazard. Mater.*, 2012, **239–240**, 316–324.
- 116 S. Chen, Y. Hu, L. Ji, X. Jiang and X. Fu, *Appl. Surf. Sci.*, 2014, **292**, 357–366.
- 117 J. Zhang, Y. Hu, X. Jiang, S. Chen, S. Meng and X. Fu, *J. Hazard. Mater.*, 2014, **280**, 713–722.
- 118 S. Wang, B. Zhu, M. Liu, L. Zhang, J. Yu and M. Zhou, *Appl. Catal. B Environ.*, 2019, **243**, 19–26.
- 119 X. Hao, J. Zhou, Z. Cui, Y. Wang, Y. Wang and Z. Zou, *Appl. Catal. B Environ.*, 2018, **229**, 41–51.
- 120 X. Zhang, J. Xiao, M. Hou, Y. Xiang and H. Chen, *Appl. Catal. B Environ.*, 2018, **224**, 871–876.
- 121 J. Chen, C. L. Dong, D. Zhao, Y. C. Huang, X. Wang, L. Samad, L. Dang, M. Shearer, S. Shen and L. Guo, *Adv. Mater.*, 2017, **29**, 1606198.
- 122 X. Zhang, B. Peng, S. Zhang and T. Peng, *ACS Sustain. Chem. Eng.*, 2015, **3**, 1501–1509.
- 123 H. Miao, J. Yang, Y. Sheng, W. Li and Y. Zhu, *Sol. RRL*, 2021, **5**, 1–9.
- 124 C. Chikwendu Okpala, *Int. J. Adv. Eng. Technol. E- Int J Adv Engg Tech*, 2006, 12–18.
- 125 S. Huang, Y. Lin, J. H. Yang and Y. Yu, *ACS Symp. Ser.*, 2013, **1140**, 219–241.
- 126 L. Yuliati, J. H. Yang, X. Wang, K. Maeda, T. Takata, M. Antonietti and K. Domen, *J. Mater. Chem.*, 2010, **20**, 4295–4298.
- 127 M. Sathish, B. Viswanathan and R. P. Viswanath, *Int. J. Hydrogen Energy*, 2006, **31**, 891–898.
- 128 Z. Zhang, C. C. Wang, R. Zakaria and J. Y. Ying, *J. Phys. Chem. B*, 1998, **102**, 10871–10878.
- 129 N. Serpone, D. Lawless and R. Khairutdinov, *J. Phys. Chem.*, 1995, **99**, 16646–16654.
- 130 P. D. Cozzoli, A. Kornowski and H. Weller, *J. Am. Chem. Soc.*, 2003, **125**, 14539–14548.

- 131 L. Manna, E. C. Scher, L. S. Li and A. P. Alivisatos, *J. Am. Chem. Soc.*, 2002, **124**, 7136–7145.
- 132 L. Zhang, X. Fu, S. Meng, X. Jiang, J. Wang and S. Chen, *J. Mater. Chem. A*, 2015, **3**, 23732–23742.
- 133 and J. C. J. A. J. Nozik, M. C. Beard, J. M. Luther, M. Law, R. J. Ellingson, *Chem. Rev.*, 2010, **110**, 6873–6890.
- 134 A. Das, Z. Han, M. G. Haghghi and R. Eisenberg, *Proc. Natl. Acad. Sci. U. S. A.*, 2013, **110**, 16716–16723.
- 135 D. V. Talapin, J. S. Lee, M. V. Kovalenko and E. V. Shevchenko, *Chem. Rev.*, 2010, **110**, 389–458.
- 136 Y. J. Gao, X. B. Li, H. L. Wu, S. L. Meng, X. B. Fan, M. Y. Huang, Q. Guo, C. H. Tung and L. Z. Wu, *Adv. Funct. Mater.*, 2018, **28**, 1801769.
- 137 K. Miladi, D. Ibraheem, M. Iqbal, S. Sfar, H. Fessi and A. Elaissari, *EXCLI J.*, 2014, **13**, 28–57.
- 138 I. J. Joye and D. J. McClements, *Trends Food Sci. Technol.*, 2013, **34**, 109–123.
- 139 C. J. Martínez Rivas, M. Tarhini, W. Badri, K. Miladi, H. Greige-Gerges, Q. A. Nazari, S. A. Galindo Rodríguez, R. Á. Román, H. Fessi and A. Elaissari, *Int. J. Pharm.*, 2017, **532**, 66–81.
- 140 C. E. Mora-Huertas, H. Fessi and A. Elaissari, *Int. J. Pharm.*, 2010, **385**, 113–142.
- 141 D. Moinard-Chécot, Y. Chevalier, S. Briançon, L. Beney and H. Fessi, *J. Colloid Interface Sci.*, 2008, **317**, 458–468.
- 142 D. Tuncel and H. V. Demir, *Nanoscale*, 2010, **2**, 484–494.
- 143 C. Yang, B. C. Ma, L. Zhang, S. Lin, S. Ghasimi, K. Landfester, K. A. I. Zhang and X. Wang, *Angew. Chemie - Int. Ed.*, 2016, **55**, 9202–9206.
- 144 P. Sarrazin, D. Chaussy, L. Vurth, O. Stephan and D. Beneventi, *Langmuir*, 2009, **25**, 6745–6752.
- 145 A. Berkefeld and S. Mecking, *Angew. Chemie - Int. Ed.*, 2006, **45**, 6044–6046.
- 146 K. Müller, M. Klapper and K. Müllen, *Macromol. Rapid Commun.*, 2006, **27**, 586–593.
- 147 B. C. Ma, S. Ghasimi, K. Landfester, F. Vilela and K. A. I. Zhang, *J. Mater. Chem. A*, 2015, **3**, 16064–16071.
- 148 L. Wang, R. Fernández-Terán, L. Zhang, D. L. A. Fernandes, L. Tian, H. Chen and H. Tian, *Angew. Chemie*, 2016, **128**, 12494–12498.
- 149 C. M. Aitchison, R. S. Sprick and A. I. Cooper, *J. Mater. Chem. A*, 2019, **7**, 2490–2496.
- 150 G. Zhang, X. Yang, Y. Li, P. Zhang and H. Mi, *ChemSusChem*, 2019, **12**, 5070–5074.
- 151 Y. Che, A. Datar, K. Balakrishnan and L. Zang, *J. Am. Chem. Soc.*, 2007, **129**, 7234–7235.

- 152 J. Yang, H. Miao, Y. Wei, W. Li and Y. Zhu, *Appl. Catal. B Environ.*, 2019, **240**, 225–233.
- 153 J. Zhou, W. Zhang, X. F. Jiang, C. Wang, X. Zhou, B. Xu, L. Liu, Z. Xie and Y. Ma, *J. Phys. Chem. Lett.*, 2018, **9**, 596–600.
- 154 P. Guo, P. Chen, W. Ma and M. Liu, *J. Mater. Chem.*, 2012, **22**, 20243–20249.
- 155 A. Batra, G. Kladnik, H. Vázquez, J. S. Meisner, L. Floreano, C. Nuckolls, D. Cvetko, A. Morgante and L. Venkataraman, *Nat. Commun.*, 2012, **3**, 1–7.
- 156 D. Liu, J. Wang, X. Bai, R. Zong and Y. Zhu, *Adv. Mater.*, 2016, **28**, 7284–7290.
- 157 M. C. Nolan, J. J. Walsh, L. L. E. Mears, E. R. Draper, M. Wallace, M. Barrow, B. Dietrich, S. M. King, A. J. Cowan and D. J. Adams, *J. Mater. Chem. A*, 2017, **5**, 7555–7563.
- 158 A. Mishra and P. Bäuerle, *Angew. Chemie - Int. Ed.*, 2012, **51**, 2020–2067.
- 159 N. Zhang, L. Wang, H. Wang, R. Cao, J. Wang, F. Bai and H. Fan, *Nano Lett.*, 2018, **18**, 560–566.
- 160 J. H. Park, G. Von Maltzahn, E. Ruoslahti, S. N. Bhatia and M. J. Sailor, *Angew. Chemie - Int. Ed.*, 2008, **47**, 7284–7288.
- 161 J. Wang, W. Shi, D. Liu, Z. J. Zhang, Y. Zhu and D. Wang, *Appl. Catal. B Environ.*, 2017, **202**, 289–297.
- 162 Z. Zhang, Y. Zhu, X. Chen, H. Zhang and J. Wang, *Adv. Mater.*, 2019, **31**, 1–6.
- 163 S. V. P. Vattikuti, *Heterostructured Nanomaterials: Latest Trends in Formation of Inorganic Heterostructures*, Elsevier Ltd., 2018.
- 164 A. Wu, C. Tian, Y. Jiao, Q. Yan, G. Yang and H. Fu, *Appl. Catal. B Environ.*, 2017, **203**, 955–963.
- 165 C. Wang, L. Wang, J. Jin, J. Liu, Y. Li, M. Wu, L. Chen, B. Wang, X. Yang and B. L. Su, *Appl. Catal. B Environ.*, 2016, **188**, 351–359.
- 166 C. J. Brinker, Y. Lu, A. Sellinger and H. Fan, *Adv. Mater.*, 1999, **11**, 579–585.
- 167 J. Bae, J. Lawrence, C. Miesch, A. Ribbe, W. Li, T. Emrick, J. Zhu and R. C. Hayward, *Adv. Mater.*, 2012, **24**, 2735–2741.
- 168 T. Isojima, S. K. Suh, J. B. V. Sande and T. A. Hatton, *Langmuir*, 2009, **25**, 8292–8298.
- 169 J. Shao, H. Xie, H. Huang, Z. Li, Z. Sun, Y. Xu, Q. Xiao, X. F. Yu, Y. Zhao, H. Zhang, H. Wang and P. K. Chu, *Nat. Commun.*, 2016, **7**, 1–13.
- 170 J. Kosco, M. Bidwell, H. Cha, T. Martin, C. T. Howells, M. Sachs, D. H. Anjum, S. Gonzalez Lopez, L. Zou, A. Wadsworth, W. Zhang, L. Zhang, J. Tellam, R. Sougrat, F. Laquai, D. M. DeLongchamp, J. R. Durrant and I. McCulloch, *Nat. Mater.*, 2020, **19**, 559–565.
- 171 C. M. Aitchison and R. S. Sprick, *Nanoscale*, 2021, **13**, 634–646.
- 172 A. Kudo and Y. Miseki, *Chem. Soc. Rev.*, 2009, **38**, 253–278.

Chapter 2

Organic Polymer-Inorganic Dots Nanocomposites

2.1. Contributions to this Chapter

HR-TEM images for organic-inorganic nano-assemblies were obtained by Dr Houari Amari. The Cyclic voltammetry (CV) measurements were performed by Lunjie Liu. DFT and TD-DFT calculations were performed by Chengxi Zhao. Samples were synthesised with the help of Ai He and Gao hui. The high throughput equipment was devised and built with the help of Yang Bai and Rob Clowes. All other work was performed by the thesis author.

2.2. Background

Multifunctional nano-objects containing discrete domains of different inorganic materials are of interest because they can achieve optical, magnetic, or electronic properties that are superior to the individual constituent materials.¹ Such nanocomposites are often formed through seeded-growth of one material on seed particles of another, thus yielding inorganic nanocomposites with core-shell or dumbbell-like morphologies.^{2–7} Other preparation methods include the physical mixing of different nanoparticles and embedding multiple inorganic nanoparticles within a silica matrix.^{8–10} Recently, the assembly of multiple building blocks into clusters using the so-called evaporation induced self-assembly (EISA) method was reported.¹¹ This approach allows for quantum dots (QDs) to be assembled into large nanoparticle superstructures; e.g., CdSe/TiO₂ colloidal spheres¹² and CdSe/multishell supraparticles.¹³ CdSe/Au nanocomposites prepared via EISA exhibited higher photocatalytic activity for hydrogen production from water and better stability compared to the CdSe nanocrystal clusters alone.¹⁴

This approach has been shown to be transferable to organic/inorganic nanocomposites and was used to prepare nanocomposites containing inorganic QDs and solution-processable alkyl-polymers.^{1,11,15–17} To do this, nano-sized hydrophobic droplets containing the solution-processable polymer and the inorganic QDs were well-dispersed in water with the aid of a surfactant. By desolvating the hydrophobic droplets, inorganic QDs are incorporated into the polymer nanoparticle matrix. Such organic/inorganic nanocomposites offer promise for application in nanomedicine through the combination of diagnostic and therapeutic components in a single delivery system.^{1,18,19} None of the reported polymers showed extended conjugation, and we saw potential to extend this approach into other areas, specifically for photocatalysis.

Composites of inorganic photocatalysts with organic photocatalysts have been extensively studied: in particular, carbon nitrides-based composites have shown excellent performance as

photocatalysts for hydrogen production from water in the presence of a sacrificial hole scavenger.^{20–22} However, these composites cannot be obtained using solution-based methods because the constituent components are not soluble, which limits the range of synthetic tuneability. Conjugated polymer nanocomposites have been far less explored so far, but recent reports of composites of pyrene-based conjugated microporous polymers (CMPs) with MoS₂²³ and tri/diethynylbenzene-benzothiadiazole polymers with TiO₂^{24,25} have shown promise. However, an *in situ* polymerisation approach was used in both of these studies where the inorganic component is added to the monomers before performing the polymerisation. This introduces synthetic limitations and, more importantly, reduces control over the physical incorporation of the inorganic components. Since most conjugated polymer photocatalysts reported to date are not solution processible,^{26,27} solution-based methods such as EISA cannot be widely used to prepare conjugated polymer composites. However, recent reports of soluble conjugated polymer photocatalysts^{28,29} now make it possible to synthesise organic/inorganic semiconductor nanocomposites using EISA.

2.3. Preparation of Nano-assemblies

2.3.1. Preparation and Characterisation of Titanium Dioxide Dots

Titanium dioxide dots (TDs) were prepared using a modified wet-chemical procedure with oleylamine (*cis*-1-amino-9-octadecene) and oleic acid ((9Z)-octadec-9-enoic acid) as the surfactants (details in **Experimental Section**).³⁰ The surfactants solubilise the TDs in chloroform and serve as stabilizing ligands.^{14,31}

High-resolution transmission electron microscopy (HR-TEM) imaging showed uniform TDs of approximately 2.7 nm diameter (**Figure 2.1**). Since diffraction contrast typically dominates the image formation, bright-field TEM produces very little contrast (**Figure 2.1a**).^{32,33} Therefore, high-angle annular dark-field scanning transmission electron microscopy (HAADF-STEM) imaging was applied to provide clear contrast as shown in **Figure 2.1b**.

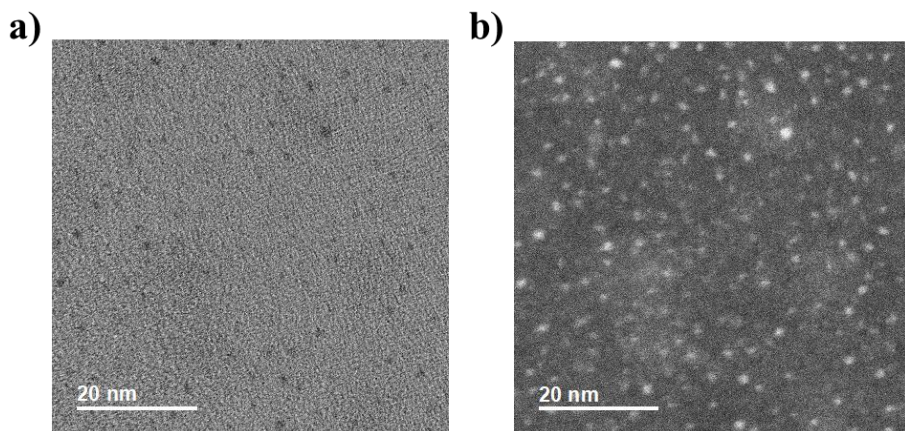


Figure 2.1. **a)** Bright-field STEM images of TiO_2 quantum dots. **b)** HAADF-STEM images of TiO_2 quantum dots.

Powder X-ray diffraction (PXRD) analysis showed that the TDs were obtained solely as TiO_2 in the anatase phase (**Figure 2.2**). The PXRD pattern exhibited obvious diffraction peaks at 25° and 48° indicating TiO_2 in the anatase phase, which was consistent with the previous report.³⁴ The diffraction peaks were broad probably because of the small size of TiO_2 particles.

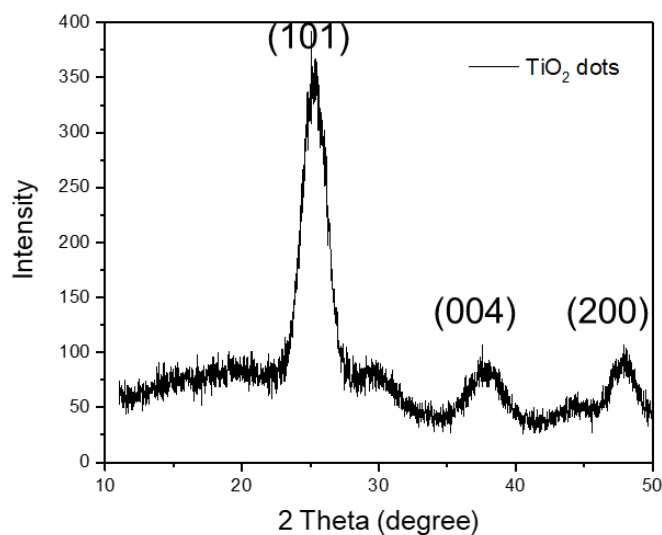


Figure 2.2. PXRD pattern of anatase TiO_2 dots.

2.3.2. Preparation and Characterisation of Soluble Polymer

The soluble organic polymer photocatalyst [poly(di-*n*-octyl-9*H*-fluorene-co-cyanobenzene), CSCP] was synthesised via Pd(0)-catalyzed Suzuki-Miyaura polycondensation of dibromobenzonitrile and the diboronic acid ester of di-*n*-octyl-9*H*-fluorene in toluene at 80°C

(Figure 2.3).^{28,35} After work-up and Soxhlet extraction, the polymer was found to be soluble in chloroform, which allowed for solution characterisation and solution processing.

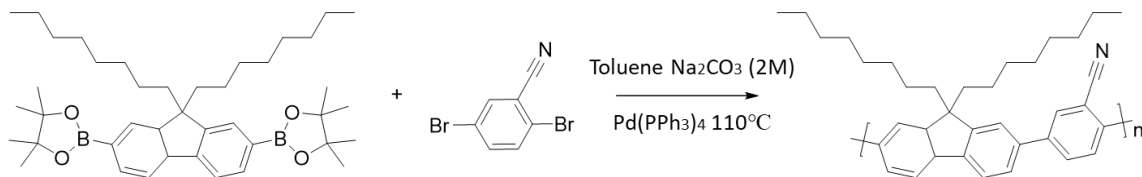


Figure 2.3. Synthesis of CSCP by Suzuki-Miyaura reaction.

Fourier-transform infrared spectroscopy (FT-IR) showed the presence of the expected alkyl C-H functionalities in polymer side-chains ($3000\text{-}2800\text{ cm}^{-1}$), and a characteristic band for the cyano-group at approximately 2225 cm^{-1} as shown in Figure 2.4a. The weight-average molecular weight of the polymer (M_n) was estimated to be 223 kg mol^{-1} by gel permeation chromatography, as calibrated against polystyrene standards (Figure 2.4b). The degree of polymerisation (DP_n) was estimated to be 453 ($DP_n = M_n/M_0$). The M_0 is the molecular weight of monomeric unit of CSCP.

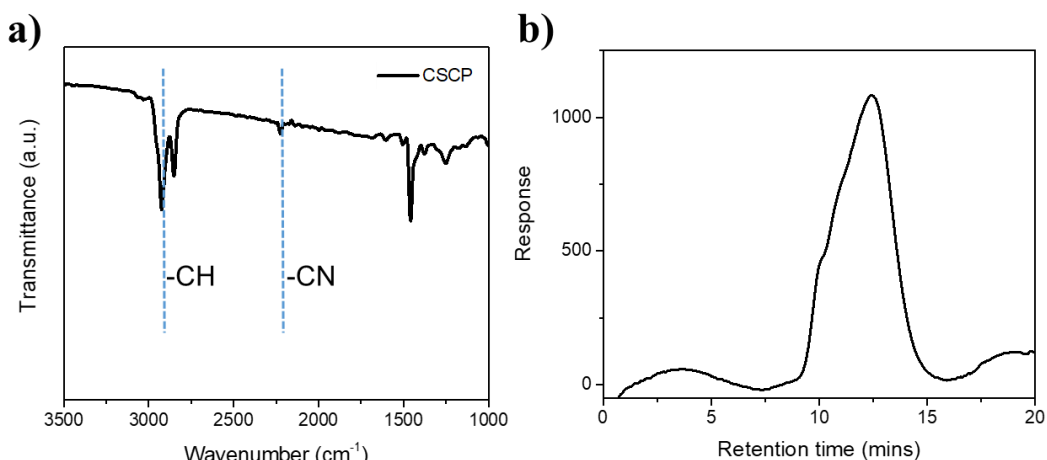


Figure 2.4. a) FT-IR of CSCP measured in the solid-state. **b)** Gel permeation chromatogram of CSCP (Chloroform was used as the mobile phase with a flow rate of 1 mL min^{-1} ; GPC was calibrated against polystyrene standards).

The solubility of CSCP allowed us to characterize it by ^1H NMR spectroscopy (Figure 2.5). This spectrum showed that 4 protons close to conjugated backbones are located at $1.8\text{-}2.3\text{ ppm}$. Other aliphatic protons of the 2-octyl side chain ($0.7\text{-}1.2\text{ ppm}$) as well as the aromatic signals ($7.7\text{-}8.1\text{ ppm}$) in the expected ratio (10:3) were observed. Residual palladium was found in the polymer sample at a concentration of 0.35 wt. %, as measured by inductively coupled plasma

mass spectrometry; this originates from the palladium catalyst used for the polycondensation reaction.

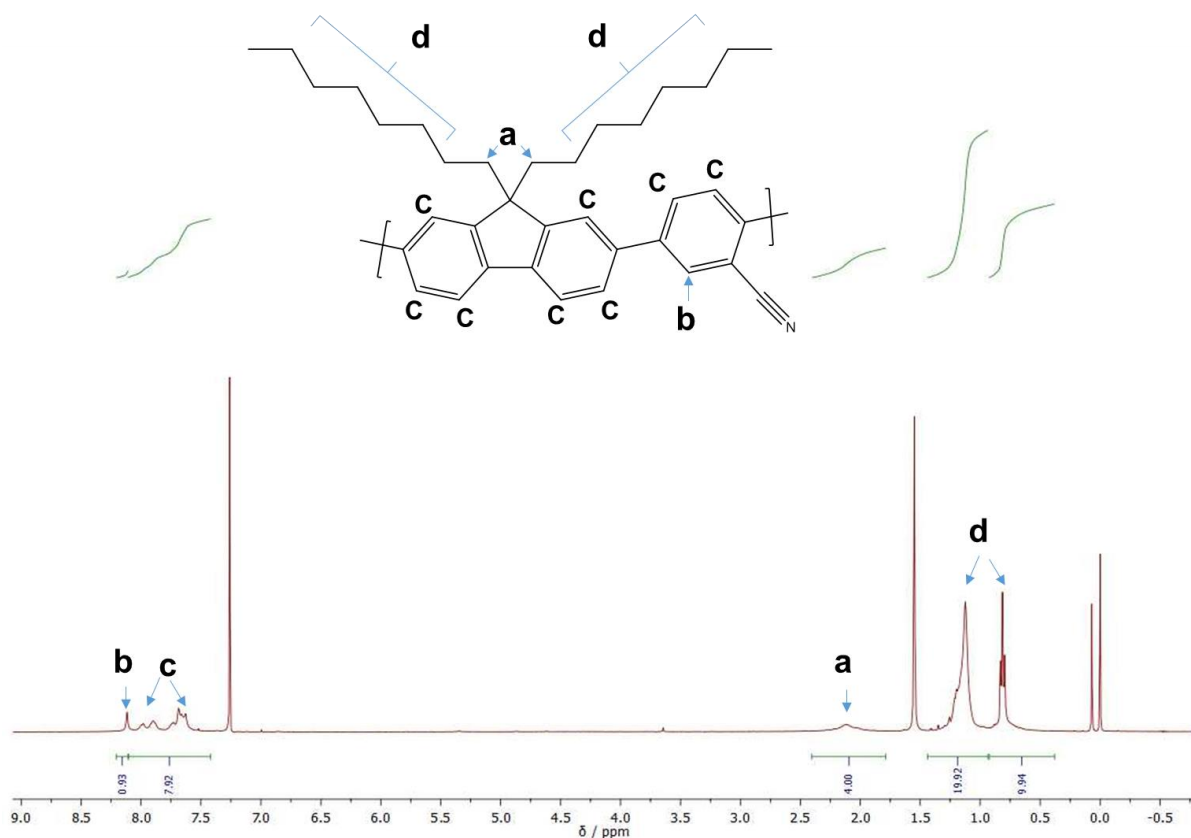


Figure 2.5. ^1H NMR spectra of CSCP in CDCl_3 .

2.3.3. Formation of Nanoassemblies

Both the TDs and CSCP polymer were soluble in chloroform and this allowed both to be combined in an oil-in-water emulsion process, which was used to make hybrid assemblies. To do this, the CSCP polymer was dissolved in chloroform along with the TDs, and this solution was emulsified in water containing sodium *n*-dodecyl sulfate (SDS) surfactant using an ultrasonic probe to produce a uniform emulsion. The emulsion was then stirred at 40 °C for around 14 hours to remove chloroform by evaporation to afford the co-assembled CSCP/TDs nanocomposites (CSCP/TDs NCs) as a clear solution, denoted hereafter as NCX%, where X is the weight percentage of polymer in the composite. The same conditions were also used to obtain NPs of the individual components; that is, CSCP-assembled nanoparticles (CSCP NPs) and TDs-assembled nanoparticles (TDs NPs), as shown in **Figure 2.6**.

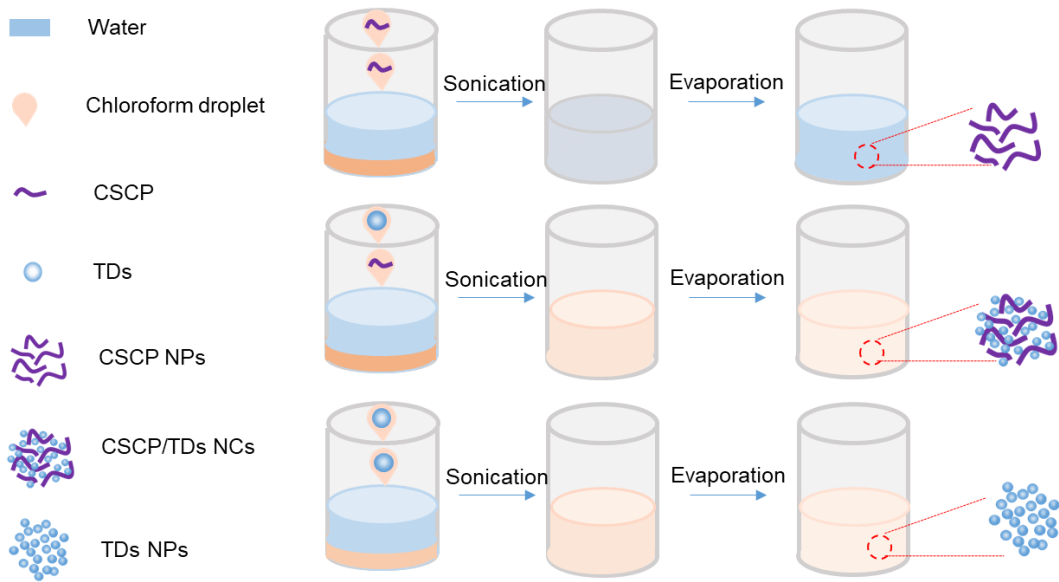


Figure 2.6. Synthesis of the nanoparticles and nanocomposites: CSCP and TDs are dissolved in chloroform (2 mL) and then emulsified with water (10 mL) in the presence of surfactant (sodium *n*-dodecyl sulfate) by ultrasonication.

As a result of chloroform evaporation when making the nanocomposites, the increase in solvent polarity forces solvophobic association between stabilizing ligands, as often observed in the 1D self-assembly of surfactants and other amphiphilic molecules (**Figure 2.7**).^{31,36,37}

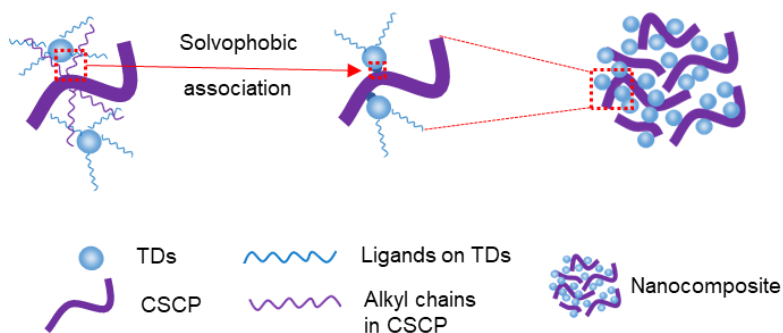


Figure 2.7. Diagram of proposed nanocomposite assembly mechanism.

We note that turbid solutions were generally obtained without stirring, indicating the formation of (undesirable) larger aggregates. After purification by dialysis for 3 days, nanocomposites containing more than 75 w/w % of TDs seemed to undergo aggregation, and sedimentation was observed (**Figure 2.8**). This result was supported by DLS data (**Figure 2.9**), which showed the formation of large aggregates. For NC10%, two size populations were observed in DLS, around 90 and 500 nm. But, the sizes of most nanoparticles were smaller than 100 nm as revealed by SEM images (*vide infra*). Therefore, the large particle sizes (larger than 300 nm) determined

by DLS were probably from the aggregation of small particles, which was consistent with the observed sedimentation. The polymer nanoparticles cannot be fully recovered by centrifugation probably because of low density.

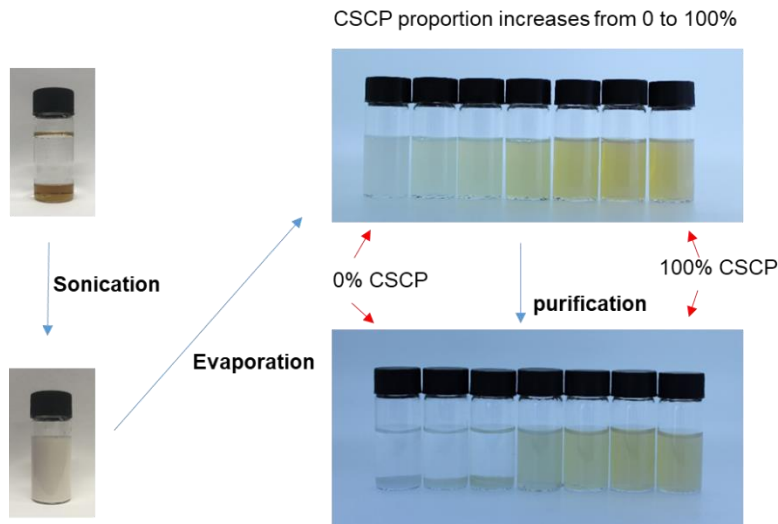


Figure 2.8. Pictures on the left side show evaporation induced self-assembly procedure and pictures on the right side show nanoparticles and nanocomposites aqueous suspension with different CSCP proportions before and after purification (CSCP proportion is 0, 10, 25, 50, 75, 90, 100% from left to right).

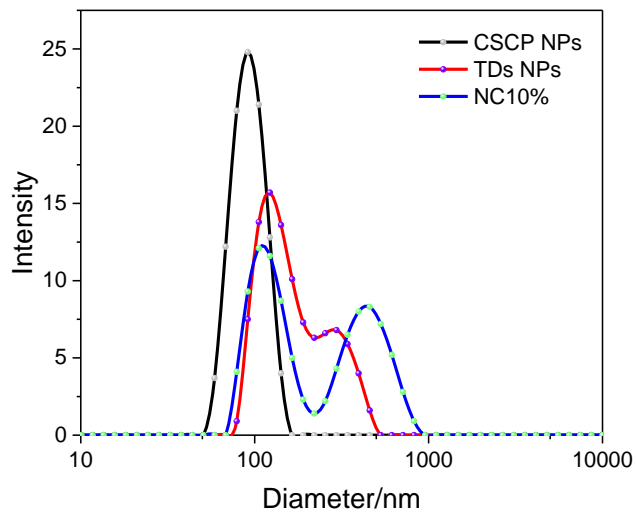


Figure 2.9. Size distribution of CSCP NPs, TDs NPs, and NC10% measured by DLS.

2.4. Morphology and Optical Properties

2.4.1. Morphology and Internal Structure

Various imaging techniques were used to study the morphology of the materials. Field-emission scanning electron microscopy (FE-SEM) images in high magnification showed that the materials were uniform spheres and statistical analysis showed that similar average sizes (around 50 nm) for TDs NPs, CSCP NPs, and CSCP/TDs NCs were obtained (**Figure 2.10** and **2.11a**). The average sizes obtained from SEM results were smaller compared to that from DLS results. We speculated that different degrees of aggregation occurred in nanoparticle dispersions. The serious aggregation probably occurred in TDs NPs and CSCP/TDs NCs because DLS results showed much larger particle sizes than SEM results. The moderate aggregation probably occurred in CSCP NPs because DLS results showed slightly larger particle sizes than SEM results.

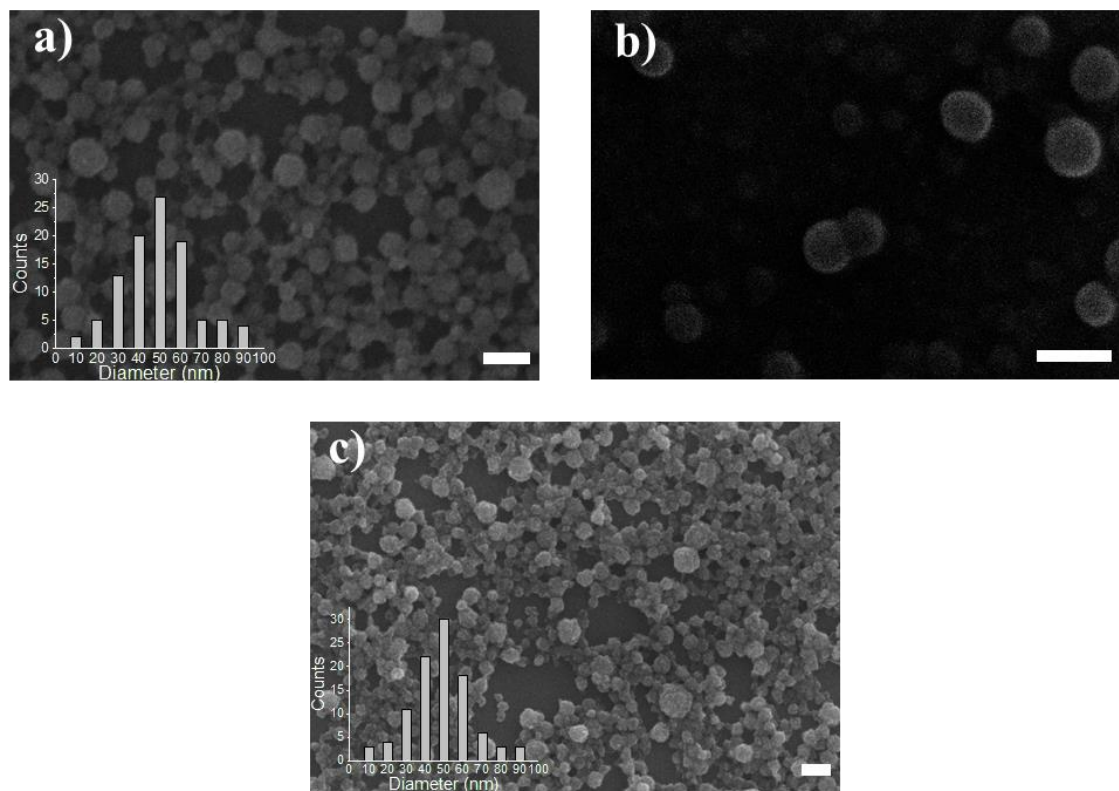


Figure 2.10. High-resolution FE-SEM images of (a) TDs NPs, (b) CSCP NPs, and (c) NC10%. Inset figures show the size distribution. Scale bars = 100 nm.

For TDs nanoparticles without CSCP, scanning transmission electron microscopy (STEM) images showed that multiple TDs were stacked together to form each nanoparticle (**Figure**

2.11b). The binding energy of Ti L edges was at around 458 eV in TDs, as estimated by STEM-electron energy loss spectroscopy (STEM-EELS, **Figure 2.12**). Fast Fourier transform pattern (FFT) of TDs NPs (**Figure 2.11c**) showed lattice fringes with *d*-spacing at 0.34, 0.23, and 0.18 nm, which can be ascribed to the (101), (004), and (200) planes of anatase TiO₂ phase, in agreement with its PXRD pattern. STEM images of pure CSCP polymer nanoparticles showed that these nanoparticles had a smooth surface and the residual palladium was found to be present as nanoparticles (**Figure 2.11d**). When both CSCP and TDs NPs were mixed together as a physical mixture, it was possible to identify both of the phases clearly by STEM, as evident from a physical mixture of CSCP and TDs NPs in a weight ratio of 1:1 (50% CSCP + 50% TDs, **Figure 2.11e**).

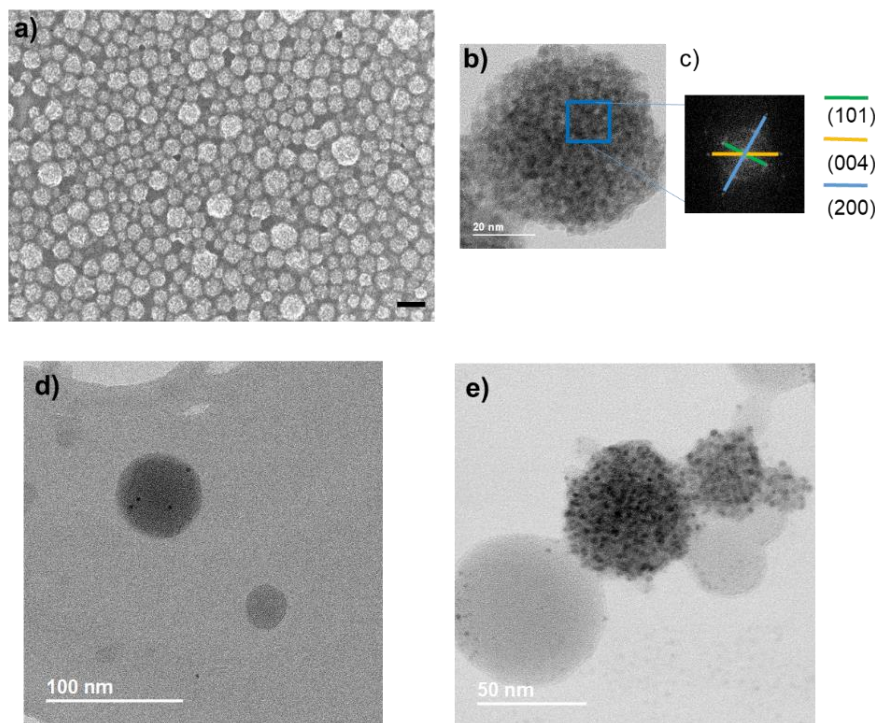


Figure 2.11. Morphology and internal structures of assembled TDs and CSCP nanoparticles. **a)** High-resolution FE-SEM image of TDs NPs (scale bar = 100 nm). **b)** STEM image of TDs NPs. **c)** Fast Fourier transform diffraction pattern of the highlighted area. **d)** STEM image of CSCP NPs. **e)** STEM image of 50% CSCP+50% TDs NPs physical mixture.

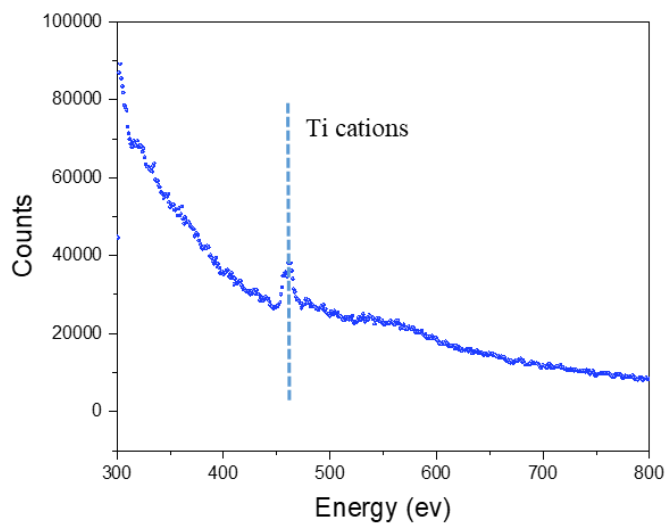


Figure 2.12. Electron energy loss spectroscopy of TDs NPs.

Next, we studied the internal structure of the CSCP/TDs NCs using both bright-field STEM and high-angle annular dark-field STEM (HAADF-STEM), which showed that the materials obtained from the emulsion process were not phase separated but were instead co-assembled nanocomposites of the polymer and TiO₂. In the case of samples consisting mostly of polymer (NC90% under bright-field STEM, **Figure 2.13a**) the TDs were found to be uniformly distributed within the nanocomposite, with few TDs exposed to the nanoparticle surface, resulting in a smooth surface. HAADF-STEM imaging was also used to provide a clear contrast between CSCP (dark in HADDF-STEM images) and TDs (bright in HADDF-STEM images) due to the large differences in their atomic numbers (**Figure 2.13a and b**). With an increased loading of TDs (NC50%, **Figure 2.13c and d**), the surface of nanocomposite became rougher and more TDs were exposed on the surface. For a highly-loaded TD nanocomposite, NC10%, no clear domains of the polymer were visible, suggesting that the amorphous polymer was embedded between the inorganic TDs (**Figure 2.13e and f**). Compared with NC10% (**Figure 2.13f**), the HAADF-STEM image for NC50% (**Figure 2.13d**) exhibited more dark areas in the nanoparticle domain, suggesting embedding of a greater amount of amorphous polymer. Bright-field STEM and HAADF-STEM images under low magnification were also obtained (**Figures 2.14-2.16**). The CSCP and TDs NPs showed spherical morphology with narrow size distribution and smooth surface (**Figures 2.14**), which was consistent with the observations in **Figure 2.11b**. It was clear to see the individual CSCP and TDs NPs in physical mixture of 50% CSCP + 50% TDs (**Figure 2.15**). Morphology and internal structures of nanocomposites were

also confirmed by images under low magnification (**Figure 2.16**), which showed similar morphological profiles to those under high magnification (**Figure 2.13**).

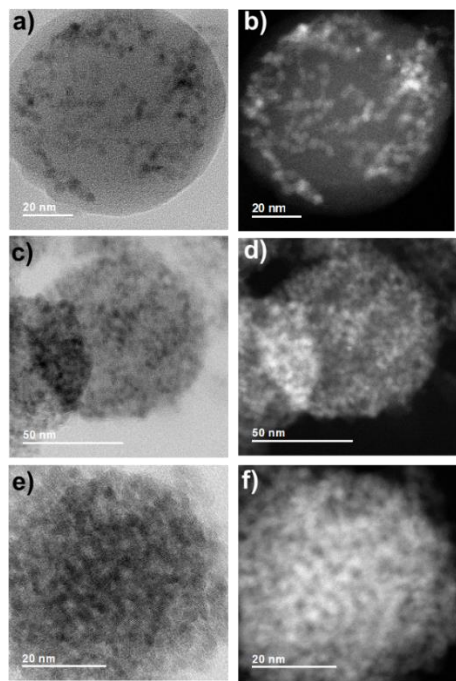


Figure 2.13. Morphology and internal structures of nanocomposites. Bright-field STEM images of (a) NC90%, (c) NC50%, and (e) NC10%. HAADF-STEM images of (b) NC90%, (d) NC50%, and (f) NC10%.

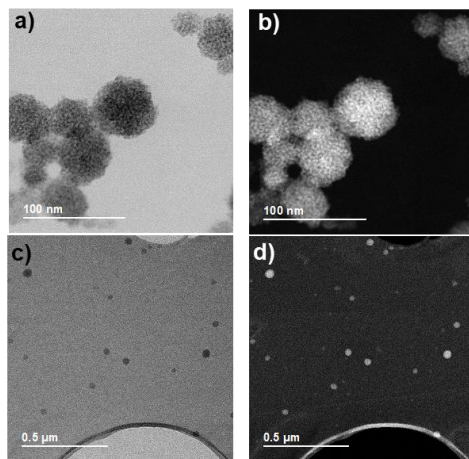


Figure 2.14. Morphology and internal structures of nanoparticles under low magnification. Bright-field STEM images of (a) TDs NPs and (c) CSCP NPs. HAADF-STEM images of (b) TDs NPs and (d) CSCP NPs.

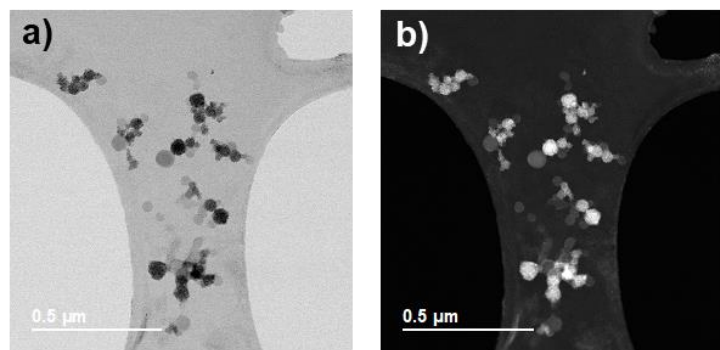


Figure 2.15. Morphology and internal structures of nanoparticle mixtures under low magnification. **a)** Bright-field STEM image of 50% CSCP+50% TDs NPs physical mixture. **b)** HAADF-STEM image of 50% CSCP+50% TDs NPs physical mixture.

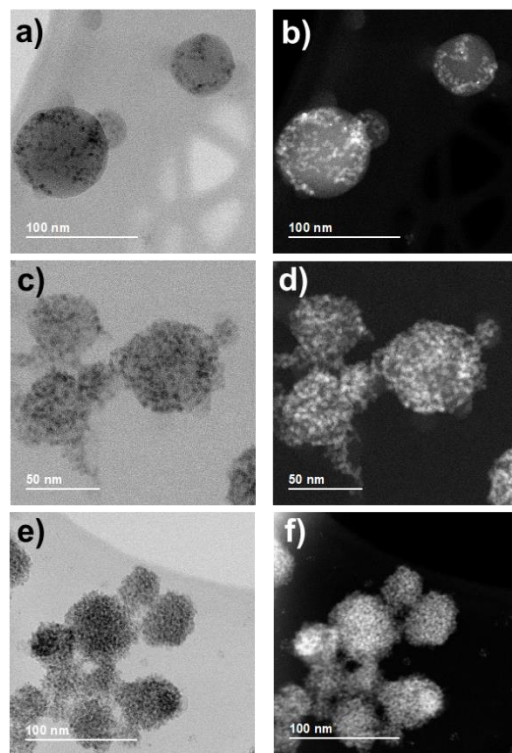


Figure 2.16. Morphology and internal structures of nanocomposites under low magnification. Bright-field STEM images of **(a)** NC90%, **(c)** NC50%, and **(e)** NC10%. HAADF-STEM images of **(b)** NC90%, **(d)** NC50%, and **(f)** NC10%.

2.4.2. Absorption and Emission Properties

UV-vis absorption spectra were measured in aqueous suspension for samples before dialysis (**Figure 2.17**). All materials were found to absorb light between 300 and 420 nm, with a characteristic peak of the conjugated polymer CSCP centred at around 364 nm for the as-prepared nanoparticles and nanocomposites. By contrast, TDs absorbed light only below 350

nm, which is typical for TiO₂ and related materials.³⁸ Within the nanocomposite series, the absorption peak of the conjugated polymer CSCP gradually decreased with decreasing amounts of CSCP. Moreover, the peak maximum was shifted from 364 nm for 25% CSCP + 75% TDs to 370 nm for NC25%. The observed shift in the case of the nanocomposites suggested an interaction between the CSCP and the TDs and might also indicate that direct intimate contact was required for this interaction to occur between the two materials. Moreover, physical mixtures did not show a shift in absorption, further showing the importance of intimate contact in the nanocomposites.

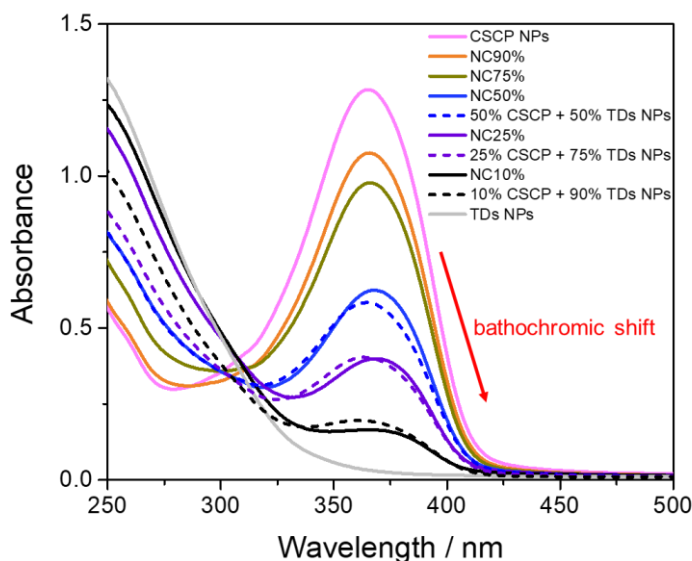


Figure 2.17. UV-vis absorption spectra measured in aqueous suspension of TDs NPs, CSCP NPs, TDs + CSCP NPs physical mixtures, and CSCP/TDs NCs with various compositions at room temperature. All measurements were performed at the same concentration (16.7 mg L⁻¹).

From UV-vis measurements, an optical-gap (E_g^{op}) of 2.75 eV was determined for CSCP (**Figure 2.18**), which was close to the predicted gap using density functional theory (**Figure 2.19**). The HOMO energy level of CSCP was measured to be at 0.5 V via cyclic voltammetry (**Figure 2.20**) and the LUMO energy level was calculated to be -2.25 V by using the equation of $E_{LUMO} = E_{HOMO} - E_g$. The conduction band of TDs was below the LUMO energy level of the polymer, but above its HOMO energy level at -0.2 V, while the valance band of the TDs was much lower at 3.2 V (**Figure 2.21**).³³

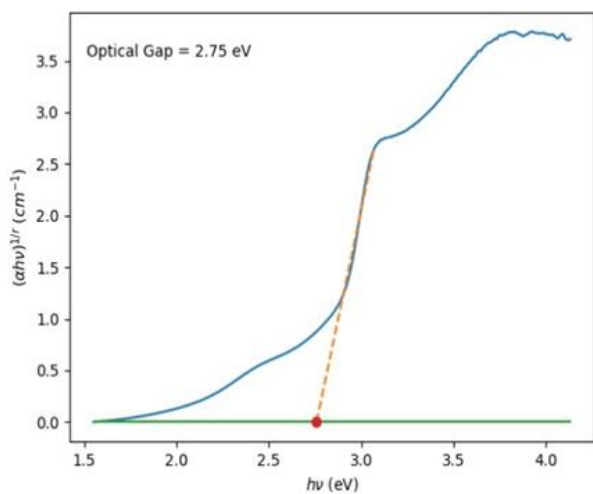


Figure 2.18. The bandgap of CSCP determined by using the Tauc method.

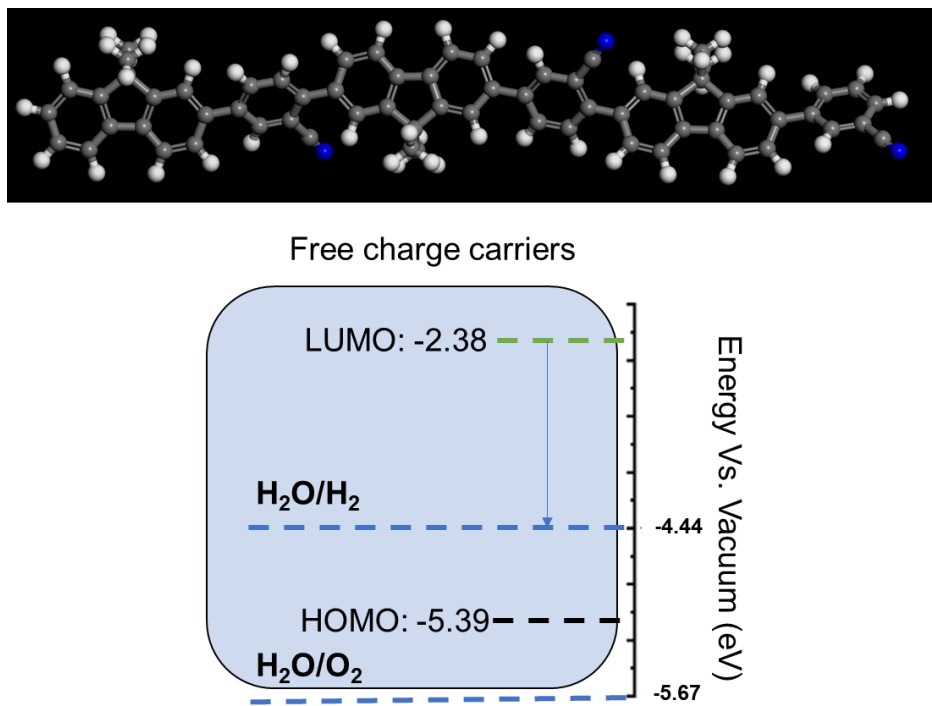


Figure 2.19. DFT calculation results from model compound of CSCP ($n = 3$; details in Experimental Section).

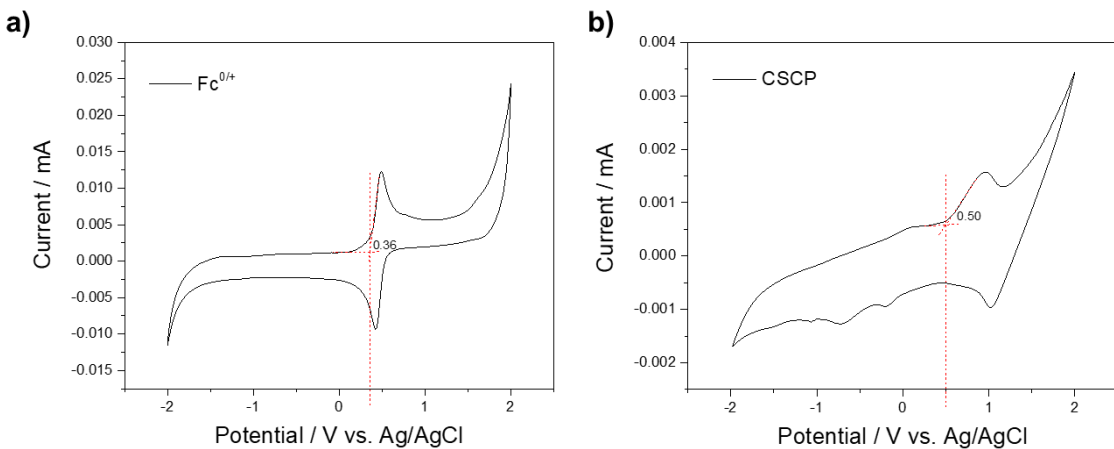


Figure 2.20. **a)** Cyclic voltammogram curve of ferrocene/ferrocenium ($\text{Fc}^{0/+}$) redox couple. **b)** Oxidative half cyclic voltammogram to determine the HOMO position of the polymer. Measurement was performed on the Bio-logic SP200 workstation with 0.1 M TBAPF₆ in CH₃CN solution. The HOMO position are determined as follows: E_{HOMO} (eV) = -4.8 - (E_{ox} - $E_{\text{Fc/Fc}^+}$) = - (0.5 - 0.36 + 4.8) eV = -4.94 eV.

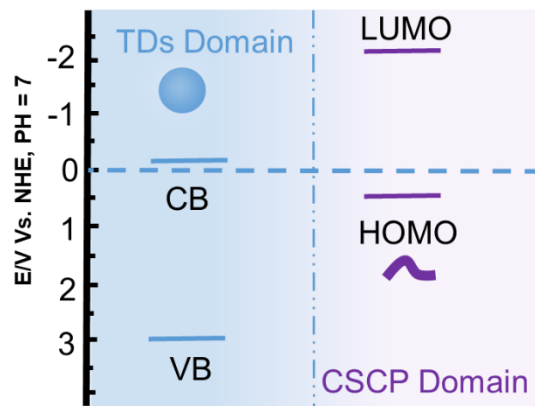


Figure 2.21. Energy levels of CSCP and TDs. LUMO: the lowest unoccupied molecular orbital; HOMO: the highest occupied molecular orbital; CB: conduction band; VB: valence band.

Steady-state photoluminescence was measured in aqueous suspension exciting at 360 nm (Figure 2.22). The CSCP NPs and nanocomposites showed strong emission peaks at approximately 420 and 440 nm, while TDs NPs showed only weak fluorescence emission due to electron transition mediated by defects levels in the bandgap.³⁹ The NC10% showed emission originating from the CSCP polymer, which was at a much higher intensity when compared to the physical mixture (10% CSCP + 90% TDs NPs), showing that intimate contact was required for energy transfer to occur. When exciting at 400 nm and beyond, that was

beyond the absorption onset of the TDs, a drop in the intensity of the emission of CSCP was observed (**Figure 2.23**), further supporting that energy transfer between the TDs and the CSCP takes place in the nanocomposites.

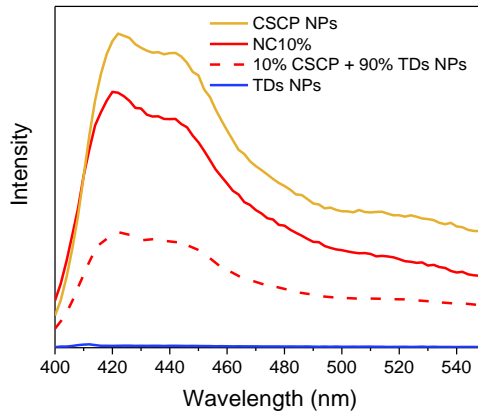


Figure 2.22. Fluorescence intensity of TDs NPs, CSCP NPs, TDs + CSCP NPs physical mixtures, and CSCP/TDs NCs with $\lambda_{\text{exc}} = 360$ nm measured at room temperature.

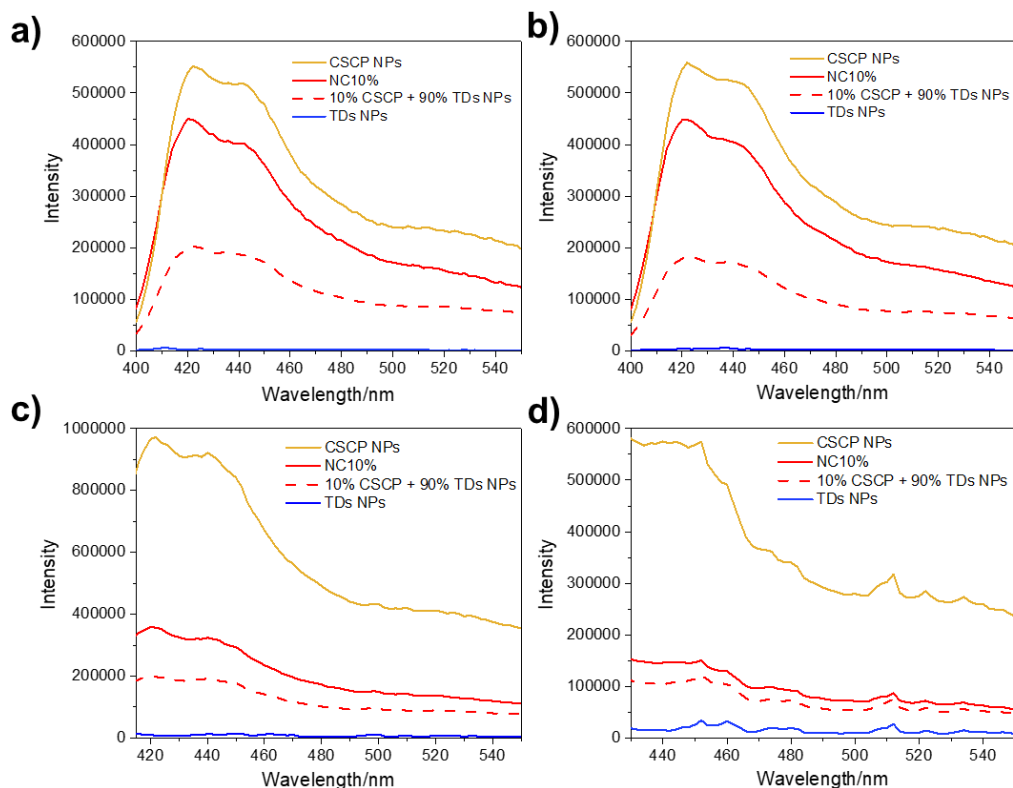


Figure 2.23. Fluorescence intensity of TDs NPs, CSCP NPs, TDs + CSCP NPs physical mixtures and CSCP/TDs NCs at (a) 360 nm, (b) 380 nm, (c) 400 nm, and (d) 420 nm excitation.

Average lifetimes of the excited state lifetimes were estimated by performing time-resolved single photon counting (TRSPC) experiments (**Figure 2.24** and **Table 2.1**). The CSCP NPs were found to have a short average PL lifetime (3.37 ns), which was typically observed for these kinds of conjugated polymers.^{40,41} The TDs NPs were found to have a weak emission, in line with PL experiments, but a longer average PL lifetime (7.57 ns). The nanocomposites had shorter lifetimes-e.g., NC10% (4.35 ns)-compared to the TDs, but nevertheless longer than the conjugated polymer CSCP. When comparing physical mixtures of TDs and CSCP NPs to nanocomposites, shorter lifetimes were observed. For example, the physical mixture of 10% CSCP + 90% TDs NPs had a shorter lifetime (3.38 ns) compared to nanocomposite of the same composition (NC10%, $\tau = 4.35$ ns). Further addition of TDs to the nanoparticle physical mixture of 10% CSCP + 90% TDs did not result in changes in the lifetime of CSCP, showing that no material interaction occurred in the absence of intimate phase contact. Taken together, this showed that the difference in the lifetime of the nanocomposites compared to the conjugated polymer and the TDs was not a simple additive effect but stems from energy transfer within the nanocomposites.

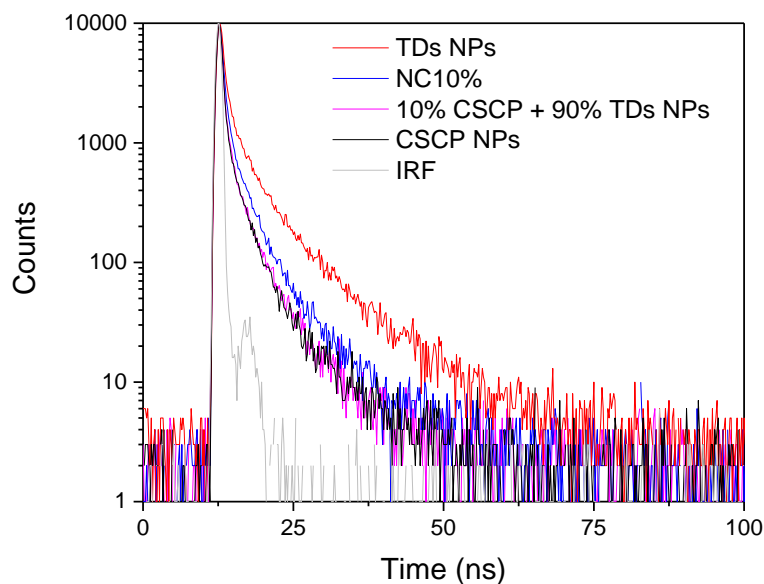


Figure 2.24. TRSPC decays monitored at 480 nm emission under 370.5 nm excitation at room temperature.

Table 2.1. Fitting parameters for time correlated fluorescence lifetime experiments for NCs and NPs ($\lambda_{\text{exc}} = 370.5$ nm and $\lambda_{\text{em}} = 480$ nm).

Sample	τ_1 (ns)	τ_2 (ns)	τ_3 (ns)	τ_4 (ns)	A ₁	A ₂	A ₃	A ₄	τ (ns) [a]
CSCP NPs	0.217	1.325	5.285	-	65.217	23.937	10.846	-	3.372
NC10%	0.322	1.671	6.836	-	59.84	28.171	11.989	-	4.350
10% CSCP + 90% TDs NPs	0.23	1.358	5.343	-	64.959	24.254	10.787	-	3.375
TDs NPs	0.25	1.108	4.611	12.828	40.723	28.596	22.081	8.6	7.568

[a] τ is the average PL lifetime calculated from the following equation:

$$\tau = \sum_{i=1}^4 (A_i \tau_i^2) / \sum_{i=1}^4 (A_i \tau_i) \quad (2.1)$$

The TRSPC decays monitored at 450 nm showed similar results to those monitored at 480 nm (**Figure 2.25**). Compared to the physical mixtures of nanoparticles, the nanocomposites exhibited a bathochromic shifted absorption, enhanced PL emission, and prolonged decay in PL lifetime. These results suggested the communication or energy transfer between the TDs and the CSCP, which might be expected to enhance the photocatalytic performance of the nanocomposites compared to the individual components.

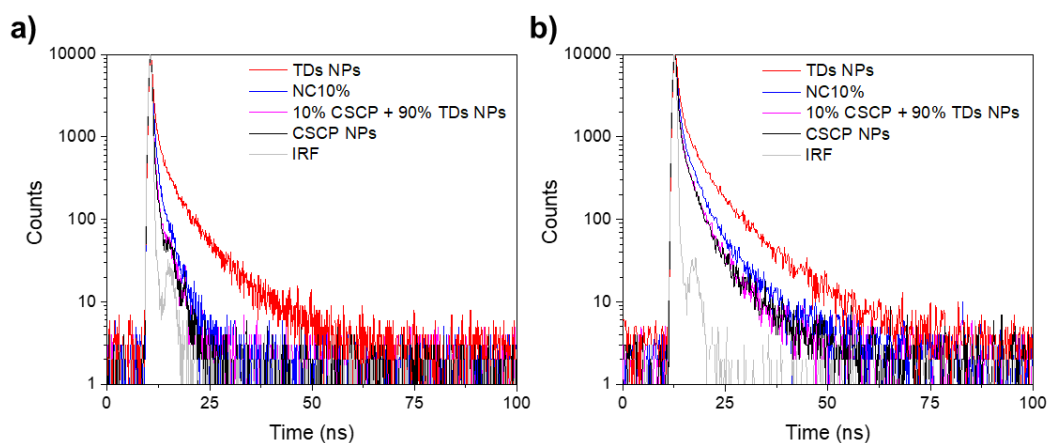


Figure 2.25. TRSPC decays monitored at (a) 450 nm and (b) 480 nm emission under 370.5 nm excitation at room temperature.

2.5. Photocatalytic Hydrogen Production from Water

2.5.1. Nanoparticles and Nanocomposites

2.5.1.1. Photocatalytic Test on Solar Simulator

We tested the photocatalytic activities of the CSCP/TDs nanocomposites for sacrificial hydrogen production from water using a high-throughput workflow that was described previously.^{40,42} For these measurements, samples were added to vials, transferred to a liquid handling system, and inertized under nitrogen. The liquid handling system then added water and the hole scavenger before capping the vials. After this, the samples were transferred to a solar simulator and illuminated with constant agitation before measuring the hydrogen production using an automated gas chromatograph.

The nanoparticles and nanocomposites were tested as prepared without any additional metal; residual palladium from the synthesis acts as the co-catalyst.^{35,43} We tested two different hole scavengers in this study, triethanolamine (TEOA), which is typically used for organic photocatalysts such as carbon nitrides,⁴⁴ and methanol, which is typically used for titanium dioxide.⁴⁵ Hydrogen evolution rates were determined using 1 mg catalyst in 5.2 mL water/scavenger mixture and are normalized to the total mass of both photocatalysts in the nanocomposite, physical mixtures, or the individual photocatalysts. All nanocomposites, as well as individual TDs and CSCP NPs, produced hydrogen from water using methanol, but higher overall HER were obtained when TEOA was used as the hole scavenger (**Figures 2.26 and 2.27**). The TDs NPs produced hydrogen with a rate of $60.1 \mu\text{mol g}^{-1} \text{ h}^{-1}$ when using TEOA as the scavenger, which steadily increased with increased content of the inorganic photocatalyst TD in the composite up to 90% w/w. The nanocomposite NC10% had the highest HER of all composites with a rate of $387.8 \mu\text{mol g}^{-1} \text{ h}^{-1}$. By comparison, the CSCP NPs had a rate of only $90.7 \mu\text{mol g}^{-1} \text{ h}^{-1}$ under the same conditions.

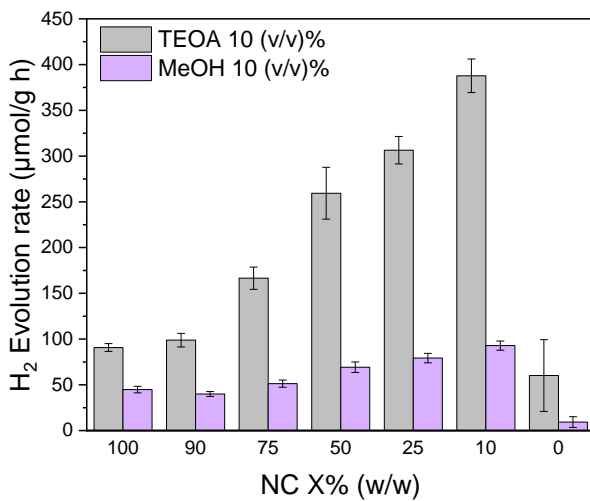


Figure 2.26. Photocatalytic hydrogen production rates under 1 sun irradiation for the NCs plotted as a function of the weight ratio of CSCP to TDs (0 corresponds to the pure TDs nanoparticles). Conditions: catalyst $192.3 \mu\text{g mL}^{-1}$ (1 mg in 5.2 mL total volume), TEOA (10 vol. % in water), 5 hours irradiation with an ABA solar simulator.

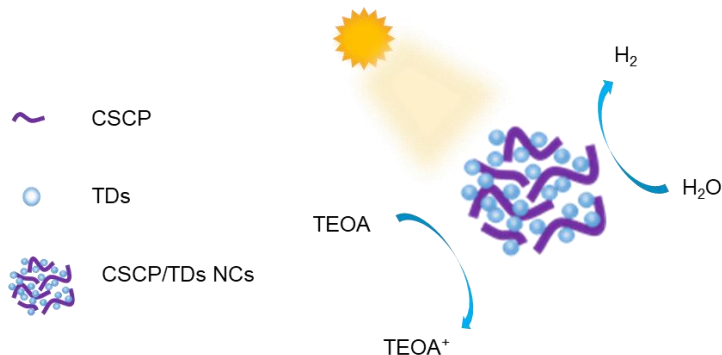


Figure 2.27. Schematic diagram of photocatalysis using nanocomposite catalyst.

2.5.1.2. Photocatalytic Test on Xe Lamp

Kinetic hydrogen evolution measurements under broadband irradiation ($\lambda > 295 \text{ nm}$, 300 W Xe light source) showed that NC10% afforded a higher HER of $1371.2 \mu\text{mol g}^{-1} \text{ h}^{-1}$ as shown in **Figure 2.28a**, with no obvious reduction in activity observed during 18 hours of illumination (**Figure 2.28b**), suggesting good stability of the nanocomposite photocatalysts. However, CSCP NPs showed decreased activity in the first two hours and no activity after two hours. This was probably because of the nanoparticle aggregation. The nanoparticle aggregation might reduce the surface area and light harvesting.

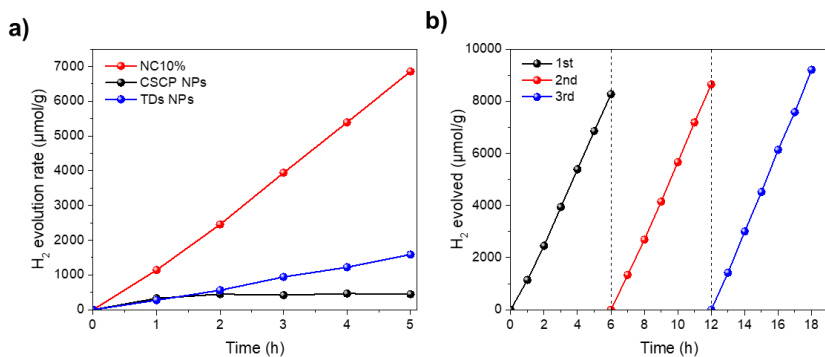


Figure 2.28. a) Time course of hydrogen production under broadband illumination of TDs NPs, CSCP NPs, and NC10%. Conditions: catalyst 2 mg in 20 mL of aqueous TEOA (10 vol. %), 5 hours irradiation with a 300 W Xe light source fitted with a $\lambda > 295$ nm filter. **b)** Time course of hydrogen production for NC10% photocatalyst, irradiated for 18 hours (degassed after every 6 hours) by 300 W Xe light source fitted with a $\lambda > 295$ nm filter using 2 mg of the catalyst in 20 mL of aqueous TEOA solution (10 vol. % in water).

NC10% also afforded an HER of $148.7 \mu\text{mol g}^{-1} \text{ h}^{-1}$ under visible light irradiation ($\lambda > 395$ nm, 300 W Xe light source), which was higher than CSCP ($88.1 \mu\text{mol g}^{-1} \text{ h}^{-1}$ in the first 2 hours) and TDs NPs (negligible) as shown in **Figure 2.29**. No obvious decrease of HER was observed for NC10%. However, the CSCP NPs experienced a significant decrease in photocatalytic activity as a function of time and, almost no H₂ production was observed after irradiation of 3 hours.

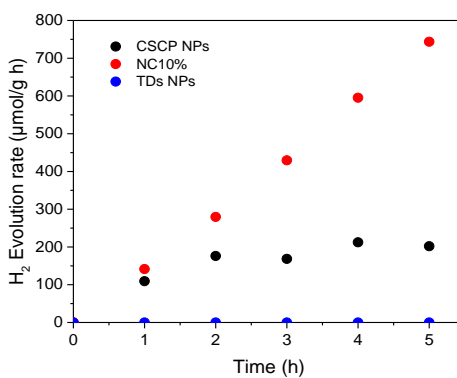


Figure 2.29. Time course of hydrogen production under broadband illumination of TDs NPs, CSCP NPs, and NC10%. Conditions: catalyst 2 mg in 20 mL of aqueous TEOA (10 vol. %), 5 hours irradiation with a 300 W Xe light source fitted with a $\lambda > 395$ nm filter.

After photocatalysis, no obvious change of UV-vis absorption spectrum was found compared

to the as-prepared sample (**Figures 2.30**), indicating the good chemical stability of NC10%. The particle morphology of NC10% after photocatalysis experiment was found to be similar to as-prepared sample before photocatalysis (**Figures 2.31**), which might suggest that no phase separation occurred during light irradiation.

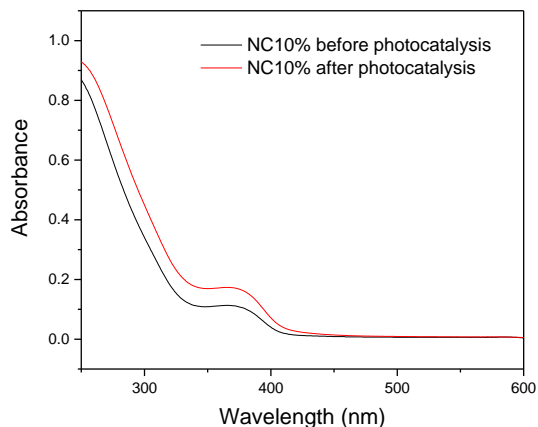


Figure 2.30. UV-vis absorption spectra of NC10% before and after photocatalysis. The sample was recovered by centrifugation at 7830 rpm and then re-dispersed in water.

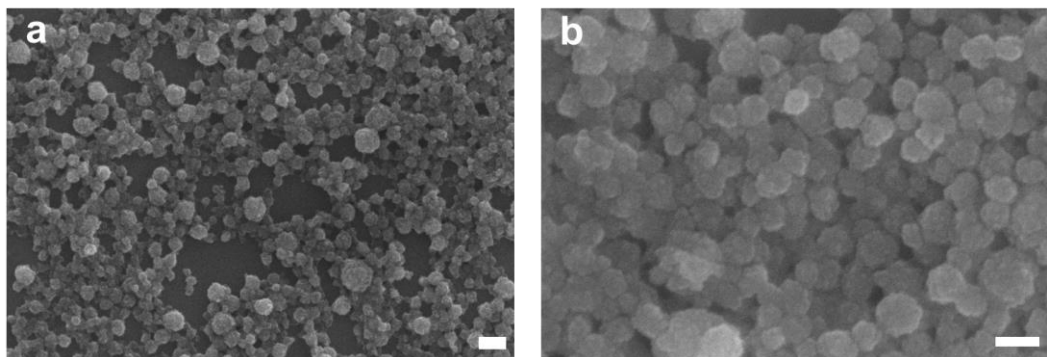


Figure 2.31. SEM images of NC10% (a) before and (b) after photocatalysis (**Figure 2.31a** is the same as **Figure 2.10c**). Scale bars = 100 nm.

The AQY of hydrogen evolution was measured at specific wavelengths using an LED light source. AQYs for NC10% were determined to be 0.05% at 420 nm, 0.34% at 395 nm, and 1.08% at 340 nm, broadly following the absorption spectrum of the composite further suggesting that the hydrogen generation is a photocatalytic process (**Figure 2.32**).

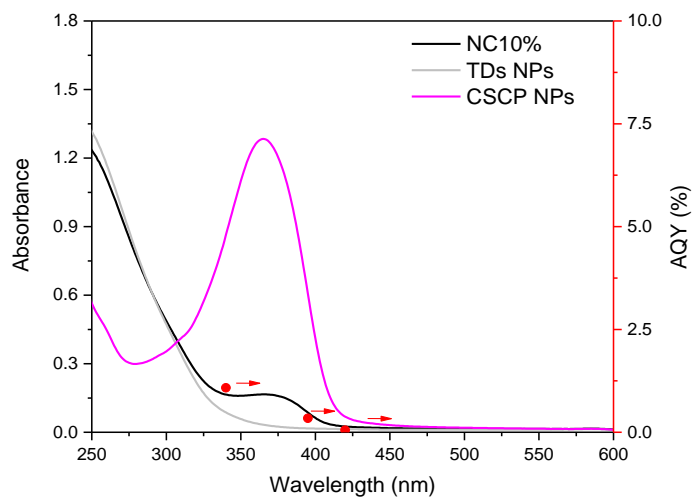


Figure 2.32. UV-vis spectra and AQY of NC10% measured with monochromatic LED light at 340, 395, and 420 nm, respectively. UV-vis spectrum of CSCP and TDs nanoparticles are also plotted (Intensity rescaled for clarity).

2.5.2. Physical Mixtures and Other Control Experiment

Physical mixtures of CSCP and TDs NP, obtained by mixing both materials immediately before the photocatalysis experiment, gave significantly lower hydrogen evolution rates of $83.2 \mu\text{mol g}^{-1} \text{ h}^{-1}$ and $69.7 \mu\text{mol g}^{-1} \text{ h}^{-1}$ for 50% CSCP + 50% TDs and 10% CSCP + 90% TDs NPs (**Figure 2.33**), respectively, compared to their analogous nanocomposites, which showed hydrogen evolution rates of $259.3 \mu\text{mol g}^{-1} \text{ h}^{-1}$ for NC50% and $387.8 \mu\text{mol g}^{-1} \text{ h}^{-1}$ for NC10%. This shows that the formation of inorganic/organic nanocomposites enhances photocatalytic activity significantly. The 50% CSCP + 50% TDs physical mixtures had similar morphology and particle size to NC50% as revealed by STEM results, but showed significantly lower photocatalytic hydrogen production performance, suggesting that the phase contact between the TDs and the CSCP plays a key role.

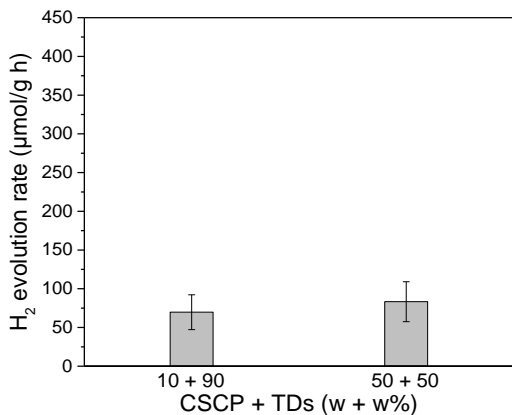


Figure 2.33. Photocatalytic hydrogen production activities for the CSCP + TDs NPs. Conditions: catalyst $192.3 \mu\text{g mL}^{-1}$ (1 mg of CSCP and TDs NPs in 5.2 mL solution), TEOA (10 vol. % in water), AM1.5G ABA certified solar simulator (1 sun), 5 hours irradiation.

The control experiment showed no hydrogen production in the absence of photocatalyst. Nanoparticles of the CSCP and the TDs also showed no appreciable hydrogen production in the dark or under illumination without a hole scavenger. However, CSCP/TDs NCs were found to produce trace amounts of hydrogen without a hole scavenger (Figure 2.34). We speculate that hydrogen partially originated from the decomposition of the organic polymer (CSCP), and therefore carried out a series of control experiments.

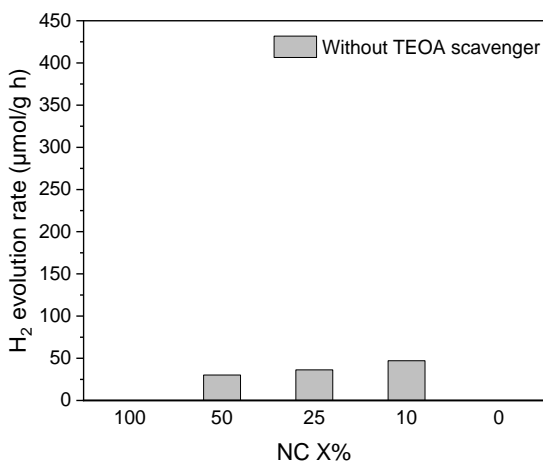


Figure 2.34. Photocatalytic hydrogen production activities for the CSCP/TDs NCs without TEOA scavenger. Conditions: Catalyst $192.3 \mu\text{g mL}^{-1}$ (1 mg of CSCP/TDs NCs in 5.2 mL solution), no scavenger, AM1.5G ABA certified solar simulator (1 sun), 5 hours irradiation.

To rule out that hydrogen originates from the decomposition of the organic polymer by the TDs nanoparticles, we made a nanocomposite with a non-conjugated polymer, polystyrene (PS). The nanocomposite of PS and TDs (PS/TDs NCs) showed a similar absorption profile to pure TDs NPs probably because polystyrene is photo-inactive (**Figure 2.35**).

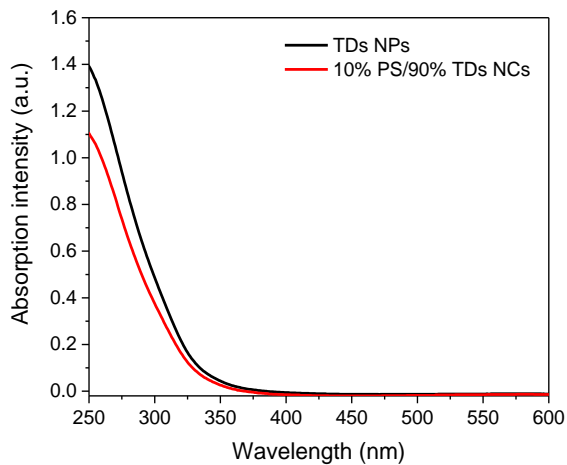


Figure 2.35. The absorption spectrum of TDs NPs and photo-inactive PS/TDs NCs.

This nanocomposite of PS and TDs showed similar particle shapes and size distributions to the analogous CSCP/TDs NCs as evident from SEM images (**Figure 2.36**), but it did not produce any hydrogen in the absence of a scavenger under illumination, suggesting that the generation of H₂ in the nanocomposites may not originate from polymer decomposition. Also, a significantly lower amount of hydrogen was produced in the presence of TEOA for the PS/TDs nanocomposite (47.2 $\mu\text{mol g}^{-1} \text{ h}^{-1}$) compared to NC10% (387.8 $\mu\text{mol g}^{-1} \text{ h}^{-1}$), suggesting that photoactive CSCP contributed a lot to the enhanced HER of CSCP/TDs NCs (**Figure 2.37**).

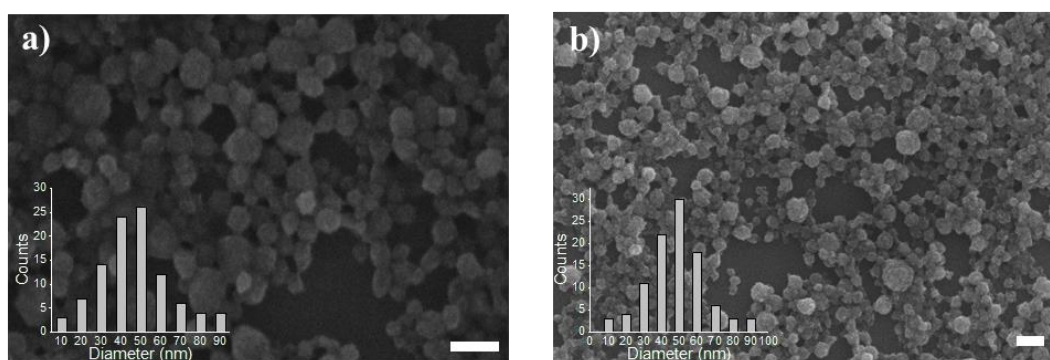


Figure 2.36. FE-SEM images of (a) 10% PS/90% TDs NCs and (b) NC10% (**Figure 2.36a** is the same as **Figure 2.10c**). Scale bars = 100 nm.

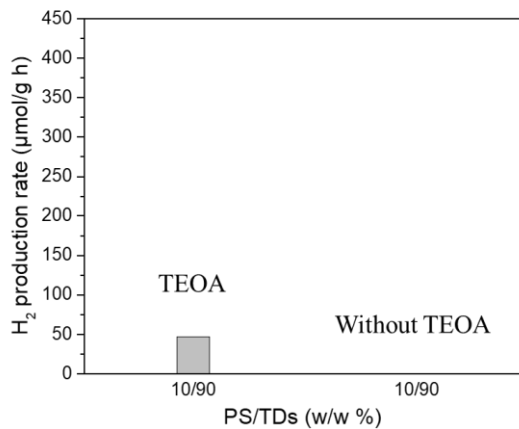


Figure 2.37. Photocatalytic hydrogen production activities for the 10% PS/90% TDs NCs with TEOA (left) and without TEOA (right). Conditions: catalyst $192.3 \mu\text{g mL}^{-1}$ (1 mg of 10% PS/90% TDs NCs in 5.2 mL solution), TEOA (10 vol. % in water), AM1.5G ABA certified solar simulator (1 sun), 5 hours irradiation.

We suspected that oleylamine (OLM), which was used as the stabilisation ligand when making the nanocomposites, could be oxidised and act as the hole scavenger as it contains an amino-group.⁴⁶ This was confirmed by adding OLM to CSCP NPs in water containing 10% of methanol (**Figure 2.38**), which resulted in the production of a higher amount of hydrogen ($284.4 \mu\text{mol g}^{-1} \text{h}^{-1}$ for additional 0.05 mL oleylamine) compared to experiment with only methanol as scavenger ($51.4 \mu\text{mol g}^{-1} \text{h}^{-1}$).

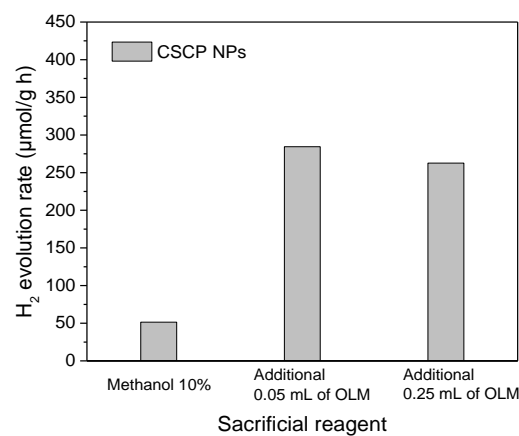


Figure 2.38. Effect of oleylamine on photocatalytic hydrogen production activities of the CSCP NPs. Conditions: Catalyst $96.2 \mu\text{g mL}^{-1}$ (0.5 mg of CSCP in 5.2 mL solution), methanol (10 vol. % in water), AM1.5G ABA certified solar simulator (1 sun), 5 hours irradiation.

In previous work, a degree of aggregation of polymer nanoparticles was shown to improve photocatalytic performance, possibly because of increased light scattering of these highly translucent suspensions.⁴⁶ This was also explored as a possibility here by making aggregates of bulk CSCP and CSCP nanoparticles with photocatalytically inactive SiO₂ nanoparticles to give composites that contained 10% polymer and 90% of SiO₂. The bulk CSCP polymer/SiO₂ composites did not produce hydrogen, and the polymer nanoparticles/SiO₂ composites produced hydrogen with a very low rate of 40.2 $\mu\text{mol g}^{-1} \text{ h}^{-1}$ (**Figure 2.39**). This suggests that aggregation of the polymer particles was not the main factor in the enhanced photocatalytic activity of these nanocomposites, but does not rule out that light scattering effects play a role here, too.

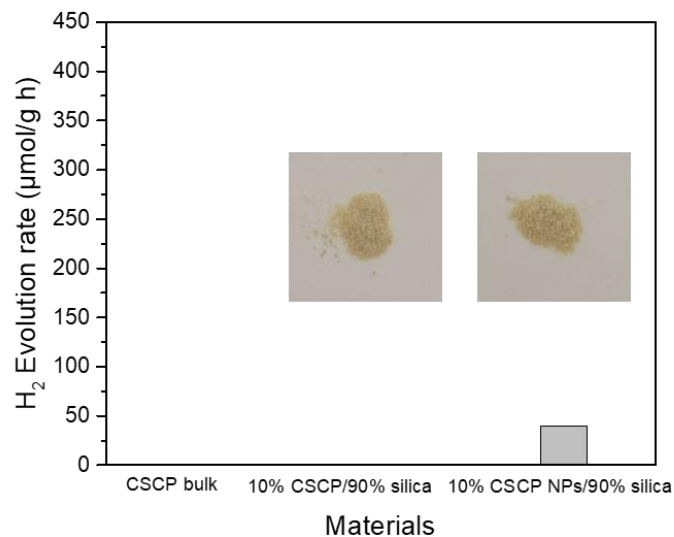


Figure 2.39. Photocatalytic hydrogen production activities for bulk polymer, 10% CSCP/90% SiO₂ and 10% CSCP NPs/90% SiO₂ normal composites. Inset shows pictures of 10% CSCP/90% SiO₂ (picture at left side) and 10% CSCP NPs/90% SiO₂ (picture at right side). Conditions: catalyst 192.3 $\mu\text{g mL}^{-1}$ (1 mg of catalysts in 5.2 mL solution), TEOA (10 vol. % in water), AM1.5G ABA certified solar simulator (1 sun), 5 hours irradiation. The 10% CSCP/90% SiO₂ was prepared by evaporation of a chloroform suspension containing CSCP and SiO₂ powder. The 10% CSCP NPs/90% SiO₂ was prepared by evaporation of a water suspension containing CSCP NPs and SiO₂ powder.

2.6. Conclusions

In conclusion, a range of nanocomposites comprising various ratios of an inorganic

semiconductor and an organic polymer photocatalyst were prepared using an emulsion induced self-assembly method. The morphology of the nanocomposites is a function of the amount of TiO₂ loaded into nanoparticles. These composites showed evidence of energy transfer between TDs and CSCP NPs, resulting in changes in light absorption, PL emission, and emission decay behaviors. The nanocomposites showed enhanced sacrificial catalytic H₂ production from water compared with nanoparticle counterparts produced from either CSCP or TDs. The composite of NC10% was found to have the highest activity, outperforming the CSCP NPs alone by a factor of 4.25 and the TDs NPs by a factor of 6.4.

The advantage of this approach lies in that parent materials can be synthesised separately and then combined in a common organic solvent, allowing for the tuning of polymer composition and thus allowing systematic control over physical and chemical properties. This EISA method provides a powerful route for the preparation of many new multifunctional organic/inorganic or organic/organic semiconductor nanocomposites. In particular, it is a potential avenue for the preparation of hybrid Z-scheme photocatalysts that do not rely on sacrificial reagents. For example, it should be possible to prepare heterostructures of hydrogen-evolving conjugated polymers with oxygen-evolving inorganic semiconductor catalysts.

2.7. Experimental

2.7.1. Preparation Methods

Materials: Sodium *n*-dodecyl sulfate (SDS; > 99%), titanium (IV) *n*-butoxide (TBT; 99%), cyclohexane (99.5%), triethanolamine (TEOA; ≥ 99%), silica (5–15 nm particle size), polystyrene ($M_w \sim 192,000$ g mol⁻¹), oleic acid (OA; 90%), tetrakis(triphenylphosphine)palladium(0), 99% and Starks' catalyst were purchased from Sigma-Aldrich. Oleylamine (OLM; 80–90%) and 2,5-dibromobenzonitrile were acquired from Acros Organics and Fluorochem, respectively. 2,2'-(9,9-Di-*n*-octyl-9H-fluorene-2,7-diyl-bis(4,4,5,5-tetramethyl-1,3,2-dioxaborolane) was obtained from Ossila. Other chemicals were obtained from commercial suppliers Sigma-Aldrich, Tokyo Chemical Industry, and Alfa Aesar. Deionized water was obtained using a Milli-Q System ($\rho = 15$ MΩ). All chemicals were used as received without further purification.

Synthesis of the cyano-benzene-co-fluorene polymer (CSCP): 2,2'-(9,9-Di-*n*-octyl-9H-fluorene-2,7-diyl-bis(4,4,5,5-tetramethyl-1,3,2-dioxaborolane) 643 mg, 1.0 mmol), 2,5-dibromobenzonitrile (260.9 mg, 1.0 mmol), toluene (17.5 mL), Na₂CO₃ (7.5 mL, 2 M), Starks'

catalyst (2 drops), and $[\text{Pd}(\text{PPh}_3)_4]$ (17.5 mg) were used in this reaction. After 2 days at 80 °C, the solvent was evaporated and the product was washed with water. The crude polymer was then further purified by Soxhlet extraction with methanol, acetone, and ethyl acetate. The high molecular weight fraction of the polymer was recovered with chloroform. The chloroform was removed and the polymer redissolved in a minimal amount of chloroform, precipitated into large access of methanol, filtered off, and dried under reduced pressure giving the product as a brown solid in 73% yield (358 mg). ^1H NMR (400 MHz, CDCl_3) δ [ppm]: 8.12 (s, 1H), 8.11-7.42 (m, 8H), 2.11 (s, 4H), 1.44-0.93 (m, 20H), 0.93-0.38 (m, 10H). $M_w = 223,600 \text{ g mol}^{-1}$ ($M_n = 61,700 \text{ g mol}^{-1}$; $D = 3.3$).

Synthesis of Titanium dioxide dots (TDs): Titanium dioxide dots were made using a modified literature procedure.³⁰ Under vigorous magnetic stirring, approximately 120 mg TBT, 3 mL OA, and 1 mL OLM were added to 10 mL cyclohexane. Then, the mixed solution was transferred into a 23 mL Teflon-lined stainless steel autoclave. After heating at 150 °C for 24 hours, a brown sol containing monodisperse TDs was obtained. TDs were precipitated by adding around 30 mL of ethanol and collected by centrifugation at 7830 rpm. After dispersing in 10 mL of cyclohexane, TDs were collected again by centrifugation after precipitation by adding 18 mL of ethanol. TDs were finally dispersed in 5 mL of cyclohexane (5.463 mg mL^{-1}).

Self-assembly of CSCP and TDs nanoparticles: 5 mL of as-prepared TDs in cyclohexane (5.463 mg mL^{-1}) were washed with around 15 mL of ethanol. After centrifugation at 7830 rpm, TDs were re-dispersed in 2.73 mL of chloroform, serving as TDs stock solution (10 mg mL^{-1}). CSCP stock solution (10 mg mL^{-1}) was prepared by dissolving 30 mg of CSCP in 3 mL of chloroform. 1 mL of TDs or CSCP stock solution was diluted with an additional 1 mL of chloroform. After bath sonication for 5 minutes, this solution was emulsified in 10 mL of SDS (3 mg mL^{-1}) aqueous solution using a Branson 550 W sonifier equipped with a 1/8" tip at 40% amplitude for 1 min (5 seconds on and 10 seconds off). The emulsion was stirred at 250 rpm overnight in an open flask (50 mL) at 40 °C to completely evaporate the residual chloroform.

Synthesis 100% TDs NPs: 30 mg SDS was first added in 10 mL of deionized water to form a clear solution. Then, 1 mL of TDs and 1 mL of chloroform were mixed together, followed by the injection of this solution into the SDS solution under ultrasonic treatment to form an oil-in-water emulsion. After evaporation of chloroform, the 100% TDs NPs aqueous suspension was dialyzed and then diluted to 10 mL with water.

Synthesis 100% CSCP NPs: 30 mg SDS was first added in 10 mL of deionized water to form a clear solution. Then, 1 mL of CSCP stock solution and 1 mL of chloroform were mixed together, followed by the injection of this solution into the SDS solution under ultrasonic treatment to form an oil-in-water emulsion. After evaporation of chloroform, the 100% CSCP NPs aqueous suspension was dialyzed and then diluted to 10 mL with water.

Self-assembly of CSCP/TDs nanocomposites: TDs and CSCP stock solution (1 mL in total) was mixed together and then dilute with an additional 1 mL of chloroform. After bath sonication for 5 minutes, this solution was emulsified in 10 mL of SDS (3 mg mL^{-1}) aqueous solution using a Branson 550 W sonifier equipped with a 1/8" tip at 40% amplitude for 1 min (5 seconds on and 10 seconds off). The emulsion was stirred overnight at 250 rpm in an open flask (50 mL) at 40°C to completely evaporate the residual chloroform, giving CSCP/TDs nanocomposites aqueous suspension.

In a typical synthesis experiment of NC10%, 30 mg SDS was first added in 10 mL of deionized water to form a clear solution. Then, a mixture of 0.9 mL of TDs and 0.1 mL of CSCP stock solution (10 mg mL^{-1}) were mixed together and diluted to 2 mL using chloroform, followed by the injection of this solution into the SDS solution under ultrasonic treatment to form an oil-in-water emulsion. After evaporation of chloroform, the NC10% aqueous suspension was dialyzed and then diluted to 10 mL. For the preparation of NC50%, all the procedures were the same except that a mixture of 0.5 mL of TDs and 0.5 mL of CSCP stock solution was applied. CSCP/TDs NCs with different CSCP to TDs ratios were obtained by simply changing the volume ratio of TDs to CSCP stock solution in the synthesis procedure.

To minimize the difference in surfactant content, NPs and NCs aqueous suspension was simultaneously dialyzed in one large beaker (2 L) for 3 days by using dialysis membrane tubing (3500 Da cut-off; the deionized water was replaced 3-4 times a day). Finally, these solutions were diluted to 10 mL with deionized water to give a concentration of 1 mg mL^{-1} .

2.7.2. Characterisation Methods

Scanning electron microscope (SEM) measurements were performed on Hitachi S-4800 cold field-emission scanning electron microscope (FE-SEM) and imaging was performed at a working voltage of 3 kV and a working distance of 8 mm using a combination of upper and lower secondary electron detectors. High-angle annular dark-field scanning transmission electron microscopy (HAADF-STEM) and bright-field transmission electron microscopy (BF-

STEM) images were obtained and electron energy loss spectroscopy (EELS) was recorded on a JEOL 2100FCs microscopy at an accelerating voltage of 200 kV. Powder X-ray diffraction (PXRD) measurements were performed on a PANalytical X’Pert PRO MPD, with a Cu X-ray source, used in high throughput transmission mode with K α focusing mirror and PIXCEL 1D detector. ^1H NMR spectra were recorded using a Bruker Avance 400 NMR spectrometer. Fourier-transform infrared spectroscopy (FT-IR) was measured on a Bruker Tensor 27 FT-IR spectrometer using bulk sample and an ATR attachment (16 scans). Single detection gel permeation chromatography (GPC) was calibrated against polystyrene standards (Agilent EasiCal PS-2 standards) and performed using an Agilent 1260 Infinity II GPC/SEC system (Agilent, UK), two PLgel 5 μm MIXED-D columns and a PL gel 5 μm guard column, with samples detected by refractive index (RI). Dynamic light scattering (DLS) measurements were performed on a Malvern Zetasizer Nano Particle Sizer, at 25 °C, in aqueous suspensions. Inductively coupled plasma optical emission spectrometry (ICP-OES) analysis was performed on an ICP-OES Agilent 5110 after a microwave digest of the materials in nitric acid (67-69%, trace metal analysis grade) to determine the palladium content. The UV-vis absorption spectra were recorded on a Shimadzu UV-2550 UV-vis spectrometer. 50 μL of nanoparticles and nanocomposites (1 mg mL $^{-1}$) aqueous suspension were diluted with 3 mL of distilled water. Steady-state photoluminescence spectra and time-correlated single photon counting (TCSPC) measurements were performed on an Edinburgh Instruments LS980-D2S2-STM spectrometer equipped with picosecond pulsed LED excitation sources and a R928 detector, with a stop count of 10000. An EPL-375 diode ($\lambda = 370.5$ nm, instrument response 100 ps, fwhm) for emission detection was used. A long-pass filter (395 nm) with a cutoff wavelength greater than the laser wavelength (370.5 nm) was employed to prevent light scattering. The instrument response (IRF) was measured with colloidal silica (LUDOX HS-40, Sigma-Aldrich). Decay times were fitted in the FAST software using suggested lifetime estimates. Samples for these measurements were prepared by adding 50 μL of nanoparticles and nanocomposites (1 mg mL $^{-1}$) aqueous suspension into 3 mL of 10% (v/v) TEOA aqueous solution.

2.7.3. Measurement Methods

Photocatalytic activity measurements: For high throughput solar simulator measurements, 1 mL of nanoparticles and nanocomposites aqueous suspensions (1 mg mL $^{-1}$) were added into sample vials (volume = 12.5 mL) and purged with nitrogen in a Sweigher Chemspeed Technologies robot for 3 hours. 4.2 mL of TEOA aqueous solution (12.3% TEOA in H $_2\text{O}$ v/v) was added into each vial via the liquid handling system under inert conditions. Then, all sample

vials were irradiated under a solar simulator (AM1.5G, Class AAA, IEC/JIS/ASTM, 1440 W xenon, 12 × 12 in., MODEL:94123A) equipped with a rocker/roller device. Gaseous products were analyzed on a Shimadzu GC-2010 equipped with Shimadzu HS-20 injecting a sample from the headspace sampler via a transfer line (temperature 150 °C) onto a Rt-Msieve 5 Å column with He as the carrier gas at a flow rate of 30 mL min⁻¹. Hydrogen was detected with a barrier discharge ionisation detector referencing against standard gas with a known concentration of hydrogen.

Kinetic measurements were conducted in a 67 mL quartz flask. 2 mL of nanoparticles or nanocomposites aqueous suspensions (10 mg mL⁻¹) and 2 mL of TEOA were dispersed into 16 mL of water to give a 10% (v/v) TEOA aqueous solution, then this solution was purged with N₂ for 30 minutes. The reaction mixture was illuminated with a 300 W Newport Xe light source (Model: 6258, Ozone free) using a $\lambda > 295$ nm or $\lambda > 395$ nm cut-off filter. The light source was cooled by water circulating through a metal jacket. Gas samples were taken with a gas-tight syringe and run on a Bruker 450-GC gas chromatograph. Hydrogen was detected with a thermal conductivity detector referencing against standard gas with a known concentration of hydrogen.

Calculation of half-reactions for free electrons/holes (CSCP): Standard reduction potentials of half-reactions for free electrons/holes and excitons were calculated using DFT and time-dependent DFT (TD-DFT). The B3LYP density functional was used for all DFT and TD-DFT calculations, together with the Def2-SVP basis set, using Gaussian 16 software. The effect of solvation by water was accounted for using the SMD solvation model.

Cyclic voltammetry methods: The CV measurement was performed on the Bio-logic SP200 workstation with 0.1 M TBAPF₆ in CH₃CN solution, which used a standard three-electrode cell (Ag/AgCl electrode as the reference electrode, Pt wire as the counter electrode, and glassy carbon electrode as the working electrode). The polymer was cast as film from its chloroform solution and dried before the measurement. The ferrocenium/ferrocene couple was used as the internal standard.

Apparent quantum yield measurements: The apparent quantum yield for the photocatalytic H₂ evolution was measured using a $\lambda = 340$ nm LED (28.6 mW), $\lambda = 395$ nm LED (69.1 mW) and $\lambda = 420$ nm LED (101.0 mW) controlled by an IsoTech IPS303DD power supply. For the measurement, 10 mL of NC10% aqueous suspension (1 mg mL⁻¹) was mixed with 15 mL of TEOA aqueous solution to give a TEOA concentration of 10% v/v. This solution was purged

with N₂ for 30 minutes before illuminating with LED. The light intensity was measured with a ThorLabs S120VC photodiode power sensor controlled by a ThorLabs PM100D Power and Energy Meter Console and the apparent quantum yield was estimated using the equation below:

$$AQY = 2 \times \frac{\text{moles of hydrogen evolved}}{\text{moles of incident photons}} \times 100\% \quad (2.2)$$

2.8. References

- 1 J. Bae, J. Lawrence, C. Miesch, A. Ribbe, W. Li, T. Emrick, J. Zhu and R. C. Hayward, *Adv. Mater.*, 2012, **24**, 2735–2741.
- 2 F. Wang, R. Deng, J. Wang, Q. Wang, Y. Han, H. Zhu, X. Chen and X. Liu, *Nat. Mater.*, 2011, **10**, 968–973.
- 3 W. Shi, H. Zeng, Y. Sahoo, T. Y. Ohulchanskyy, Y. Ding, Z. L. Wang, M. Swihart and P. N. Prasad, *Nano Lett.*, 2006, **6**, 875–881.
- 4 H. Gu, R. Zheng, X. X. Zhang and B. Xu, *J. Am. Chem. Soc.*, 2004, **126**, 5664–5665.
- 5 H. Yu, M. Chen, P. M. Rice, S. X. Wang, R. L. White and S. Sun, *Nano Lett.*, 2005, **5**, 379–382.
- 6 E. V. Shevchenko, M. I. Bodnarchuk, M. V. Kovalenko, D. V. Talapin, R. K. Smith, S. Aloni, W. Heiss and A. P. Alivisatos, *Adv. Mater.*, 2008, **20**, 4323–4329.
- 7 H. Wen, H. Zhu, X. Chen, T. F. Hung, B. Wang, G. Zhu, S. F. Yu and F. Wang, *Angew. Chemie - Int. Ed.*, 2013, **52**, 13419–13423.
- 8 A. Sousa-Castillo, M. Comesaña-Hermo, B. Rodríguez-González, M. Pérez-Lorenzo, Z. Wang, X. T. Kong, A. O. Govorov and M. A. Correa-Duarte, *J. Phys. Chem. C*, 2016, **120**, 11690–11699.
- 9 N. Insin, J. B. Tracy, H. Lee, J. P. Zimmer, R. M. Westervelt and M. G. Bawendi, *ACS Nano*, 2008, **2**, 197–202.
- 10 D. K. Yi, S. T. Selvan, S. S. Lee, G. C. Papaefthymiou, D. Kundaliya and J. Y. Ying, *J. Am. Chem. Soc.*, 2005, **127**, 4990–4991.
- 11 C. J. Brinker, Y. Lu, A. Sellinger and H. Fan, *Adv. Mater.*, 1999, **11**, 579–585.
- 12 L. Liu, J. Hensel, R. C. Fitzmorris, Y. Li and J. Z. Zhang, *J. Phys. Chem. Lett.*, 2010, **1**, 155–160.
- 13 D. Vanmaekelbergh, L. K. Van Vugt, H. E. Bakker, F. T. Rabouw, B. De Nijs, R. J. A. Van Dijk-Moes, M. A. Van Huis, P. J. Baesjou and A. Van Blaaderen, *ACS Nano*, 2015, **9**, 3942–3950.
- 14 R. Shi, Y. Cao, Y. Bao, Y. Zhao, G. I. N. Waterhouse, Z. Fang, L. Z. Wu, C. H. Tung, Y. Yin and T. Zhang, *Adv. Mater.*, 2017, **29**, 1–7.
- 15 T. Isojima, S. K. Suh, J. B. V. Sande and T. A. Hatton, *Langmuir*, 2009, **25**, 8292–8298.
- 16 J. H. Park, G. Von Maltzahn, E. Ruoslahti, S. N. Bhatia and M. J. Sailor, *Angew. Chemie - Int. Ed.*, 2008, **47**, 7284–7288.
- 17 J. Shao, H. Xie, H. Huang, Z. Li, Z. Sun, Y. Xu, Q. Xiao, X. F. Yu, Y. Zhao, H. Zhang, H. Wang and P. K. Chu, *Nat. Commun.*, 2016, **7**, 1–13.
- 18 Z. Gu, A. Biswas, M. Zhao and Y. Tang, *Chem. Soc. Rev.*, 2011, **40**, 3638–3655.

- 19 J. Shi, A. R. Votruba, O. C. Farokhzad and R. Langer, *Nano Lett.*, 2010, **10**, 3223–3230.
- 20 Z. Zhao, Y. Sun and F. Dong, *Nanoscale*, 2015, **7**, 15–37.
- 21 G. Liao, Y. Gong, L. Zhang, H. Gao, G.-J. Yang and B. Fang, *Energy Environ. Sci.*, 2019, **12**, 2080–2147.
- 22 Y. Shi, J. Chen, Z. Mao, B. D. Fahlman and D. Wang, *J. Catal.*, 2017, **356**, 22–31.
- 23 S. Zang, G. Zhang, Z.-A. Lan, D. Zheng and X. Wang, *Appl. Catal. B Environ.*, 2019, **251**, 102–111.
- 24 Y. Xiang, X. Wang, X. Zhang, H. Hou, K. Dai, Q. Huang and H. Chen, *J. Mater. Chem. A*, 2018, **6**, 153–159.
- 25 X. Zhang, J. Xiao, M. Hou, Y. Xiang and H. Chen, *Appl. Catal. B Environ.*, 2018, **224**, 871–876.
- 26 Y. Wang, A. Vogel, M. Sachs, R. S. Sprick, L. Wilbraham, S. J. A. Moniz, R. Godin, M. A. Zwijnenburg, J. R. Durrant, A. I. Cooper and J. Tang, *Nat. Energy*, 2019, **4**, 746–760.
- 27 X. Wang, G. Zhang and Z.-A. Lan, *Angew. Chemie, Int. Ed.*, 2016, **55**, 15712–15727.
- 28 D. J. Woods, R. S. Sprick, C. L. Smith, A. J. Cowan and A. I. Cooper, *Adv. Energy Mater.*, 2017, **7**, 1700479.
- 29 J. Kosco, M. Bidwell, H. Cha, T. Martin, C. T. Howells, M. Sachs, D. H. Anjum, S. Gonzalez Lopez, L. Zou, A. Wadsworth, W. Zhang, L. Zhang, J. Tellam, R. Sougrat, F. Laquai, D. M. DeLongchamp, J. R. Durrant and I. McCulloch, *Nat. Mater.*, 2020, **19**, 559–565.
- 30 X. Xu, Z. Gao, Z. Cui, Y. Liang, Z. Li, S. Zhu, X. Yang and J. Ma, *ACS Appl. Mater. Interfaces*, 2016, **8**, 91–101.
- 31 Z. Huang, Y. Liu, Q. Zhang, X. Chang, A. Li, L. Deng, C. Yi, Y. Yang, N. M. Khashab, J. Gong and Z. Nie, *Nat. Commun.*, 2016, **7**, 1–8.
- 32 C. Kübel, A. Voigt, R. Schoenmakers, M. Otten, D. Su, T. C. Lee, A. Carlsson and J. Bradley, *Microsc. Microanal.*, 2005, **11**, 378–400.
- 33 K. Sader, A. Brown, R. Brydson and A. Bleloch, *Ultramicroscopy*, 2010, **110**, 1324–1331.
- 34 K. Thamaphat, P. Limsuwan and B. Ngotawornchai, *Kasetsart J.(Nat. Sci.)*, 2008, **42**, 357–361.
- 35 Y. Bai, D. J. Woods, L. Wilbraham, C. M. Aitchison, M. A. Zwijnenburg, R. S. Sprick and A. I. Cooper, *J. Mater. Chem. A*, 2020, **8**, 8700–8705.
- 36 S. E. Paramonov, H. W. Jun and J. D. Hartgerink, *J. Am. Chem. Soc.*, 2006, **128**, 7291–7298.
- 37 Y. Che, A. Datar, K. Balakrishnan and L. Zang, *J. Am. Chem. Soc.*, 2007, **129**, 7234–

- 38 T. Baran, S. Wojtyła, A. Minguzzi, S. Rondinini and A. Vertova, *Appl. Catal. B Environ.*, 2019, **244**, 303–312.
- 39 Y. Zhao, C. Li, X. Liu, F. Gu, H. Jiang, W. Shao, L. Zhang and Y. He, *Mater. Lett.*, 2007, **61**, 79–83.
- 40 Y. Bai, L. Wilbraham, B. J. Slater, M. A. Zwijnenburg, R. S. Sprick and A. I. Cooper, *J. Am. Chem. Soc.*, 2019, **141**, 9063–9071.
- 41 M. Sachs, R. S. Sprick, D. Pearce, S. A. J. Hillman, A. Monti, A. A. Y. Guilbert, N. J. Brownbill, S. Dimitrov, X. Shi, F. Blanc, M. A. Zwijnenburg, J. Nelson, J. R. Durrant and A. I. Cooper, *Nat. Commun.*, 2018, **9**, 1–11.
- 42 C. B. Meier, R. Clowes, E. Berardo, K. E. Jelfs, M. A. Zwijnenburg, R. S. Sprick and A. I. Cooper, *Chem. Mater.*, 2019, **31**, 8830–8838.
- 43 J. Kosco, M. Sachs, R. Godin, M. Kirkus, L. Francas, M. Bidwell, M. Qureshi, D. Anjum, J. R. Durrant and I. McCulloch, *Adv. Energy Mater.*, 2018, **8**, 1802181.
- 44 X. Wang, K. Maeda, A. Thomas, K. Takanabe, G. Xin, J. M. Carlsson, K. Domen and M. Antonietti, *Nat. Mater.*, 2009, **8**, 76–80.
- 45 Y. K. Kho, A. Iwase, W. Y. Teoh, L. Mädler, A. Kudo and R. Amal, *J. Phys. Chem. C*, 2010, **114**, 2821–2829.
- 46 C. M. Aitchison, R. S. Sprick and A. I. Cooper, *J. Mater. Chem. A*, 2019, **7**, 2490–2496.
- 47 G. Liu, P. Niu, L. Yin and H. M. Cheng, *J. Am. Chem. Soc.*, 2012, **134**, 9070–9073.
- 48 S. Zhang, F. Ding, X. Luo and X. Lin, *J. Alloys Compd.*, 2016, **673**, 93–101.
- 49 S. Meng, Z. Cao, X. Fu and S. Chen, *Appl. Surf. Sci.*, 2015, **324**, 188–197.

Chapter 3

Donor-acceptor Nanocomposites

3.1. Contributions to this Chapter

HR-TEM images for donor-acceptor nanocomposites were obtained by Dr Mounib Bahri. The high throughput synthesis and measurement were devised and built with the help of Dr Xiaobo Li and Rob Clowes. Some of the figures were prepared with the help of Ni Wang. All other work was performed by the thesis author.

3.2. Background

Organic photocatalysts have some inherent drawbacks, such as strong exciton binding energies, low charge-carrier mobilities, and short charge migration path lengths. In **Chapter 2**, we addressed this issue by introducing polymer/inorganic dots interface, which facilitates charge transfer, resulting in enhanced photocatalytic H₂ production activity compared with parent polymer or inorganic dots nanoparticles. However, the overall performance is unsatisfactory with an activity of around 1.3 mmol g⁻¹ h⁻¹.

The biggest challenge in the fabrication and applications of organic-inorganic composite is the poor compatibility of organic-inorganic interfaces due to the polarity differences between inorganic and organic materials.¹ We speculate that the low photocatalytic performance of organic/inorganic nanocomposite (**Chapter 2**) is likely to be a result of incompatibility of organic-inorganic interfaces. Heterojunctions of thin films containing two dissimilar organic semiconductor materials (organic/organic heterojunctions) have shown great progress in organic light-emitting diode displays (OLEDs) and organic photovoltaic cell technologies (OPVs).² Especially in the OPV area, recent studies showed that nanoscale blends of a donor and an acceptor ensure that excitons can reach an interface and dissociate into free charge carriers, leading to significantly enhanced photocurrents and efficiencies.^{3,4} In principle, this concept should also be transferable to organic polymer photocatalysts by making donor/acceptor nanocomposite without using any surfactant. In **Chapter 3**, we investigate the photocatalytic performance of nanocomposites of molecular acceptors and polymeric donors that are often used in OPV areas.

3.3. High Throughput Photocatalytic Performance

We studied five conjugated polymer donors (D1-D5) and four molecular acceptors (A1-A4) (**Figure 3.1**). The four molecular acceptors include three fullerene derivatives-based acceptors (A1-A3) and one non-fullerene-based acceptor (A4). The energy levels of these conjugated polymer donors and molecular acceptors are presented in **Figure 3.2**. These conjugated

polymer donors and molecular acceptors have more positive LUMO energy levels than proton reduction energy level. Water dispersible donor-acceptor nanocomposites (DANCs) were prepared using a nanoprecipitation strategy,⁵ as shown in **Figure 3.3**. A tetrahydrofuran (THF) solution containing the polymer donor and the molecular acceptor was injected into the water with continuous sonication, followed by the evaporation of the THF (detailed procedures in the **Experimental Section**). Colloidal suspensions of DANCs were obtained (**Figure 3.4**) after THF removal. It is well known that the composition ratio between donor and acceptor is critical for photovoltaic performance. Likewise here for photocatalysis, we screened a broad range of relative donor-to-acceptor ratios to give a total DANC library of 237 samples. The photocatalytic hydrogen evolution performance of this library was then screened using a high-throughput parallel 48-sample photocatalysis screen, as introduced previously by our group.⁶

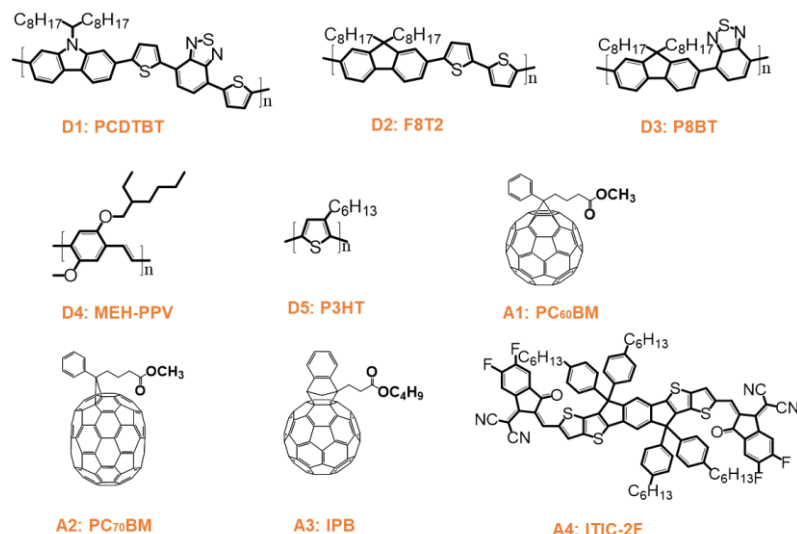


Figure 3.1. Chemical structures of the conjugated polymer donors and molecular acceptors studied here.

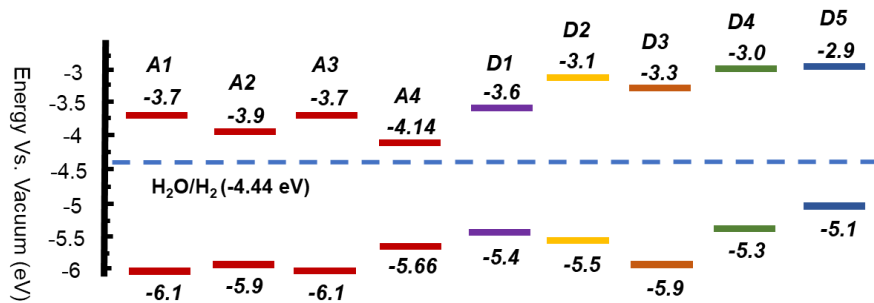


Figure 3.2. Energy levels of the conjugated polymer donors and molecular acceptors studied here (obtained from commercial supplier Ossila except D5 obtained from reference⁷).

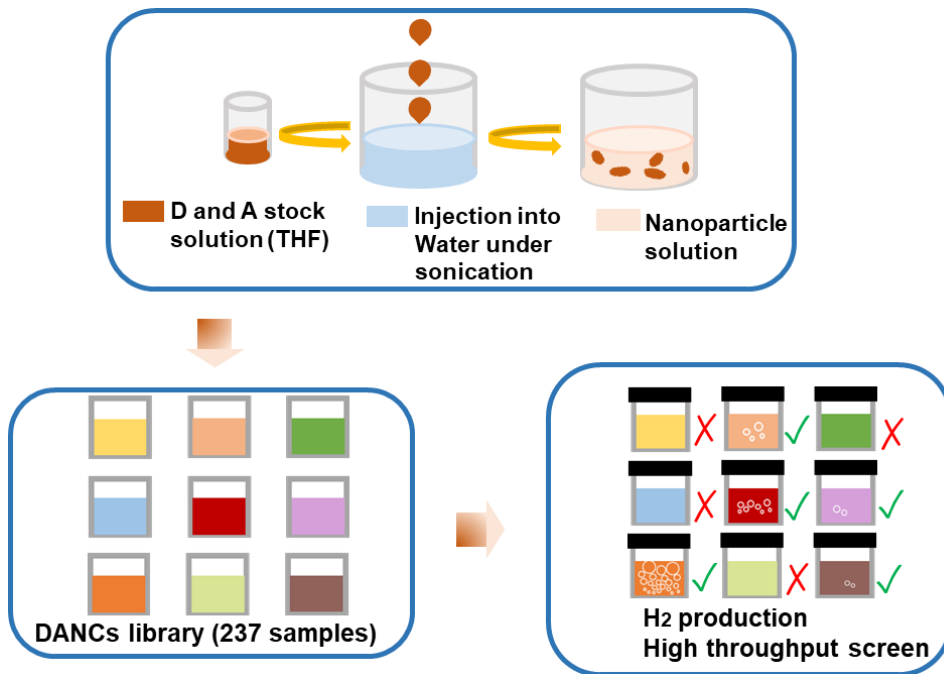


Figure 3.3. Nanoprecipitation process used to prepare the DANCs and scheme representing high-throughput screening process for measurement of photocatalytic activity.

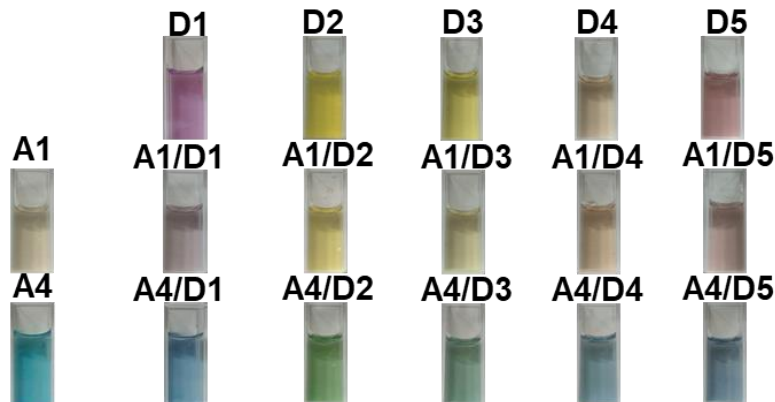


Figure 3.4. Photographs showing DANCs aqueous suspensions in cuvettes.

3.3.1. Conjugated Polymer Donors/fullerene acceptors

The sacrificial photocatalytic hydrogen evolution rate for A1-A4/D1-D5 DANC combinations is strongly dependent on donor/acceptor composition ratios (w/w %). DANCs combinations that involved A3 showed little improvement in hydrogen evolution rate (HER) with respect to the pure donor polymers or molecular acceptors (**Figure 3.5**). The hydrogen evolution rate is proportional to the area of the circles. For scale, the maximum hydrogen evolution rate found was 42.9 mmol g⁻¹ h⁻¹ for 83.3:16.7 w/w % DANC of A3/D1, which is highlighted in **Figure**

3.5. The same scale was used for **Figure 3.6**, **Figure 3.7**, and **Figure 3.14**.

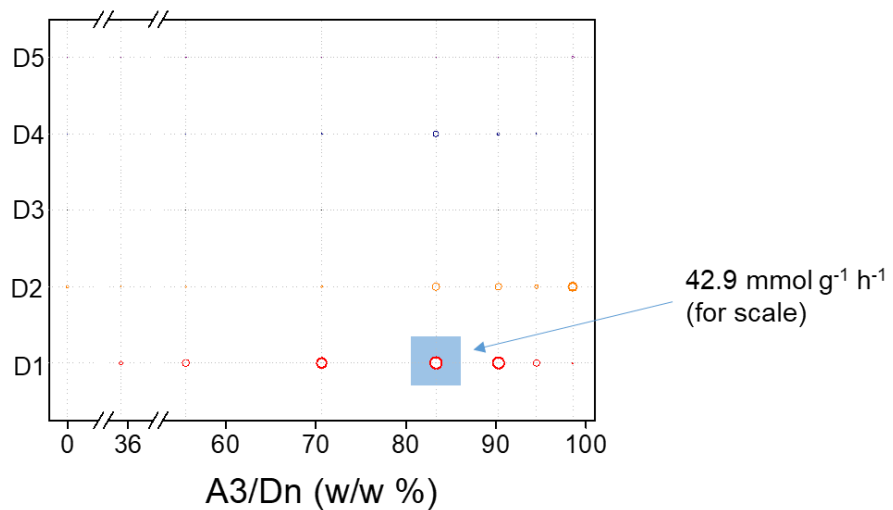


Figure 3.3. Sacrificial photocatalytic hydrogen production activities for A3/Dn plotted as a function of the acceptor weight fraction that was added in the nanoprecipitation process (100 % corresponds to the pure acceptor nanoparticle). Testing conditions: catalyst concentration = 20-100 $\mu\text{g mL}^{-1}$ (0.1-0.5 mg in 5 mL water); ascorbic acid (0.04 M); Pt loading based on total mass of donor and acceptor: (3 wt. % using a stock solution of H_2PtCl_6 , 8 wt. % in water); light source = solar simulator, 1 sun; irradiation time = 2 hours. Some circles are invisible because the HERs are very low.

By contrast, combinations involving A2 showed synergies at acceptor ratios in the range 70–90 w/w %, particularly for polymer D1 (**Figure 3.6**). A2/D1 DANC at a mass ratio of 83.3/16.7 achieved an HER of $84.3 \text{ mmol g}^{-1} \text{ h}^{-1}$, which was much higher than pure A2 ($0.6 \text{ mmol g}^{-1} \text{ h}^{-1}$) and D1 nanoparticles ($1.0 \text{ mmol g}^{-1} \text{ h}^{-1}$).

However, much higher HERs were observed for DANCs that included A1 (**Figure 3.7**), especially for combinations of A1/D1 and A1/D2. The highest performance, $165.2 \pm 25.7 \text{ mmol g}^{-1} \text{ h}^{-1}$, was observed for A1/D1 DANCs at a mass ratio of 70.6/29.4. This HER is 55 times higher than the HER for the pure acceptor, A1 ($3.0 \pm 0.7 \text{ mmol g}^{-1} \text{ h}^{-1}$), and 165 times higher than the pure polymer donor, D1 ($1.0 \pm 0.4 \text{ mmol g}^{-1} \text{ h}^{-1}$), respectively, showing a strong synergistic effect in these DANCs. Combining polymer D1 with PC70BM (A2) (**Figure 3.6**) or [60]IPB (A3) (**Figure 3.5**) gives the same compositional trend in HER (a maximum at around 70-90 w/w % acceptor), but the HERs are much lower than observed for PC60BM (A1) (**Figure 3.7**).

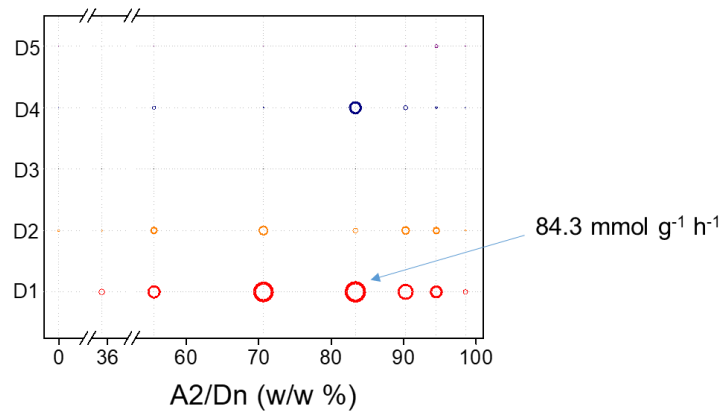


Figure 3.4. Sacrificial photocatalytic hydrogen production activities for A2/Dn plotted as a function of the acceptor weight fraction that was added in the nanoprecipitation process (100 % corresponds to the pure acceptor nanoparticle). Testing conditions: catalyst concentration = 20-100 $\mu\text{g mL}^{-1}$ (0.1-0.5 mg in 5 mL water); ascorbic acid (0.04 M); Pt loading based on total mass of donor and acceptor: (3 wt. % using a stock solution of H_2PtCl_6 , 8 wt. % in water); light source = solar simulator, 1 sun; irradiation time = 2 hours.

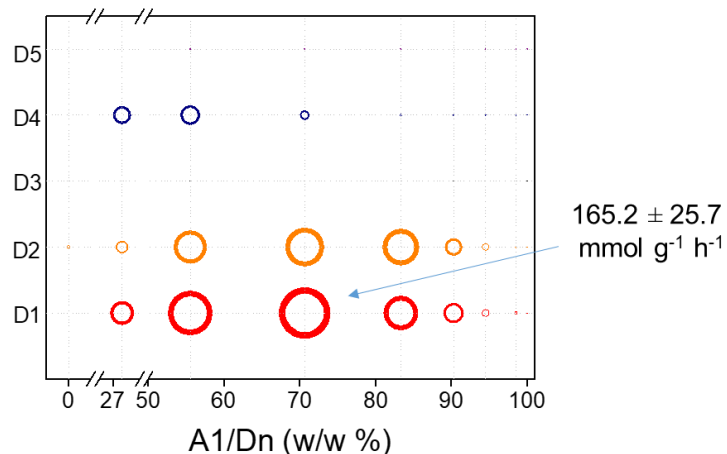


Figure 3.5. Sacrificial photocatalytic hydrogen production activities for A1/Dn plotted as a function of the acceptor weight fraction that was added in the nanoprecipitation process (100 % corresponds to the pure acceptor nanoparticle). Testing conditions: catalyst concentration = 20-100 $\mu\text{g mL}^{-1}$ (0.1-0.5 mg in 5 mL water); ascorbic acid (0.04 M); Pt loading based on total mass of donor and acceptor: (3 wt. % using a stock solution of H_2PtCl_6 , 8 wt. % in water); light source = solar simulator, 1 sun; irradiation time = 2 hours.

The results of a more exhaustive search of the variation of HER with A1/D1 composition are shown in **Figure 3.8**, which substantiates the conclusions of the high-throughput screening (i.e.,

around 70 w/w % A1 gives the maximum HER). The co-precipitation of both donor and acceptor is important for the HER: physical mixtures of A1 and D1 nanoparticles (A1 + D1) showed significantly lower HERs compared with the A1/D1 DANCs (**Figure 3.9**; activities 23 times lower when A1 mass ratio is 70.6 %), suggesting that the formation of donor-acceptor junctions is essential.

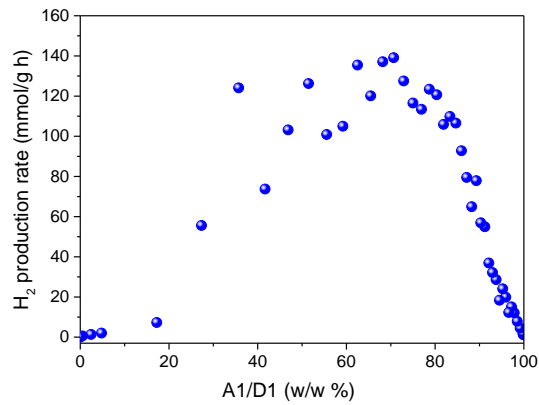


Figure 3.6. Photocatalytic hydrogen production rate for A1/D1 DANCs as a function of A1 fraction. Conditions: Catalyst concentration: 20-100 $\mu\text{g mL}^{-1}$ (0.1-0.5 mg in 5 mL water); ascorbic acid: 0.04 M; Pt loading: 3% wt. % (using H_2PtCl_6 8 wt. % in water); light source: solar simulator, 1 sun; irradiation time: 2 hours.

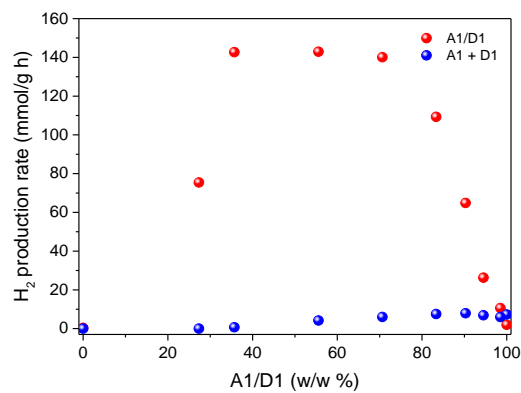


Figure 3.7. H₂ production rate of A1/D1 and A1 + D1 as a function of A1 fraction. Conditions: catalysts concentration: 20-100 $\mu\text{g mL}^{-1}$ (0.1-0.5 mg in 5 mL water); ascorbic acid: 0.04 M; Pt loading: 3 wt. % (using H_2PtCl_6 8 wt. % in water); light source: solar simulator; irradiation time: 2 hours.

We then tried to prepare donor-acceptor nanoparticles that might form a core-shell structure. To obtain the A1-D1 core-shell structure, the A1 THF solution was first injected into the water

to form the nanoparticle core, and then the shell was formed by injection of D1 THF solution. It should note that no direct evidence was obtained to prove the core-shell structure. A1 and D1 might have the same contrast in TEM images probably because they are mainly carbon-based materials without heavy atoms. The same method was used for preparing D1-A1 except that A1 was added later than D1. The resulting A1-D1 and D1-A1 DANC showed higher H₂ production activity than A1 + D1 but lower than A1/D1 at acceptor ratios in the range of 0-90 w/w % (**Figure 3.10**), further suggesting that intimate contact is required for the synergistic effect in these DANCs.

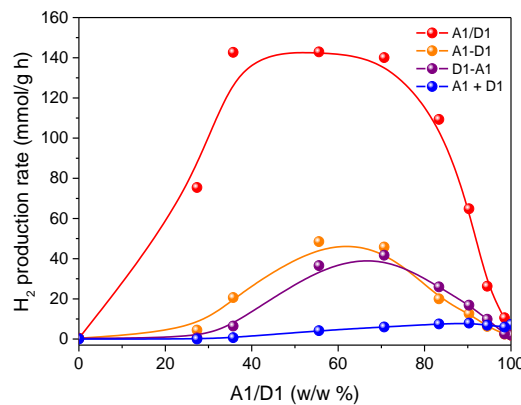


Figure 3.8. H₂ production rate of A1/D1, A1-D1, D1-A1, and A1 + D1 as a function of A1 fraction. Conditions: catalysts concentration: 20-100 $\mu\text{g mL}^{-1}$ (0.1-0.5 mg in 5 mL water); ascorbic acid: 0.04 M; Pt loading: 3 wt. % (using H₂PtCl₆ 8 wt. % in water); light source: solar simulator; irradiation time: 2 hours.

We also studied the effect of ascorbic acid concentration (0.02-0.5 M), co-catalyst type (a range of 11 co-catalyst precursors), and co-catalyst loading (0.5%-9% Pt loading) on the HER for the A1/D1 DANC (70.6 wt. % A1). The HER could be further improved to 179.0 mmol g⁻¹ h⁻¹ from 165.2 mmol g⁻¹ h⁻¹ (screening conditions) by using 0.2 M ascorbic acid and 3% Pt loading (**Figure 3.11**). We screened a series of co-catalysts precursors including Na₂PdCl₄, H₂PtCl₆, Fe(NO₃)₃, AgNO₃, Co(NO₃)₂, Cu(NO₃)₂, Zn(NO₃)₂, HAuCl₄, (NH₄)₂RhCl₆, Na₃RhCl₆, and Na₃IrCl₆. Platinum was found to be the most efficient co-catalyst among these co-catalysts precursors (**Figure 3.12**). We also tried to tune the morphology and size of the A1/D1 DANCs by introducing surfactants during nanoprecipitation (**Figure 3.13**), but this was found to markedly decrease the HER. No appreciable hydrogen generation could be detected for A1/D1 (70.6 wt. % A1) in the absence of the scavenger (ascorbic acid), Pt, or light irradiation.

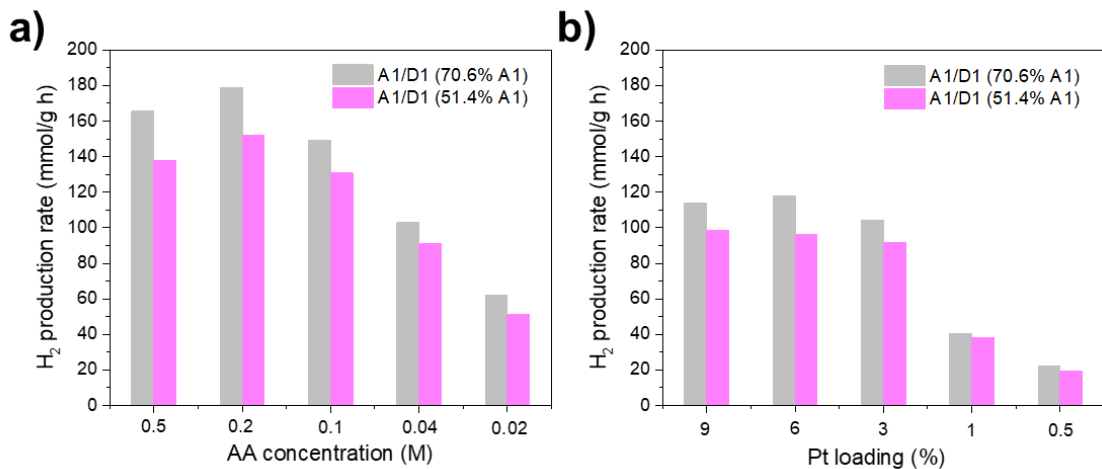


Figure 3.9. **a)** Effect of ascorbic acid concentration on H_2 production rate under solar simulator irradiation. Catalyst concentration: 46 or 34 $\mu\text{g mL}^{-1}$ (0.23 or 0.17 mg in 5 mL water); ascorbic acid: 0.02-0.5 M; Pt loading: 3 wt. % (using H_2PtCl_6 8 wt. % in water); light source: solar simulator; irradiation time: 2 hours. **b)** Amount of Pt loading effect on H_2 production rate under solar simulator. Catalyst concentration: 46 or 34 $\mu\text{g mL}^{-1}$ (0.23 or 0.17mg in 5 mL water); ascorbic acid: 0.04 M; Pt loading: 0.5-9% (using H_2PtCl_6 8 wt. % in water); light source: solar simulator; irradiation time: 2 hours.

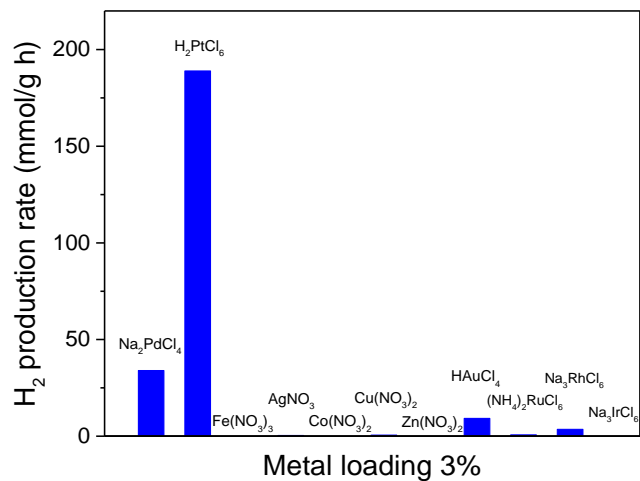


Figure 3.10. Hydrogen production rates for A1/D1 DANCs using various metal precursors. Catalyst concentration: 46 $\mu\text{g mL}^{-1}$ (0.23 in 5 mL water); ascorbic acid: 0.04 M; metal loading: 3 wt. %; light source: solar simulator; irradiation time: 2 hours.

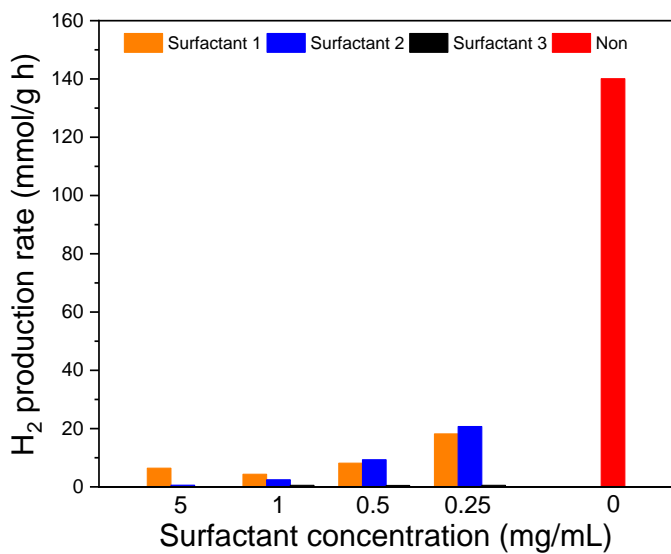


Figure 3.11. Effect of surfactants with different concentration on the H₂ production rate for A1/D1 (70.6% A1). Conditions: catalysts concentration: 46 µg mL⁻¹ (0.23 in 5 mL water); ascorbic acid: 0.04 M; Pt loading: 3 wt. %; light source: solar simulator; irradiation time: 2 hours. Surfactant 1: SDS, surfactant 2: Poly(sodium 4-styrenesulfonate) and surfactant 3: Poly(styrene-*alt*-maleic acid) sodium salt solution.

3.3.2. Conjugated Polymer Donors/non-fullerene acceptors

Recently, high-performing non-fullerene-based molecular acceptors have surpassed the most efficient fullerene acceptors for organic photovoltaics,^{8,9} which inspired us to prepare DANC photocatalysts using ITIC-2F (A4) as a non-fullerene based acceptor. As shown in **Figure 3.14**, A4/D1 (70.6 wt. % A4) exhibited the highest HER of 166.8 mmol g⁻¹ h⁻¹ among all the combinations studied here. This activity was around 7.5 and 167 times higher than the parent A4 (22.0 mmol g⁻¹ h⁻¹) and D1 (1.0 ± 0.4 mmol g⁻¹ h⁻¹) nanoparticles, respectively. The most promising combinations were found to be A1/D1 and A1/D2 (**Figure 3.7**) and A4/D1, and A4/D2 (**Figure 3.14**). The physical mixtures of A4 and D1 nanoparticles (A4 + D1) showed significantly lower HERs compared with the A4/D1 DANCs (**Figure 3.15**; activities 18 times lower when A4 mass ratio is 70.6 %), again suggesting that the formation of donor-acceptor junctions is essential.

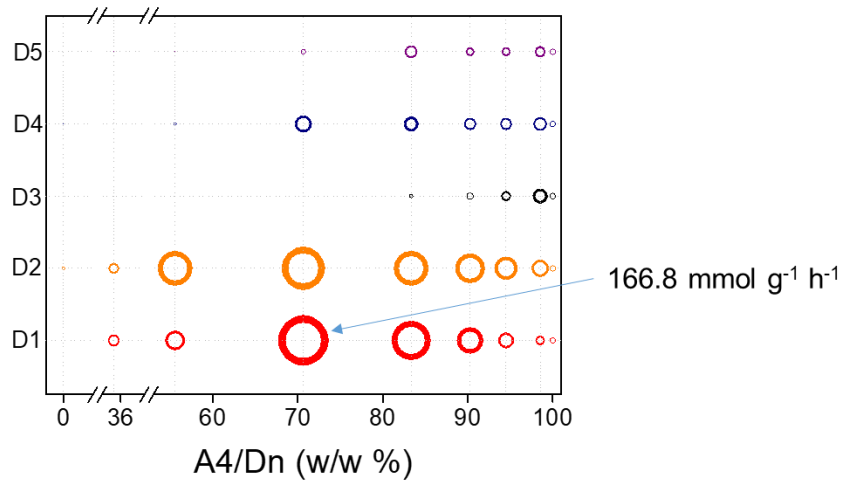


Figure 3.12. Sacrificial photocatalytic hydrogen production activities for A4/D_n plotted as a function of the acceptor weight fraction that was added in the nanoprecipitation process (100 % corresponds to the pure acceptor nanoparticle). Testing conditions: catalyst concentration = 20-100 $\mu\text{g mL}^{-1}$ (0.1-0.5 mg in 5 mL water); ascorbic acid (0.04 M); Pt loading based on total mass of donor and acceptor: (3 wt. % using a stock solution of H_2PtCl_6 , 8 wt. % in water); light source = solar simulator, 1 sun; irradiation time = 2 hours.

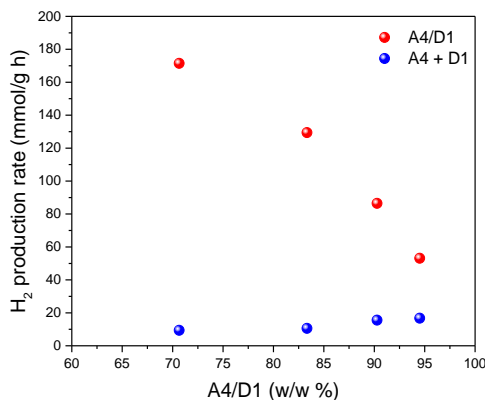


Figure 3.13. H_2 production rate of A4/D1 and A4 + D1 as a function of A4 fraction. Conditions: catalysts concentration: 20-100 $\mu\text{g mL}^{-1}$ (0.1-0.5 mg in 5 mL water); ascorbic acid: 0.04 M; Pt loading: 3 wt. % (using H_2PtCl_6 8 wt. % in water); light source: solar simulator; irradiation time: 2 hours.

3.4. Characterisations

3.4.1. Morphology and Absorption Properties

Scanning and transmission electron microscopy (SEM and TEM) images showed that different

A1 to D1 mass ratios showed similar particle size and morphology (**Figure 3.16**). The A1/D1 DANCs also showed similar particle size and morphology to A1 and D1 nanoparticles. The optical properties were then investigated by UV-vis absorption spectra. As shown in **Figure 3.17a**, Dn nanoparticles in water showed broad absorption peaks in the visible light region. As a result of synergistic light harvesting of D1 and A1, A1/D1 DANCs exhibited nearly panchromatic absorption toward the solar spectrum as presented in **Figure 3.17b and c**.

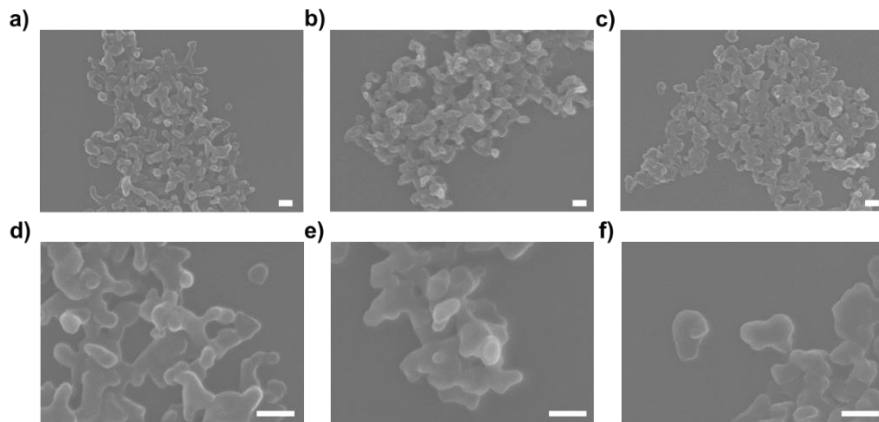


Figure 3.14. SEM images of (a) A1/D1 (83.3% A1), (b) A1/D1 (70.6% A1), and (c) A1/D1 (35.7% A1), and images of (d) A1/D1 (83.3% A1), (e) A1/D1 (70.6% A1), and (f) A1/D1 (35.7% A1) under high magnification. Scale bars = 100 nm.

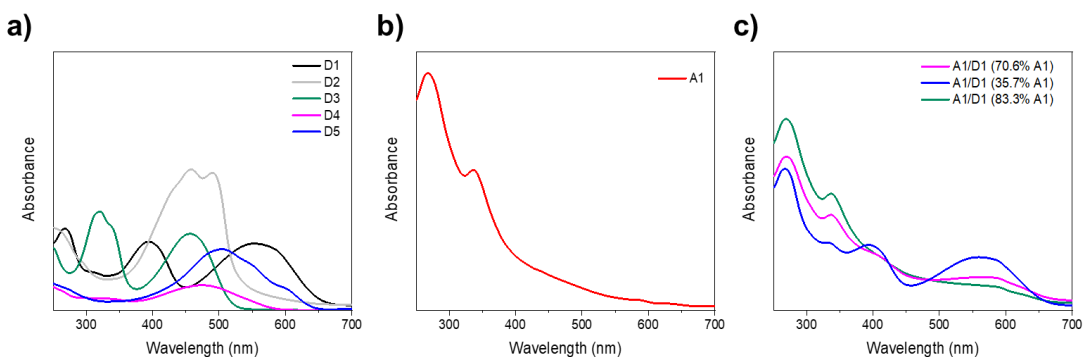


Figure 3.15. a) Adsorption spectra of Dn nanoparticles in water. b) Adsorption spectra of A1 nanoparticle in water. c) Adsorption spectra A1/D1 nanoparticles at various mass ratios of A1 to D1 in water.

While fullerene-based acceptors mainly absorbed light around the UV region, non-fullerene-based acceptor (A4) showed strong absorption towards the infrared region as revealed in **Figure 3.18**. The physical mixture of A4 + D1 showed a similar absorption profile to A4/D1 DANC. Long-wavelength absorption should be beneficial for photocatalysis from the point of view of light harvesting.

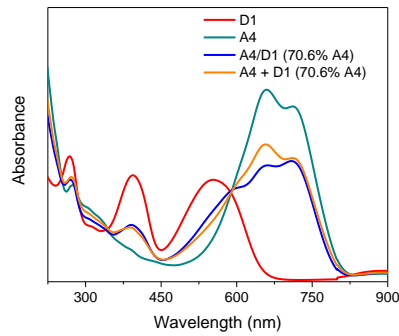


Figure 3.18. Adsorption spectra of A4, D1, A4 + D1, and A4/D1 nanoparticles in water.

3.4.2. Emission Properties

To get a better understanding of charge transfer behaviour between donor and acceptor, photoluminescence (PL) spectra were then measured. As shown in **Figure 3.19a**, D1 and A1 exhibited strong emission peaks centred at around 725 nm, which originate from the fast recombination of photoexcited electron/hole pairs. The dramatic PL quenching was observed for both A1/D1 and A4/D1 DANCs (**Figure 3.19a and b**), suggesting efficient charge transfer between donor and acceptor due to reduced recombination of photogenerated charge carriers.

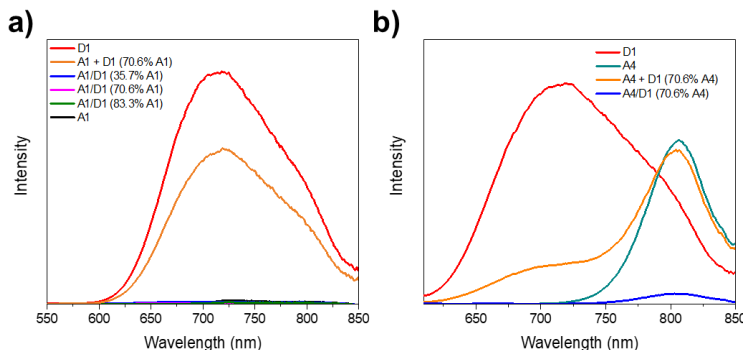


Figure 3.19. a) Emission spectra of A1, D1, A1 + D1, and A1/D1 with $\lambda_{\text{exc}} = 375 \text{ nm}$ in water.
b) Emission spectra of A4, D1, A4 + D1, and A4/D1 with $\lambda_{\text{exc}} = 600 \text{ nm}$ in water.

As shown in **Figure 3.19b**, D1 and A4 exhibited strong emission peaks centred at around 725 and 810 nm, respectively. We then measured excitation spectra of A4/D1 at 700 and 790 nm emission (**Figure 3.20**). Two excitation peaks were observed for D1 (from 300 to 650 nm), whereas A4 had two close excitation peaks at around 675 and 725 nm. These results were consistent with UV-vis absorption spectra. The dramatic excitation quenching was observed for A4/D1 DANC, which can be correlated with its efficient PL quenching. The A4 + D1 physical mixture showed significantly lower excitation intensity compared to A4/D1,

suggesting that the phase contact between A4 and D1 played a key role. By contrast, physical mixture samples of A1 + D1 and A4 + D1 showed strong emission, suggesting that charge transfer does not occur, which can correlate with their negligible H₂ production activities (**Figure 3.20b**).

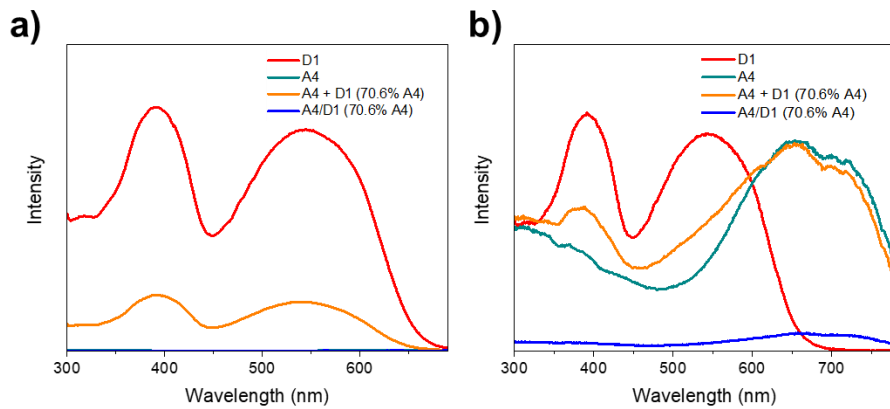


Figure 3.20. Excitation spectra of A4, D1, A4 + D1, and A4/D1 measured at (a) 700 nm and (b) 790 nm emission in water.

The emission intensity at 700 nm of A4 + D1 gradually grew when the donor fraction increased. However, no appreciable emission at 700 nm but a quickly decreased emission at 806 nm was found for A4/D1 when donor fraction increased (**Figure 3.21**). To illustrate this more quantitatively, emission at 806 nm and 700 nm of A4 + D1 and A4/D1 were plotted (**Figure 3.22**) as a function of the D1 fraction. The observed emission quenching of A4/D1 DANCs strongly indicates the efficient charge transfer between A4 and D1.

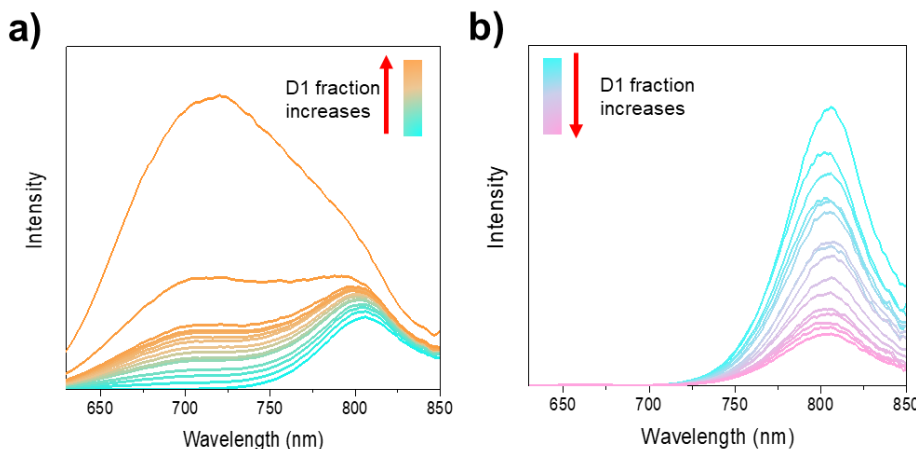


Figure 3.16. a) Emission spectra of A4 + D1 with $\lambda_{\text{exc}} = 600$ nm (A4 fraction from 100 to 0 %). b) Emission spectra of A4/D1 with $\lambda_{\text{exc}} = 600$ nm (A4 fraction from 100 to 75 %).

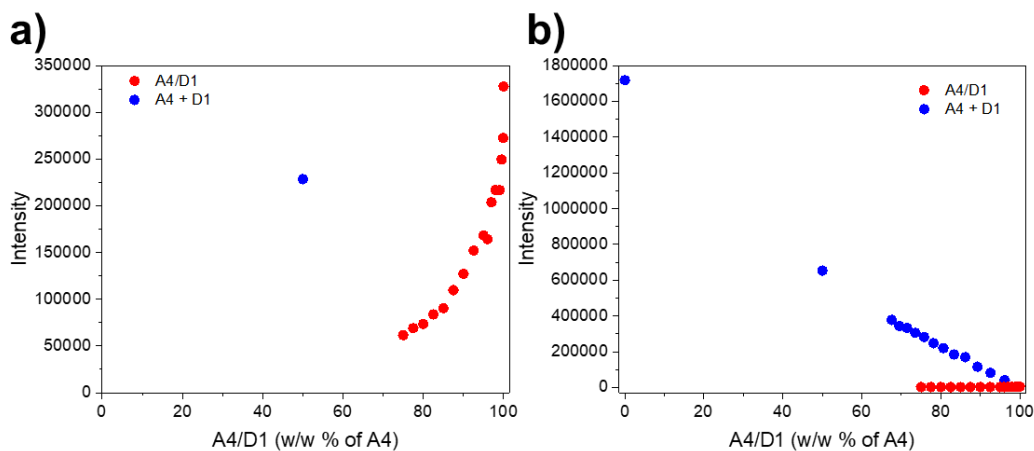


Figure 3.17. Emission intensity at (a) 806 nm and (b) 700 nm as a function of the A4 fraction ($\lambda_{\text{exc}} = 600 \text{ nm}$).

We further investigated the PL behavior of a counter-example (A1/D5), which was not an efficient DANCs catalyst due to its low HER (Figure 3.23). The result showed a relatively strong emission probably because of strong recombination of photogenerated charge carriers, indirectly suggesting that the high photocatalytic performance of A1/D1 benefits from reduced recombination of photogenerated charge carriers. Based on the optical properties of DANCs, efficient H₂ production of DANCs materials is likely to be a result of extended absorption and reduced recombination of photogenerated charge carriers.

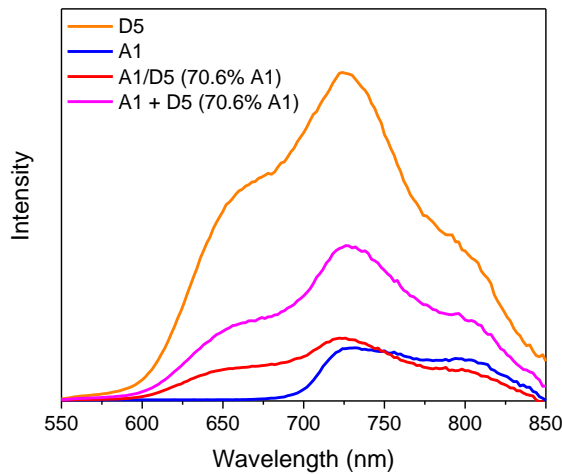


Figure 3.23. Emission spectra of A1, D5, A1 + D5, and A1/D5 with $\lambda_{\text{exc}} = 450 \text{ nm}$ in water.

3.5. Kinetic Photocatalytic Performance

3.5.1. Photocatalytic Performance

The time-course photocatalytic hydrogen evolution rates for A1/D1 DANCs were investigated. A1/D1 DANCs showed an initial HER of $105.2 \text{ mmol g}^{-1} \text{ h}^{-1}$ ($120.9 \mu\text{mol h}^{-1}$) in the first 2 hours under visible light illumination ($\lambda > 420 \text{ nm}$) using condition 1 (Figure 3.24). Similar initial rates were observed for the other two sets of reaction conditions, which had different ascorbic acid concentrations and Pt loadings (Figure 3.24). The hydrogen evolution activity decreased over time, but the DANCs were still active after 18 hours irradiation, with a rate of $37.8 \text{ mmol g}^{-1} \text{ h}^{-1}$ over the last 4 hours. Therefore, the A1/D1 DANC both exhibited excellent H₂ production rates and had much better stability compared with previously reported pure polymer nanoparticle photocatalysts,^{10–12} which showed activity for only 1, 4, and 11 hours, respectively. The catalyst mass used here (1.15 mg) was also higher than for earlier studies (around 0.05 and 0.33 mg polymer).^{10,11}

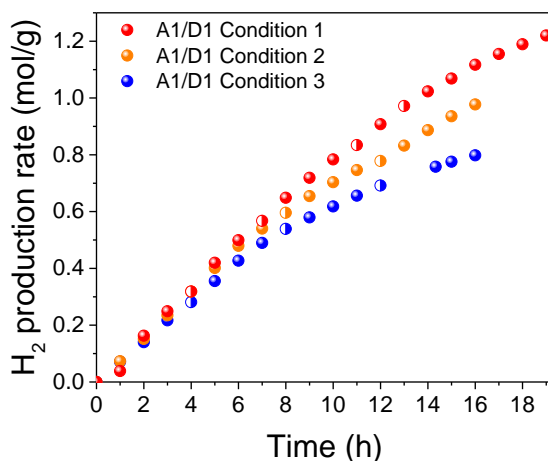


Figure 3.18. Time course of hydrogen production for A1/D1 DANCs, irradiated by 300 W Xe lamp fitted with a $\lambda > 420 \text{ nm}$ filter using 1.15 mg of the catalyst. Condition 1: 0.1 M ascorbic acid and 9 wt. % Pt; condition 2: 0.2 M ascorbic acid and 9 wt. % Pt; condition 3: 0.2 M ascorbic acid and 3 wt. % Pt. Half circle points represent the beginning of the next run after degassing.

At lower catalysis loadings, even higher hydrogen evolution rates of $247.8 \text{ mmol g}^{-1} \text{ h}^{-1}$ and $383.4 \text{ mmol g}^{-1} \text{ h}^{-1}$ were observed for 0.23 mg and 0.115 mg of A1/D1 DANCs (70.6 wt. % A1), respectively (Figure 3.25). This was probably because of the increased chance to contact with scavengers at lower catalysis loadings. Also, the light used to induce reaction might be

partially blocked by catalysts when catalysis loadings were high. Therefore, the light might be more efficiently utilised at lower catalysis loadings. Of course, for practical applications, the amount of hydrogen produced per unit area irradiated is the most important parameter, and hence such low catalyst loadings are less useful.

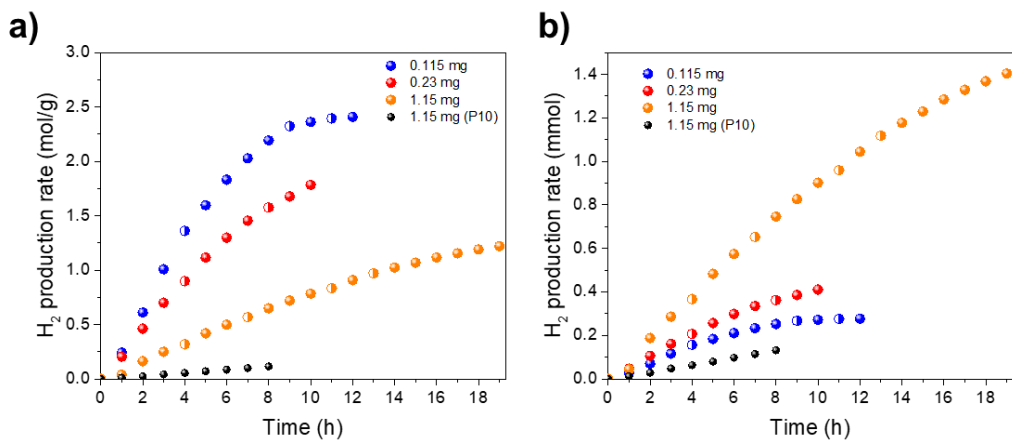


Figure 3.19. **a)** Time course of mass-normalized H_2 production of A1/D1 DANCs. **b)** Time course of non-mass-normalized H_2 production of A1/D1 DANCs. Conditions: ascorbic acid: 0.1 M; Pt loading: 9 wt. % Pt; light source: 300 W Xe light source fitted with a $\lambda > 420$ nm filter. Half circle points represent the beginning of the next measurement after degassing.

Compared to P10, one of the most efficient organic photocatalysts developed by our group,¹³ the A1/D1 DANC catalyst was almost 6 times more active in terms of mass-normalized rate over 8 hours ($85.0 \text{ mmol g}^{-1} \text{ h}^{-1}$ for A1/D1 versus $14.3 \text{ mmol g}^{-1} \text{ h}^{-1}$ for P10 under the same conditions) (Figure 3.26). An apparent quantum yield (AQY) of 3.02 % was obtained at a long wavelength of 595 nm (Figure 3.27), which places these A1/D1 DANCs among the most efficient photocatalysts for sacrificial hydrogen evolution in suspension-based systems (Table 3.1). The AQY recorded at 420, 490 and 515 nm were 3.72%, 3.43%, and 3.16%, respectively (Figure 3.27). These three similar AQY yields are consistent with the relatively flat UV-vis spectra of the sample in this spectral range (Figure 3.27), suggesting that hydrogen generation is a photocatalytic process.

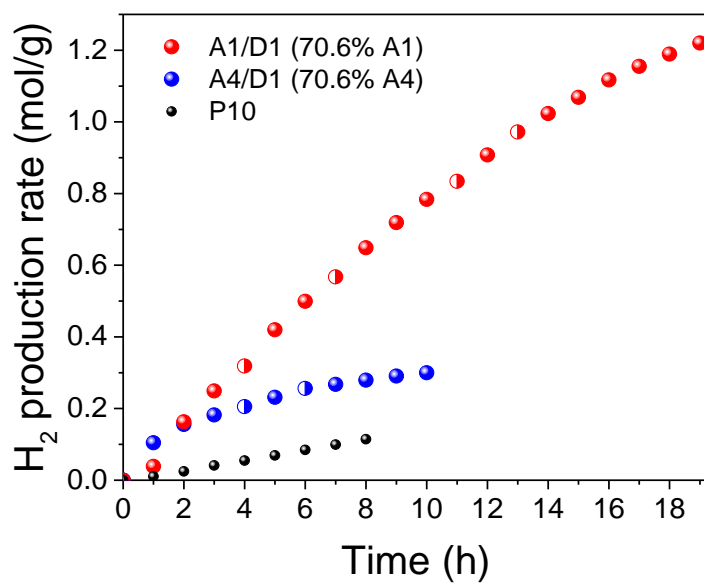


Figure 3.20. Time course of hydrogen production for A1/D1 DANC, A4/D1 DANC, and bulk P10 irradiated by 300 W Xe lamp fitted with a $\lambda > 420$ nm filter using 1.15 mg of catalysts. Conditions: 0.1 M ascorbic acid and 9 wt. % Pt; Half circle points represent the beginning of the next run after degassing.

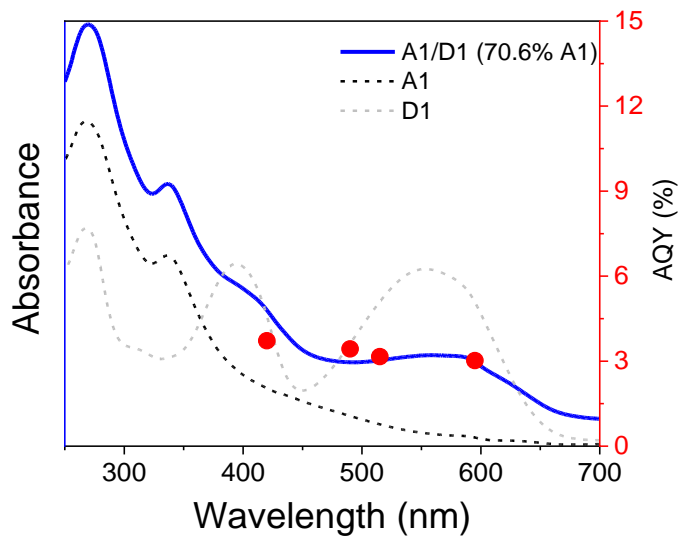


Figure 3.21. UV-vis spectra and AQYs of A1/D1 measured with monochromatic LED light at 420, 495, 515, and 595 nm, respectively. UV-vis spectra of pure A1 and D1 nanoparticles are plotted with dashed lines (Intensity rescaled for clarity).

Table 3.1. Photocatalytic performance of various reported organic photocatalysts. Note that the HER and AQY depend on the irradiation source and experimental set-up, and hence these values can only be compared in a qualitative sense.

Materials	HER (mmol g ⁻¹ h ⁻¹)	AQY	Journal and publication year	Reference
DBTD-CMP ₁	9.2 ($\lambda > 420$ nm)	0.2% (500 nm)	<i>ACS Catal.</i> 2018	¹⁴
FS-COF	10.1 ($\lambda > 420$ nm)	0.6% (600 nm)	<i>Nat. Chem.</i> 2018	¹⁵
FS-COF+dye	16.3 ($\lambda > 420$ nm)	2.2% (600 nm)		
g-C ₄₀ N ₃ -COF	4.1 ($\lambda > 420$ nm)	3.2% (520 nm) 0.29% (578 nm)	<i>Nat. Commun.</i> 2019	¹⁶
Polymer dots PIFDTBT/g-C ₃ N ₄	0.58 ($\lambda > 400$ nm)	~0.5% (500 nm) ~0.5% (600 nm)	<i>Appl. Catal. B Environ.</i> 2019	¹⁷
CTF-BT/Th	6.6 ($\lambda > 420$ nm)	~2.5% (500 nm) N/A (550 nm)	<i>Angew. Chem. Int. Ed.</i> 2019	¹⁸
DA-HM	4.14 ($\lambda > 420$ nm)	~2% (500 nm)	<i>Angew. Chem. Int. Ed.</i> 2018	¹⁹
g-C ₃ N ₄ -MF ₁₀₀	3.6 ($\lambda > 420$ nm)	~4% (500 nm) ~2% (550 nm)	<i>Nano Energy</i> 2019	²⁰
P3/CN	13 ($\lambda = 420\sim780$ nm)	~15.8% (550 nm) ~1.5% (630 nm)	<i>Adv. Funct. Mater.</i> 2018	²¹
Polymer dots PFTFQ-PtPy15	12.7 ($\lambda > 420$ nm)	0.4% (515 nm)	<i>ACS Catal.</i> 2018	¹²
Polymer dots PFODTBT	63 ($\lambda > 420$ nm)	0.6% (550 nm)	<i>Energy Environ. Sci.</i> 2017	¹⁰
Pt-PVP-Tp-COF	8.4 ($\lambda > 420$ nm)	0.6% (475 nm)	<i>Angew. Chem. Int. Ed.</i> 2019	²²
Polymer dots P8T2/g-C ₃ N ₄	0.93 ($\lambda > 400$ nm)	0.8% (550 nm)	<i>J. Mater. Chem. A</i> , 2019	²³
P10	3.2 ($\lambda > 420$ nm)	11.6% (420 nm) N/A (595 nm)	<i>Nat. Commun.</i> 2018	¹³
Ter-CTF-0.7	19.3 ($\lambda > 420$ nm)	14.78% (550 nm)	<i>ACS Catal.</i> 2019	²⁴
A1/D1 DANCs	105.2 ($\lambda > 420$ nm)	3.16% (515 nm) 3.02% (595 nm)	This work	

3.5.2. Characterisations after Photocatalysis

Phase separation from solution was observed after photocatalysis (**Figure 3.28a and b**), which might suggest that this is a primary cause for loss of HER over time. A4/D1 samples exhibited an HER of $104.4 \text{ mmol g}^{-1} \text{ h}^{-1}$ in the first hour (**Figure 3.26**) but experienced a great loss of photocatalytic activity during irradiation. We observed that the A4/D1 DANCs aggregated much more quickly than the A1/D1 samples (**Figure 3.28c and d**), perhaps explaining the more rapid deactivation.

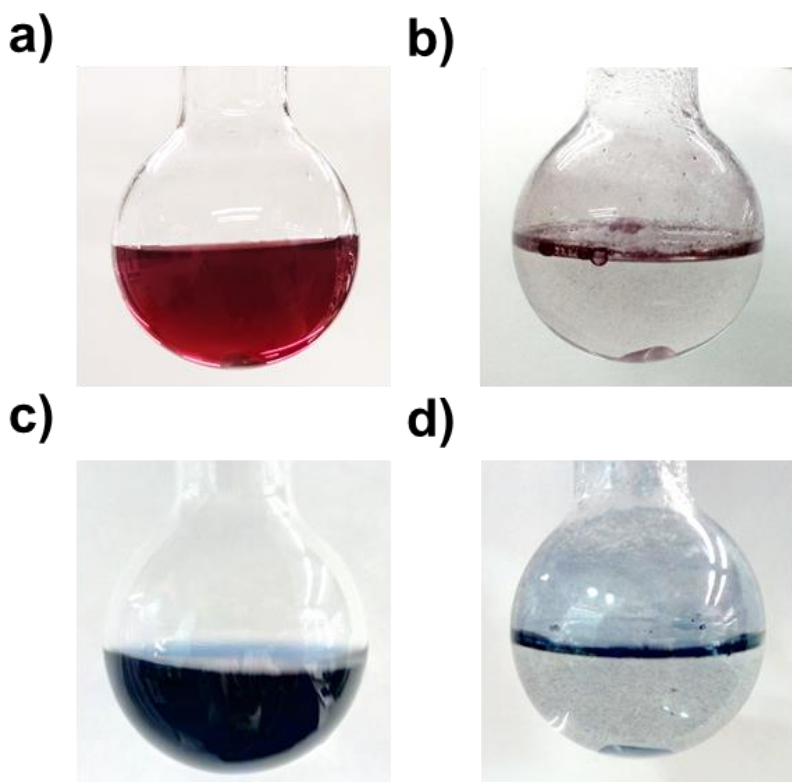


Figure 3.28. Images of aqueous A1/D1 reaction dispersion in a 69 mL flask (a) before and (b) after photocatalysis experiment (19 hours irradiation). Also, aqueous A4/D1 reaction dispersion (c) before and (d) after photocatalysis experiment (10 hours irradiation).

SEM characterisations of the A1/D1 samples before and after photocatalysis supported particle aggregation (**Figure 3.29**). The large aggregation was observed after photocatalysis (**Figure 3.29b**). The A1/D1 samples were collected after photocatalysis and redissolved into THF solvent for characterisation by UV-vis and ^1H NMR spectroscopy. No obvious changes occurred before and after photocatalysis (**Figure 3.30**). We, therefore, suggest that the observed rate loss for A1/D1 is due to the aggregation of the DANCs during photocatalysis, rather than chemical decomposition. Note also that no such deactivation occurs over 8 hours for P10,

which is not nanoparticulate. We speculated that instability might come from the aggregation which was probably caused by light irradiation, stirring, or bubbling with N₂.

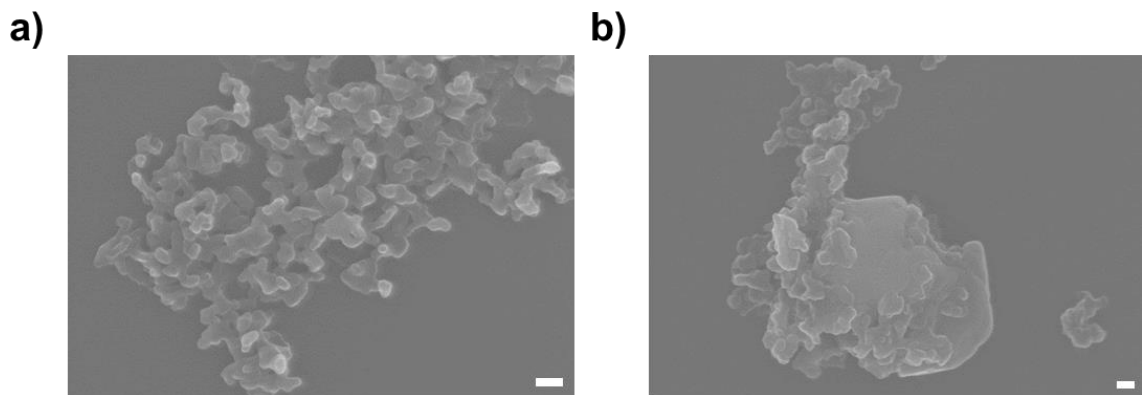


Figure 3.29. **a)** SEM images of A1/D1 before photocatalysis experiment. **b)** SEM images of A1/D1 after photocatalysis experiment. Scale bars = 100 nm.

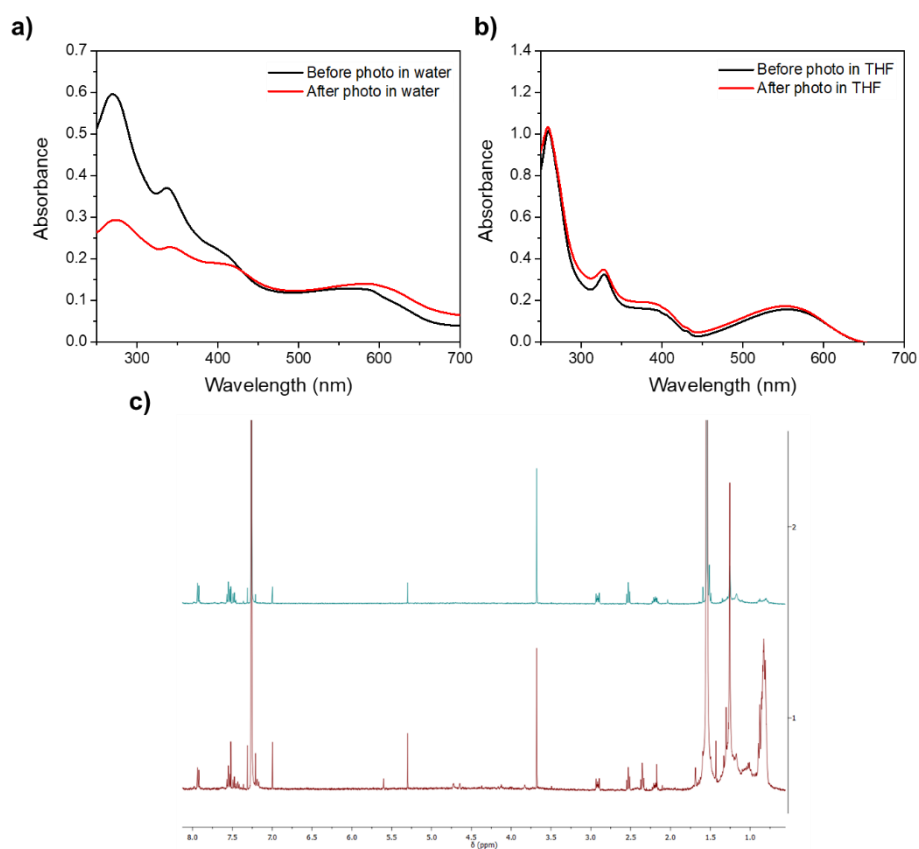


Figure 3.22. **a)** Absorption spectra of A1/D1 before and after photocatalysis experiment in water. **b)** Absorption spectra of A1/D1 before and after photocatalysis experiment in THF. **c)** ¹H NMR of A1/D1 before (top) and after (down) photocatalysis experiment.

3.6. Ternary System

In OPV, It has been shown that enhanced light harvesting, improved charge transfer, reduced charge recombination, and improved photostability have been achieved after the introduction of a third component into binary donor-acceptor organic solar cells (OSC), termed ternary solar cells (TSC), often in the forms of two donors and one acceptor or one donor and two acceptors.^{25–31} Inspired by the high performance of HER achieved on binary donor-acceptor nanocomposites, then we extended these binary nanocomposites to ternary donor_n-donor_m-acceptor or donor-acceptor_n-acceptor_m nanocomposites (donor_n:donor_m = 1:1 or acceptor_n:acceptor_m = 1:1).

3.6.1. Random Screen on Ternary System

Compared to A1/D1 and A1/D2 binary DANCs, A1/D1D2 ternary DANCs did not show enhanced photocatalytic activity (**Figure 3.31**). The combinations of acceptors and donors were screened randomly. No enhanced photocatalytic activity was observed probably because of the weak interaction between these acceptors and donors. We then tested more ternary DANCs. Ternary A1/D1D3, A1/D1D4, A1/D1D5, A1/D1D6, A1/D2D3, A1/D2D5, and A1/D2D6 also showed no improvement (**Figures 3.32 and 3.33**).

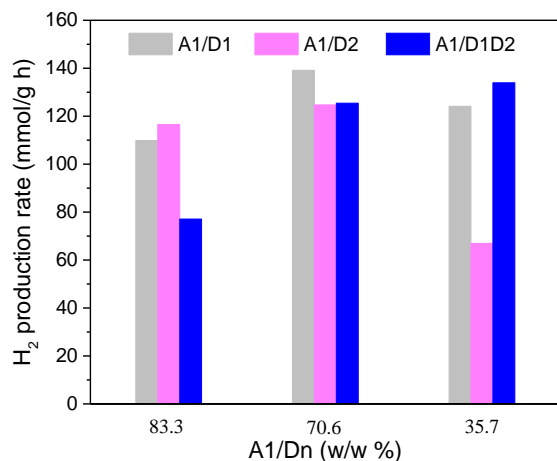


Figure 3.23. Hydrogen production rates for A1/D1D2 ternary system with different compositions. Catalyst concentration: 60, 46, and 28 $\mu\text{g mL}^{-1}$ in 5 mL water; ascorbic acid: 0.04 M; Pt loading: 3 wt. %; light source: solar simulator; irradiation time: 2 hours.

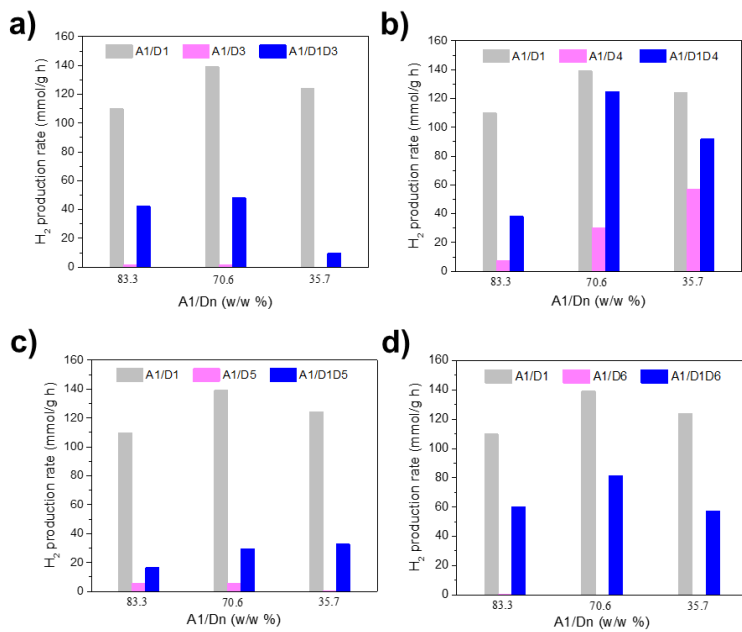


Figure 3.24. Hydrogen production rates for various ternary systems with different compositions. Catalyst concentration: 60, 46, and 28 $\mu\text{g mL}^{-1}$ in 5 mL water; ascorbic acid: 0.04 M; Pt loading: 3 wt.%; light source: solar simulator; irradiation time: 2 hours.

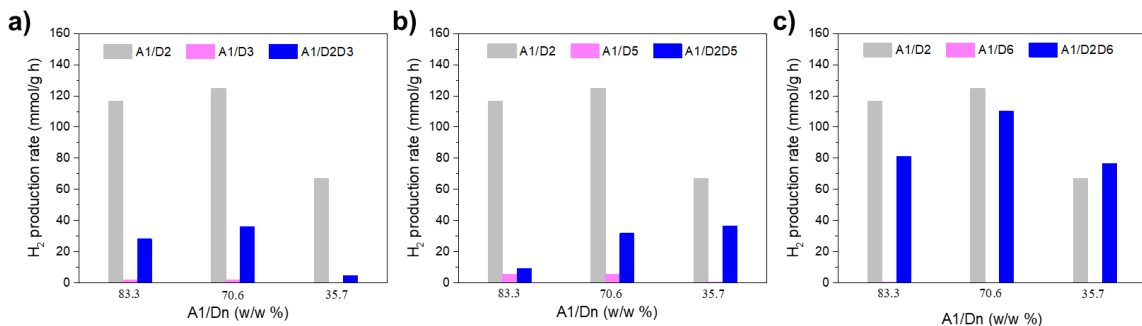


Figure 3.25. Hydrogen production rates for various ternary systems with different compositions. Catalyst concentration: 60, 46, and 28 $\mu\text{g mL}^{-1}$ in 5 mL water; ascorbic acid: 0.04 M; Pt loading: 3 wt.%; light source: solar simulator; irradiation time: 2 hours.

However, after the random screening of more samples, we found that the hydrogen production rate of A1/D3D5 was significantly improved in the presence of both D3 and D5. A1/D3D5 reached an HER of 87.1 $\text{mmol g}^{-1} \text{h}^{-1}$, which is much higher than the rate obtained for binary A1/D3 (1.6 $\text{mmol g}^{-1} \text{h}^{-1}$) or A1/D5 (5.4 $\text{mmol g}^{-1} \text{h}^{-1}$) DANCs with the same compositions (**Figure 3.34**).

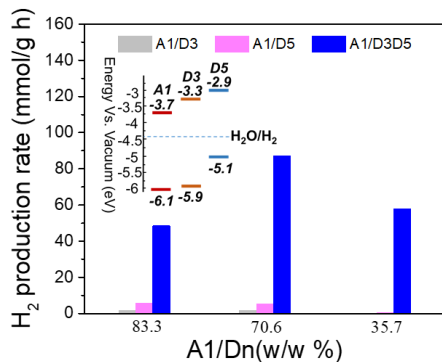


Figure 3.34. Hydrogen evolution rates of A1/D3D5 ternary nanocomposites of various compositions. Catalyst concentrations: 0.3, 0.23, and 0.14 mg in 5 mL water; ascorbic acid: 0.04 M; Pt loading: 3 wt. %; light source = solar simulator; irradiation time = 2 hours. Inset: HOMO and LUMO band levels of donors and acceptors.

Enhancement to the performance was also accomplished in A1/D3D4, A1/D3D5, A1/D4D5, A1/D4D6, A1/D2D4, and A1/D5D6 DANCs (**Figures 3.35 and 3.36**). In ternary A1/D4D5 DANC, enhancement was achieved when A1 ratio was 83.3 and 70.6% (**Figures 3.35c**). However, no enhancement was observed under low A1 ratio (35.7%). Ternary A1/D4D6 DANC showed similar results. The enhancement was achieved only under high A1 ratio. By contrast, Ternary A1/D2D4 DANC showed increased photocatalytic performance under low A1 ratio (70.6 and 35.7%). Although ternary systems were complicated, enhanced activities were achieved compared to binary systems.

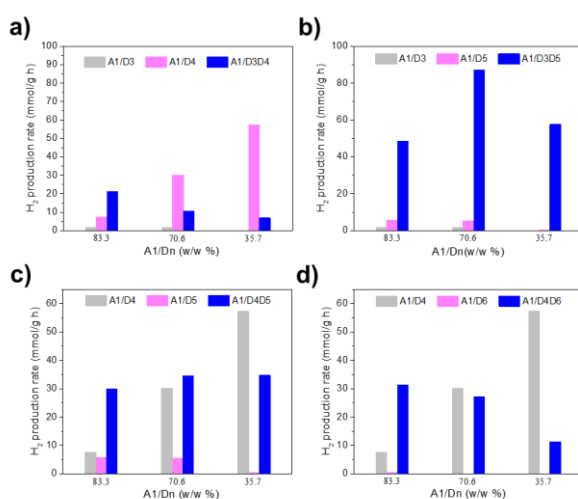


Figure 3.26. Hydrogen production rates for various ternary systems with different compositions. Catalyst concentration: 60, 46, and 28 $\mu\text{g mL}^{-1}$ in 5 mL water; ascorbic acid: 0.04 M; Pt loading: 3 wt. %; light source: solar simulator; irradiation time: 2 hours.

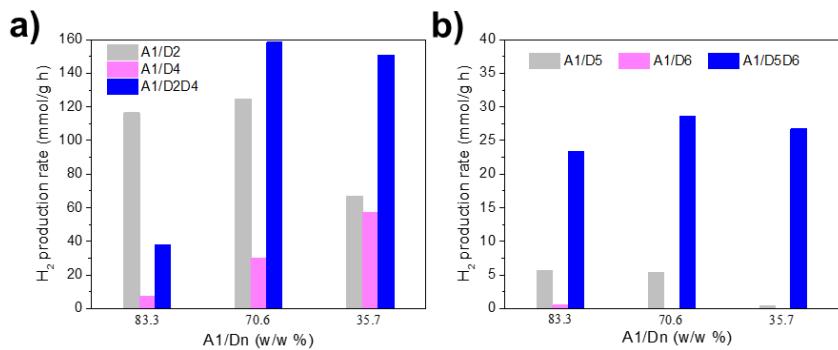


Figure 3.27. Hydrogen production rates for various ternary systems with different compositions. Catalyst concentration: 60, 46, and 28 $\mu\text{g mL}^{-1}$ in 5 mL water; ascorbic acid: 0.04 M; Pt loading: 3 wt. %; light source: solar simulator; irradiation time: 2 hours.

3.6.2. Machine Learning Assisted Ternary System

3.6.2.1. Background

The above results show that ternary donor_n-donor_m-acceptor nanocomposites have the potential to be efficient photocatalysts with proper design/selection of components. The introduction of an additional component into the binary blend makes charge/energy transfer between each component more complicated, resulting in an indeed complex photophysical process.³¹ As exemplified in TSC studies, several operational principles with different electron/energy transfer pathways, including energy transfer, cascade charge transfer, parallel-like, and alloy models, were proposed,³¹ which have different requirements on the electronic energy levels of components. Moreover, the morphology and microscopic phase of the ternary system depend on components, which play key roles in charge separation efficiency. As a result of the nature of the complexity, the development of general guidelines for the design of ternary photocatalysts has been prevented.

Through the chain and side-chain engineering approaches, the energy levels and structures of conjugated polymer donor materials can be widely tuned, providing a diverse library of donor materials.^{32,33} On the acceptors, the development of non-fullerene acceptors offers a very wide range of chemical structures and electron affinities.⁴ The extensive screen on multicomponent performance based on this large library is time-consuming and, a large proportion of results are unsatisfactory like the test results in **Section 3.6.1**. Moreover, the diversity of donor/acceptor library raises an interesting multicomponent optimisation challenge: how to rationally select components for ternary nanocomposites photocatalysts to ensure efficient charge transfer

between components and enhanced light harvesting.

Here, we applied a machine learning approach (**Figure 3.37**) to guide us to explore and find highly efficient ternary nanocomposites photocatalysts from a selection of fourteen conjugated polymer donors (D1-D14) and eight small organic acceptors (A1-A8) (**Figures 3.38 and 3.39**). Two polymer donors (D1 and D8) were found to have low solubility in THF and therefore were not used in this research.

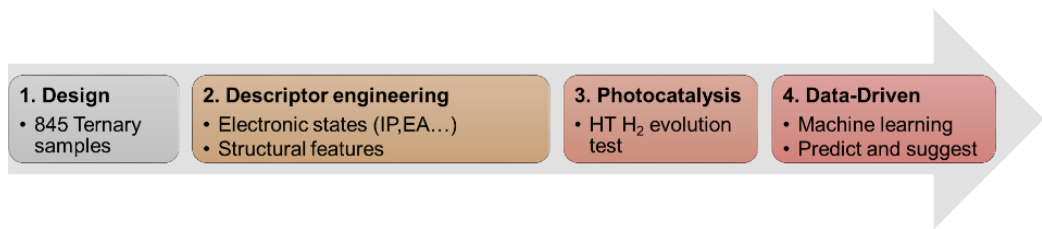


Figure 3.28. Scheme of proposed machine learning approach.

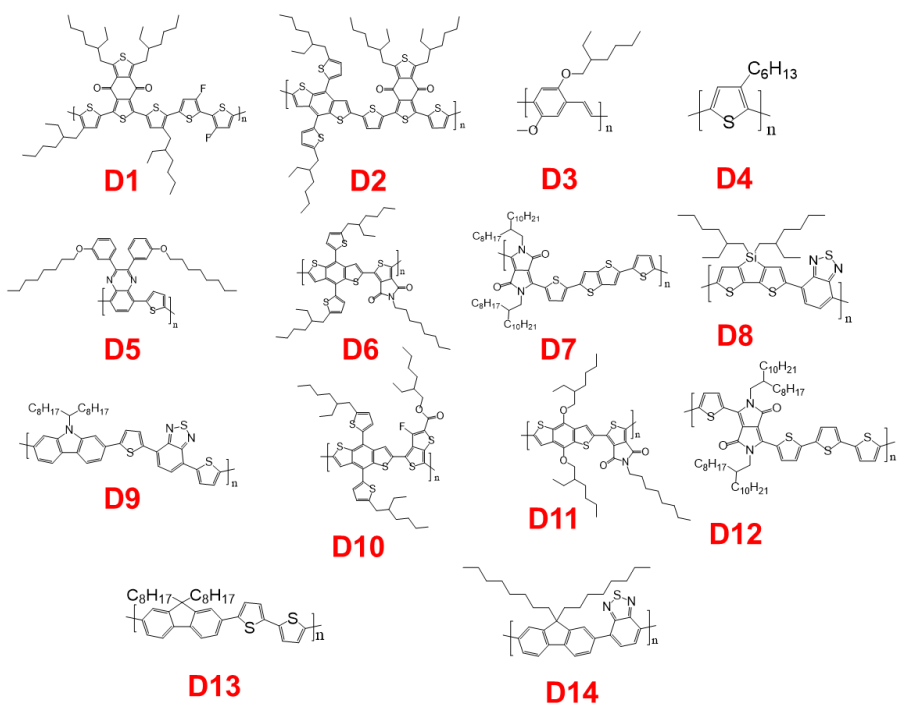


Figure 3.38. Molecular structures of donors (D1-D14).

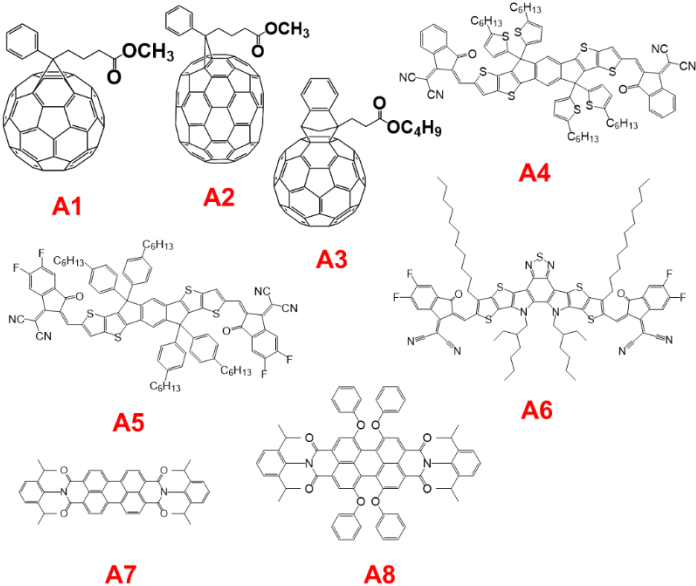


Figure 3.39. Molecular structures of acceptors (A1-A8).

3.6.2.2. Dataset

The acceptors include 3 fullerene-based, 2 PDI-based, and 3 non-fullerene-based molecules. Two rules were set up to create the dataset of ternary photocatalyst; they are 1) only two categories, D_nD_mA and DA_nA_m, exist in our dataset and 2) no repetition of either donor or acceptor in one hybrid catalyst. Overall, the designed dataset contains 845 ternary photocatalysts samples by using 12 unique donors and 8 unique acceptors.

3.6.2.3. Descriptor Engineering

To encode electronic properties, we computed the equilibrium geometry of each donor and acceptor at DFT level using wB97XD functional, together with the Def2-SVP basis set using the Gaussian 16 software. We also calculated several electronic features that contribute to the photocatalytic performance of *i*th molecule, which are reorganisation energy (RE), the ionisation potential energy (E_i^{IP}), and the electron affinity energy (E_i^{EA}). More in detail, we calculated both hole reorganisation energy (E_i^{hRE}) and electron reorganisation energy (E_i^{eRE}) for each donor and acceptor. Finally, we gathered these features as a 4 elements vector $V_i^{el} = (E_i^{IP}, E_i^{EA}, E_i^{hRE}, E_i^{eRE})$ to describe the electronic features of either donor or acceptor in the paired catalysts. Except for electronic features, we also calculated the structure properties of catalysts to capture the similarity relationship of catalytic activities. We chose Morgan fingerprints algorithm as the additional feature and defined the features of the fingerprints for

a paired catalyst as a 3 elements vector $V_{ijk}^{fps} = (V_i^{fps}, V_j^{fps}, V_k^{fps})$ where each component i, j , and k has a 2048 length bit fingerprints vector (V_{mol}^{fps}) calculated by RDKit package. To summarise, we described and calculated both electronic and structural features and concatenated them into a vector as the chemical space $P_{ijk} = (V_{ijk}^{el}, V_{ijk}^{fps})$, containing 15 elements. These 845 ternary paired catalysts with computed electronic and structure features are used to pick a subset for experiment and training machine learning models that are used for performance prediction of hybrid catalysts.

3.6.2.4. Model Selection and Machine Learning

Since 845 hybrid catalysts were designed *in silico*, we picked 104 catalysts from the calculated chemical space by using the Kennard-Stone (KS) algorithm as a representative subset (**Figure 3.40a**) and the initial training set of future optimisations. This sampling method selects the subset from uniform regions to describe the chemical space as much as it can. It can give more confidence in predictions made later in the development of machine model because the KS sampled data set covered more regions of chemical space than the randomly sampled set. After the initial step (step 0), we used machine learning prediction result to discover higher catalytic activity by active learning. More specifically, we did a 5 fold cross-validation to determine the values of the five hyperparameters (α , and $\theta_1, \theta_2, \theta_3, \theta_4$ in **Equation 3.1**) by Bayes optimisation in 50 cycles using Skopt package. The surrogate model is the cost function of each machine learning model, either the logistic function for classification or the root mean square error (RMSE) for regression. Then, we used the trained model to do prediction of the rest unselected samples and give the probability of positive (high catalytic activity) class by classification model or the real catalytic activity values by the regression model. Then, we selected a small number (less than 20 samples) of the highest probability of the positive class of catalysts or activity of catalysts to do the next step experiments. During each step, we performed parallel experiments with different mass ratios of donor and acceptor to exploit the maximum synergy interaction and picked the highest hydrogen evolution rate (HER) as the true value of the catalytic activity.

$$\mathcal{K}(P_{ijk}, P_{lmn}) = \alpha * e^{-\left(\theta_1 D_{el}^2(P_{ijk}, P_{lmn}) + \theta_2 D_{fps}^2(V_i^{fps}, V_l^{fps}) + \theta_3 D_{fps}^2(V_j^{fps}, V_m^{fps}) + \theta_4 D_{fps}^2(V_k^{fps}, V_n^{fps})\right)} \quad (3.1)$$

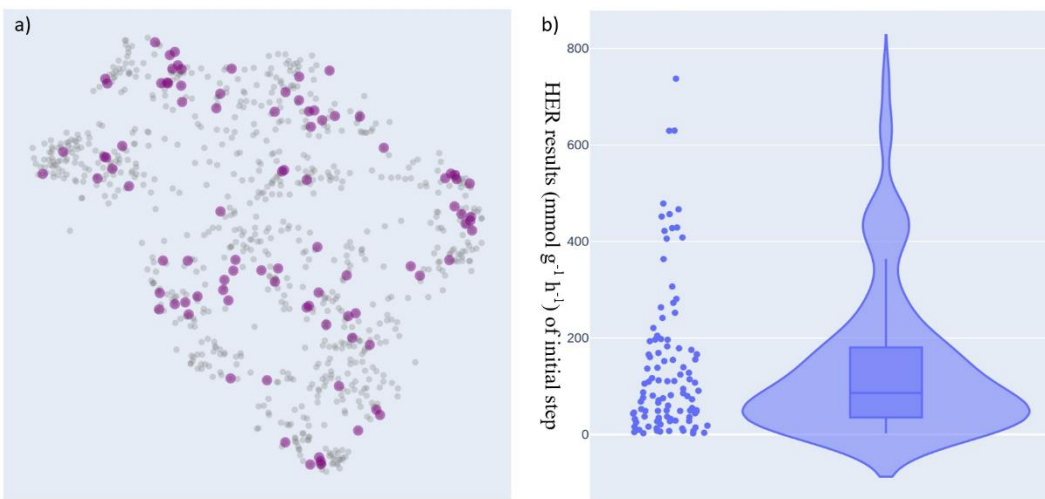


Figure 3.29. **a)** Location of the catalysts selected by the KS algorithm (Purple colour) and unselected samples (Grey colour) in 2D chemical space calculated by UMAP algorithm with equal contribution of each descriptor. **b)** Experimental data distribution of the representative dataset: left side, the points of each experimental sample; right side, violin plot of the HER values within box plot.

However, due to some limitations such as the small size of training set and unbalanced data distribution (**Figure 3.40b**), we cannot get a reasonable validation result ($R^2 < 0.5$) based on regression models. Since few samples have HER values higher than $200 \text{ mmol g}^{-1} \text{ h}^{-1}$, we assigned a negative class with HER values smaller than 150 and a positive class with HER values ($\text{mmol g}^{-1} \text{ h}^{-1}$) larger than 150, which gives the ratio of 7:3 between negative and positive class. By transforming a regression problem into a low-resolution classification problem, the classification model (SVM) can do virtual screen to help increase the ratio of positive samples (**Figure 3.41a**) with 78% accuracy at producing binary classification problems (**Table 3.2**). To increase the ratio of negative and positive class, we used 20 prediction samples with the highest probability of positive class to perform the next active learning step (step 1) and these experimental results also can be considered as the test set of the model in step 0. After the experiment, we collected all HER results to training the SVM model again and got the prediction for step 2. We selected the top 24 highest probability samples from the positive class in this step. Finally, we can achieve an acceptable regression model (KRR) with $0.66 R^2$ after step 2 (**Figure 3.41b**) since the unbalanced data distribution was improved (**Figure 3.41c**) comparing with step 0 (**Figure 3.40b**) by discovering more samples with high catalytic activities in step 1 and step 2.

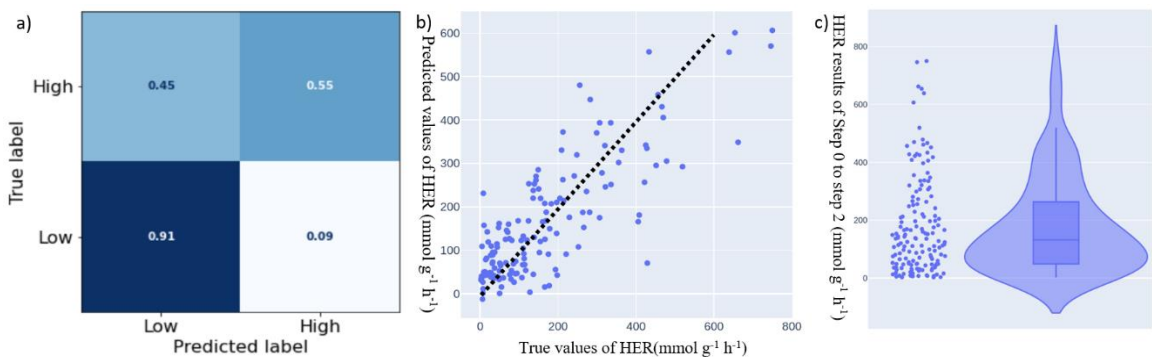


Figure 3.30. a) Confusion matrix for the step 0 SVM binary classifier. b) The 5-fold cross-validation results for the step 2 KRR regressor. c) Experimental data distribution of the HER values including from step 0 to step 2: left side, the points of each experimental sample; right side, violin plot of the HER values within box plot.

Table 3.2. Binary classification results across all steps.

Steps	Machine learning models	Accuracy/5-fold	F1-score/5-fold	Number of test set	Test accuracy (by SVM)
0	SVM	0.78	0.59	20	0.80
1	SVM	0.83	0.77	24	0.54
2	SVM and KRR	0.80 and $R^2 = 0.66$ for KRR	0.79	9	0.78

3.6.2.5. Machine Learning Guided Search Outcome.

Table 3.3 showed the top 10 most active ternary nanocomposite photocatalysts with H₂ production rates higher than 500 mmol g⁻¹ h⁻¹. Among these 10 nanocomposites, 3 of them were found in the initial screen of 114 nanocomposites, but 7 of them were found by machine learning guided search of 54 samples. Moreover, the highest HER (749.8 mmol g⁻¹ h⁻¹) achieved by ternary nanocomposite photocatalysts (D6D13A4) was found in step 1, and this mass-normalized activity is more than 52.4 times and 1.9 times higher than the most efficient organic polymer photocatalyst P10 (14.3 mmol g⁻¹ h⁻¹) and the most efficient binary nanocomposite photocatalyst A1/D1 (383.4 mmol g⁻¹ h⁻¹) under solar simulator irradiation in Section 3.5.1, respectively (Figure 3.42). Most of the hydrogen production activities were reproducible, but the repeatability was relatively poor. The HERs could be affected by many

factors such as sonication time, the new batch of polymer solution, heating conditions, and so on.

Table 3.3. The top 10 most active ternary nanocomposite photocatalysts. Catalyst concentration: 10 $\mu\text{g mL}^{-1}$ in 5 mL water; ascorbic acid: 0.04 M; Pt loading: 3 wt. %; light source: solar simulator; irradiation time: 1 hour.

Nanocomposites	HER ($\text{mmol g}^{-1} \text{h}^{-1}$)	Steps
D6D13A8	629.3	0
D6A5A7	737.4	0
D9A1A8	629.7	0
D9D13A2	661.9	1
D5D13A4	638.7	1
D6D13A4	749.8	1
D9D13A4	746.0	1
D13D10A4	653.9	1
D13D6A6	519.3	2
D5D9A4	606.5	3

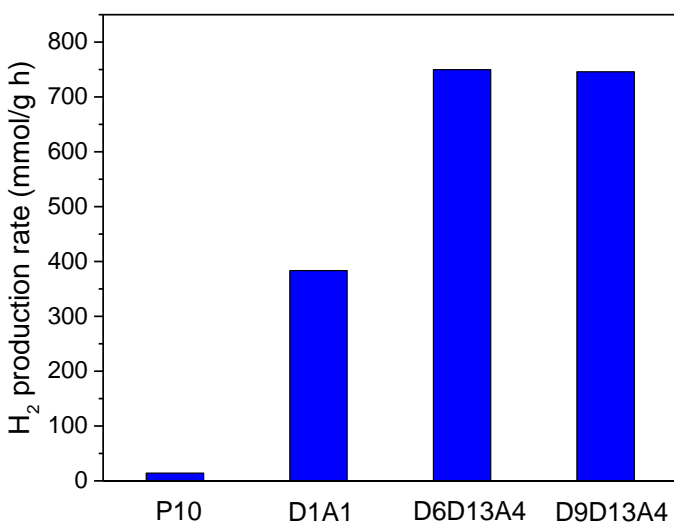


Figure 3.42. The comparison of ternary system (D6D13A4 and D9D13A4) with the best binary D1/A1 and organic polymer P10. Catalyst concentration: $10 \mu\text{g mL}^{-1}$ in 5 mL water; ascorbic acid: 0.04 M; Pt loading: 3 wt. %; light source: solar simulator; irradiation time: 1 hour.

3.7. Conclusions

To summarize, high-throughput screening was used to discover both binary and ternary DANCs with sacrificial hydrogen evolution rates that greatly outperform the constituent donors and acceptors. This illustrates that a key principle from the field of organic photovoltaics can be translated into direct photocatalysis using organic materials. Non-fullerene acceptors gave a higher photocatalytic performance, which is again related to recent progress in OPV. Our results imply that catalyst lifetime may be limited by colloidal stability, rather than chemical decomposition, at least for short irradiation times (< 1 day), suggesting the potential to improve catalyst lifetimes in the future by creating more stable colloids.

The development of molecular acceptors and polymer donors offers a very wide range of chemical structures but meanwhile induces complexity when making composites, especially for the ternary system. We use machine learning as a general guideline for the design and discovery of efficient ternary photocatalysts based on various molecular acceptors and polymer donors for H_2 evolution from water. The top 10 ternary nanocomposite photocatalysts achieved remarkable H_2 production rates that are higher than $500 \text{ mmol g}^{-1} \text{ h}^{-1}$. The most efficient one showed an HER of $749.8 \text{ mmol g}^{-1} \text{ h}^{-1}$.

In the future, an interesting extension would be to add even more components into the nanocomposite system, including light-harvesting components, co-catalysts, mimicking the functionality of the natural photosynthesis system.

3.8. Experimental

3.8.1. Preparation Methods

Materials: For binary and ternary system: Poly[*N*-9'-heptadecanyl-2,7-carbazole-*alt*-5,5-(4',7'-di-2-thienyl-2',1',3'-benzothiadiazole)] (D1), poly(9,9-di-*n*-octylfluorene-*alt*-bithiophene), poly[(9,9-di-*n*-octylfluorenyl-2,7-diyl)-co-bithiophene] (D2), poly(9,9-di-*n*-octylfluorene-*alt*-benzothiadiazole) (D3), poly[2-methoxy-5-(2-ethylhexyloxy)-1,4-phenylenevinylene] (D4), poly(3-hexylthiophene-2,5-diyl) (D5), [6,6]-phenyl-C61-butyric acid methyl ester (A1), [6,6]-phenyl-C71-butyric acid methyl ester (A2), indene-C60-propionic acid butyl ester (A3) and 3,9-bis(2-methylene-((3-(1,1-dicyanomethylene)-6,7-difluoro)-indanone))-5,5,11,11-tetrakis(4-hexylphenyl)-dithieno[2,3-d:2',3'-d']-*s*-indaceno[1,2-b:5,6-b']dithiophene (A4) were obtained from Ossila (U.K). For machine learning guided ternary system: Poly[[5,7-bis(2-ethylhexyl)-4,8-dioxo-4*H*,8*H*-benzo[1,2-c:4,5-c']dithiophene-1,3-diyl[3,3'''-bis(2-ethylhexyl)-3'',4'-difluoro[2,2':5',2'':5'',2''''-quaterthiophene]-5,5'''-diyl]] (D1), Poly[(2,6-(4,8-bis(5-(2-ethylhexyl)thiophen-2-yl)-benzo[1,2-b:4,5-b']dithiophene))-*alt*-(5,5-(1',3'-di-2-thienyl-5',7'-bis(2-ethylhexyl)benzo[1',2'-c:4',5'-c']dithiophene-4,8-dione)] (D2). Poly[2-methoxy-5-(2-ethylhexyloxy)-1,4-phenylenevinylene] (D3), Poly(3-hexylthiophene-2,5-diyl) (D4), Poly[[2,3-bis(3-octyloxyphenyl)-5,8-quinoxalinediyl]-2,5-thiophenediyl] (D5), Poly[(5,6-dihydro-5-octyl-4,6-dioxo-4*H*-thieno[3,4-c]pyrrole-1,3-diyl)[4,8-bis[5-(2-ethylhexyl)-2-thienyl]benzo[1,2-b:4,5-b']dithiophene-2,6-diyl]] (D6), Poly[2,5-(2-octyldodecyl)-3,6-diketopyrrolopyrrole-*alt*-5,5-(2,5-di(thien-2-yl)thieno[3,2-b]thiophene)] (D7), Poly[(4,4-bis(2-ethylhexyl)-dithieno[3,2-b:2',3'-d]silole)-2,6-diyl-*alt*-(2,1,3-benzothiadiazole)-4,7-diyl] (D8), Poly[*N*-9'-heptadecanyl-2,7-carbazole-*alt*-5,5-(4',7'-di-2-thienyl-2',1',3'-benzothiadiazole)] (D9), Poly[4,8-bis(5-(2-ethylhexyl)thiophen-2-yl)benzo[1,2-b:4,5-b']dithiophene-2,6-diyl-*alt*-(4-(2-ethylhexyl)-3-fluorothieno[3,4-b]thiophene)-2-carboxylate-2-6-diyl] (D10), Poly[(5,6-dihydro-5-octyl-4,6-dioxo-4*H*-thieno[3,4-c]pyrrole-1,3-diyl)[4,8-bis[(2-ethylhexyl)oxy]benzo[1,2-b:4,5-b']dithiophene-2,6-diyl]] (D11), Poly[2,5-bis(2-octyldodecyl)pyrrolo[3,4-c]pyrrole-1,4(2*H*,5*H*)-dione-3,6-diyl-*alt*-(3'',4'-difluoro[2,2';5',2'':5'',2''''-quaterthiophen]-5,5'''-diyl)] (D12), Poly(9,9-dioctylfluorene-*alt*-bithiophene) (D13), Poly(9,9-dioctylfluorene-*alt*-benzothiadiazole) (D14),

[6,6]-Phenyl-C61-butyric acid methyl ester (A1), [6,6]-Phenyl-C71-butyric acid methyl ester (A2), [60]IPB (A3), 3,9-bis(2-methylene-(3-(1,1-dicyanomethylene)-indanone))-5,5,11,11-tetrakis(5-hexylthienyl)-dithieno[2,3-d:2',3'-d']-s-indaceno[1,2-b:5,6-b']dithiophene (A4), 3,9-bis(2-methylene-((3-(1,1-dicyanomethylene)-6,7-difluoro)-indanone))-5,5,11,11-tetrakis(4-hexylphenyl)-dithieno[2,3-d:2',3'-d']-s-indaceno[1,2-b:5,6-b']dithiophene (A5), and 2,2'-(2Z,2'Z)-((12,13-bis(2-ethylhexyl)-3,9-diundecyl-12,13-dihydro-[1,2,5]thiadiazolo[3,4-e]thieno[2'',3'':4',5']thieno[2',3':4,5]pyrrolo[3,2-g]thieno[2',3':4,5]thieno[3,2-b]indole-2,10-diyl)bis(methanylylidene))bis(5,6-difluoro-3-oxo-2,3-dihydro-1H-indene-2,1-diylidene))dimalononitrile (A6) were obtained from Ossila (U.K). *N,N'*-Bis(2,6-diisopropylphenyl)-3,4,9,10-perylenetetracarboxylic Diimide (A7) and *N,N'*-Bis(2,6-diisopropylphenyl)-1,6,7,12-tetraphenoxy-3,4,9,10-perylenetetracarboxylic Diimide (A8) were obtained from Tokyo Chemical Industry. Poly(sodium 4-styrenesulfonate), poly(styrene-*alt*-maleic acid) sodium salt solution, sodium dodecyl sulfate (SDS), ascorbic acid (AA), hexachloroplatinic acid solution (8 wt. % in water), and tetrahydrofuran (THF inhibitor-free) were purchased from Sigma-Aldrich. Metal precursors were obtained from commercial suppliers Sigma-Aldrich, Tokyo Chemical Industry, and Alfa Aesar. The deionized water was purified using a Milli-Q System ($\rho = 15 \text{ M}\Omega$). All chemicals were used as received without further purification.

Synthesis of binary DANCs: The donor and acceptor materials were dissolved in anhydrous THF with a concentration of 0.2 mg mL^{-1} and 1 mg mL^{-1} ,⁷ respectively, serving as stock solution. A volume of 1 mL of the donor and the acceptor stock solutions was mixed together and sonicated for a few minutes. Next, 0.5 mL of this mixture was added rapidly into a vial containing 5 mL of deionized water with or without surfactants (surfactant concentration ranging from 0.25 to 5 mg mL^{-1}) under continuous sonication for around 10 seconds. For the preparation of A1/D1 with a mass ratio of 83.3/16.7, a volume of 0.5 mL of D1 and 0.5 mL of A1 stock solutions was mixed together and sonicated for a few minutes. Next, 0.5 mL of this mixture was added rapidly into a vial containing 5 mL of deionized water under continuous sonication for around 10 seconds. All samples were placed in a cover-free sample holder on a hot plate at 130°C for 5 hours to completely evaporate the residual THF. For the preparation of pure donor or acceptor nanomaterials, all procedures were the same except that 1 mL of donor or acceptor stock solution was used.

Synthesis of binary core-shell DANCs: The donor and acceptor materials were dissolved in anhydrous THF with a concentration of 0.2 mg mL^{-1} and 1 mg mL^{-1} , respectively, serving as

stock solution. A specific amount of donor stock solution was added rapidly into a vial containing 5 mL of deionized water under continuous sonication for around 10 seconds. Then, a specific volume of acceptor stock solution was added to this solution under continuous sonication for another 10 seconds. The total amount of donor and acceptor stock solution was determined to be 1 mL. For the preparation of A1-D1 core-shell DANC with a mass ratio of 83.3/16.7, 0.25 mL of A1 stock solution was first added rapidly into a vial containing 5 mL of deionized water under continuous sonication for around 10 seconds. Then, 0.25 mL of D1 stock solution was added into this solution under continuous sonication for another 10 seconds. All samples were placed in a cover-free sample holder on a hot plate at 130 °C for 5 hours to completely evaporate the residual THF.

Synthesis of ternary DANCs for random test: The donor and acceptor materials were dissolved in anhydrous THF with a concentration of 0.2 mg mL⁻¹ and 1 mg mL⁻¹, respectively, serving as stock solution. A volume of 1 mL of the donor_n, donor_m, and the acceptor stock solutions were mixed together and sonicated for a few minutes (donor_n:donor_m = 1:1). Next, 0.5 mL of this mixture was added rapidly into a vial containing 5 mL of deionized water under continuous sonication for around 10 seconds. For the preparation of A1/D1D2 with an acceptor to donor mass ratio of 83.3/16.7, a volume of 0.25 mL of D1, 0.25 mL of D2, and 0.5 mL of A1 stock solutions were mixed together and sonicated for a few minutes. Next, 0.5 mL of this mixture was added rapidly into a vial containing 5 mL of deionized water under continuous sonication for around 10 seconds. All samples were placed in a cover-free sample holder on a hot plate at 130 °C for 5 hours to completely evaporate the residual THF.

Synthesis of ternary DANCs for machine learning guided screen: The donor and acceptor materials were dissolved in anhydrous THF with a concentration of 0.1 mg mL⁻¹, serving as stock solution. A volume of 1 mL of the donor_n, donor_m, acceptor_n and acceptor_m stock solutions was mixed together (mixture of three components; donor_n:donor_m = 1:1 or acceptor_n:acceptor_m = 1:1) and sonicated for a few minutes. Next, 0.5 mL of this mixture was added rapidly into a vial containing 5 mL of deionized water under continuous sonication for around 10 seconds. For the preparation of A1/D1D2 with an acceptor to donor mass ratio of 1:1, a volume of 0.25 mL of D1, 0.25 mL of D2, and 0.5 mL of A1 stock solutions were mixed together and sonicated for a few minutes. Next, 0.5 mL of this mixture was added rapidly into a vial containing 5 mL of deionized water under continuous sonication for around 10 seconds. All samples were placed in a cover-free sample holder on a hot plate at 130 °C for 5 hours to completely evaporate the residual THF.

3.8.2. Characterisation Methods

SEM measurements were carried out on Hitachi S-4800 cold field emission scanning electron microscope (FE-SEM). Images were collected at a working voltage of 10 kV and a working distance of 3.4 mm using a combination of upper and lower secondary electron detectors. Samples were dropped on silica wafer before imaging. TEM images were collected on a Tescan FIB SEM S8000G in TEM mode. ^1H NMR spectra were recorded at 400 MHz using a Bruker Advance 400 NMR spectrometer. The UV-vis absorption spectra and steady-state photoluminescence spectra were measured on a Shimadzu UV-2550 UV-vis spectrometer and an Edinburgh Instruments LS980-D2S2-STM spectrometer, respectively. Samples with good aqueous dispersibility were synthesised by a moderate evaporation method (heating overnight at 60 °C with stirring) and diluted with an appropriate amount of water to keep the sample concentration at 0.01 mg mL⁻¹ before measuring the spectrum.

3.8.3. Measurement Methods

Photocatalytic activity measurements: For high throughput solar simulator measurements, certain amounts of 1 M ascorbic acid solution and hexachloroplatinic acid solution were added into vials (Volume = 12.5 mL) containing 5 ml of as-prepared DANCs aqueous suspension. The photocatalytic H₂ production activities were then evaluated using a high-throughput degas-irradiation-analysis system. Specifically, after purging with nitrogen for 3 hours in a Sweigher robot (Chemspeed Technologies), the vials were capped with pierceable caps using a capper tool in a nitrogen atmosphere. Next, up to 48 vials were illuminated using a solar simulator (A4.5G, Class AAA, IEC/JIS/ASTM, 1440 W xenon, 12 × 12 in., MODEL:94123A) for 2 hours. The samples were rotated and rocked on their sides during irradiation. Gaseous products were injected via a transfer line equipped with a headspace injector and the H₂ production was analyzed using a Shimadzu HS-GC.

Kinetic measurements were conducted in a 69 mL quartz flask. Catalysts (normally 1.15 mg for A1/D1) were dispersed into 0.1 M ascorbic acid water solution (25 mL) with diluted hexachloroplatinic acid solution as a platinum precursor (3% to 9% loading). After bubbling with N₂ for 30 min to remove O₂, the reaction mixture was illuminated with a 300 W Newport Xe light-source (Model: 6258, Ozone free) using a 420 nm cut-off filter. The light source was cooled by water circulating through a metal jacket. Gas samples were taken out by using a gas-tight syringe and run on a Bruker 450-GC gas chromatograph. Hydrogen was detected with a thermal conductivity S3 detector referencing against standard gas with a known concentration

of hydrogen. Any hydrogen dissolved in the reaction mixture was not measured and the pressure increase generated by the evolved hydrogen was neglected in the calculations. After photocatalysis experiment, samples were recovered by washing with water and centrifuging twice at 14000 rpm for 15 min. For calculation of the initial hydrogen evolution rate for A1/D1, the first hour of activity was not counted because of the induction time needed for Pt co-catalyst photodeposition to occur.

Apparent quantum yield measurements: The apparent quantum yield for the photocatalytic H₂ evolution was measured using a $\lambda = 420$ nm LED (129.5 mW), $\lambda = 490$ nm LED (97.1 mW), $\lambda = 515$ nm LED (65.7 mW), and $\lambda = 595$ nm LED (115.0 mW) controlled by an IsoTech IPS303DD power supply. The six vials of A1/D1 samples, prepared by nanoprecipitation strategy, were mixed together and then diluted to 25 mL with deionized water. Then, 440 mg of ascorbic acid (0.1 M) and diluted hexachloroplatinic acid (9% loading) were added before illuminating with LED. The light intensity was measured with a ThorLabs S120VC photodiode power sensor controlled by a ThorLabs PM100D Power and Energy Meter Console and the apparent quantum yield was estimated using the equation below:

$$AQY = 2 \times \frac{\text{moles of hydrogen evolved}}{\text{moles of incident photons}} \times 100\% \quad (3.2)$$

3.9. References

- 1 S. L. Wu, F. Liu, H. C. Yang and S. B. Darling, *Mol. Syst. Des. Eng.*, 2020, **5**, 433–444.
- 2 N. R. Armstrong, W. Wang, D. M. Alloway, D. Placencia, E. Ratcliff and M. Brumbach, *Macromol. Rapid Commun.*, 2009, **30**, 717–731.
- 3 M. C. Scharber and N. S. Sariciftci, *Prog. Polym. Sci.*, 2013, **38**, 1929–1940.
- 4 P. Cheng, G. Li, X. Zhan and Y. Yang, *Nat. Photonics*, 2018, **12**, 131–142.
- 5 S. Schubert, J. T. Delaney and U. S. Schubert, *Soft Matter*, 2011, **7**, 1581–1588.
- 6 Y. Bai, L. Wilbraham, B. J. Slater, M. A. Zwijnenburg, R. S. Sprick and A. I. Cooper, *J. Am. Chem. Soc.*, 2019, **141**, 9063–9071.
- 7 T. Ameri, J. Min, N. Li, F. Machui, D. Baran, M. Forster, K. J. Schottler, D. Dolfen, U. Scherf and C. J. Brabec, *Adv. Energy Mater.*, 2012, **2**, 1198–1202.
- 8 W. Zhao, S. Li, H. Yao, S. Zhang, Y. Zhang, B. Yang and J. Hou, *J. Am. Chem. Soc.*, 2017, **139**, 7148–7151.
- 9 J. Hou, O. Inganäs, R. H. Friend and F. Gao, *Nat. Mater.*, 2018, **17**, 119–128.
- 10 P. B. Pati, G. Damas, L. Tian, D. L. A. Fernandes, L. Zhang, I. B. Pehlivan, T. Edvinsson, C. M. Araujo and H. Tian, *Energy Environ. Sci.*, 2017, **10**, 1372–1376.
- 11 L. Wang, R. Fernández-Terán, L. Zhang, D. L. A. Fernandes, L. Tian, H. Chen and H. Tian, *Angew. Chemie - Int. Ed.*, 2016, **55**, 12306–12310.
- 12 P. J. Tseng, C. L. Chang, Y. H. Chan, L. Y. Ting, P. Y. Chen, C. H. Liao, M. L. Tsai and H. H. Chou, *ACS Catal.*, 2018, **8**, 7766–7772.
- 13 M. Sachs, R. S. Sprick, D. Pearce, S. A. J. Hillman, A. Monti, A. A. Y. Guilbert, N. J. Brownbill, S. Dimitrov, X. Shi, F. Blanc, M. A. Zwijnenburg, J. Nelson, J. R. Durrant and A. I. Cooper, *Nat. Commun.*, 2018, **9**, 1–11.
- 14 Z. Wang, X. Yang, T. Yang, Y. Zhao, F. Wang, Y. Chen, J. H. Zeng, C. Yan, F. Huang and J. X. Jiang, *ACS Catal.*, 2018, **8**, 8590–8596.
- 15 X. Wang, L. Chen, S. Y. Chong, M. A. Little, Y. Wu, W. H. Zhu, R. Clowes, Y. Yan, M. A. Zwijnenburg, R. S. Sprick and A. I. Cooper, *Nat. Chem.*, 2018, **10**, 1180–1189.
- 16 S. Bi, C. Yang, W. Zhang, J. Xu, L. Liu, D. Wu, X. Wang, Y. Han, Q. Liang and F. Zhang, *Nat. Commun.*, 2019, **10**, 1–10.
- 17 W. Zhou, T. Jia, D. Zhang, Z. Zheng, W. Hong and X. Chen, *Appl. Catal. B Environ.*, 2019, **259**, 118067.
- 18 W. Huang, Q. He, Y. Hu and Y. Li, *Angew. Chemie - Int. Ed.*, 2019, **58**, 8676–8680.
- 19 H. Ou, X. Chen, L. Lin, Y. Fang and X. Wang, *Angew. Chemie - Int. Ed.*, 2018, **57**, 8729–8733.

- 20 H. Che, C. Liu, G. Che, G. Liao, H. Dong, C. Li, N. Song and C. Li, *Nano Energy*, 2019, 104273.
- 21 F. Yu, Z. Wang, S. Zhang, H. Ye, K. Kong, X. Gong, J. Hua and H. Tian, *Adv. Funct. Mater.*, 2018, **28**, 1–13.
- 22 J. Ming, A. Liu, J. Zhao, P. Zhang, H. Huang, H. Lin, Z. Xu, X. Zhang, X. Wang, J. Hofkens, M. B. J. Roeffaers and J. Long, *Angew. Chemie - Int. Ed.*, 2019, 18458–18462.
- 23 W. Zhou, T. Jia, H. Shi, D. Yu, W. Hong and X. Chen, *J. Mater. Chem. A*, 2019, **7**, 303–311.
- 24 L. Guo, Y. Niu, S. Razzaque, tan and S. Jin, *ACS Catal.*, 2019, **9**, 9438–9445.
- 25 Y. Yang Michael, W. Chen, L. Dou, W. H. Chang, H. S. Duan, B. Bob, G. Li and Y. Yang, *Nat. Photonics*, 2015, **9**, 190–198.
- 26 Q. An, F. Zhang, J. Zhang, W. Tang, Z. Deng and B. Hu, *Energy Environ. Sci.*, 2016, **9**, 281–322.
- 27 R. Yu, H. Yao and J. Hou, *Adv. Energy Mater.*, 2018, **8**, 1–9.
- 28 T. Ameri, P. Khoram, J. Min and C. J. Brabec, *Adv. Mater.*, 2013, **25**, 4245–4266.
- 29 L. Lu, M. A. Kelly, W. You and L. Yu, *Nat. Photonics*, 2015, **9**, 491–500.
- 30 W. Huang, P. Cheng, Y. M. Yang, G. Li and Y. Yang, *Adv. Mater.*, 2018, **30**, 1–24.
- 31 N. Gasparini, A. Salleo, I. McCulloch and D. Baran, *Nat. Rev. Mater.*, 2019, **4**, 229–242.
- 32 J. Mei and Z. Bao, *Chem. Mater.*, 2014, **26**, 604–615.
- 33 Z. G. Zhang and Y. Li, *Sci. China Chem.*, 2015, **58**, 192–209.

Chapter 4

Organic Molecular Nanoparticles

4.1. Contributions to this Chapter

HR-TEM images for nanospheres and nanofibres were obtained by Dr Mounib Bahri. The Photoelectrochemical measurements and Raman spectra were performed by Lunjie Liu. Crystal data was collected and analyzed by Dr Marc Little. TDFT and TD-DFT calculations were performed by Dr Tao liu. Some of the figures were prepared with the help of Ni Wang. All other work was performed by the thesis author.

4.2. Background

The proper molecular design of organic semiconductors can endow them with size/shape/composition-dependent optoelectronic properties. Substituents with a higher electronegativity in porphyrin molecules lead to larger molecular dipoles (largest dipoles of 4.08 Debye).¹ The large molecular dipole results in a built-in electric field, which promotes the separation of photogenerated carriers and contributes to excellent photocatalytic performances.¹ A rational design of donor-acceptor organic molecules is proved to be an effective way to achieve large molecular dipole.² Moreover, the unique D-A characteristics are beneficial for the spatial separation of photogenerated electrons and holes.³

Molecular packing in aggregation state is also crucial for the determination of optoelectronic properties of materials.⁴ Nanoparticle photocatalysts based on small organic molecule has attracted a lot of attention in recent years.^{1,3,5–10} The structure flexibility and morphology tunability of these nanoparticles provide an opportunity to fine-tune the photochemical properties.^{1,11,12} The charge carrier mobility may vary by more than 10 orders of magnitude depending on the degree of order (amorphous, semicrystalline, crystalline) in a molecular solid-state material.¹³ Also, crystalline packing directly impacts the energy flow mechanisms, e.g., excited state dynamics, in crystalline molecular assemblies.¹⁴ It has been demonstrated that H-type π - π stacking in molecular nano-assemblies lowers the absolute energy levels of CB and VB, leading to a narrowing of bandgap that enhances light absorption.¹⁵

Molecular packing significantly affects aggregation-state properties such as charge carrier mobility, excited state dynamics, and light absorption, which are essential for photocatalytic performance. For instance, the J-aggregates state of porphyrin nano-assemblies showed higher photocatalytic activity towards dye degradation than its amorphous state because delocalized π electrons in J-aggregates facilitate electron transfer.¹¹ The control on molecular packing of perylene monoimide results in different photocatalytic H₂ production performance due to the

formation of charge-transfer excitons in desired packing structure.¹⁴ These prove that molecular packing can significantly affect photocatalytic performance. However, the preferred packing may be different for each photocatalysis reaction.¹⁶ This raises the interesting potential to tune the packing mode of organic aggregate for multiple photocatalysis reactions.

Photocatalytic H₂ evolution and H₂O₂ synthesis are promising for the conversion of solar energy into storable fuels or chemicals.^{17–20} With few exceptions that designed for H₂O₂ production from pure water,¹⁹ almost all reported organic molecule-based photocatalysts are made for sacrificial H₂ production.^{1,3,5–10}

4.3. Molecular Structure and Solution-state Properties

We synthesised a small organic molecule of 2,6-bis(4-cyanophenyl)-4-(9-phenyl-9H-carbazol-3-yl)pyridine-3,5-dicarbonitrile (CN90). This is a donor-acceptor molecule bearing pyridinedicarbonitrile derivative as acceptor unit (A) and carbazole as donor unit (D) (**Figure 4.1**). The successful synthesis of CN90 was characterized by NMR, MS, and elemental analysis (**Experimental Section**).

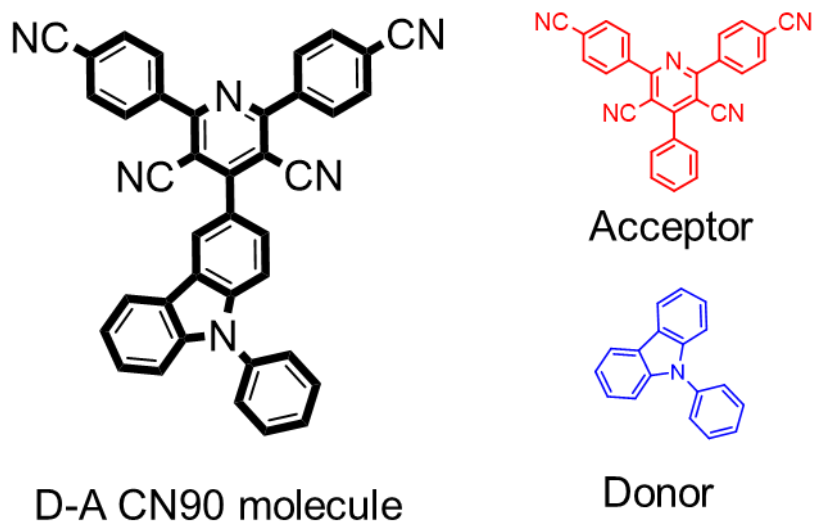


Figure 4.1. Molecular structures of CN90, acceptor, and donor molecule.

CN90 molecule in THF showed the lowest energy absorption band centred at 368 nm. However, donor and acceptor molecules in THF almost did not absorb light with wavelength longer than 350 nm. The absorption band of CN90 (368 nm) is not shown on either donor or acceptor molecule, suggesting the nature of the band is intramolecular charge transfer (I_{tra}CT) (**Figure 4.2**). Spatially separated HONTO and LUNTO orbitals indicate that the lowest energy excitation is delocalised (**Figure 4.3**). Intramolecular charge transfer from donor to acceptor

may occur when HONTO and LUNTO orbitals are spatially separated.

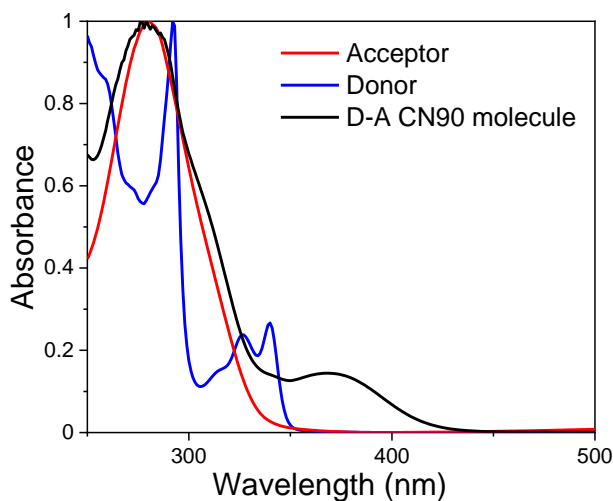


Figure 4.2. Absorption spectra of D-A CN90, acceptor, and donor molecule (20 μM) in THF.

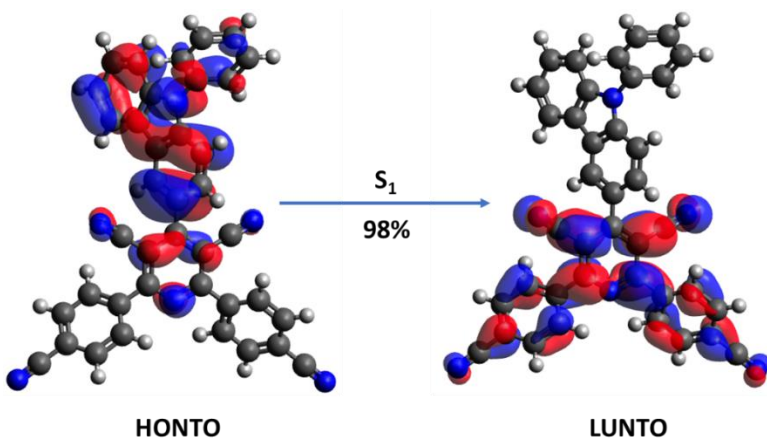


Figure 4.3. Electron density distributions of HONTO (highest occupied natural transition orbitals) and LUNTO (lowest unoccupied natural transition orbitals) calculated by time-dependent density functional theory (TD-DFT) in Gaussian 16 at the CAM-B3LYP/6-31G(d) level. Isosurface = 0.03 a.u., rendered using Avogadro. Blue N, grey C, white H. Blue: positive, red: negative isosurfaces of molecular orbitals.

Photoluminescence emission spectra of CN90 showed broad and featureless emission peaks (**Figure 4.4**), which is a common character of I_{tra}CT states.²¹ The emission spectra of CN90 experienced redshifts as solvent polarities increased (**Figure 4.4**), again consistent with the I_{tra}CT feature. The emission peak of CN90 was centred at around 530 nm in toluene but 690

nm in acetone. The CN90 emission in acetone showed two downward peaks from 400 to 500 nm, which were probably because of deviations from background subtraction. Interestingly, CN90 achieved a remarkable Stokes shift of 301 nm (**Figure 4.5**), one of the largest shifts reported.² Compared to low concentration (20 μmol), a redshift of peak was observed under high concentration (170 μmol) probably due to the overlap of absorption and emission spectra. This might also result from the aggregation of CN90 under high concentration. Analysis of the solvatochromism using the Lippert-Mataga method²² showed that CN90 has a large 14.0 Debye dipole of the excited state (**Figure 4.6**). The dipole is a measure of polarity, so the large dipole moment of CN90 is beneficial for the photogenerated charge separation.²³

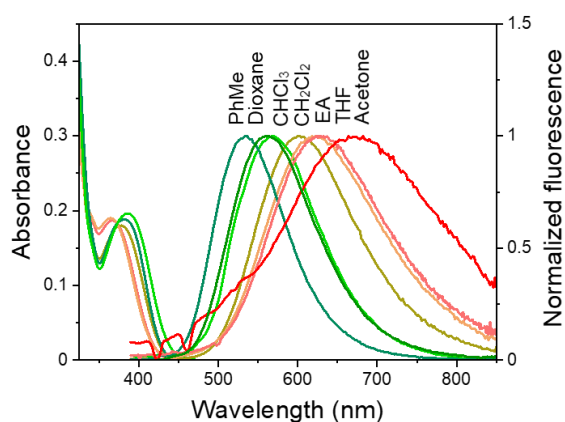


Figure 4.4. Absorption and emission spectra ($\lambda_{\text{exc}} = 375 \text{ nm}$) of CN90 (20 and 5 μM for absorption and emission measurement, respectively) in different solvents at ambient temperature.

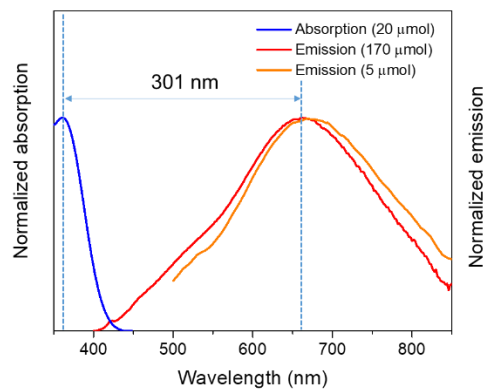


Figure 4.5. Absorption and emission spectra ($\lambda_{\text{exc}} = 375 \text{ nm}$) of CN90 in acetone with a massive Stokes shift of 301 nm.

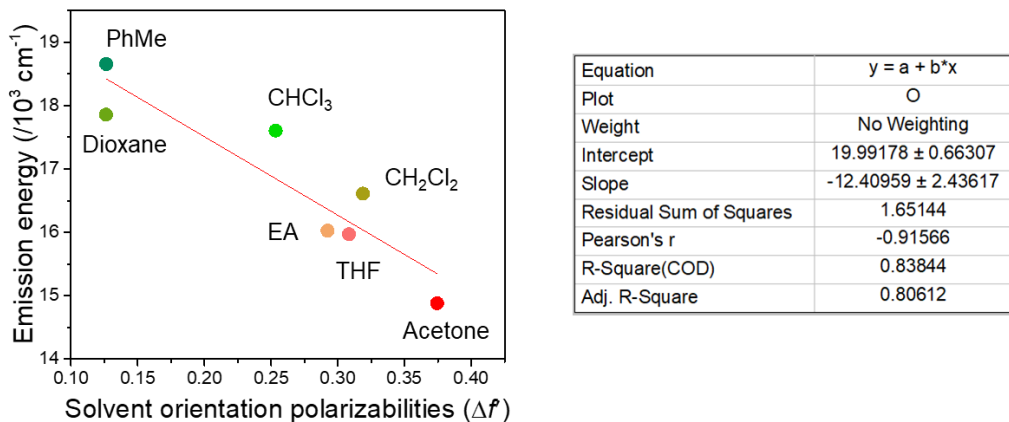


Figure 4.6. Lippert-Mataga plot of emission energy ($\bar{v}_{\max}/10^3 \text{ cm}^{-1}$) for CN90 versus solvent orientation polarizabilities ($\Delta f'$).

Lippert-Mataga equation is defined as:

$$\bar{v}_f = -\frac{-2\mu_e^2}{hca^3} \Delta f' + \bar{v}_0 \quad (4.1)$$

$$\Delta f' = \frac{\varepsilon - 1}{2\varepsilon + 1} - \frac{n^2 - 1}{4n^2 + 2} \quad (4.2)$$

Where $\Delta f'$ = Solvent orientation parameter; \bar{v}_f = Fluorescence emission maxima; μ_e = Excited state dipole moment; a = Radius of the Onsager cavity; ε = Dielectric constant; n = Refractive index.

By simplifying Equations (4.1) and (4.2), we get the following equation:

$$\mu_e = \left(\text{slope} \times \frac{hca^3}{2} \right)^{\frac{1}{2}} \quad (4.3)$$

Radius of the Onsager cavity can be obtained from:

$$a = \left(\frac{3V}{4\pi} \right)^{\frac{1}{3}} \quad (4.4)$$

Where V is the volume of the molecule in \AA^3 .

$V = 664.24 \text{ \AA}^3$ (volume of CN90 is calculated by using B97D3/def2svp method in Gaussian16)

Slope = 12409.59 cm^{-1}

Combining Equations (4.3) and (4.4), we obtain the excited state dipole moment of CN90 ($\mu_e = 14.0 \text{ Debye}$).

4.4. Nanoparticles

4.4.1. Morphology

Nanoparticles of CN90 were prepared using the nanoprecipitation method by injecting THF solution of CN90 into H₂O with variable THF/H₂O ratios (**Figure 4.7**).²⁴ A pale yellow suspension was obtained at THF/H₂O ratio of 1%, whereas increasing the ratio to 10% resulted in an orange suspension (**Figure 4.8**). Scanning electron microscopy (SEM) images disclosed that particles in pale yellow and orange solutions had nanosphere and nanofibre morphologies, respectively (**Figure 4.8**). Therefore, nanospheres were formed at low THF/H₂O ratio, whereas nanofibres were formed at high THF/H₂O ratio. The nanospheres had smooth surface and high morphology purities, and the average diameter of nanospheres was estimated to be around 100 nm (**Figure 4.9**). Nanofibres had a width of around 40 nm (**Figure 4.8**), but the length of nanofibres was not uniform ranging from 400 to 1000 nm.

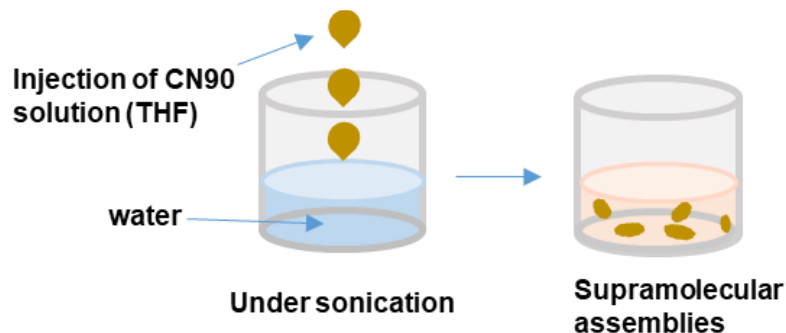


Figure 4.7. Synthesis diagram of CN90 nanoparticles.

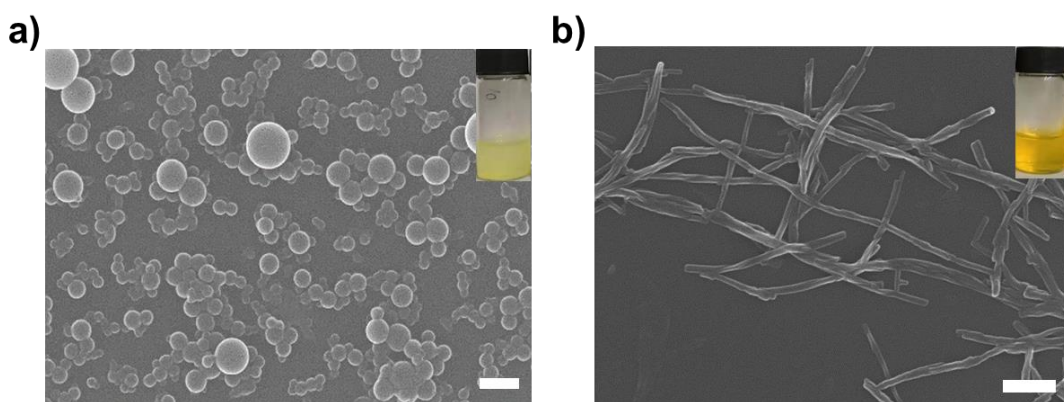


Figure 4.8. **a)** SEM images of CN90-s; inset picture is CN90-s aqueous suspension (scale bar = 300 nm). **b)** SEM images of CN90-f; inset picture is CN90-f aqueous suspension (scale bar = 200 nm).

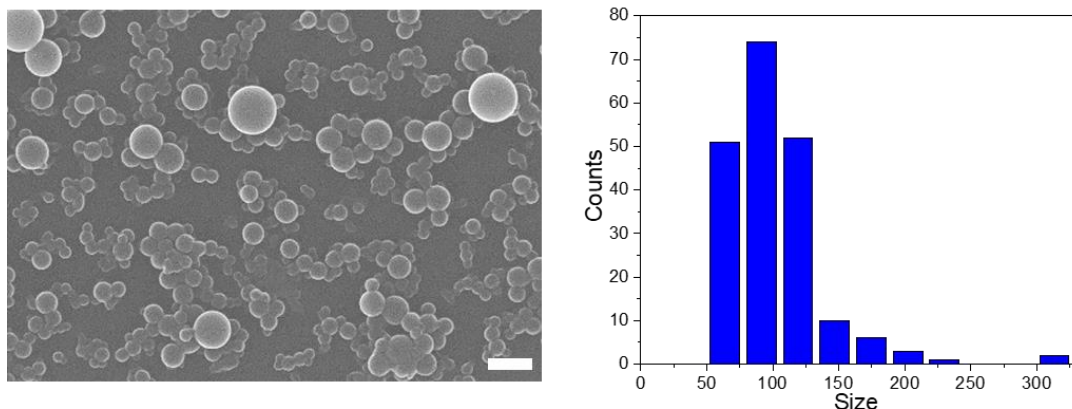


Figure 4.9. Statistic analysis of 200 nanospheres in SEM image (scale bar = 300 nm) of CN90-s.

4.4.2. Structure

CN90-s (nanospheres) did not show noticeable diffraction peaks from the Powder X-ray diffraction (PXRD) pattern (**Figure 4.10**), indicating an amorphous state of CN90-s. PXRD pattern of CN90-f (nanofibres) displayed typical π - π stacking peak centred at 23.8° and peak at the small angle, indicating the presence of π - π stacking and limited long-range structural order in CN90-f (**Figure 4.10**).

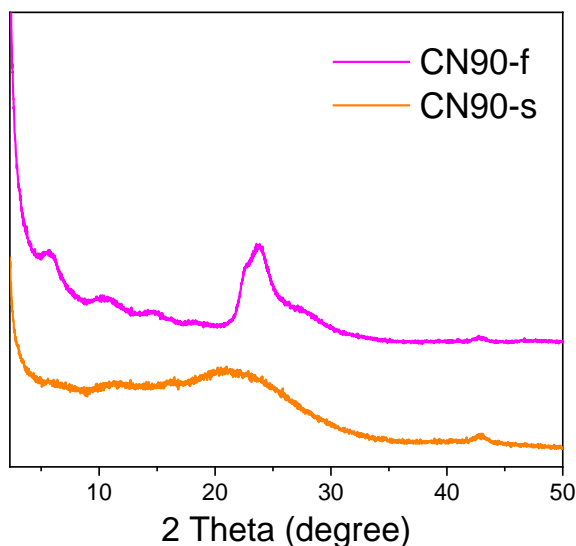


Figure 4.10. PXRD pattern of CN90-s and CN90-f.

To gain further insight into the packing of CN90 in CN90-f, we grew single crystals from two

different conditions (**Figure 4.11**). CN90-f had similar yellow colour to crystal 1. By contrast, crystal 2 showed organic colour, which was similar to the colour of CN90-f obtained from filtration.



Figure 4.11. Pictures of crystal 1, CN90-s, CN90-f, and crystal 2 in solid-state.

Initially, we sublimed CN90 at 683 K under dynamic vacuum and obtained crystals with orthorhombic $P2_12_12_1$ (**Figure 4.12 and Table 4.1**). In the $P2_12_12_1$ structure, the adjoining aromatics of the D and A unit twist by $\sim 71^\circ$, preventing CN90 molecules from forming aligned stacks. Instead, CN90 intertwines along the a -axis, with π - π interactions at a distance of ~ 4.3 Å evident between D-A and A-A parts of adjacent CN90 molecules. The stacks of twisted intertwined CN90 molecules are then held together by a network of $C\equiv N \cdots H-C(\text{aryl})$ interactions at distances of around 2.7 Å. We also grew crystals of a triclinic $P\bar{1}$ CN90 phase from a chloroform/toluene mixture solution (**Figure 4.13 and Table 4.1**). In the $P\bar{1}$ structure, the adjoining aromatics of the D and A units only twist by $\sim 37^\circ$, and the CN90 molecules instead pack in an eclipsed arrangement along the a -axis. The repeat distance between the CN90 molecules in the stacks is 3.8 Å, indicating strong π - π interactions exist. There is a zig-zag 1-D network of CN90 molecules that interact through $C\equiv N \cdots H-C(\text{aryl})$ motifs in the extended crystal structure, which instead of being close-packed, pack in an offset arrangement. The packing of CN90 molecules creates a sizeable solvent-filled void that occupies 29% of the crystal structure using a probe radii of 1.2 Å.

Table 4.1. Crystal data of two phases.

	CN90 $P2_12_12_1$ Phase	CN90 $P\bar{1}$ Phase
Crystallisation Conditions	Sublimations at 683 K under dynamic vacuum.	Evaporation of chloroform/toluene mixture solution
Space Group	$P2_12_12_1$	$P\bar{1}$
Wavelength [Å]	Mo-K α	Mo-K α
Collection Temperature	100 K	100 K
Formula	$C_{39}H_{20}N_6$	$C_{39}H_{20}N_6$
M_r	572.61	572.61
Crystal Size (mm)	$0.23 \times 0.10 \times 0.10$	$0.11 \times 0.03 \times 0.01$
Crystal System	Orthorhombic	Triclinic
a [Å]	7.2777(2)	3.8191(3)
b [Å]	15.9020(5)	23.476(2)
c [Å]	24.7232(7)	24.8757(18)
α [°]	90	97.255(7)
β [°]	90	90.834(6)
γ [°]	90	93.943(7)
V [Å 3]	2861.22(14)	2206.6(3)
Z	4	2
D_{calcd} [g cm $^{-3}$]	1.329	0.862
μ [mm $^{-1}$]	0.081	0.052
$F(000)$	1184	592
2 θ range [°]	3.29 – 62.49	3.54 – 52.84
Reflections collected	21104	11066
Independent reflections, R_{int}	7632, 0.0289	6433, 0.0614
Obs. Data [$I > 2\sigma$]	6713	4266
Data / restraints / parameters	7632 / 0 / 406	6433 / 270 / 406
Final R1 values ($I > 2\sigma(I)$)	0.0390	0.1570
Final R1 values (all data)	0.0470	0.1912
Final wR(F^2) values (all data)	0.0988	0.3958
Goodness-of-fit on F^2	1.048	1.080
Largest difference peak and hole [e.Å $^{-3}$]	0.393 / -0.259	0.622 / -0.555
CCDC		

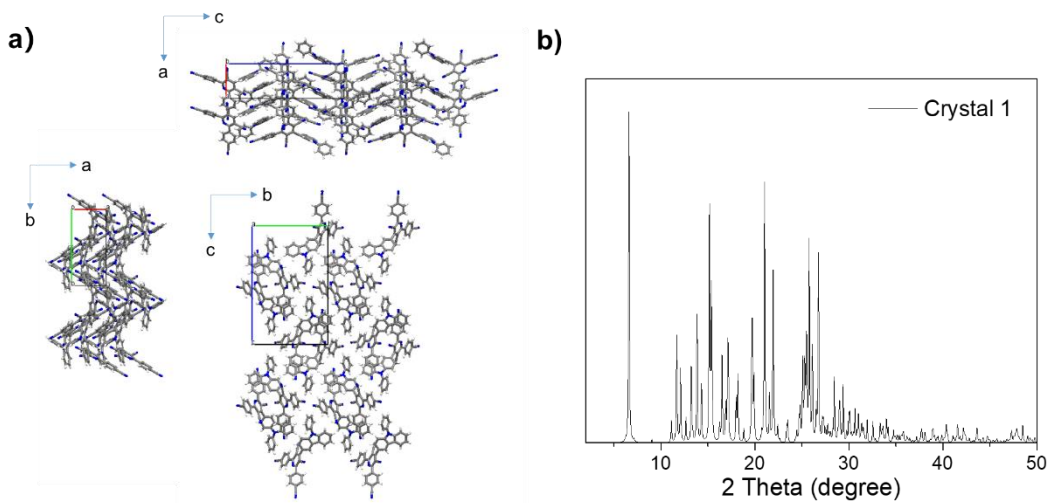


Figure 4.12. **a)** Structure of crystal 1 obtained from solvent evaporation (grey, C; blue, N; white, H). **b)** Simulated PXRD pattern of crystal 1.

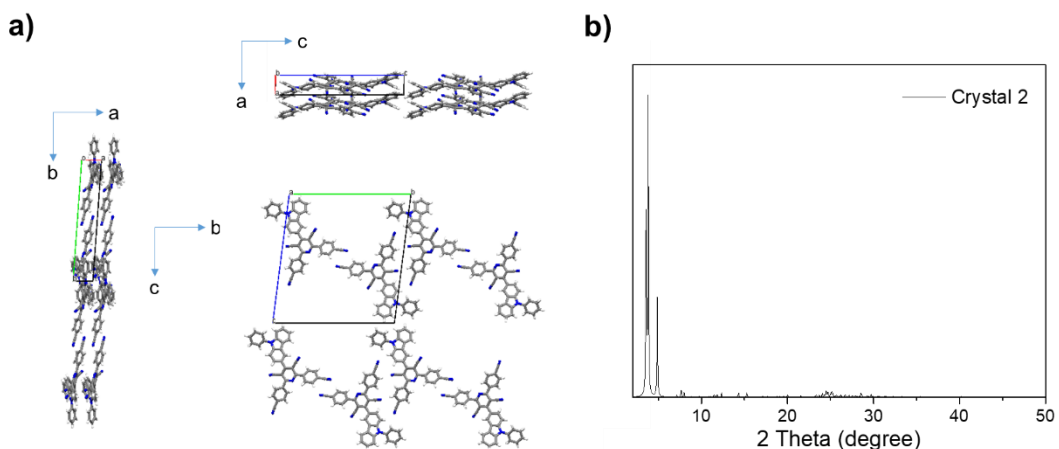


Figure 4.13. **a)** Structure of crystal 2 obtained from solvent evaporation (grey, C; blue, N; white, H). **b)** Simulated PXRD pattern of crystal 2.

The PXRD pattern of CN90-f showed a distinct feature corresponding to *d*-spacings of 3.7-3.9 Å, which would be consistent with layered structures with a similar interlayer spacing to Crystal 2. Raman spectra revealed that CN90-f and crystal 2 had similar Raman shift profiles, as opposed to CN90-s and crystal 1. Two stretching vibration peaks from cyano-group (around 2230 cm^{-1}) were observed on CN90-f, indicating a distinct environment for cyano-group, like that observed in crystal 2, but only one stretching vibration of cyano-group was observed in CN90-s and crystal 1 (**Figure 4.14**). In addition, as shown in (**Figures 4.15**), CN90-f and crystal 2 had similar UV-vis absorption profiles in solid-state, in contrast with CN90-s and

crystal 1. Thus, based on the above results, we reason that the structure of CN90-f is composed of a similar molecular π - π packing as crystal 2 (**Figure 4.16**).

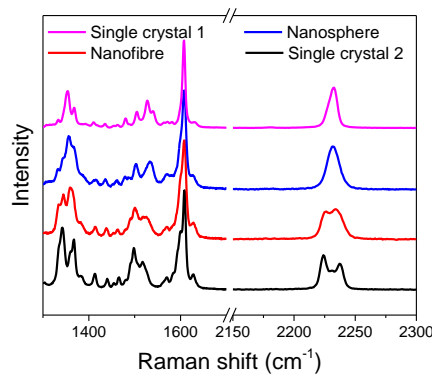


Figure 4.14. Raman spectra of two single crystals, CN90-s, and CN90-f (785 nm laser).

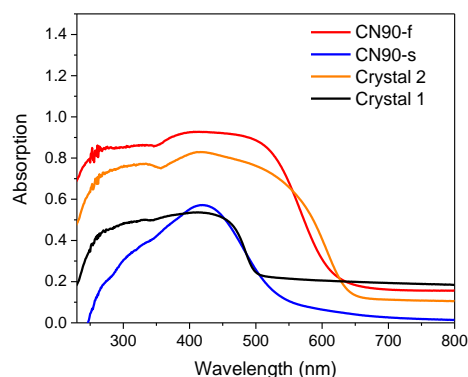


Figure 4.15. Absorption spectra of CN90-f, CN90-s, crystal 1, and crystal 2 in solid-state at room temperature.

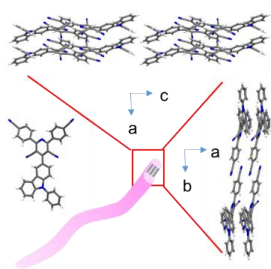


Figure 4.16. Schematic representation of CN90-f nanostructure including two side views extracted from single crystal 2. Grey, carbon; blue, nitrogen; white, hydrogen.

4.4.3. Absorption and Emission

Figure 4.17 was the UV-vis spectra of CN90 nanoparticles in H₂O after removing THF by heating. In CN90-f, the lowest energy absorption band redshifted to 412 nm, which could be attributed to the intermolecular π-π interaction. The emission of CN90-f (650 nm) was also redshifted by 70 nm compared with CN90-s (**Figure 4.17**). The weaker emission intensity of CN90-f compared to CN90-s could be attributed to quenching induced by intermolecular π-π stacking interaction²⁵ and energy gap law.²⁶

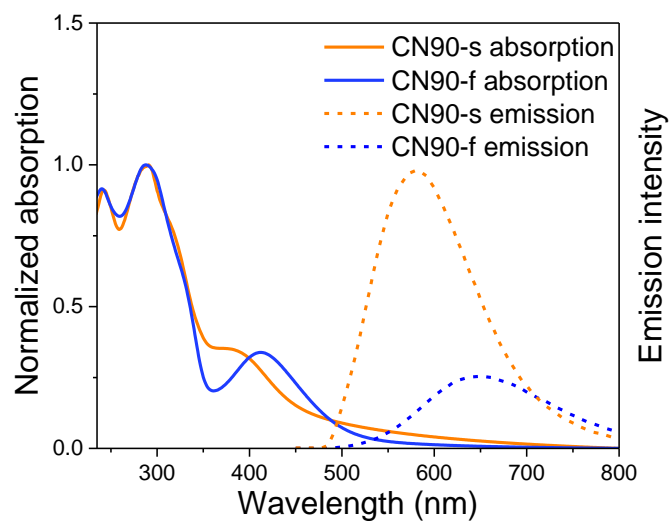


Figure 4.17. Absorption and emission spectra ($\lambda_{\text{exc}} = 390 \text{ nm}$) of CN90-s and CN90-f in water. Measurements were carried out at room temperature.

The removal of THF did not alter the size and morphology of the nanoparticles as shown in SEM images (**Figures 4.18 and 4.19**). Nanospheres had similar size and morphology profiles before and after removing THF when THF to H₂O ratio was lower than 1/25. No significant change was observed in morphology of nanofibres when THF to H₂O ratio was higher than 1/10. CN90-s showed a similar UV-vis absorption profile to that of CN90 molecule in THF solution, indicating that I_{tra}CT was the dominant excitation state in CN90-s (**Figure 4.20**). It may be reasonable that CN90-s nanoparticles in an amorphous state have a similar optical property to the CN90 molecule in the solution state.

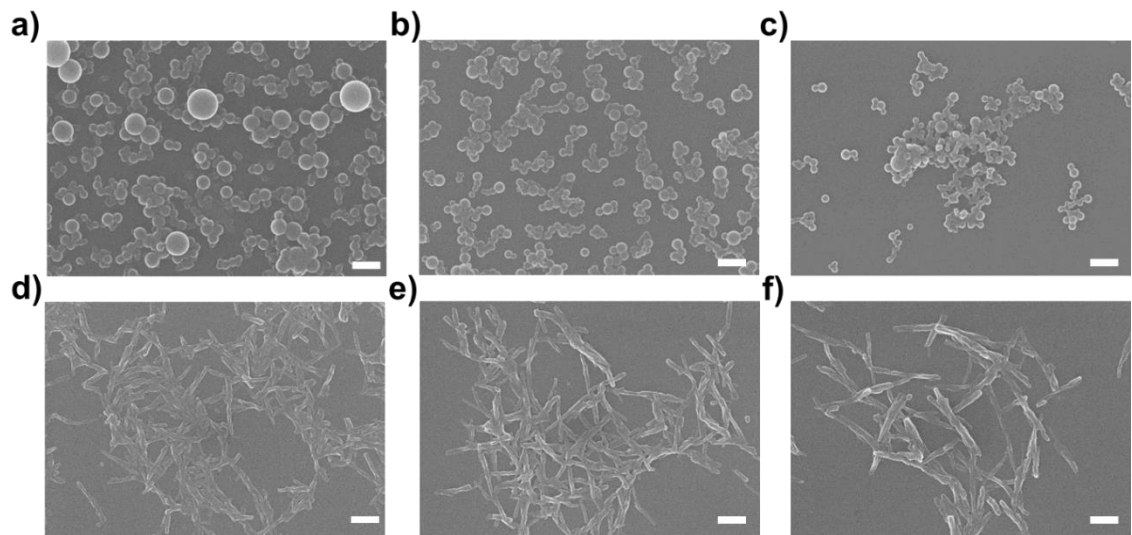


Figure 4.18. SEM images of nanospheres prepared when THF fraction is (a) 1/100, (b) 1/50, and (c) 1/25. SEM images of nanofibres prepared when THF fraction is (d) 1/10, (e) 1/5, and (f) 2/5. Scale bars = 300 nm. These are pristine samples without removing THF.

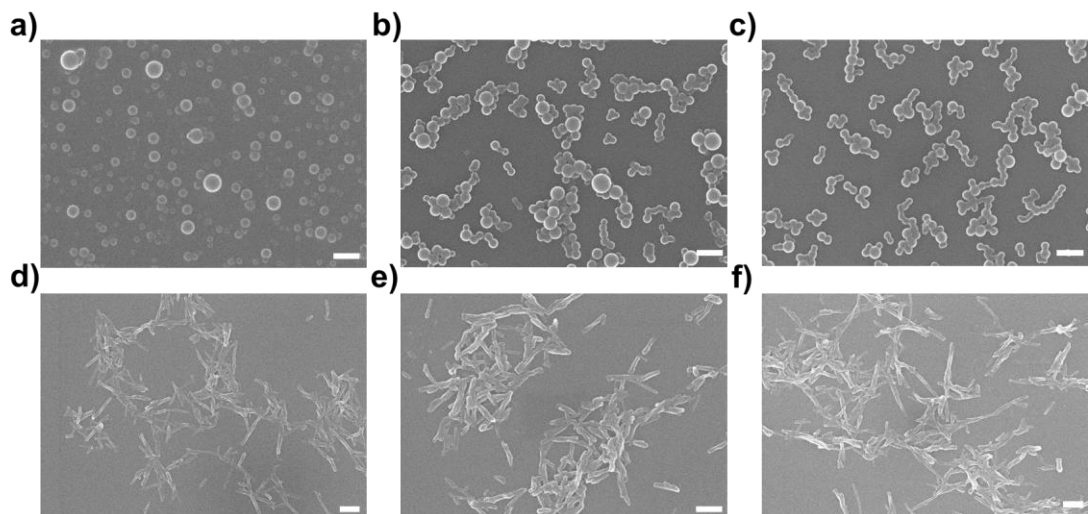


Figure 4.19. SEM images of nanospheres prepared when THF fraction is (a) 1/100, (b) 1/50, and (c) 1/25. SEM images of nanofibres prepared when THF fraction is (d) 1/10, (e) 1/5, and (f) 2/5. Scale bars = 300 nm. These are samples after removing THF.

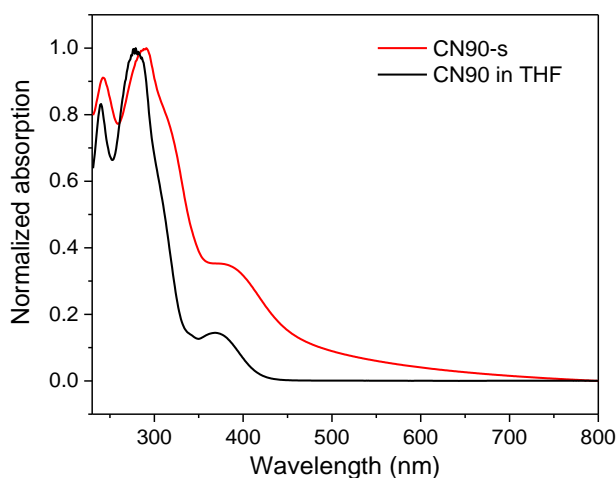


Figure 4.20. Absorption spectra of CN90-s in H_2O and CN90 in THF at ambient temperature. (368 nm for I_{tra}CT band of CN90 molecule in THF *versus* 374 nm for I_{tra}CT band of CN90-s in H_2O).

4.4.4. Morphology Transformation

It was observed that nanospheres transformed into nanofibres over time, which depended on THF/ H_2O ratio (**Figure 4.21**). Nanospheres formed first and then transformed to nanofibres in few days at THF/ H_2O ratio of 1/25. A much quicker transformation (around 30 min aging) was observed with THF/ H_2O ratio of 1/10 (**Figure 4.22**). THF/ H_2O ratio lower than 1/25 resulted in the formation of stable nanospheres in a month, while THF/ H_2O ratio higher than 1/10 immediately led to the formation of nanofibres. Adding THF into the nanosphere aqueous suspension also promoted the transformation to nanofibres (**Figure 4.23**). However, adding water into nanofibres suspension did not observe the transformation from nanofibres to nanospheres.

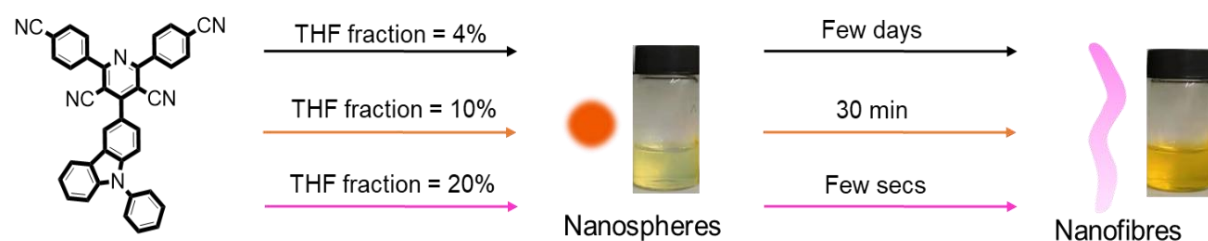


Figure 4.21. Schematic representation of morphology transformation.

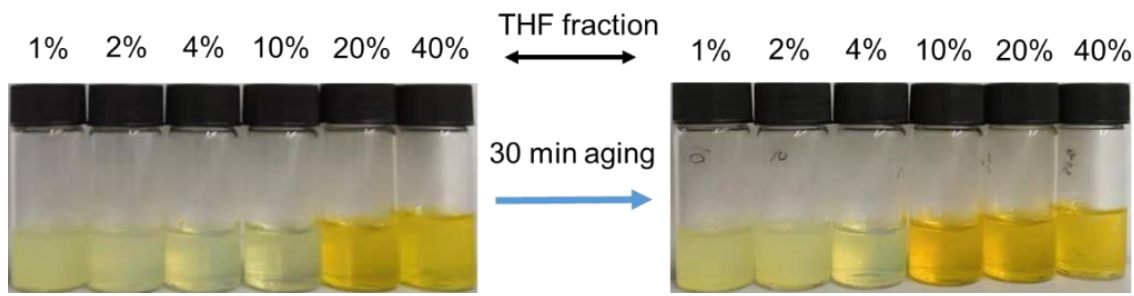


Figure 4.22. Pictures of as-prepared nanoparticles in THF/H₂O mixture solution and the color change after 30 min aging time. THF/H₂O (5 mL of H₂O) from left to right hand side is 1%, 2%, 4%, 10%, 20%, and 40%, respectively.

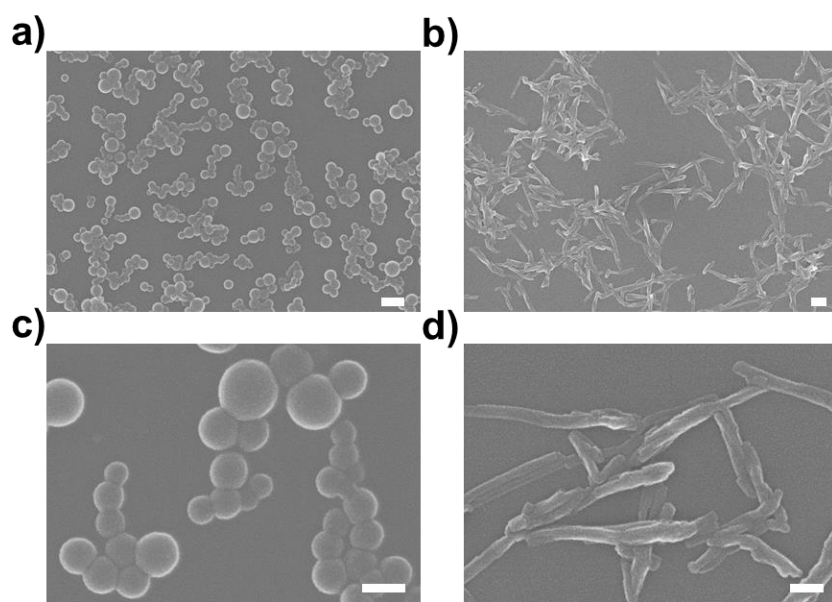


Figure 4.23. **a)** SEM image of nanospheres prepared when THF fraction 2% under low magnification. Scale bars = 200 nm. **b)** Nanofibres after morphology transformation by adding 0.9 mL of THF under low magnification. Scale bars = 200 nm. **c)** SEM image of nanospheres prepared when THF fraction 2% under high magnification. Scale bars = 100 nm. **d)** Nanofibres after morphology transformation by adding 0.9 mL of THF under high magnification. Scale bars = 100 nm.

In-situ UV-vis absorption spectra of CN90 nanoparticle evolution process showed that I_{tra}CT band was initially formed (peaking at around 377 nm) and subjected to gradually increasing redshift with increasing aging time (**Figure 4.24**). A new band originating from I_{ter}CT appeared at about 408 nm gradually became dominant at the expense of I_{tra}CT band. This suggested that the main interaction force of the transformation from nanospheres to nanofibres was the intermolecular π - π interaction of CN90-f. The appearance of the isobestic point at 392 nm

during the nanoparticle evolution process indicated a stoichiometric conversion from nanosphere to nanofibre structure. Moreover, the growth of CN90-f occurred after a lag time and exhibited a nonlinear sigmoidal transition (inset figure of **Figure 4.24**), suggesting that transformation included two kinetics (nucleation of seeded nanospheres and elongation of nanofibres).²⁷

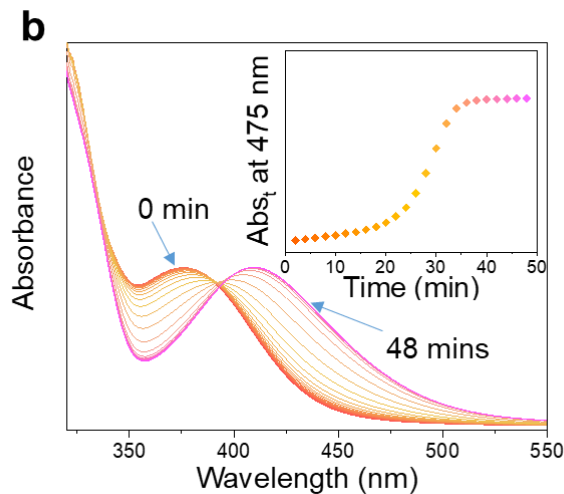


Figure 4.24. UV/Vis Absorption spectra of CN90-f ($\text{THF}/\text{H}_2\text{O} = 10\%$) growth process (recorded every 2 min); inset figure shows the kinetics of CN90-f growth process (absorbance at 475 nm). Measurement was carried out at ambient temperature. Start point: orange colour; end point: purple colour.

In-situ emission spectra of the transformation process showed the bathochromic shifted emission peak maxima along with the reduced intensity over evolution (**Figure 4.25**). The starting and ending points were consistent with the emission of CN90-s and CN90-f in water dispersion. **Figure 4.26** was the in-situ time-resolved single photon counting (TRSPC) experiments. The early stage of the nanosphere had a dominant PL lifetime of around 135 ns. The proportion of this slow decay component gradually decreased from ~70% to ~33% during 36 min aging time (**Figures 4.26 and 4.27**), then, a newly appeared fast decay component (around 6 ns) became more substantial with the evolution of structure into nanofibres (**Figures 4.26 and 4.27**). This showed that the excited state of CN90 nanoparticles was determined by their molecular packing in aggregates. Moreover, in early stage of CN90 assembly, nanoparticles exhibited double-exponential decay (**Figures 4.26 and 4.27**). However, the decay curves did not agree with the double-exponential decay model in later stage but were described well by a triple-exponential decay model. The newly appeared fast decay component

(around 6 ns) was more substantial in the later stage confirming that more emission came from the I_{ter}CT, suggesting the transformation from I_{tra}CT to I_{ter}CT during self-assembly process.

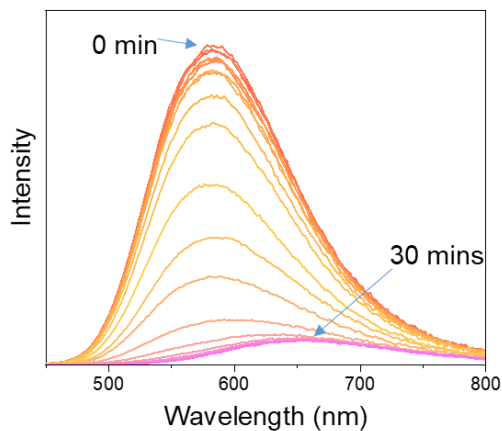


Figure 4.25. Emission spectrum of CN90-f (THF/H₂O = 10%) growth process with $\lambda_{\text{exc}} = 390$ nm (recorded every 1.5 min). Measurement was carried out at ambient temperature. Start point: orange colour; end point: purple colour.

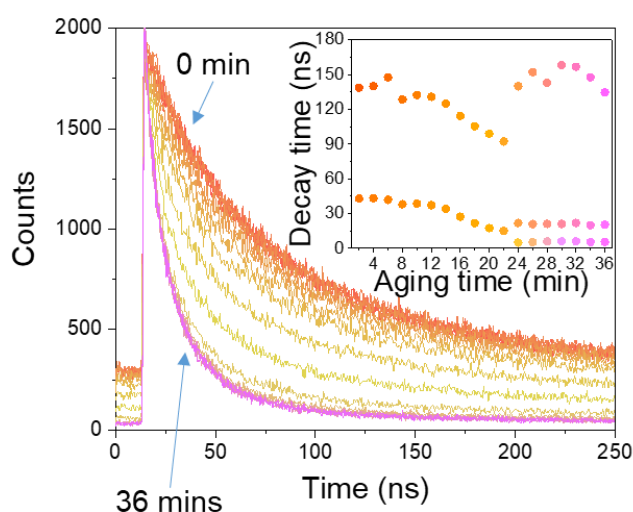


Figure 4.26. TRSPC Decays of CN90-f (THF/H₂O = 10%) growth process monitored at 670 nm emission under 405 nm laser excitation (recorded every 2 min); inset figure shows decay components changes during 36 min aging time. Measurement was carried out at ambient temperature. Start point: orange colour; end point: purple colour.

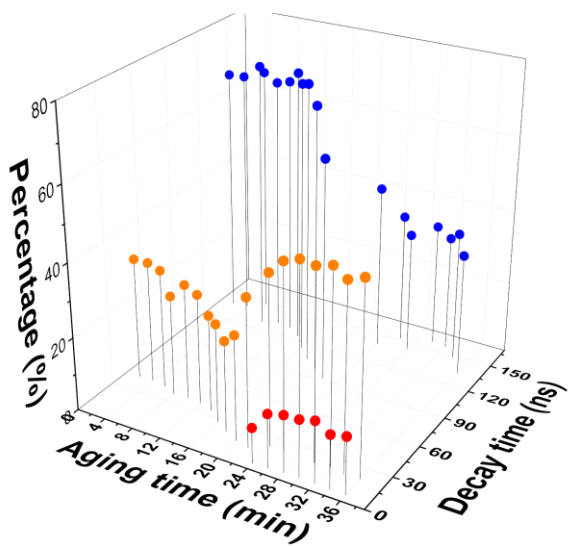


Figure 4.27. The proportion of decay components during 36 min aging time. Three types of decay components (fast: red; medium: orange; slow: blue).

4.5. Photocatalysis Measurement

CN90 nanofibres showed significantly higher HER than CN90 nanospheres under 1 sun illumination (wavelength: 350 nm-1000 nm) (**Figures 4.28 and 4.29**). CN90-f (31.85 mmol g⁻¹ h⁻¹) showed a more than 72 times higher hydrogen production rate (HER) than CN90-s (0.44 mmol g⁻¹ h⁻¹). On the other hand, CN90-s generated H₂O₂ at a high production rate of 3.56 mmol g⁻¹ h⁻¹ from pure water, but its counterpart, CN90-f, is inactive for H₂O₂ production (**Figure 4.28**).

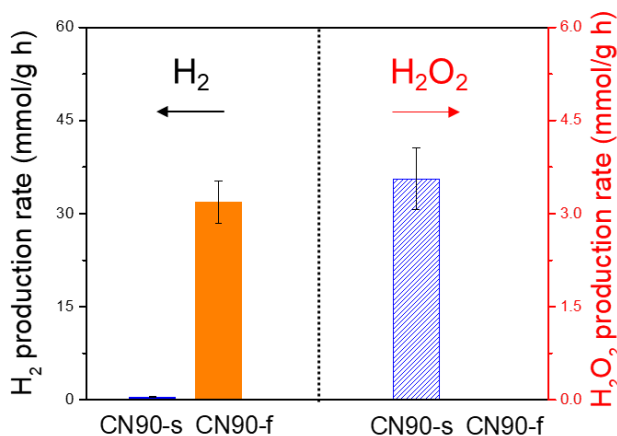


Figure 4.28. Photocatalytic H₂ (left) and H₂O₂ (right) production activities of CN90-s and CN90-f (0.5 mg catalyst in 5 mL water; light source = solar simulator, 1 sun; irradiation time

= 1 hour). Condition for H₂ production: degassing with N₂; ascorbic acid (0.04 M); Pt loading: 3 wt. %. Condition for H₂O₂ production: degassing with O₂.

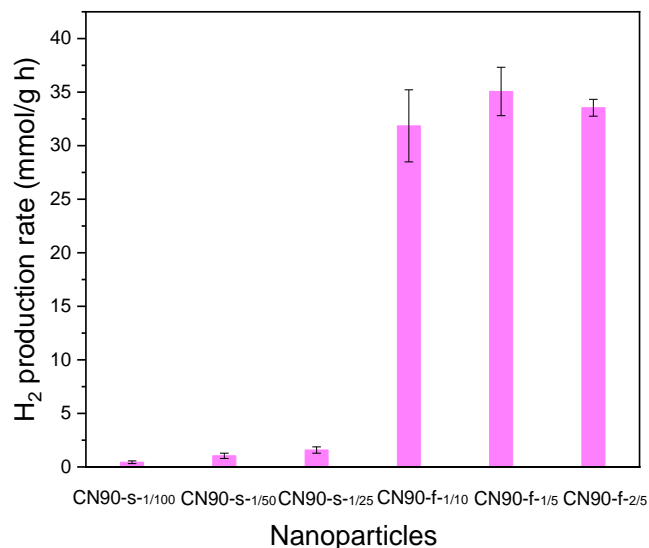


Figure 4.29. Sacrificial photocatalytic hydrogen production activities for CN90 nanospheres and nanofibres under irradiation by solar simulator. Testing conditions: catalyst concentration = 0.1 mg mL⁻¹ (0.5 mg in 5 mL water); ascorbic acid (0.04 M); Pt loading: 3 wt. % using a stock solution of H₂PtCl₆, 8 wt. % in water; light source = solar simulator, 1 sun; irradiation time = 1 hour. In CN90-s-x and CN90-f-x, x is THF to H₂O volume ratio when using nanoprecipitation method to prepare nanoparticles.

4.5.1. Photocatalytic Hydrogen Evolution

Kinetic hydrogen evolution measurements under visible light irradiation (> 420 nm) showed that CN90-f afforded an average HER of 11.7 mmol g⁻¹ h⁻¹, with no reduction in activity observed during 34 hours of photoreaction (**Figure 4.30**). The generated H₂ after 22 hours irradiation is 644.5 µmol for CN90-f, which is more than 17.5 times higher than CN90-s (36.7 µmol). The apparent quantum yields (AQYs) for CN90 were determined to be 2.86% at 490 nm, 4.97% at 420 nm, 4.20% at 405 nm, and 3.86% at 395 nm, broadly following the absorption spectrum of CN90-f suggesting that the hydrogen generation is a photocatalytic process (**Figure 4.31**).

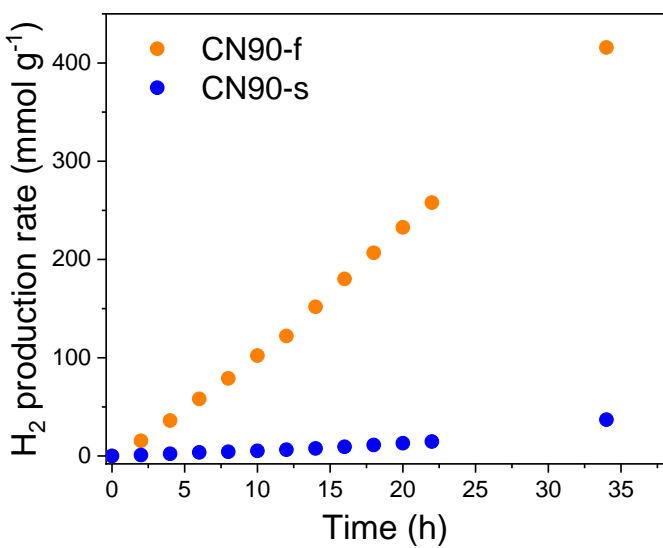


Figure 4.30. Time course of H_2 production for CN90-s and CN90-f, irradiated by 300 W Xe lamp fitted with a $\lambda > 420$ nm filter using 2.5 mg of the catalyst. Testing condition: 2.5 mg catalyst in 25 mL water; ascorbic acid (0.1 M); Pt loading: 3 wt. %.

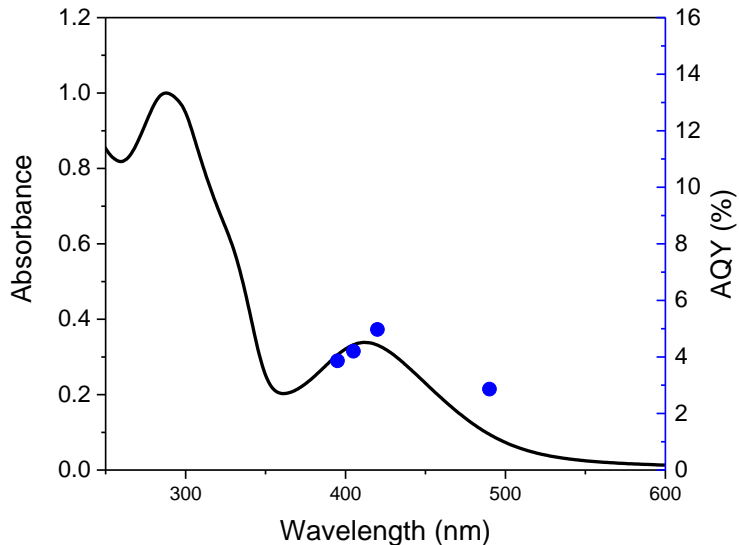


Figure 4.31. UV-vis spectrum and AQYs of CN90-f (with NaBr) measured with monochromatic LED light at 395, 405, 420, and 490 nm, respectively (intensity rescaled for clarity).

4.5.2. Photocatalytic Hydrogen Peroxide Evolution

The H_2O_2 production of CN90-s over time showed an average rate of $281.4 \mu\text{mol g}^{-1} \text{ h}^{-1}$ in 14

hours under visible light irradiation in pure water (**Figure 4.32**). **Table 4.2 and 4.3** is the summary of the reported photocatalytic H₂O₂ and H₂ production performances on selected organic photocatalysts. It was revealed that the CN90-s and CN90-f is one of the most efficient molecular photocatalysts, respectively, compared to its corresponding counterpart.

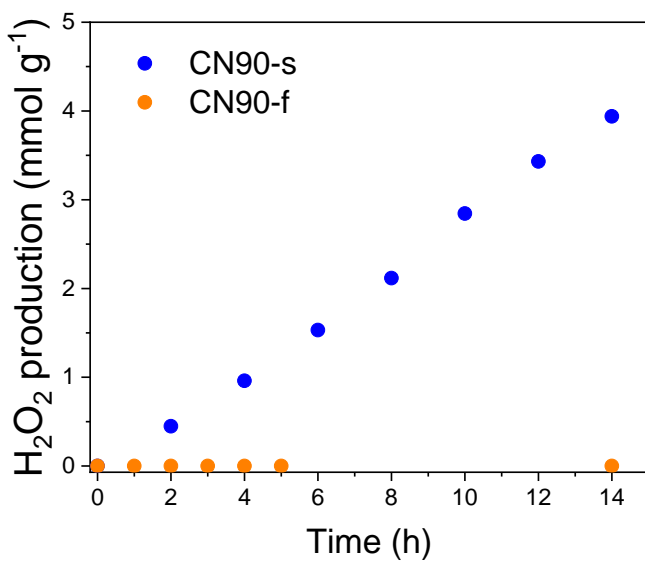


Figure 4.32. Time course of H₂O₂ production for CN90-s and CN90-f, irradiated by 300 W Xe lamp fitted with a $\lambda > 420$ nm filter using 5 mg of the catalyst in O₂ environment (around 30 mL H₂O).

Table 4.2. Photocatalytic H₂ production performance of various reported molecular photocatalysts. Note that the HER and AQY depend on the irradiation source and experimental set-up, and hence these values can only be compared in a qualitative sense.

Materials	HER (mmol g ⁻¹ h ⁻¹) or amount of H ₂ produced (μL)	AQY for HER	Co-catalysts	Journal and publication year	Reference
THPP nanorods	19.5 mmol g ⁻¹ h ⁻¹ ($\lambda > 420$ nm)		Pt 5%	<i>Nano Lett.</i> 2018	⁵
SQAP-C4 nanobelts	1.93 mmol g ⁻¹ h ⁻¹ ($\lambda > 400$ nm)		Pt 1%	<i>J. Mater. Chem.</i> 2020	⁹
P-PMPDI nanobelts	11.7 mmol g ⁻¹ h ⁻¹ ($\lambda > 400$ nm)	2.06% (420 nm)	Pt 3%	<i>Chem. Commun.</i> 2019	⁷
2CzPN	4.59 mmol g ⁻¹ h ⁻¹ ($\lambda > 420$ nm)	7.5% (420 nm)	Pt 1%	<i>Chemsuschem.</i> 2019	³
Fluorescein nanosheet	0.34 mmol g ⁻¹ h ⁻¹ ($\lambda > 420$ nm)	1.2% (420 nm)	Pt 1%	<i>Sci China Mater.</i> 2018	²⁸

TBAP- α	3.1 mmol g ⁻¹ h ⁻¹ ($\lambda > 420$ nm)	Pt 1%	<i>J. Mater. Chem. A</i> , 2020	29
SA-TCPP	0.07 mmol g ⁻¹ h ⁻¹ (full spectrum)	Pt 5% for HER	<i>Adv. Mater.</i> 2019	1
RhB-C18	3.7 mmol g ⁻¹ h ⁻¹ ($\lambda > 360$ nm)	0.059 (longpass filter (525 nm))	Pt	<i>Chem. Sci.</i> 2020
T3-PMI	0.52 μ mol h ⁻¹ ($\lambda = 400\text{-}700$ nm)		Mo ₃ S ₁₃ ²⁻	<i>J. Am. Chem. Soc.</i> 2017
CA-PDDA	0.29 μ mol h ⁻¹ ($\lambda = 400\text{-}700$ nm)		Ni	<i>Nat. Chem.</i> 2014
CA-PDDA-L5	0.37 μ mol h ⁻¹		Ni	<i>J. Am. Chem. Soc.</i> 2015
CN90-f	11.7 mmol g ⁻¹ h ⁻¹ or 29.29 μ mol h ⁻¹ ($\lambda > 420$ nm)	4.97% (420 nm)	Pt 3%	This work

Table 4.3. Photocatalytic H₂O₂ performance of various reported organic molecule-based catalysts in pure water. Note that the H₂O₂ production rate and concentration depend on the irradiation source and experimental set-up, and hence these values can only be compared in a qualitative sense.

Materials	Light source	H ₂ O ₂ production rate / (μ mol g ⁻¹ h ⁻¹)	H ₂ O ₂ concentration/ (μ M)	Journal and publication year	Reference
g-C ₃ N ₄ /PDI	Xe lamp ($\lambda > 420$ nm)	20.5 - 23.5		<i>Angew. Chem.</i> 2014	32
g-C ₃ N ₄ /PDI/rGO	Xe lamp ($\lambda > 420$ nm)	20.5 - 23.5		<i>J. Am. Chem. Soc.</i> 2016	33
Biscoumarin-containing acenes film	White LED (30 mW cm ⁻²)	~ 97		<i>J. Mater. Chem. A</i> , 2017	34
NDI-G	White LED (120 mW cm ⁻²)		~ 150 (4 hours)	<i>Adv. Sustainable Syst.</i> 2019	35
QNC-S	White LED (105 mW cm ⁻²)		~ 60 (4 hours)	<i>Adv. Sustainable Syst.</i> 2019	35
Epindolidione colloidal nanoparticles	White LED (105 mW cm ⁻²)		~ 70 (5 hours)	<i>ACS Appl. Mater. Interfaces.</i> 2018	36
CN90-s	Xe lamp ($\lambda > 420$ nm)	281	159.9 (4 hours) 656.6 (14 hours)	This work	
CN90-s	Solar simulator (1 sun)	3560	356 (1 hour)	This work	

We then investigated the mechanism of H₂O₂ production on CN90-s. Adding electron scavenger (AgNO₃) leads to a sharp decrease in H₂O₂ production rate, and hole scavenger (ascorbic acid, AA) was found to significantly boost H₂O₂ production (**Figure 4.33**). No obvious influence on H₂O₂ production was observed by using tert-butyl alcohol (TBA), a ·OH

capturer, which indicates that ·OH did not participate in the H₂O₂ production reaction. However, the use of 1,4-benzoquinone (BQ), a ·O₂⁻ capturer, almost quenched H₂O₂ production, suggesting that the ·O₂⁻ is essential for H₂O₂ production. Also, increasing the concentration of O₂ in reactor lead to an increased H₂O₂ production rate (**Figure 4.33**). Based on the above control experiments, we concluded that H₂O₂ is produced via stepwise two-electron oxygen reduction (O₂ → ·O₂⁻ → H₂O₂).

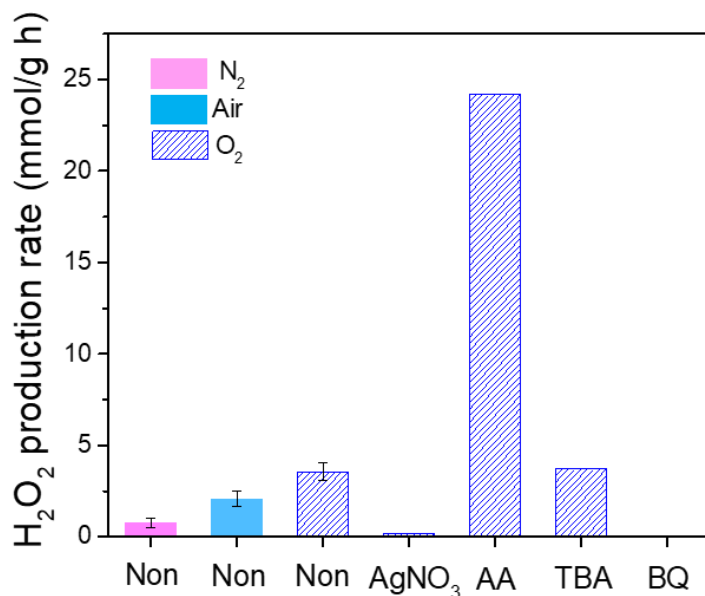


Figure 4.33. Photocatalytic H₂O₂ production activities of CN90-s in different gas environments and, upon the addition of different sacrificial agents (10 mM) in O₂ environment. Conditions: 0.5 mg catalyst in 5 mL water; light source = solar simulator, 1 sun; irradiation time = 1 hour.

Photocatalytic water oxidation showed that CN90-s can oxidize H₂O to O₂ in the presence of electron scavenger AgNO₃ (**Figure 4.34**), supporting the proposed mechanism. Nitrogen production was also observed in photocatalytic water oxidation process probably because of the decomposition (self-oxidation) of CN90-s. The electronic energy levels of CN90-s and CN90-f were estimated by combining Mott-Schottky analysis (**Figures 4.35**) and Tauc plots (**Figure 4.36**). The conduction band potential (E_{CB}) was estimated by Mott-Schottky analysis and bandgap (E_g) was obtained from Tauc plots. The valence band potentials (E_{VB}) of CN90-s and CN90-f were calculated via the equation of E_{VB} = E_{CB} + E_g. Both CN90-s and CN90-f are thermodynamically feasible for water reduction, oxygen reduction, and water oxidation reactions (**Figure 4.37**).

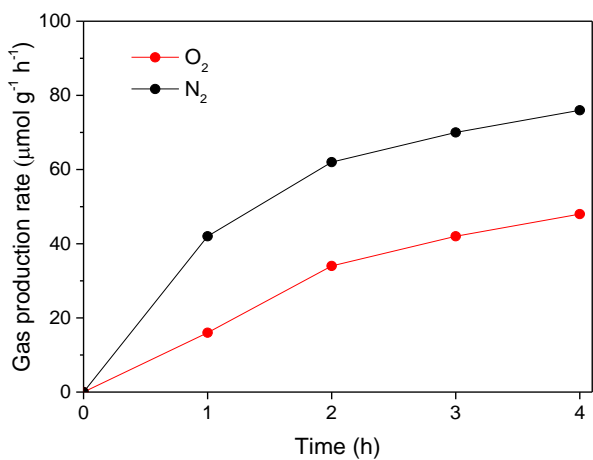


Figure 4.34. Photocatalytic water oxidation of CN90-s under vacuum. Test conditions: catalysts: 50 mg in 100 mL water; AgNO_3 (10 mM); La_2O_3 (0.2 g); temperature: 12 °C; light source: 300 W Xe lamp fitted with a $\lambda > 420$ nm filter.

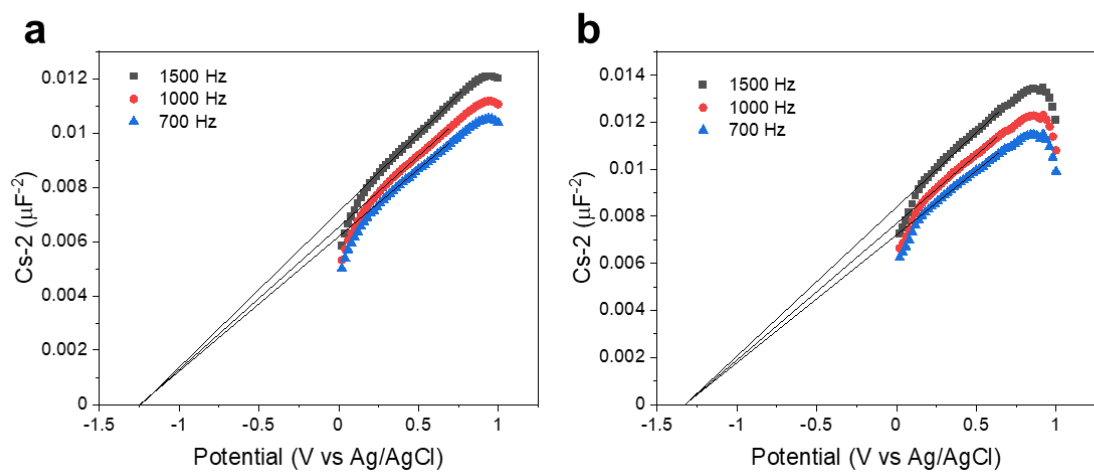


Figure 4.35. Mott-Schottky plots for (a) CN90-f and (b) CN90-s at different frequencies. The potentials of flat band (E_{fb}) are determined at -1.32 and -1.24 V for CN90-s and CN90-f *versus* Ag/AgCl based on the Mott-Schottky formula, which is further converted into -1.12 and -1.04 V *versus* normal hydrogen electrode (NHE) according to the equation of $E_{NHE} = E_{\text{Ag}/\text{AgCl}} + 0.197$ V. For many n-type semiconductors, E_{fb} is considered to be about 0.1 V more positive than its conduction band potentials (E_{CB}). Therefore, the E_{CB} of CN90-s and CN90-f is estimated to be about -1.22 and -1.14 V (vs. NHE, PH = 7).

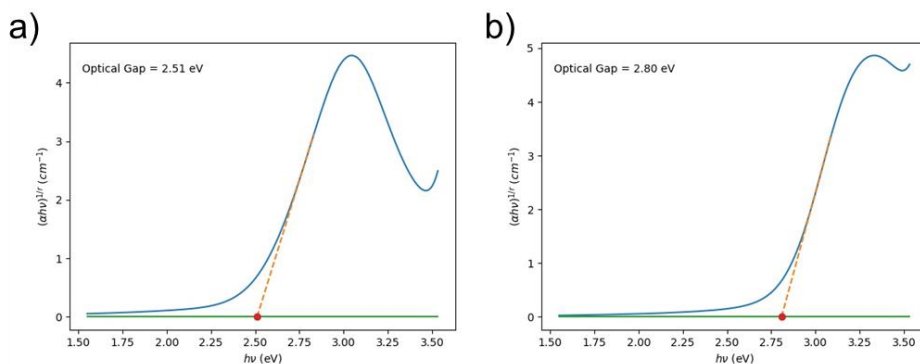


Figure 4.35. a) Bandgap of CN90-f determined by Tauc plots. b) Bandgap of CNP-90 determined by Tauc plots. The bandgap of CN90-s and CN90-f is 2.80 and 2.51 eV, respectively. The valence band potentials (E_{VB}) of CN90-s and CN90-f are calculated to be 1.58 and 1.37 V via equation E_{VB} = E_{CB} + E_g.

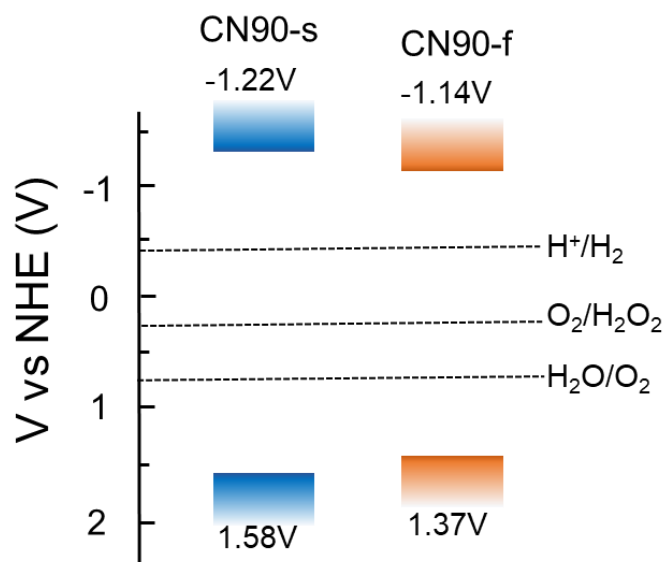


Figure 4.36. Schematic diagram of the energy levels of CN90-s and CN90-f.

4.5.3 Stability

After 27 hours photocatalytic hydrogen evolution, no decomposition on structure and morphology of CN90-f was observed as revealed by ¹H NMR (**Figure 4.38**) and HRTEM (**Figure 4.39**). Lattice spacing and energy-dispersive X-ray spectroscopy (EDX) analysis confirmed the presence of Pt with well-defined 3-nm sized Pt nanoparticles on CN90-f surface (**Figures 4.39 and 4.40**).

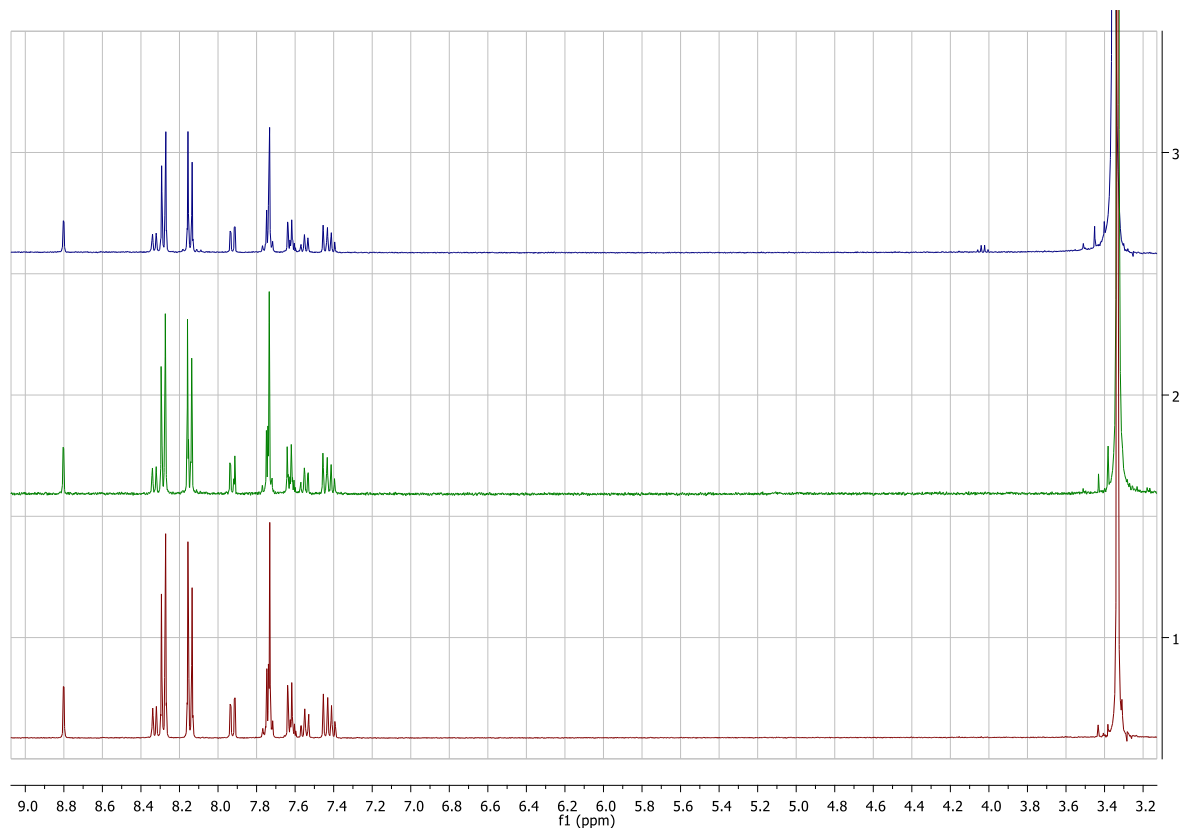


Figure 4.37. ¹H NMR spectrum of CNP-90 (top) and CNP-90 (middle) after photocatalytic H₂ production experiment and CN90 molecule (bottom) before photocatalysis.

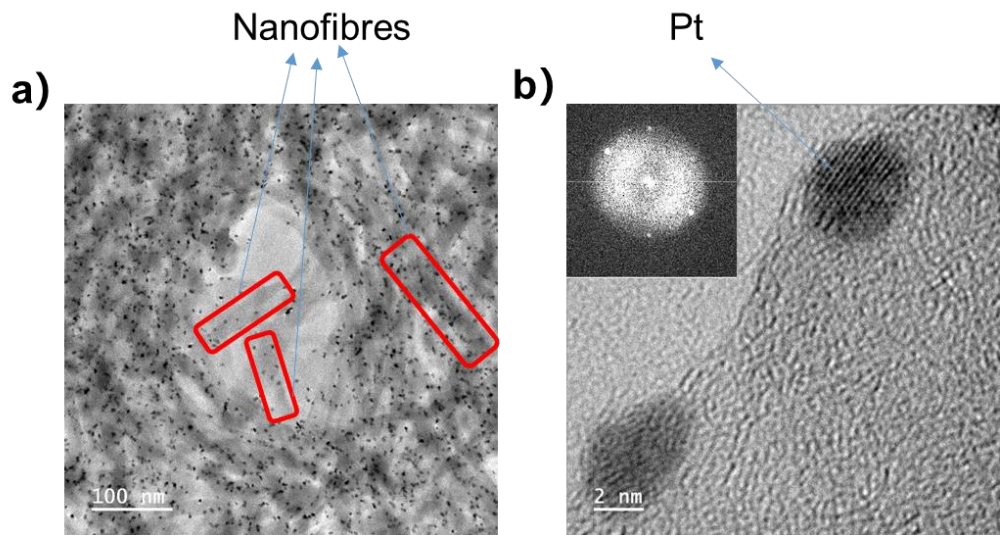


Figure 4.38. a) HRTEM images of CN90-f with Pt nanoparticles after photocatalysis. b) Fast Fourier transform analysis showing (111) planes of Pt metal with 0.22 nm *d*-spacing.

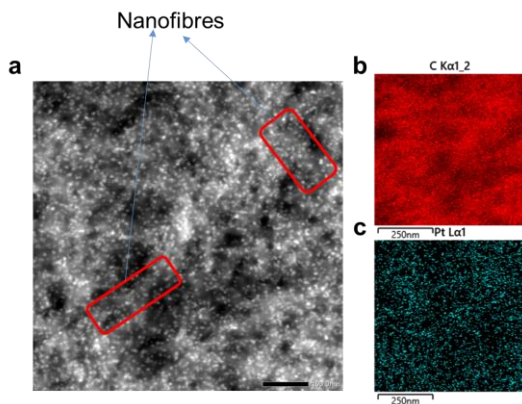


Figure 4.40. **a)** Images of CN90-f with Pt nanoparticles. **b)** and **c)** EDX maps of **(b)** C and **(c)** Pt.

CN90-s showed continuous H_2O_2 production over 125 hours irradiation (**Figure 4.41**). However, ^1H NMR spectra of CN90-s after long-term photoreaction showed the occurrence of decomposition of CN90 (**Figure 4.42**). In photocatalytic water oxidation, the formation of N_2 , a self-oxidation product of nitrogen-contained photocatalyst by photogenerated holes,³⁷ was observed. Also, the decomposition of CN90-s in photocatalytic H_2O_2 production was mitigated by the presence of an electron donor, ascorbic acid (**Figure 4.43**). Thus, we infer based on the above observations that the decomposition to CN90-s is mainly due to the self-oxidation by photogenerated holes. We suggest that the photostability of CN90-s could be improved by introducing proper water oxidation co-catalyst, as exemplified on other organic photocatalysts.³⁸

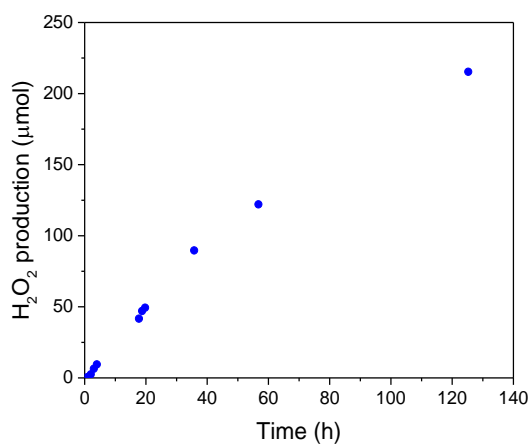


Figure 4.39. Time course of H_2O_2 production irradiated by 300 W Xe lamp fitted with a $\lambda > 420$ nm filter using 30 mg of CN90-s in O_2 environment.

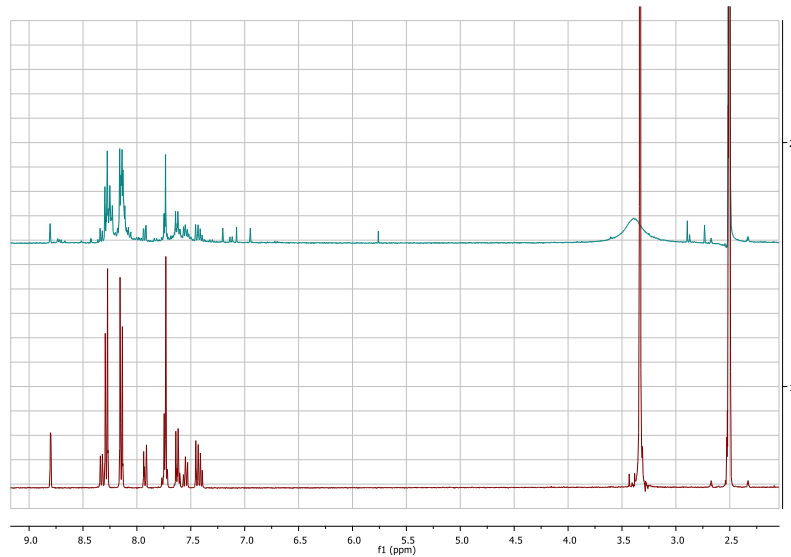


Figure 4.40. ¹H NMR spectrum of CN90-s before (bottom) and after (top) photocatalytic H₂O₂ production. Testing conditions: catalyst concentration: 50 mg in 30 mL water; irradiation time = 125 hours; light source = 300 W Xe lamp fitted with a $\lambda > 420$ nm filter; gas environment = O₂.

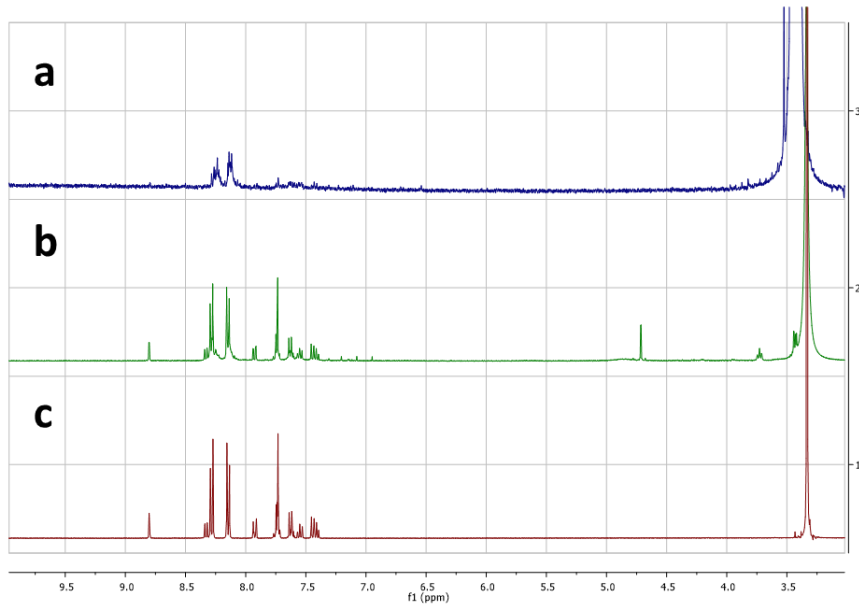


Figure 4.41. ¹H NMR spectrum of CN90-s after (top) and before (bottom) photocatalytic H₂O₂ production without AA, and ¹H NMR spectrum of CN90-s after (middle) photocatalytic H₂O₂ production with AA (0.1 M). Testing conditions: catalyst concentration = 0.167 mg mL⁻¹ (5 mg in 30 mL water); irradiation time = 5 hours; light source = 300 W Xe lamp fitted with a $\lambda > 420$ nm filter; scavenger = with or without 0.1M AA; gas environment = O₂.

4.6. Conclusions

In summary, we have synthesised a small organic molecule (CN90) bearing pyridinedicarbonitrile derivative as acceptor unit (A) and carbazole as donor unit (D). This molecule (solution-state) achieved a remarkable Stokes shift of 301 nm and a large 14.0 Debye dipole of excited state. A nanoprecipitation method was applied to prepare CN90 nanoparticles. The morphology of CN90 nanoparticles can be finely controlled by simply changing the ratio of THF to H₂O. Morphology transformation was also observed showing that nanospheres (CN90-s) in an amorphous state are initially formed and then transform to nanofibres (CN90-f) with ordered π-π stacking structure. The change in molecular packing leads to the conversion of intramolecular interaction to intermolecular interaction, which results in different optical and electrochemical properties of CN90-s and CN90-f.

Interestingly, compared to nanospheres (0.44 mmol g⁻¹ h⁻¹), nanofibres (31.85 mmol g⁻¹ h⁻¹) showed a more than 72 times higher photocatalytic H₂ production rate under the identical test conditions. On the other hand, CN90-s produce H₂O₂ with a high rate of 3.56 mmol g⁻¹ h⁻¹ from pure water, but its counterpart, CN90-f, is inactive for H₂O₂ production under the same photocatalytic measurement conditions. Both H₂O₂ and H₂ production rates achieved by CN90-s and CN90-f, respectively, are one of the highest values ever reported on small organic molecule base photocatalyst in the literature. The different aggregate states result in their photophysical properties, such as energy band levels and light absorption, being different, which triggers the photocatalytic direction switching between photocatalytic H₂ evolution and H₂O₂ production. The presence of π-π stacking is beneficial to charge separation and transfer along molecular stacking direction in nanofibres as well as light absorption, which significantly improved the H₂ production efficiency of CN90-f, compared to amorphous CN90-s. However, the CN90-f is completely inactive for photocatalytic H₂O₂ production from neat water in the presence of O₂, although possessing the preferred characteristics for photocatalysis. CN90-f has reduced redox potentials for oxygen reduction and water oxidation, though, their driving forces are still thermodynamically enough. An efficient photocatalytic H₂O₂ production rate was achieved on CN90-s that have a large driving force for oxygen reduction and water oxidation though it is amorphous. The D-A characteristic of CN90 molecule and its large dipole of excited state (14.0 Debye), help to build in electric field in molecule, which promotes charge separation and facilitates the photocatalytic performances. This study will have significant and general impacts on the preparation of small organic nanostructures with tunable morphology,

and the development of highly efficient organic molecule-based nanocatalysts.

4.7. Experimental

4.7.1. Preparation Methods

Materials: All the reagents and solvents used for the synthesis were commercially available from Alfa Aesar, Sigma-Aldrich, Fluorochem, Tokyo Chemical Industry, Carbosynths, and used as received without further purification. Tetrahydrofuran (anhydrous, inhibitor-free) was obtained from Sigma-Aldrich. The deionized water was obtained from a Milli-Q System ($\rho = 15 \text{ M}\Omega$).

Synthesis of 2,6-bis(4-cyanophenyl)-4-(9-phenyl-9H-carbazol-3-yl)pyridine-3,5-dicarbonitrile (CN90): 5 mmol (0.850) (4-(2-cyanoacetyl)benzonitrile), 3 mmol 9-Phenyl-9H-carbazole-3-carboxaldehyde (0.813 g), and 15 mmol ammonium acetate (1.15 g) were discharged into the reaction flask, then 15 ml acetic acid was added. The reaction mixture was heated to 110 °C for overnight. The resultant precipitates were filtered and washed with methanol. Then, the solids were oxidised with 2,3-dichloro-5,6-dicyano-*p*-benzoquinone in acetic acid solution under 110 °C for 1 hour, followed by filtration and methanol washing. The solids were purified by column, giving the final product as an orange powder (yield = 83%). ^1H NMR (400 MHz, DMSO) δ 8.80 (dd, $J = 1.8, 0.5$ Hz, 1H), 8.33 (d, $J = 7.6$ Hz, 1H), 8.31-8.25 (m, 4H), 8.18-8.10 (m, 4H), 7.92 (dd, $J = 8.6, 1.8$ Hz, 1H), 7.78-7.70 (m, 4H), 7.67-7.59 (m, 2H), 7.55 (ddd, $J = 8.3, 7.1, 1.2$ Hz, 1H), 7.48-7.37 (m, 2H). Chemical Formula: C₃₉H₂₀N₆, Elemental Analysis: calcd., C, 81.80; H, 3.52; N, 14.68; found C, 81.31; H, 3.47; N, 14.57. HRMS (m/z): [MH]⁺ calcd. 573.1822; found 573.1816.

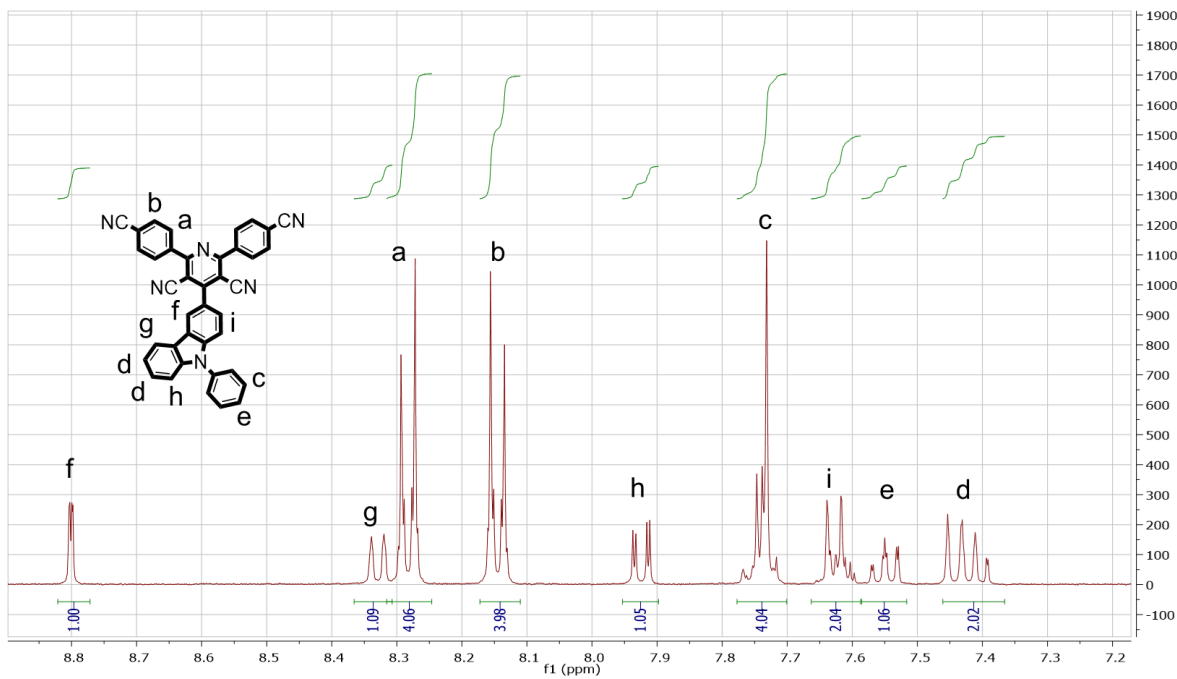


Figure 4.42. ^1H NMR spectrum of CN90 molecule. The peak of residual impurity corresponds to water (3.33 ppm).

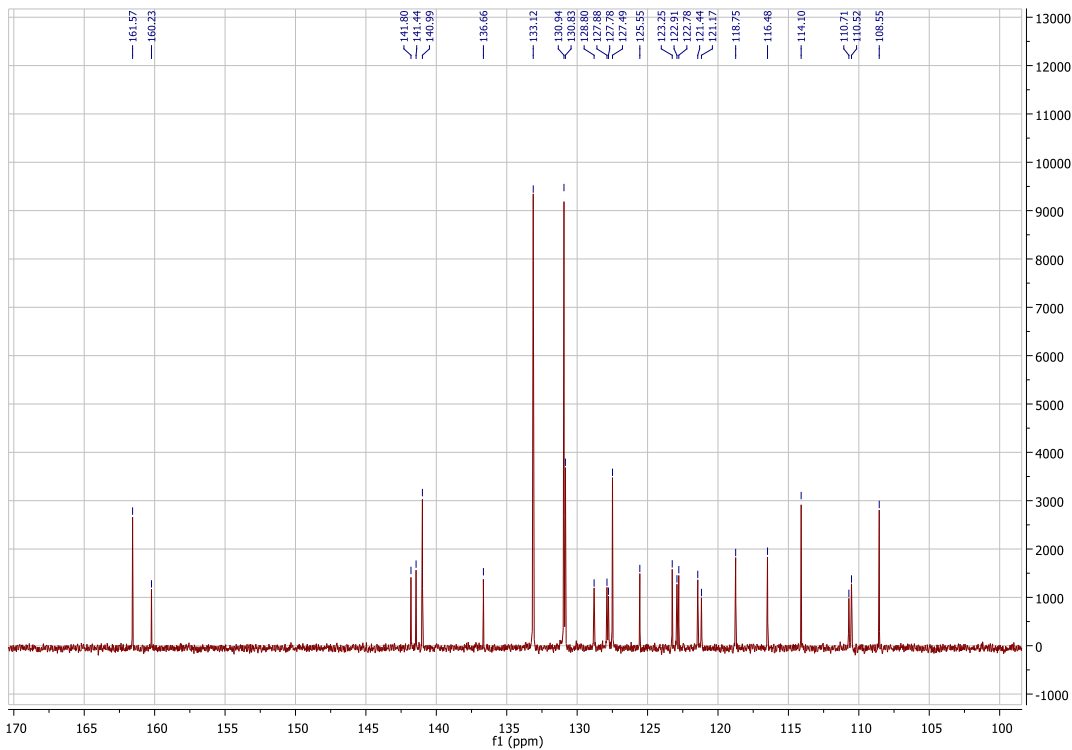


Figure 4.43. ^{13}C NMR spectrum of CN90 molecule.

Synthesis of CN90 nanoparticles: The CN90 molecule was dissolved in anhydrous THF with a concentration of 10 mg mL^{-1} , 5 mg mL^{-1} , 2.5 mg mL^{-1} , 1 mg mL^{-1} , 0.5 mg mL^{-1} , and 0.25 mg mL^{-1} .

mL^{-1} , respectively, serving as stock solution. A specific volume of stock solution was added rapidly into a vial containing 5 mL of deionized water under continuous sonication for around 5 seconds, resulting in the formation of CN90-s-X and CN90-f-X, where X is the THF to H_2O volume ratio. To prepare nanospheres, 50 μL of 10 mg mL^{-1} , 100 μL of 5 mg mL^{-1} , and 200 μL of 2.5 mg mL^{-1} stock solution were used to produce CN90-s- $1/100$, CN90-s- $1/50$, and CN90-s- $1/25$, respectively. To prepare nanofibres, 500 μL of 1 mg mL^{-1} , 1 mL of 0.5 mg mL^{-1} , and 2 mL of 0.25 mg mL^{-1} stock solution were used to produce CN90-f- $1/10$, CN90-f- $1/5$, and CN90-f- $2/5$, respectively. For photocatalytic measurements, THF is removed by placing all samples in a cover-free sample holder on a hot plate at 130 °C for 5 hours.

4.7.2. Characterisation Methods

^1H and ^{13}C NMR spectra were carried out on Bruker Avance 400 NMR spectrometer at 400 MHz and 100 MHz, respectively. The scanning electron microscope (SEM) measurements were performed on Hitachi S-4800 cold field emission scanning electron microscope (FE-SEM) at a working voltage of 10 kV and a working distance of around 8.4 mm. The transmission electron microscope (TEM) measurements were operated on a JEOL 2100 Plus microscopy at a low accelerating voltage of 200 kV. Powder X-ray diffraction (PXRD) measurements were performed under high throughput transmission mode, using a Panalytical Empyrean diffractometer, X-ray focusing mirror, and PIXcel detector with Cu $\text{K}\alpha$ radiation. Thermogravimetric analysis (TGA) was performed on an EXSTAR6000 under nitrogen in open aluminium pans. Fourier-transform infrared spectroscopy (FT-IR) was measured on a Bruker Tensor 27 FT-IR spectrometer using bulk sample and an ATR attachment (16 scans). Raman spectroscopy was performed on inVia reflex qontor confocal Raman microscope using 785 nm laser. UV-visible absorption spectra were recorded on a Shimadzu UV-2550 UV-vis spectrometer at room temperature. For in-situ measurement, 0.5 mL of THF containing 0.1 mg of CN90 was added into 5 mL of deionized water, and then half of this solution is added into a quartz cuvette quickly before recording the adsorption spectrum every 1.5 min. Steady-state photoluminescence spectra and time-correlated single photon counting (TCSPC) measurements were performed on an Edinburgh Instruments LS980-D2S2-STM spectrometer equipped with picosecond pulsed LED excitation sources (excitation = 390 nm) and a R928 detector, with a stop count of 2000. An EPL-375 diode ($\lambda = 370.5 \text{ nm}$, instrument response 100 ps, fwhm) for emission detection was used. Colloidal silica (LUDOX HS-40, Sigma-Aldrich) was used to measure the instrument response (IRF). Decay times were fitted in the FAST software using suggested lifetime estimates and were finally determined by the Chi square. For

in-situ UV/Vis absorption measurement, 0.5 mL THF containing 0.5 mg of CN90 was added into 5 mL deionized water, and then this solution was diluted by 10 times with THF/H₂O mixture (0.5 mL THF and 5 mL water) before recording absorption spectra. For in-situ emission and lifetime decay measurements, 0.5 mL THF containing 0.5 mg of CN90 was added into 5 mL deionized water, and then this solution is added into a quartz cuvette quickly before recording emission and lifetime decay spectra. Single crystal X-ray data for CN90 was measured on a Rigaku MicroMax-007 HF rotating anode diffractometer (Mo-K α radiation, $\lambda = 0.71073 \text{ \AA}$, Kappa 4-circle goniometer, Rigaku Saturn724+ detector) and data reduction was performed using CrysAlisPro.

4.7.3. Measurement Methods

4.7.3.1. Photocatalysis Measurements

The high throughput measurements: The catalysts (0.5 mg) were dispersed into 0.04 M ascorbic acid water solution (5 mL) with diluted hexachloroplatinic acid solution as a platinum precursor (3%) in small vials (Volume = 12.5 mL). After purging with nitrogen in a Sweigher Chemspeed Technologies robot for 3 hours, these vials were sealed with pierceable caps. Then, all sample vials were irradiated under a solar simulator (AM1.5G, Class AAA, IEC/JIS/ASTM, 1440 W xenon, 12 × 12 in., MODEL:94123A) equipped with a roller device. Gaseous products were analyzed on a Shimadzu GC-2010 equipped with Shimadzu HS-20 thought injecting a sample from the headspace sampler via a transfer line (temperature 150 °C) onto a Rt-Msieve 5 Å column with He as the carrier gas (30 mL min⁻¹). Hydrogen was detected with a barrier discharge ionisation detector referencing against standard gas with a known concentration of hydrogen. Control experiments showed that no hydrogen production occurred in the absence of a photocatalyst, illumination, or a hole scavenger. For H₂O₂ measurement, the catalyst solutions (0.5 mg in 5 mL water) with or without sacrificial agents (10 mM) were sealed in small vials (Volume = 12.5 mL). After purging with oxygen for 2 min, all sample vials were irradiated under a solar simulator (AM1.5G, Class AAA, IEC/JIS/ASTM, 1440 W xenon, 12 × 12 in., MODEL:94123A) equipped with a roller device. 1 mL of solution was filtrated with a 0.22 μm filter to remove the photocatalyst, and the amount of H₂O₂ generated was quantified using UV-vis spectroscopy.

The Kinetic measurements: Kinetic H₂ production measurements were conducted in a 75 mL quartz flask using a 300 W Newport Xe light-source (Model: 6258, Ozone free) equipped with a $\lambda > 420 \text{ nm}$ cut-off filter. 25 mL of CN90-s or CN90-f aqueous suspension (0.1 mg mL⁻¹),

440 mg of ascorbic acid, and a certain amount of hexachloroplatinic acid solution were added into the flask. This solution was then purged with N₂ for at least 30 min to remove O₂. Gas products were taken with a gas-tight syringe and then run through a Molecular Sieve 13X 60-80 mesh 1.5 m × 1/8" × 2 mm ss column at 50 °C with an argon flow of 40.0 mL min⁻¹ by using Bruker 450-GC gas chromatograph equipped with a thermal conductivity detector referencing against standard gas with a known concentration of hydrogen. Hydrogen dissolved in the reaction mixture was not measured. Kinetic H₂O₂ production measurements were conducted in a 75 mL quartz flask using a 300 W Newport Xe light-source (Model: 6258, Ozone free) equipped with a λ > 420 nm cut-off filter. Around 30 mL of CN90-s or CN90-f (5 mg) aqueous suspension was bubbled with oxygen for 15 min. At certain time intervals, 1 mL solution was sampled and filtrated with a 0.22 μm filter to remove the photocatalyst. Then the amount of H₂O₂ generated was quantified using UV-vis spectroscopy. Kinetic O₂ production measurements were carried out on the Perfect Light system at 12 °C using a 300 W xenon lamp with λ > 420 nm cut-off filter. 50 mg of CN90-s were dispersed in 100 mL of 10 mM AgNO₃ (aq) solution with 0.2 g La₂O₃ in the reaction cell with a magnetic stirrer.

Hydrogen peroxide analysis: The amount of H₂O₂ was analyzed by iodometry.⁴¹ 0.5 mL of filtrated solution, 1 mL of 0.1 mol L⁻¹ potassium hydrogen phthalate (C₈H₅KO₄) aqueous solution, and 1 mL of 0.4 mol L⁻¹ potassium iodide (KI) aqueous solution were mixed, which was then kept in dark for 30 min. The H₂O₂ molecules reacted with iodide anions (I⁻) under acidic conditions to produce triiodide anions (I³⁻) possessing a strong absorption at around 350 nm.⁴¹ The amount of I³⁻ was determined using UV-vis spectroscopy based on the absorbance at 350 nm, from which the amount of H₂O₂ produced during each reaction was estimated.

4.7.3.2. Apparent Quantum Yield Measurements

The apparent quantum yield for the photocatalytic H₂ evolution was measured using a λ = 395 nm LED, λ = 405 nm LED, λ = 420 nm LED, and λ = 490 nm LED controlled by an IsoTech IPS303DD power supply. For the measurement, 8 vials of CN90-f sample (each vial containing 0.1 g NaBr), prepared by nanoprecipitation strategy, were mixed together and then diluted to 25 mL with deionized water. Then, 440 mg of ascorbic acid (0.1 M) and diluted hexachloroplatinic acid (3% Pt loading) were added before illuminating with LED. The light intensity was measured with a ThorLabs S120VC photodiode power sensor controlled by a ThorLabs PM100D Power and Energy Meter Console and the apparent quantum yield was estimated using the equation below:

$$AQY = 2 \times \frac{\text{moles of hydrogen evolved}}{\text{moles of incident photons}} \times 100\% \quad (4.5)$$

4.7.3.3. Density Functional Theory Calculations

The structure of CN90 was optimized by CAM-B3LYP density functional,⁴² together with the 6-31G* basis set, using the Gaussian 16 software. Frequency calculation was carried out to ensure there is no imaginary frequency. The effect of solvation by DMF was accounted for by using the PCM/SMD solvation model. The lowest-lying excited states were studied by the TD-DFT method based on the optimised geometry with the same level of theory. Properties of excited states were calculated by Multiwfn.^{43,44} The overlap between the hole distribution and the electron distribution index S_r is 0.37 a.u., electron-hole separation distance index D is 5.2 Angstrom, charge separation index t is 2.92 Angstrom, these three parameters all indicate that electron and hole are largely separated. The dipole moment of the ground state is 7.6 Debye and that of the excited state is 17.5 Debye, which is consistent with the experimentally measured value of 14.0 Debye, also confirming the charge separation for the first excited states.

4.7.3.4. Photoelectrochemical Measurements

Photocurrent response and Mott-Schottky measurements were performed using a three-electrode setup containing working electrode (samples on FTO), counter electrode (Pt wire), and reference electrode (Ag/AgCl) on Bio-logic SP200 workstation. The light source was a solar simulator with light intensity of 1 sun. The electrolyte (0.5M Na₂SO₄) was degassed for 30 min by bubbling with N₂ before the measurement. The electrochemical impedance spectroscopy (EIS) spectra and photocurrent were recorded at -0.1 V vs. Ag/AgCl. For sample preparation, 0.5 mg of samples were mixed with 50 μL of water and 5 μL of Nafion (5 wt. %). After sonication for 10 min, 20 μL of this mixed solution was dropped onto FTO glass for measurements (1 cm²).

4.8. References

- 1 Z. Zhang, Y. Zhu, X. Chen, H. Zhang and J. Wang, *Adv. Mater.*, 2019, **31**, 1–6.
- 2 A. Dhara, T. Sadhukhan, E. G. Sheetz, A. H. Olsson, K. Raghavachari and A. H. Flood, *J. Am. Chem. Soc.*, 2020, **142**, 12167–12180.
- 3 G. Zhang, X. Yang, Y. Li, P. Zhang and H. Mi, *ChemSusChem*, 2019, **12**, 5070–5074.
- 4 Q. Li and Z. Li, *Acc. Chem. Res.*, 2020, **53**, 962–973.
- 5 N. Zhang, L. Wang, H. Wang, R. Cao, J. Wang, F. Bai and H. Fan, *Nano Lett.*, 2018, **18**, 560–566.
- 6 G. Yang, C. Lin, X. Feng, T. Wang and J. Jiang, *Chem. Commun.*, 2020, **56**, 527–530.
- 7 K. Kong, S. Zhang, Y. Chu, Y. Hu, F. Yu, H. Ye, H. Ding and J. Hua, *Chem. Commun.*, 2019, **55**, 8090–8093.
- 8 A. S. Weingarten, R. V. Kazantsev, L. C. Palmer, D. J. Fairfield, A. R. Koltonow and S. I. Stupp, *J. Am. Chem. Soc.*, 2015, **137**, 15241–15246.
- 9 M. Xu, K. Kong, H. Ding, Y. Chu, S. Zhang, F. Yu, H. Ye, Y. Hu and J. Hua, *J. Mater. Chem. C*, 2020, **8**, 930–934.
- 10 O. Dumele, J. Chen, J. V. Passarelli and S. I. Stupp, *Adv. Mater.*, 2020, **32**, 1–32.
- 11 P. Guo, P. Chen, W. Ma and M. Liu, *J. Mater. Chem.*, 2012, **22**, 20243–20249.
- 12 M. C. Nolan, J. J. Walsh, L. L. E. Mears, E. R. Draper, M. Wallace, M. Barrow, B. Dietrich, S. M. King, A. J. Cowan and D. J. Adams, *J. Mater. Chem. A*, 2017, **5**, 7555–7563.
- 13 J. Brinckmann, H. Notbohm and P. K. Müller, *Unimolecular and Supramolecular Electronics I*, 2005, vol. 247.
- 14 R. V. Kazantsev, A. J. Dannenhoffer, A. S. Weingarten, B. T. Phelan, B. Harutyunyan, T. Aytun, A. Narayanan, D. J. Fairfield, J. Boekhoven, H. Sai, A. Senesi, P. I. O'Dogherty, L. C. Palmer, M. J. Bedzyk, M. R. Wasielewski and S. I. Stupp, *J. Am. Chem. Soc.*, 2017, **139**, 6120–6127.
- 15 J. Wang, W. Shi, D. Liu, Z. J. Zhang, Y. Zhu and D. Wang, *Appl. Catal. B Environ.*, 2017, **202**, 289–297.
- 16 J. Wang, D. Liu, Y. Zhu, S. Zhou and S. Guan, *Appl. Catal. B Environ.*, 2018, **231**, 251–261.
- 17 A. Kudo and Y. Miseki, *Chem. Soc. Rev.*, 2009, **38**, 253–278.
- 18 G. Zhang, Z. A. Lan and X. Wang, *Angew. Chemie - Int. Ed.*, 2016, **55**, 15712–15727.
- 19 X. Zeng, Y. Liu, X. Hu and X. Zhang, *Green Chem.*, 2021, **23**, 1466–1494.
- 20 H. Hou, X. Zeng and X. Zhang, *Angew. Chemie - Int. Ed.*, 2020, **59**, 17356–17376.

- 21 A. C. Benniston, A. Harriman, D. J. Lawrie and A. Mayeux, *Phys. Chem. Chem. Phys.*, 2004, **6**, 51–57.
- 22 H. Beens, H. Knibbe and A. Weller, *J. Chem. Phys.*, 1967, **47**, 1183–1184.
- 23 Y. Guo, W. Shi and Y. Zhu, *EcoMat*, 2019, **1**, 1–20.
- 24 S. Schubert, J. T. Delaney and U. S. Schubert, *Soft Matter*, 2011, **7**, 1581–1588.
- 25 G. Qian, Z. Zhong, M. Luo, D. Yu, Z. Zhang, Z. Y. Wang and D. Ma, *Adv. Mater.*, 2009, **21**, 111–116.
- 26 J. V. Caspar and T. J. Meyer, *J. Phys. Chem.*, 1983, **87**, 952–957.
- 27 S. Ogi, K. Sugiyasu, S. Manna, S. Samitsu and M. Takeuchi, *Nat. Chem.*, 2014, **6**, 188–195.
- 28 G. Q. Zhang, W. Ou and Y. Sen Xu, *Sci. China Mater.*, 2018, **61**, 1001–1006.
- 29 C. M. Aitchison, C. M. Kane, D. P. Mcmahon, P. R. Spackman, A. Pulido, X. Wang, L. Wilbraham, L. Chen, R. Clowes, M. A. Zwijnenburg, R. S. Sprick, M. A. Little, G. M. Day and A. I. Cooper, *J. Mater. Chem. A*, 2020, **8**, 7158–7170.
- 30 H. Shigemitsu, Y. Tani, T. Tamemoto, T. Mori, X. Li, Y. Osakada, M. Fujitsuka and T. Kida, *Chem. Sci.*, 2020, **11**, 11843–11848.
- 31 A. S. Weingarten, R. V. Kazantsev, L. C. Palmer, M. McClendon, A. R. Koltonow, A. P. S. Samuel, D. J. Kiebala, M. R. Wasielewski and S. I. Stupp, *Nat. Chem.*, 2014, **6**, 964–970.
- 32 Y. Shiraishi, S. Kanazawa, Y. Kofuji, H. Sakamoto, S. Ichikawa, S. Tanaka and T. Hirai, *Angew. Chemie - Int. Ed.*, 2014, **53**, 13454–13459.
- 33 Y. Kofuji, Y. Isobe, Y. Shiraishi, H. Sakamoto, S. Tanaka, S. Ichikawa and T. Hirai, *J. Am. Chem. Soc.*, 2016, **138**, 10019–10025.
- 34 M. K. Węsławski, M. Jakešová, M. Charyton, N. Demitri, B. Koszarna, K. Oppelt, S. Sariciftci, D. T. Gryko and E. D. Głowacki, *J. Mater. Chem. A*, 2017, **5**, 20780–20788.
- 35 M. Gryszel, R. Rybakiewicz and E. D. Głowacki, *Adv. Sustain. Syst.*, 2019, **3**, 1–9.
- 36 M. Gryszel, M. Sytnyk, M. Jakešová, G. Romanazzi, R. Gabrielsson, W. Heiss and E. D. Głowacki, *ACS Appl. Mater. Interfaces*, 2018, **10**, 13253–13257.
- 37 K. Maeda, X. Wang, Y. Nishihara, D. Lu, M. Antonietti and K. Domen, *J. Phys. Chem. C*, 2009, **113**, 4940–4947.
- 38 J. Zhang, M. Grzelczak, Y. Hou, K. Maeda, K. Domen, X. Fu, M. Antonietti and X. Wang, *Chem. Sci.*, 2012, **3**, 443–446.
- 39 T. J. Miao and J. Tang, *J. Chem. Phys.*, 2020, **152**, 194201.
- 40 S. Liu, X. Wang, H. Liu, L. Shen, D. Zhao and X. Li, *J. Mater. Chem. C*, 2020, **8**, 3536–3544.

- 41 Z. Wei, M. Liu, Z. Zhang, W. Yao, H. Tan and Y. Zhu, *Energy Environ. Sci.*, 2018,
11, 2581–2589.
- 42 T. Yanai, D. P. Tew and N. C. Handy, *Chem. Phys. Lett.*, 2004, **393**, 51–57.
- 43 T. Lu and F. Chen, *J. Comput. Chem.*, 2012, **33**, 580–592.
- 44 Z. Liu, T. Lu and Q. Chen, *Carbon N. Y.*, 2020, **165**, 461–467.

Chapter 5

Summary & outlook

Organic photocatalysts generally have strong exciton binding energies and low charge carrier mobilities, resulting in the recombination of photogenerated charge carriers which limits photocatalytic activity.¹ In this thesis, we addressed these issues by introducing organic/inorganic or organic/organic interfaces or D-A structure into organic nanoparticles which facilitates the charge separation. As a result, significant improvements in photocatalytic H₂ evolution performance were achieved.

The nanocomposite of inorganic semiconductor (TiO₂ dots, TDs) and organic polymer (cyano-substituted soluble conjugated polymer, CSCP) was prepared using emulsion evaporation induced self-assembly method. Introducing TDs in polymer matrix results in changes in light absorption, PL emission, and emission decay behaviors of polymer because of the energy transfer between TDs and CSCP NPs. The nanocomposites NC10% achieved improved photocatalytic H₂ production performance ($1.37 \text{ mmol g}^{-1} \text{ h}^{-1}$) compared with nanoparticle counterparts produced from CSCP nanoparticles, TDs nanoparticles, and bulk composite.

However, the highest HER achieved among these nanocomposites was around $1.3 \text{ mmol g}^{-1} \text{ h}^{-1}$, which is behind the levels of activities previously observed for bulk polymers or polymer nanoparticles along.^{2,3} The unsatisfactory performance is likely to be a result of the poor compatibility of organic/inorganic interfaces due to the polarity differences between inorganic and organic materials.⁴ Also, the hydrophobic surfactant on the surface of inorganic dots may reduce the chance of charge or energy transfer between inorganic dots and polymers. Therefore, the preparation of organic/organic nanocomposite without using any surfactant should be considered.

Then, we transferred the bulk heterojunction concept of OPV into organic photocatalysts by preparing donor/acceptor nanocomposites (DANCs) through a surfactant-free nanoprecipitation method. The high throughput synthesis and test methods allow us to quickly discover highly efficient binary DANCs with hydrogen production performance that greatly outperform the parent donors and acceptors. The best combination A1/D1 achieved an impressive HER of $383.4 \text{ mmol g}^{-1} \text{ h}^{-1}$ under irradiation of solar simulator. The kinetic HER measurement for this material showed an initial HER of $105.2 \text{ mmol g}^{-1} \text{ h}^{-1}$ ($120.9 \mu\text{mol h}^{-1}$) in the first 2 hours under visible light illumination, but the activity was gradually decreased in the next 18 hours irradiation. The stability of nanocomposite under irradiation remains an issue. Further investigations should focus on improving the stability of colloids catalysts.

Encouraged by the above result, we integrated the high throughput synthesis and test methods

with a machine learning strategy to accelerate the discovery of efficient ternary photocatalysts for H₂ evolution from water. The top 10 ternary nanocomposite photocatalysts achieved remarkable H₂ production rates (>500 mmol g⁻¹ h⁻¹), and the most efficient one showed an HER of 749.8 mmol g⁻¹ h⁻¹. In the future, an interesting extension would be to add oxygen evolution catalysts or co-catalysts into nanocomposite system to achieve overall water splitting. It would be also possible to add even more components into nanocomposite system, raising interest in multi-components optimisation. The charge transfer pathway and structure are not clear in these nanocomposites, which brings difficulty in the study of structure-activity relationships.

At last, we prepared organic nanoparticles with tunable morphology and molecular packing from a small organic molecule (CN90) that contained pyridinedicarbonitrile derivative as acceptor unit and carbazole as donor unit. This molecule assembles in THF/H₂O mixture solution from an amorphous state to order state along with morphology transformation from nanospheres (CN90-s) to nanofibres (CN90-f). The investigation in optical properties showed conversion from intramolecular interaction to intermolecular interaction when morphology transformation from nanospheres to nanofibres. Different molecular packing was proposed to be the reason for this interaction and morphology transformation, which leads to different excited state kinetics and photocatalytic performance of CN90-s and CN90-f.

The CN90-f (31.85 mmol g⁻¹ h⁻¹) showed a more than 72 times higher photocatalytic H₂ production rate (31.85 mmol g⁻¹ h⁻¹ for CN90-f versus 0.44 mmol g⁻¹ h⁻¹ for CN90-s), but a much lower H₂O₂ production rate than CN90-s under the same conditions (negligible for CN90-f versus 3.56 mmol g⁻¹ h⁻¹ for CN90-s). This H₂O₂ and H₂ production performance placed CN90-s and CN90-f among the most efficient small organic molecule-based photocatalysts for H₂O₂ and H₂ production, respectively. This demonstrates the potential to tune the packing mode of organic aggregate for multiple photocatalysis reactions and establish structure-activity relationships. However, we found the decomposition of CN90-s in photocatalytic H₂O₂ production probably because of the self-oxidation by photogenerated holes, which could be mitigated by introducing a proper water oxidation co-catalyst.⁵

We have demonstrated that the formation of nanocomposites or nanocomposites can improve photocatalytic H₂ production activities because the charge transfer between materials reduces the recombination of photogenerated electrons and holes. Also, particle size and packing mode can significantly affect photocatalytic performance. While we have achieved very high HER from these organic nanomaterials, long-term stability remains an issue. The photogenerated

charge carriers may decompose polymer itself rather than water, which is likely to be the main reason for the poor stability of these organic materials.⁵ The most effective way to increase stability is to suppress the reaction between polymer and charge carriers. Aggregation also could play a role in deactivation,⁶ but this is not clear and needs further investigation in the future. Some other strategies to address the stability issue might include using proper co-catalysts or inorganic supports such as silica gel or nano-clay. The future direction can also focus on combining an oxygen-evolving catalyst with a hydrogen-evolving catalyst for overall water splitting that does not rely on scavengers. Beyond this, it should be possible that these organic nanoparticle photocatalysts can be used in the field of CO₂ reduction, N₂ fixation, anti-bacterial, and so on.

In summary, we present effective strategies to make organic/inorganic nanocomposites, donor-acceptor nanocomposite, nanoparticles of a donor-acceptor organic molecule for photocatalytic hydrogen production. Hope that the findings of this thesis will encourage the development of organic nanoparticles and nanocomposites photocatalysts and, eventually, enable efficient, scalable, and stable solar fuel production from water.

References

- 1 Y. Chen, C. Yan, J. Dong, W. Zhou, F. Rosei, Y. Feng and L. N. Wang, *Adv. Funct. Mater.*, DOI:10.1002/adfm.202104099.
- 2 Y. Bai, L. Wilbraham, B. J. Slater, M. A. Zwijnenburg, R. S. Sprick and A. I. Cooper, *J. Am. Chem. Soc.*, 2019, **141**, 9063–9071.
- 3 C. M. Aitchison, R. S. Sprick and A. I. Cooper, *J. Mater. Chem. A*, 2019, **7**, 2490–2496.
- 4 S. L. Wu, F. Liu, H. C. Yang and S. B. Darling, *Mol. Syst. Des. Eng.*, 2020, **5**, 433–444.
- 5 J. Zhang, M. Grzelczak, Y. Hou, K. Maeda, K. Domen, X. Fu, M. Antonietti and X. Wang, *Chem. Sci.*, 2012, **3**, 443–446.
- 6 H. Yang, X. Li, R. S. Sprick and A. I. Cooper, *Chem. Commun.*, 2020, **56**, 6790–6793.